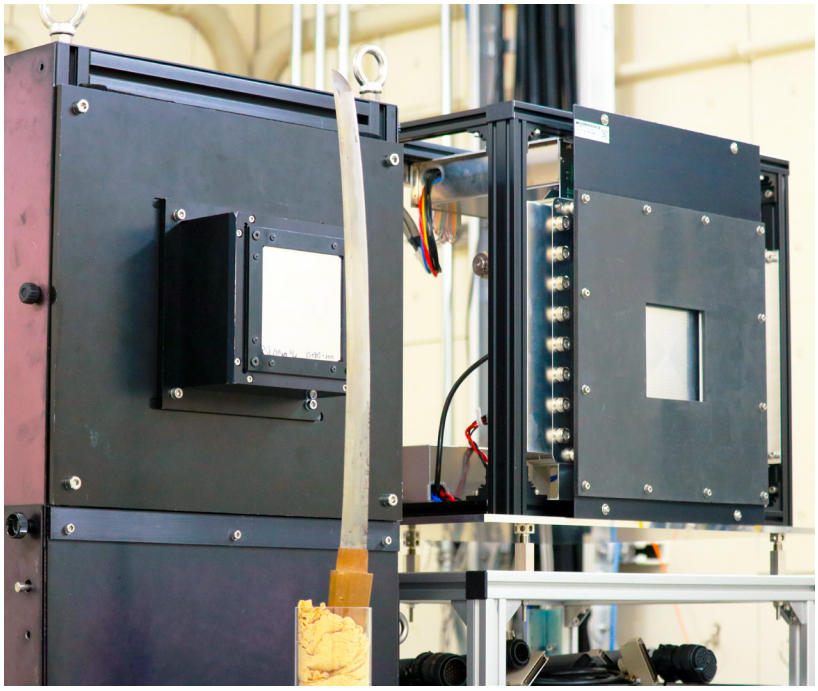

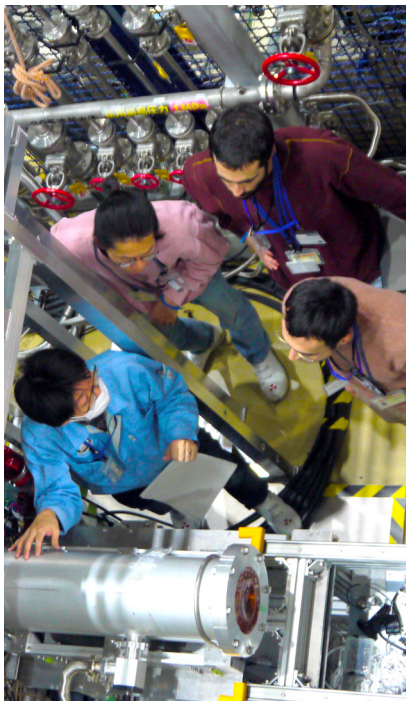

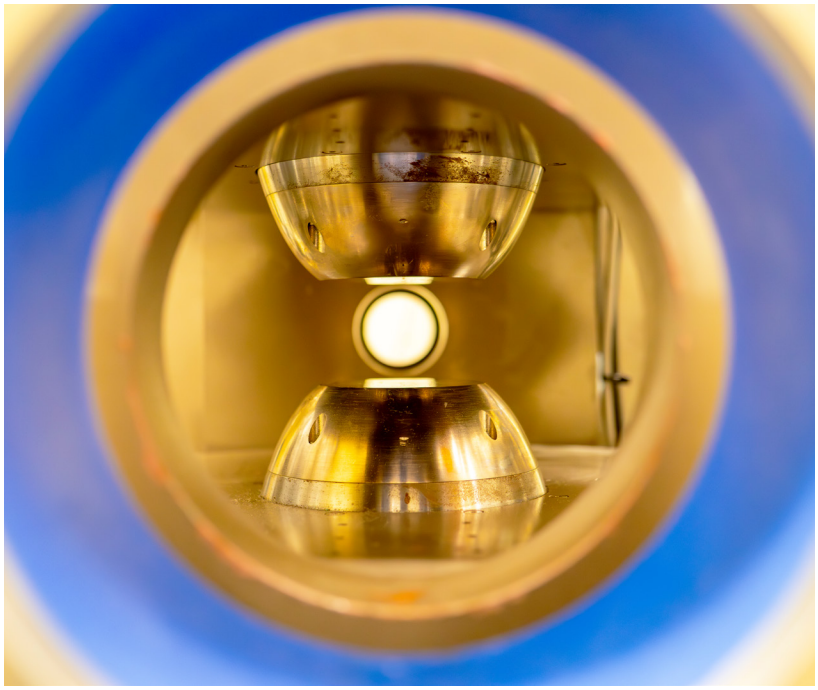

J-PARC

ANNUAL REPORT 2024

Vol.2: Materials and Life Science Experimental Facility

MLF ANNUAL REPORT

Cover photographs

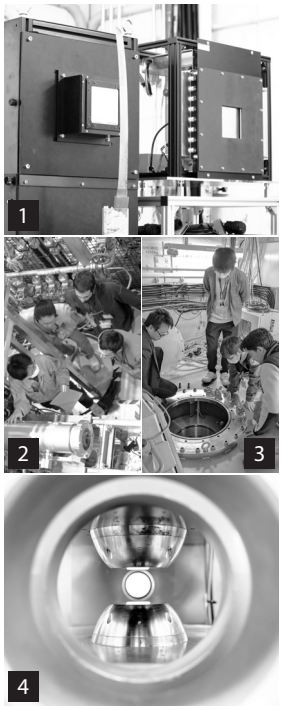

1 : Measuring a Japanese sword at the neutron imaging instrument, RADEN BL22

2 : Hans on experiment at the 8th Neutron and Muon School (Muon S1)

3 : Hans on experiment at the 8th Neutron and Muon School (NOVA BL21)

4 : A view of inside a dipole magnet installed at SHARAKU BL17

J-PARC MLF
Materials and Life Science Division
J-PARC Center
https://mlfinfo.jp/en

J-PARC was jointly constructed and is now operated by the High Energy Accelerator Research Organization (KEK) and the Japan Atomic Energy Agency (JAEA).

Comprehensive Research Organization for Science and Society
https://neutron.cross.or.jp/en

J-PARC 24-02

Preface

Toshiya Otomo
Division Head of Materials and Life Science Division, MLF

The neutron target system has undergone continuous improvements to achieve stable operation at 1 MW proton power and a 2-year lifetime for the target vessel. In 2024, MLF operated stably with a beam power equivalent to 1 MW (the highest record) from April 8th to May 29th. This marks a significant milestone for MLF. However, the neutron target system encountered difficulties since then, resulting in the outage of user programs. In June, there were issues with water detection in the Helium Vessel. In December, there was a gas leak from the mercury circulation system pipe. The former trouble led to the termination of the 2024A operation, a week earlier than initially planned. The latter terminated all user programs in FY 2024. This is a serious situation for MLF, and we sincerely apologize for the inconveniences caused by the outage.

In addition to the risk reduction of the neutron target system maintenance, the "MLF-double" project is underway to enhance the effectiveness of MLF. Not only scientific outcomes, but also strengthening the robustness of the facility operation, gaining neutron and muon flux at the sample position, constructing beamlines at vacant beam ports, forming sustainable development teams of devices and software, and so on are on the list of MLF-double, and some of them have already been completed. It is crucial to engage in discussions with the community regarding the MLF roadmap from short-term to long-term. MLF-double is the middle-term roadmap until 2030, and the target station two (TS2) aiming at starting user programs with TS2 until 2040 is the long-term one. These are continuous roadmaps to pursue higher potentialities of neutron and muon science. Opportunities to discuss with the community of MLF have been established since 2024. At the MLF symposium (domestic) in March 2024, MLF-double was presented. In the J-PARC symposium in October 2024, future plans of J-PARC, ISIS, SNS, ESS, and PSI were presented. Additionally, five satellite meetings of the J-PARC symposium were held: the 19th Korea-Japan Meeting on Neutron Science, Deuterium Science Entering an Advanced Phase, Future on Muon Elemental Analysis (FUME), the 9th International Symposium of Quantum Beam Science at Ibaraki University (ISQBS2024), and a Workshop on Polarized Neutron Sciences and Technology.

Advancements in neutron and muon science have led to the exploration of new fields. The application of muons to interdisciplinary studies with heritage science and quantum beams (muon, neutron, and synchrotron radiation) has emerged as a global trend. Two international conferences in this field were held in Cyprus and China: the International Conference on Neutron in Heritage Science (NHS2024). Additionally, the 9th Symposium on "Integration of Arts and Sciences" in Akihabara, Tokyo, attracted over 200 attendees, including online participants.

Two annual meetings were convened to identify new applications and fields for MLF activities. The Annual Meeting on Industrial Application for Neutron was held on July 21-22 as a hybrid meeting to effectively utilize MLF and the reactor neutron source JRR-3 of JAEA by enterprises and industries. Approximately 247 participants attended in person, while 135 participated online. MLF consistently engages with these parties and organizations to foster mutual benefits through the utilization of quantum beams. The Neutron & Muon School was held from December 9-13 as a KEK-IINAS School (Inter-Institution Network for Accelerator Science) at J-PARC and JRR-3 campuses. 72 participants attended online lectures, while 31 attended face-to-face lectures and theses-on-training sessions.

We will continue to maximize the utilization of MLF, one of the most advanced neutron and muon facilities. We cordially request your collaboration in shaping the profound impact of MLF activities.

Materials and Life Science Division, Japan Proton Accelerator Research Complex
https://mlfinfo.jp/en

Preface

Mitsuhiro Shibayama
Director, CROSS

The Comprehensive Research Organization for Science and Society (CROSS), a partner institution of the Materials and Life Science Experimental Facility (MLF), is honored to release the J-PARC MLF ANNUAL REPORT 2024 (MLF-AR2024), which includes sections on R&D Highlights, Neutron Sources, Neutron Science, Muon Science and more. The Neutron Science and Technology Center (NSTC) of the CROSS is a registered organization of the J-PARC's Specific Neutron Beamline Facility, appointed by the Japanese government in 2011. It supports the activities of the 7 public beamlines of the MLF (BL01 4SEASONS, BL02 DNA, BL11 PLANET, BL15 TAIKAN, BL17 SHARAKU, BL18 SENJU, and BL22 RADEN), provides high-quality user support to the MLF users, both academic and industrial researchers, and promotes the use of the facility. The CROSS established a new base, the Neutron Industrial Application Promotion Center (NIAPC) in April 2023, and from 2023, this center is in charge of the two beamlines of Ibaraki Prefecture (BL03 iBIX and BL20 iMATERIA).

In FY2024, there was the positive news that the pulsed neutron source at the J-PARC Materials and Life Science Experimental Facility (MLF) achieved its long-standing goal, set at the time of its construction, of "sustained operation at a proton beam power equivalent to 1000 kW (1 MW)" during the operational run that began on April 8, 2024. On the other hand, the 2024A user operation period (April to June) at the J-PARC MLF was limited to 68.5 days out of a planned 71.5 due to a malfunction of the MLF target. The 2024B period (November to March) was restricted to low-power operation for internal use only due to issues that included an issue with the mercury circulation system piping. As a result, user operation in FY2024 was limited to 68.5 days out of a planned 125. In the selection of general use (short-term) proposals for the 2024B period (November 2024 to March 2025), 151 proposals were submitted for the public neutron beamlines (367 for the entire MLF), and 52 were accepted (135 for the entire MLF), for an acceptance rate of 34%. Furthermore, as user operations for external users could not be conducted during the 2024B period, 53.5 days of experiments scheduled for that period have been postponed to the 2025A period. The total numbers of (short-term) neutron proposals submitted and accepted in the two proposal rounds in FY2024 were 727 and 332, respectively, and those for the Public Beamlines were 295 and 117, respectively. Despite these circumstances, many significant results have been produced by the MLF. As of the outcome, 213 scientific papers (excluding proceedings) were published from the MLF in 2024, among which were 79 papers from the Public Beamlines. The details are included in the Research and Development Highlights collected in this volume. The numbers of press releases were 22 from the MLF and 7 from the Public Beamlines, and 1 from the Ibaraki Prefecture Beamlines. These numbers illustrate the high level of activity of the Public Beamlines and the MLF, which have been used by a wide range of users from academia and various industries. The special program for new users "New User Promotion (NUP)", which started in 2016, continued its operation in 2024, and 6 NUP neutron users conducted experiments at the MLF. Meanwhile, the "Priority Use for National Projects" and "Promotion for Industrial Use," which were newly launched in fiscal year 2024, also had a call for proposals for the 2024B period.

Regarding public relations, CROSS is in charge of the secretariat for "J-JOIN", which is operated by J-PARC MLF, Ibaraki Prefecture, JRR-3 (JAEA and the University of Tokyo), and CROSS. It is working to further promote the use of neutrons by renewing the website. (https://j-join.cross.or.jp).

I hope this Annual Report will provide useful information on the current status of the MLF operations and recent scientific achievements, the technical R&D reports. On behalf of the CROSS, I sincerely welcome your visit to the MLF.

Neutron Science and Technology Center, Comprehensive Research Organization for Science and Society
https://neutron.cross.or.jp/en

Contents

Research and Development Highlights

Neutron Source

Neutron Science

Muon Science

MLF Safety

MLF Operations in 2024

Organization Chart

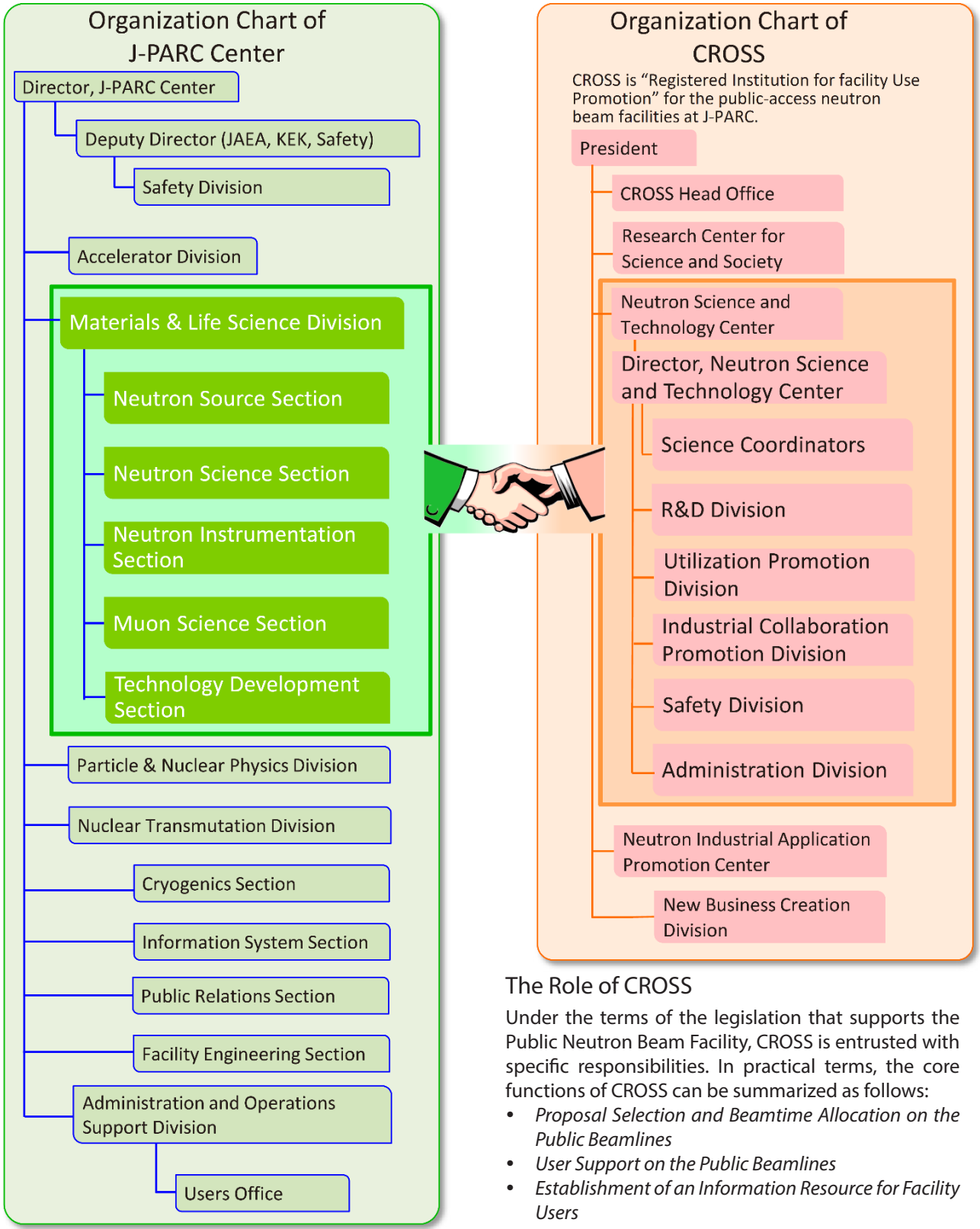

The Role of CROSS

Under the terms of the legislation that supports the Public Neutron Beam Facility, CROSS is entrusted with specific responsibilities. In practical terms, the core functions of CROSS can be summarized as follows:

- *Proposal Selection and Beamtime Allocation on the Public Beamlines*
- *User Support on the Public Beamlines*
- *Establishment of an Information Resource for Facility Users*
- *Outreach and Facility Utilization Promotion*
- *Contract Beamline Assessment and Selection*

J-PARC Map

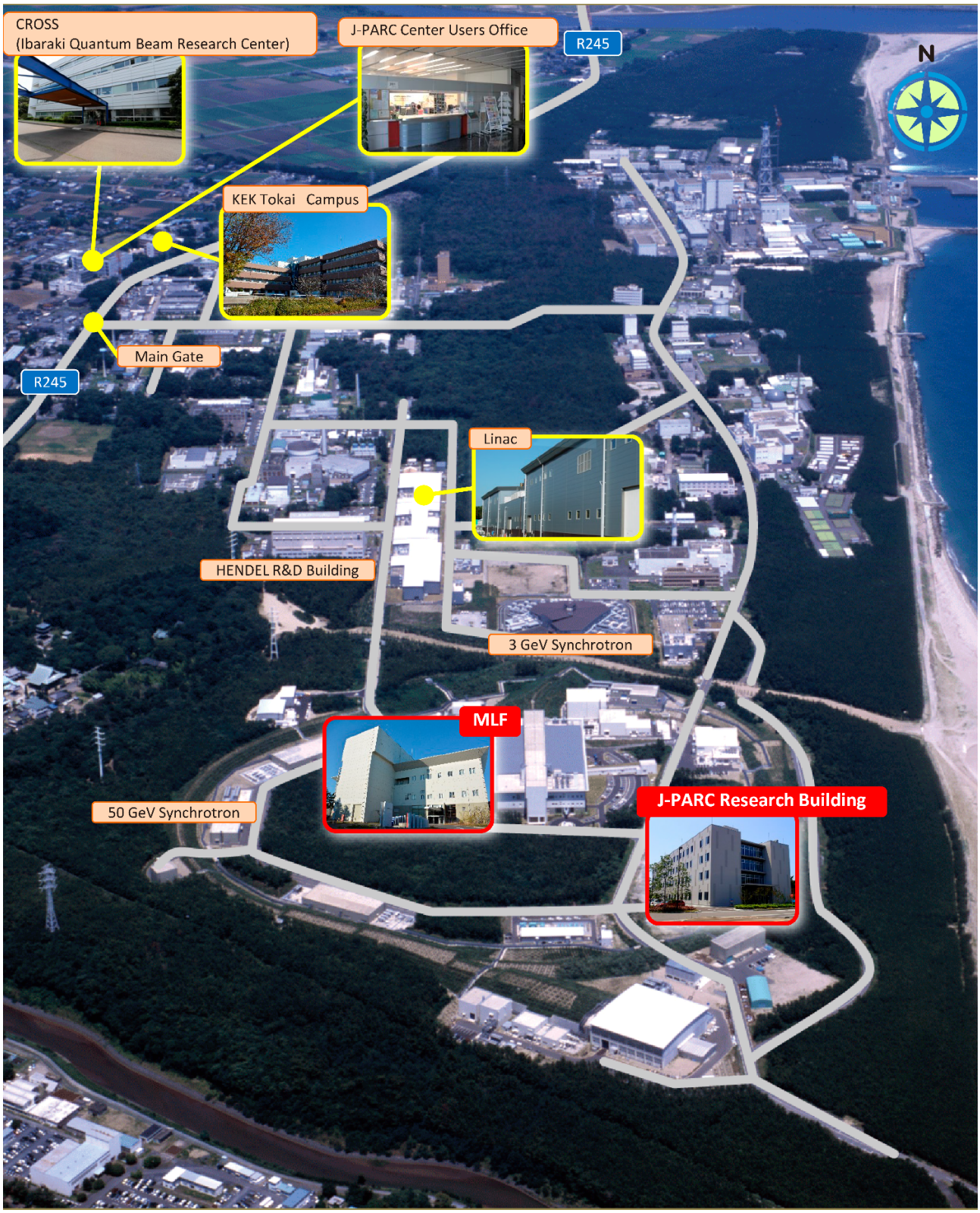
CROSS
(Ibaraki Quantum Beam Research Center)
J-PARC Center Users Office
R245
N
KEK Tokai Campus
Main Gate
R245
Linac
HENDEL R&D Building
3 GeV Synchrotron
MLF
J-PARC Research Building
50 GeV Synchrotron

Muon and Neutron Instruments

Muon Source

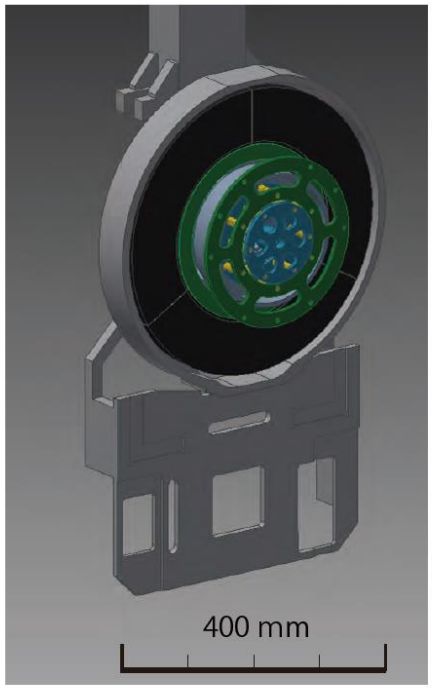

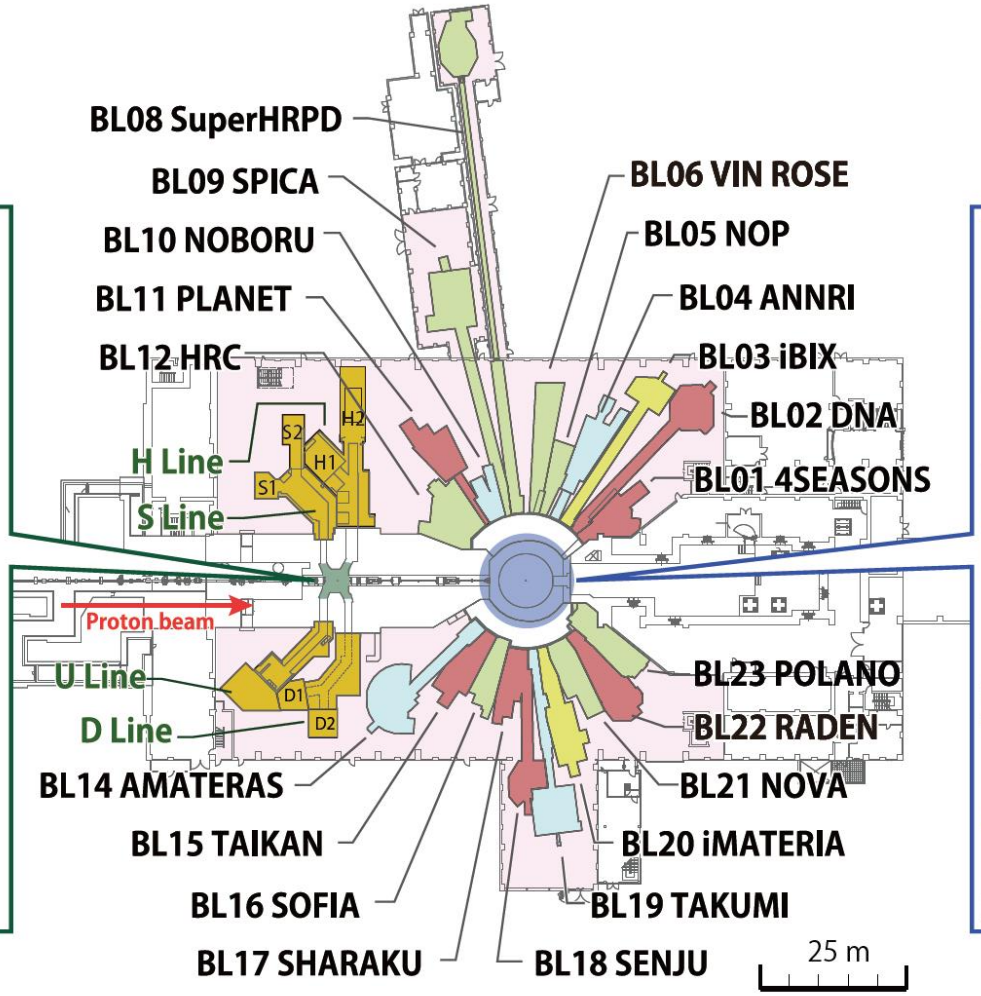

Neutron Source

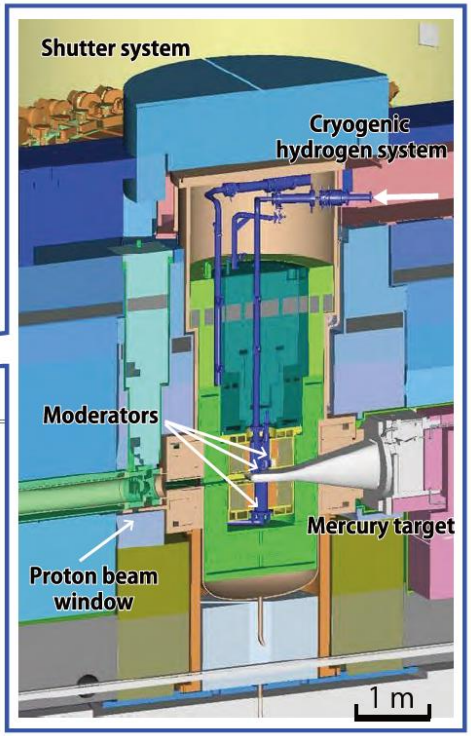

Muon Instruments

Neutron Instruments

JAEA

KEK

Public beam lines

Ibaraki Pref.

As of March 2025

Research and Development Highlights

Configuration and Dynamics of Hydride Ions in the Nitride-Hydride Catalyst Ca_3CrN_3H

1. Introduction

The novel mixed-anion nitride-hydride Ca_3CrN_3H has recently emerged as a promising catalyst for ammonia synthesis [1,2]. Its high catalytic efficiency arises, in part, from the diffusion of hydride ions (H^-) through the material's channel-like crystal structure (Figure 1) [2]. However, the local coordination environment (configuration) and precise stoichiometry of the hydride ions, both essential for understanding their diffusivity, remain unclear. To address these questions, this study combines inelastic neutron scattering (INS) with machine-learning molecular dynamics (MLMD) simulations to investigate the configuration and vibrational dynamics of hydride ions in Ca_3CrN_3H [3].

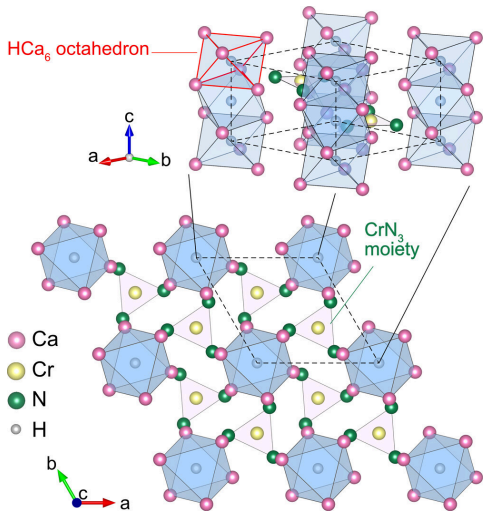

Figure 1. Schematic crystal structure of Ca_3CrN_3H.

2. Vibrational dynamics

INS measurements were taken on a powder sample of Ca_3CrN_3H at 7 K at the BL01 4SEASONS spectrometer [4]. The resulting spectrum exhibits a series of peaks between 80 and 130 meV (Figure 2). Comparison with the theoretical spectrum, obtained from phonon calculations based on the machine-learning interatomic potential, enables assignment of these peaks to vibrational modes of the hydride ions. A prominent feature is the dispersive mode spanning over the full 80–130 meV range, which is associated with vibrations along the *c* axis and where in-phase and out-of-phase vibrations are observed at 87 and 125 meV, respectively. The dispersive nature of this mode reflects strong interactions between neighboring hydride ions, due to their relative proximity (2.5 Å) along the *c* axis. In contrast, dispersion is not expected in $Ca_3CrN_3H_{0.5}$, where the reduced hydride ion concentration increases the interionic spacing along the *c* axis and suppresses such interactions. These observations indicate that the vibrational dynamics of hydride ions are closely related to the occupancy of adjacent hydride sites, and consequently that the stoichiometry of hydride ions can be probed through its INS spectrum.

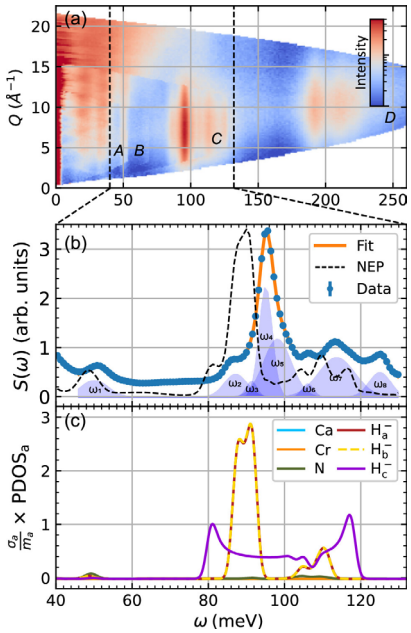

Figure 2. (a) INS data of Ca_3CrN_3H, as measured on BL01 4SEASONS at 7 K with four incident neutron energies: 64.2 meV (*A*), 95.2 meV (*B*), 156 meV (*C*), and 299 meV (*D*). (b) $S(\omega)$ obtained by Q-integration of spectrum *C*, together with a fit of the peaks with Gaussians (shaded areas) and a theoretical INS spectrum of Ca_3CrN_3H obtained from the phonon calculation. (c) Partial vibrational density of state (PDOS), weighted by the total neutron cross section and the atomic mass of each element. H_a^-, H_b^-, and H_c^- denote the PDOS of H^- projected along the *a*, *b*, and *c* axis, respectively.

3. Configurations of hydride ions

Next, MLMD calculations of the compositions $Ca_3CrN_3H_x$, with x in the range of 0.64–1, were performed. The package Graphics Processing Units Molecular Dynamics (GPUMD) [5,6] was employed. GPUMD uses a neural network-based machine-learning potential [6], which was trained based on density functional calcula-

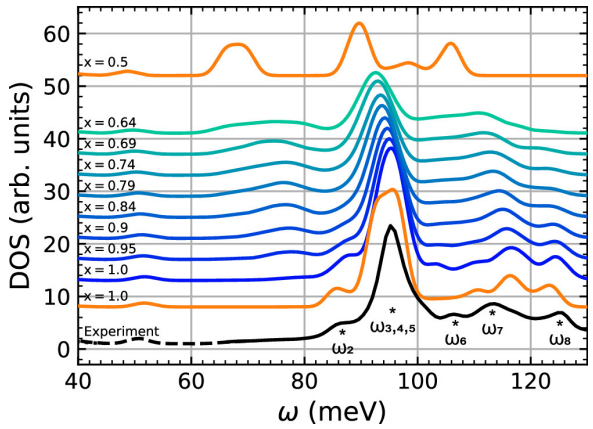

Figure 3. MLMD calculated and experimental DOS: (blue lines) MLMD for $Ca_3CrN_3H_x$ with x in the 0.64–1. (orange lines) Phonon calculations for Ca_3CrN_3H and $Ca_3CrN_3H_{0.5}$. (black lines) INS data using. The calculated DOS lines are shifted vertically for clarity and scaled horizontally by a factor of 1.055 in order to match the experimental data.

tions of $Ca_3CrN_3H_x$. As anticipated, the vibrational peaks associated with motions along the *c* axis are strongly influenced by variations in *x* (Figure 3). Specifically, as *x* decreases from 0.95, the intensity of the 87 meV peak (corresponding to out-of-phase vibrations) progressively diminishes, while the 125 meV peak (associated with in-phase vibrations) shifts downward in energy and becomes broadened. Detailed spectral analysis attributes these changes to a transformation of local hydride configurations. At high occupancy, configurations of the type H^-–H^-–H^- (three neighboring hydride ions) dominate. With decreasing *x*, these are increasingly replaced by H^-–H^-–V_H^- (a hydride ion adjacent to one hydride ion and one vacancy) and V_H^-–H^-–V_H^- (a hydride ion adjacent to two vacancies). Experimentally, however, no such downshift is observed, implying that the hydride content in our sample exceeds $x > 0.95$. We suggest that this high occupancy is directly linked to the material's high catalytic performance in ammonia synthesis, since surface hydride ions participate in the hydrogenation steps of the catalytic cycle.

4. Conclusions

In summary, this study elucidates the vibrational dynamics and local configurations of hydride ions in the channel-like crystal structure of the nitride-hydride Ca_3CrN_3H. The results demonstrate strong interactions between neighboring hydride ions, with most ions coordinated by two others and an average site occupancy of at least 95%. These findings highlight that the vibrational properties of Ca_3CrN_3H serve as sensitive indicators of its hydride stoichiometry and, by extension, its catalytic activity.

This approach may be broadly applicable to other mixed-anion materials where lattice hydrides play a central role in catalysis. Examples include the two-dimensional nitride-hydride Ca_2NH [7] and the oxide-hydride $BaTiO_{2.5}H_{0.5}$ [8], where hydride ions are likewise essential for catalytic performance.

References

[1] Y. Cao *et al.*, Angew. Chem., Int. Ed. **61**, e202209187 (2022).
[2] Y. Cao *et al.*, ChemSusChem. **16**, e202300234 (2023).
[3] L.Fine, *et al.*, Chem. Mater. **37**(1), 489-496 (2025).
[4] R. Kajimoto *et al.*, J. Phys. Soc. Jpn. **80**, SB025 (2011).
[5] Z. Fan *et al.*, Comput. Phys. Commun. **218**, 10-16 (2017).
[6] Z. Fan *et al.*, J. Chem. Phys. **157**, 114801 (2022).
[7] M. Kitano *et al.*, Chem. Sci. **7**, 4036-4043 (2016).
[8] Y. Kobayashi *et al.*, J. Am. Chem. Soc. **139**, 18240-18246 (2017).

L. Fine[1,2], R. Lavén[2], Z. Wei[3], T. Tsumori[3], H. Kageyama[3], R. Kajimoto[4], M. Jimenéz-Ruiz[1], M. M. Koza[1], and M. Karlsson[2]
[1]*Institut Laue Langevin, France;* [2]*Department of Chemistry and Chemical Engineering, Chalmers University of Technology, Sweden;* [3]*Department of Energy and Hydrocarbon Chemistry, Kyoto University, Japan;* [4]*Neutron Science Section, Materials and Life Science Division, J-PARC Center*

Gyroid-Structured Polymer Films Showing Highly Activated Surface Proton Hopping Conduction

1. Introduction

Proton-conducting polymer electrolyte membranes are important components used in fuel cells and various sensors. Nafion, developed by DuPont in the late 1960s, is the most versatile polymer electrolyte with high proton conductivity and excellent mechanical stability. Nafion membranes contain water nanochannels surrounded by hydrophobic walls bearing SO_3^- sites thinly. These water nanochannels function as fast proton conduction pathways. There are three types of proton conduction mechanisms in the water nanochannels: Mechanisms I, II, and III [1-3].

Mechanism I: Proton transport mechanism (Grotthuss mechanism) via formation/breakage of hydrogen bond networks of water molecules in the bulk water region at the center of the water nanochannels.

Mechanism II: Mechanism in which oxonium ions diffuse and move in the water pool (Vehicle mechanism).

Mechanism III: Surface proton hopping conduction (SPHC) mechanism in which protons move from a SO_3^- site present on the surface of the hydrophobic wall to an adjacent SO_3^- site via intermediate water molecules. An important characteristic of Mechanism III is that proton hopping speed is expected to be significantly enhanced by decreasing the distance between the SO_3^- sites.

The proton conductivity of each mechanism is represented by σ^G, σ^E, and σ^Σ, respectively, and the proton conductivity of the polymer electrolyte membranes is the sum of them, $\sigma^G+\sigma^E+\sigma^\Sigma$. These three proton conductivities are on the order of 10^{-3}–10^{-1}, 10^{-4}–10^{-2} and 10^{-5} S cm^{-1}, respectively. It indicates that the Grotthuss mechanism generally governs the proton conductivity of the polymer membranes.

To date, we have designed an artificially designed amphiphilic zwitterion (**GZ**) as shown in Figure 1a. A gyroid-nanostructured polymer film (hereinafter referred to as **Film-G**) with an extremely precise nanostructure has been created by self-assembly and in situ polymerization of **GZ** (Figure 1b, c) [4]. An important feature of **Film-G** is that the SO_3^- sites are arranged very precisely along a gyroid minimum surface (G-surface) (Figure 1d). The SO_3^- sites are shown as orange spheres. This film shows high proton conductivity on the order of 10^{-2}–10^{-1} S cm^{-1} when it absorbs

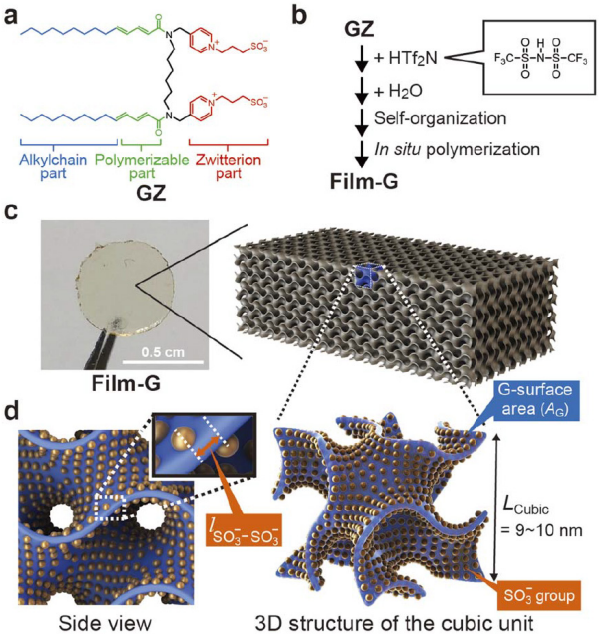

Figure 1. (a) Structure of amphiphilic zwitterion monomer **GZ**. (b) Preparation scheme for a gyroid nanostructured polymer film (**Film-G**). (c) A photograph of **Film-G** and 3D image of the gyroid nanostructure in **Film-G**. (d) 3D image of a cubic cell in **Film-G**. A water nanosheet is constructed along a gyroid minimal surface (G-surface) shown in blue. The positions of the SO_3^- groups of **GZ** are displayed as orange spheres. Reproduced from Ref. 5 with permission from the Royal Society of Chemistry.

about 16 wt% of water [4]. When we investigated the structure and function of **Film-G**, we found that the distance between the SO_3^- sites in **Film-G** is extremely small, approximately 6 Å. It was also found that the activation energy E_a of the proton conductivity is extremely small. Based on these results, we led a hypothesis that the proton conduction in **Film-G** should be predominantly governed by the SPHC mechanism. There is no report in the world that achieves a high proton conductivity of 10^{-1} S cm^{-1} only by the SPHC mechanism. In the present study, we expected that understanding the water dynamics in **Film-G** is important for revealing the proton conduction mechanism in **Film-G**, and therefore we performed QENS studies for **Film-G**.

2. QENS experiments

QENS experiments were carried out for **Film-G**/6H_2O containing 6 water molecules per zwitterion

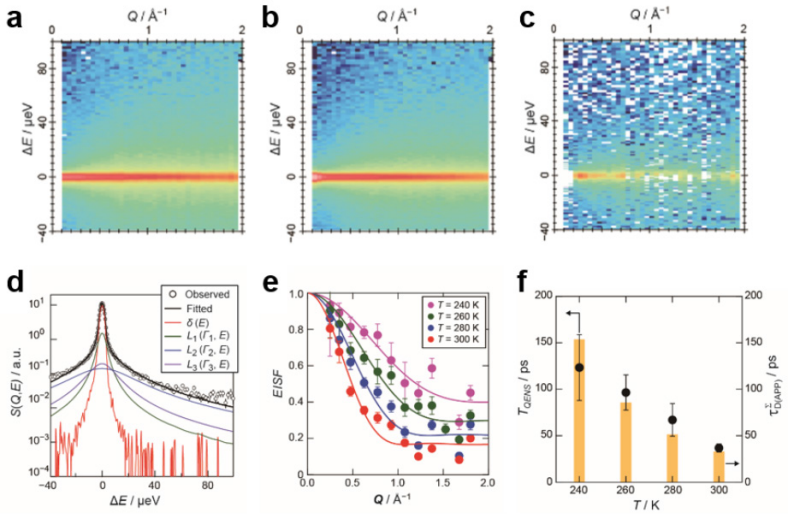

Figure 2. Contour maps of QENS data of (a) **Film-G**/6H_2O and (b) **Film-G**/6D_2O at 300 K. (c) A differential contour map between **Film-G**/6H_2O and **Film-G**/6D_2O. (d) Fitting of the QENS profile of **Film-G**/6H_2O at Q = 0.78 Å^{-1} and 300 K. (e) Q dependence of EISF of 6H_2O in **Film-G**/6H_2O. (f) Relaxation time of the mobile water molecules (τ_{QENS}) estimated from HWHM of L_3 in 6H_2O. τ_D values of **Film-G** at various temperatures are also shown in yellow bar graph. Reproduced from Ref. 5 with permission from the Royal Society of Chemistry.

part. The same experiments were also performed for **Film-G**/6D_2O. The measurements were conducted at 300, 280, 260, and 240 K. Contour maps of QENS data of **Film-G**/6H_2O and **Film-G**/6D_2O at 300 K are shown in Figure 2a and 2b. There is a strong sharp scattering intensity at $\Delta E = 0$ and a moderate broad scattering intensity centered at $\Delta E = 0$, indicating that elastic and quasi-elastic components exist in the films. To understand the dynamics of the water molecules in **Film-G**, we have created a differential contour map between the two using a scaling factor derived from the weight ratio of the two samples in the dry state (Figure 2c). In the differential contour map, a broad scattering intensity was found, meaning that there is a certain amount of mobile water molecules in **Film-G**/6H_2O.

The obtained QENS results were fitted by the following phenomenological equation

$$S(Q,E) = \left\{A_0\delta(E) + \sum_{i=1}^{3} A_i L_i(\Gamma_i, E)\right\} \otimes R(Q,E)$$

where $A_0\,\delta(E)$ denotes the elastic component with the coefficient A_0 and the delta-function $\delta(E)$, A_i is the coefficient of the i-th Lorentzian-function, $L_i(\Gamma_i, E)$, where Γ_i is the half width at half maximum of the Lorentzian-function, $R(Q, E)$ refers to the instrumental resolution function. The QENS data of **Film-G**/6H_2O were successfully fitted with a delta function and three Lorentzian functions, L_1-L_3 (Figure 2d). Based on the QENS data of **Film-G**/6D_2O, L_1 and L_2 are found to be attributed to the dynamics of the **GZ** molecules while L_3 is found to result from that of the water molecules. In order to reveal the spatial information of the observed dynamics of the water molecules, the Q dependence of L_3 was examined. Although the obtained data was scattered, Γ_3 was found to be almost constant with respect to Q, indicating that the observed dynamics corresponding to L_3 are local modes, such as rotation and/or local jumps of the water molecules. A similar trend was also observed at the other temperatures. For further consideration, the Q dependence of the elastic incoherent scattering factor (EISF) was calculated and plotted (Figure 2e). These results were successfully reproduced by a diffusion model in a confined sphere.[6] In **Film-G**/6H_2O, the hydration degree reaches a situation where protons on the G-surface wobble not only water molecules near a proton but also distant ones connecting through hydrogen-bonding networks. Consequently, a large part of water molecules on the G-surface exists as mobile state.

The relaxation time of these mobile water molecules (τ_{QENS}) was evaluated using the following formula,

$$\tau_{QENS} = \hbar\frac{1}{\Gamma_3}$$

where $\hbar$ is $h/2\pi$. The value τ_{QENS} was estimated to be 37 ± 4 ps at 300 K, which is consistent with the mean jump time (τ_D) for a proton hop estimated from the proton conductivity results (Figure 2f). This consistency is also observed at other temperatures. These results suggest that the dynamics of the mobile water molecules are deeply involved in the SPHC mechanism.

3. Future Plans

In the present study, we have revealed that the SPHC mechanism is a potential mechanism for creating advanced proton conductive polymer electrolytes. These findings will pave a new way to develop next-generation energy devices, including fuel cells and biosensors. We will continue further experiments to reveal the more details of the dynamics of water molecules involved in the SPHC mechanism in order to make clear the important factors for activating the SPHC mechanism, which will lead to the construction of a new strategy for creating a proton-conductive polymer materials contributing to a sustainable world.

References

[1] T. J. Peckham, S. Holdcroft, *Adv. Mater.* **22**, 4667 (2010).
[2] M. Eikerling, A. A. Kornyshev, *J. Electroanal. Chem.* **502**, 1 (2001).
[3] P. Choi, N. H. Jalani, R. Datta, *J. Electrochem. Soc.* **152**, E123 (2005).
[4] T. Kobayashi, Y. -X. Li, A. Ono, X.-b. Zeng, T. Ichikawa, *Chem. Sci.* **10**, 6245 (2019).
[5] T. Ichikawa, T. Yamada, N. Aoki, Y. Maehara, K. Suda, T. Kobayashi, *Chem. Sci.* **15**, 7034 (2024).
[6] F. Volino, A. J. Dianoux, *Mol. Phys.* **41**, 271 (1980).

T. Ichikawa[1] and T. Yamada[2]
[1]*Department of Biotechnology and Life Science, Tokyo University of Agriculture and Technology;* [2]*Neutron Science and Technology Center, CROSS*

Single Hydrogen Atom Controls Redox Behavior of Iron–Sulfur Clusters in Ferredoxin

1. Introduction

Within living organisms, various proteins, including those containing iron-sulfur (Fe-S) clusters, assist in redox reactions. Fe-S clusters exist in multiple types, such as 2Fe-2S, 3Fe-4S, and 4Fe-4S [1]. Ferredoxin (Fd) is a small protein with Fe-S cluster(s), that is found in almost all organisms and participates in various electron transfer reactions within cells. There are many types of Fds that cover a wide range of redox potentials (-700 to +500 mV).

Bacillus thermoproteolyticus Fd (*Bt*Fd) possesses a [4Fe-4S] cluster. To date, the high-resolution (0.92 Å resolution) structure of Fd has been determined using X-ray crystallography [2], revealing the Fe-S cluster and its surrounding fine structure. However, many aspects of the structural factors that promote electron transfer and the mechanisms that maintain their potential remain unclear.

In this study, we aimed to elucidate the mechanism of electron transfer in Fd by combining neutron crystallography, which can identify precise hydrogen atom positions, with density functional theory (DFT) calculations.

2. Experimental procedures

In neutron crystallography, crystals several orders of magnitude larger than those used in X-ray crystallography are required to obtain high-quality diffraction data. Therefore, we applied the button dialysis method to crystallize *Bt*Fd. The concentrations of *Bt*Fd were 38 – 64 mg/mL, and a 30 – 100 μL button size was used. After several weeks of dialysis at 4 °C in a 0.1 M MES buffer (pH 6.5–7.0) containing 200 mM NaCl and 76 – 89 % saturated ammonium sulfate, large crystals (approximately 2.3 mm^3) were obtained. Before the neutron diffraction experiments, the crystals were soaked in a deuterated solution for approximately two weeks (with five solution exchanges). Time-of-flight neutron diffraction data were collected at room temperature at BL03 iBIX of the Japan Proton Accelerator Research Complex (J-PARC, Tokai, Japan). Additionally, X-ray diffraction data of the same crystal were collected at room temperature at NW12A of the Photon Factory Advanced Ring (PF-AR, Tsukuba, Japan) with a beam intensity reduced to 1 %.

The integration of X-ray and neutron diffraction data enabled the determination of the three-dimensional structure, including the hydrogen atoms of *Bt*Fd, at 1.6 Å resolution (Figure 1) [3].

3. Neutron structure of *Bt*Fd

The overall structure of *Bt*Fd was nearly identical to the previously reported cryo-X-ray structure at 0.92 Å resolution [2]. When all residues were superimposed using the least-squares method, the root mean square deviation (RMSD) for the Cα atoms was 0.16 Å. The neutron-scattering-length density map clearly showed the [4Fe-4S] cluster; however, the density of sulfur atoms was very low compared to that of most other atoms, including iron atoms. This was a reasonable result because of the small neutron-scattering length of sulfur atoms, which allowed us to reconfirm the absolute positions of iron and sulfur within the [4Fe-4S] cluster, which were difficult to discriminate directly using X-rays. Furthermore, the hydrogen atoms surrounding the [4Fe-4S] cluster were visualized, enabling the determination of the hydrogen bond directions (donor-acceptor relationships) and clarifying the structure of the hydrogen-bond network (Figure 1).

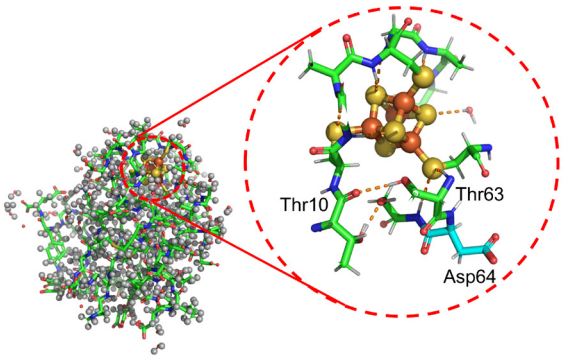

Figure 1. Overall structure of *Bt*Fd and close-up view of the 4Fe-4S cluster region.

4. Density functional theory calculations

Based on the precise three-dimensional structure, including the hydrogen atom positions of *Bt*Fd, we calculated the electronic structure around the Fe-S cluster using density functional theory (DFT). This revealed, for the first time, that the lowest unoccupied molecular orbital (LUMO) extends not only around the Fe-S cluster but also to Asp64, which is located more than 10 Å

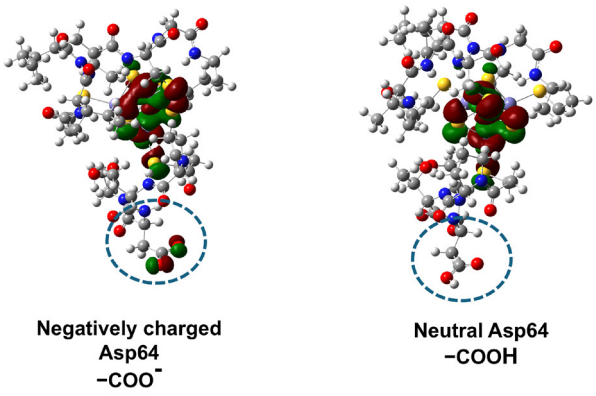

Figure 2. Distribution of LUMO. Red and green indicate positive and negative phases, respectively. Left: When Asp64 is negatively charged. Right: When Asp64 accepts H^+ and becomes neutral [3].

away from the Fe-S cluster (Figure 2, left). Interestingly, the LUMO distribution to Asp64 was observed only when the Asp64 side chain lacked a hydrogen atom at the carboxyl group (–COO^-) and was not observed when a hydrogen atom was present (–COOH) (Figure 2, right).

5. Oxidation rates

Because the electron transfer rate to oxygen depends on the potential, the electron behavior calculated by DFT is thought to be reflected in the oxidation rate of the Fe-S cluster in air. Therefore, we evaluated the oxidation rate by utilizing the fact that the UV-vis spectrum of the *Bt*Fd solution changes depending on the oxidation/reduction state. Most Asp64 mutations exhibited slower oxidation rates than those of wild-type *Bt*Fd (Figure 3). In contrast, mutations in aspartic acid residues other than Asp64 did not significantly alter the oxidation rates.

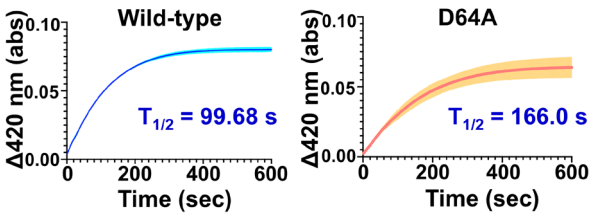

Figure 3. Time-dependent changes in the absorbance of *Bt*Fds at 420 nm. The standard deviations, calculated from at least three measurements, are shown in light colors [3].

6. Importance of the acidic residue in Fd

To confirm whether the results obtained with *Bt*Fd apply to Fd from different biological sources, we attempted to overexpress and purify eight types of Fd from eukaryotes, Archaea, and bacteria. Among these, we successfully obtained three types of Fd, possessing [4Fe-4S] or [3Fe-4S] clusters. In the [4Fe-4S] type Fd from *Staphylococcus haemolyticus*, a close relative of *Bacillus thermoproteolyticus*, mutation of Asp65 (corresponding to Asp64 in *Bt*Fd) similarly slowed the air oxidation rate. The air oxidation rate of the [3Fe-4S] type Fd from *Desulfovibrio gigas* was already very slow, but it became even slower when Glu53, corresponding to Asp64 in *Bt*Fd, was mutated to Ala. Surprisingly, in the [4Fe-4S] type Fd from the archaeon *Geoglobus acetivorans*, which is phylogenetically quite distant from *Bt*Fd, mutating Glu56 (corresponding to Asp64 in *Bt*Fd) to Ala also slowed the oxidation rate.

7. Summary

This study experimentally determined the precise structure of *Bt*Fd using neutron crystallography and revealed a hydrogen-bonding network involving [4Fe-4S] clusters. DFT calculations based on this three-dimensional structure, including hydrogen atom positions, demonstrated that the protonation states of Asp64 significantly influenced the electronic orbitals of the Fe-S clusters. Furthermore, spectroscopic and electrochemical analyses provided experimental results that supported DFT calculations. These findings revealed the existence of a "nano-switch mechanism" in Fd, where the presence or absence of a single hydrogen atom from the side chain of Asp64 (or its acidic amino acid counterpart) alters the electronic state of the Fe-S cluster. Additionally, similar investigations of various Fd species suggest that this mechanism may be widely conserved across biological systems.

References

[1] D.C. Johnson *et al.*, Annu. Rev. Biochem. **74**, 247-81 (2005).

[2] K. Fukuyama *et al.*, J. Mol. Biol. **315**, 1155-1166 (2002).

[3] K. Wada *et al.*, eLife, **10.7554/eLife.102506.2**, (2024).

M. Unno[1,2], K. Kobayashi[1], K. Kusaka[3], N. Yano[4], Y. Kitagawa[5], and K. Wada[6]

[1]*Institute of Quantum Beam Science, Ibaraki Univ.;* [2]*Research and Education Center for Atomic Sciences, Ibaraki Univ.;* [3]*Neutron Science and Technology Center, CROSS;* [4]*Diffraction and Scattering Division, JASRI;* [5]*Graduate School of Engineering Science, Univ. Osaka;* [6]*Department of Medical Sciences, Univ. Miyazaki*

Measurement of the Spin Angular Correlation of Individual γ-rays at BL04, ANNRI

1. Introduction

In the 1960s, large parity-violating (P-odd) asymmetries were observed in the p-wave resonances of several medium-heavy nuclei [1]. These effects originate from the weak interaction between nucleons but are enhanced by about six orders of magnitude compared with those in free nucleon–nucleon scattering. This enhancement is explained by the interference between s- and p-wave resonances, known as the *s–p mixing model* [2]. The model accounts for the enhanced parity violation in compound nuclei and also predicts that time-reversal (T)–odd interactions can be strongly amplified under similar conditions. Violation of time-reversal invariance, equivalent to CP violation under the CPT theorem, is a key signature of physics beyond the Standard Model. The NOPTREX collaboration aims to explore such T-violation by exploiting the large symmetry-violation amplification in compound nuclear reactions at J-PARC, while experimental verification of the s–p mixing model remains an essential step. The model predicts characteristic spin–angular correlations among the neutron momentum, neutron spin, γ-ray momentum, and γ-ray spin in (n, γ) reactions; investigating these correlations provides a direct test of the mixing mechanism.

Recent experiments at J-PARC have studied these correlations in various nuclei, including ^{139}La, ^{117}Sn, and ^{131}Xe (see Ref. [3] and references therein). Among them, ^{139}La is a promising target for T-violation searches because its p-wave resonance appears at low neutron energy—well matched to the intense low-energy beam at MLF—and due to its high natural isotopic abundance. In our previous study [4], the s–p mixing model and the enhancement factor for possible T-violating effects were examined by comparing the angular correlations of γ rays emitted in the transition to the ground state of ^{140}La with the transmission asymmetry of polarized neutrons through polarized lanthanum. This framework can be extended to γ transitions to excited states, providing further information on the exit channels and a more detailed understanding of the s–p mixing process. In this report, we introduce the results presented in our paper published last year on spin correlations for both the ground and several excited states in the ^{139}La(n, γ)^{140}La reaction [3]. The results discussed in Ref. [3] are based on a reanalysis of the data obtained from experiments conducted in 2019–2020 and details of the experiment can be found in Ref [5].

2. Experiment

The Accurate Neutron–Nucleus Reaction measurement Instrument (ANNRI) at beamline BL04 of the MLF is equipped with twenty-two high-purity Ge detectors surrounding the target position. These detectors measure γ rays emitted from the target with high energy resolution at different angles, allowing individual γ transitions to be clearly identified. Using the time-of-flight (TOF) method, the neutron energy inducing each γ emission is also determined, enabling event selection for specific neutron resonances.

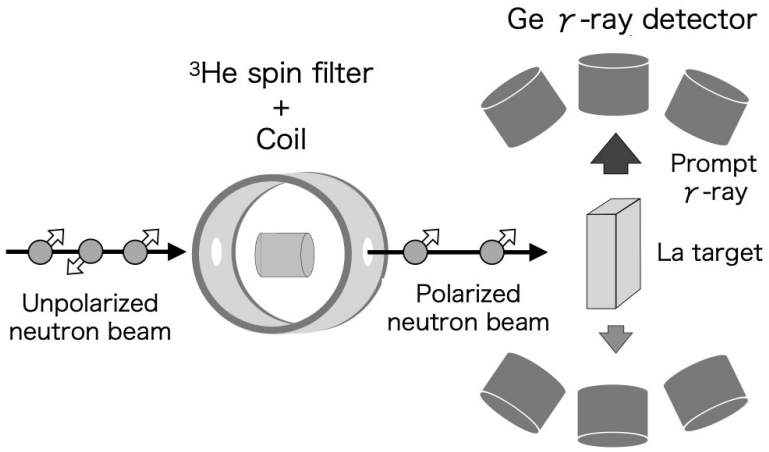

Figure 1. A ^{3}He spin filter and holding coil upstream of the target polarized neutrons horizontally, perpendicular to the beam direction. γ-rays emitted from the target were detected with the surrounding Ge detectors.

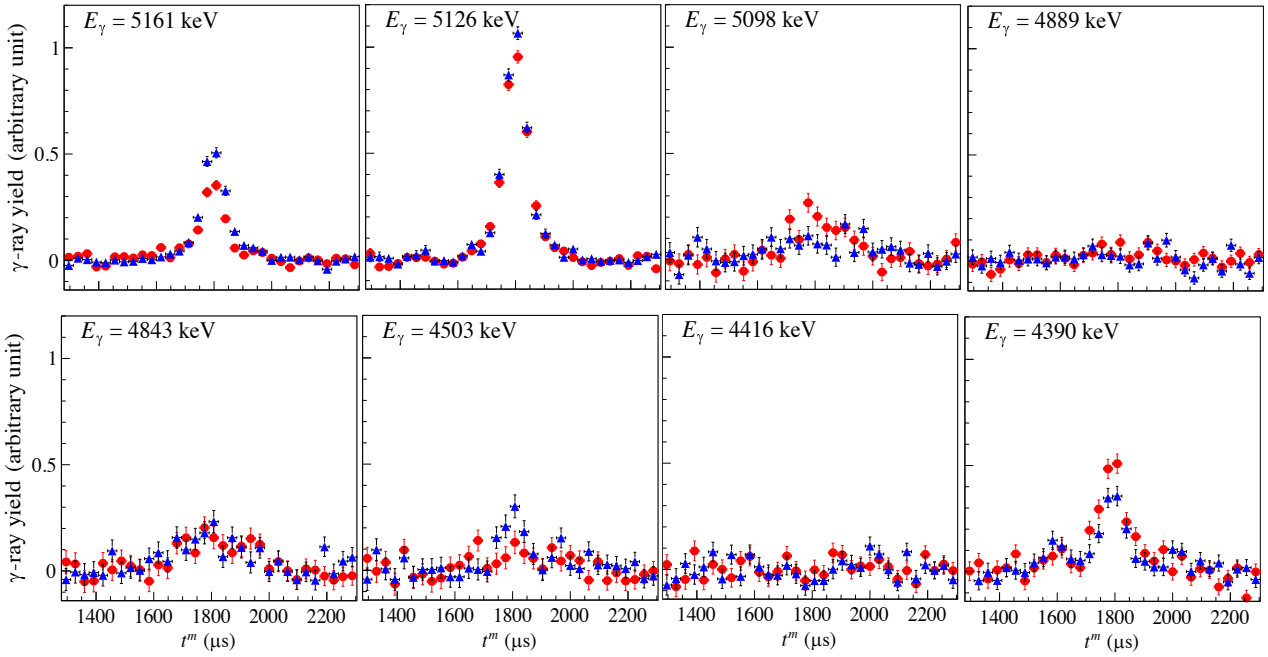

Figure 2. Time-of-flight spectra around the p-wave resonance at E = 0.75 eV (t~1800 s). Red and blue points correspond to opposite neutron spin directions. The numbers in the upper-left corners indicate the γ-ray energies.

The experimental setup is shown in Fig. 1. Upstream of the target, ex-situ ^{3}He spin filter [6] was installed to produce a polarized neutron beam. Because the neutron absorption cross section of ^{3}He strongly depends on the relative spin orientation between the neutron and ^{3}He nuclei, neutrons transmitted through the polarized cell become polarized parallel to the ^{3}He spin. The ^{3}He spin filter can polarize neutrons in the epithermal energy region, making it well suited for this experiment focusing on eV-range resonances. The ^{3}He spin direction was reversed approximately every four hours using the adiabatic fast-passage NMR technique [7]. The neutron polarization was determined from the transmission rate measured with a Li-glass detector placed downstream of the target.

3. Results

The analysis focused on γ rays emitted in transitions to the ground and seven low-lying excited states of ^{140}La. After correcting detector efficiency and subtracting Compton-scattered and non-resonant components, event yields at the p-wave resonance of 0.75 eV were plotted separately for each neutron spin direction (Fig. 2). Several transitions showed clear differences in peak height between the two spin states near the resonance energy.

The asymmetry was defined as the difference in event counts for the two spin directions divided by their sum, eliminating the need for absolute cross-section normalization and canceling common systematic uncertainties. This advantage originates from the use of a ^{3}He spin filter, where the neutron spin can be reversed simply by flipping the ^{3}He polarization without altering the beam or detector setup. The measured asymmetries were corrected for the neutron polarization and for the probability of post-scattering absorption events.

4. Summary and Future Plans

For the ^{139}La p-wave resonance, γ rays from transitions to several low-lying states of ^{140}La were analyzed. Spin–angular correlation effects arising from s–p interference were observed in multiple transitions.

To calculate angular correlations for transitions to excited states, additional information on the exit channels—such as the spins and branching ratios of the final states—is required. A γ-ray polarimeter compatible with the ANNRI setup has been developed to measure correlation terms involving circularly polarized γ rays [8]. An in-situ spin-exchange optical pumping (SEOP) system was also implemented at ANNRI to ensure long-term stable polarized-neutron experiments, essential for collecting sufficient statistics in small-asymmetry measurements. Details of this development are presented in a separate article in this Annual Report by S. Endo.

Future work will involve a comprehensive analysis combining the present results for excited states with

theoretical calculations and other correlation terms.

References

[1] G. Mitchell *et al.*, Physics Reports. **354**(3), 157-241 (2001).
[2] V. V. Flambaum *et al.*, Nucl. Phys. A **435**, 352 (1985).
[3] M. Okuizumi *et al.*, Phys. Rev. C **111**, 034611 (2025).
[4] R. Nakabe *et al.*, Phys. Rev. C **109**, L041602 (2024).
[5] T. Yamamoto *et al.*, Phys. Rev. C **101**, 064624 (2020).
[6] T. Okudaira *et al.*, NIM Phys. Res. A **977**, 164301 (2020).
[7] T. Ino *et al.*, J. Phys.: Conf. Ser. **340**, 012006 (2012).
[8] S. Endo *et al.*, Eur. Phys. J. A **60**, 166 (2024).

M. Okuizumi[1], C. J. Auton[2], S. Endo[3,4], H. Fujioka[5] , K. Hirota[6], T. Ino[6], K. Ishizaki1[1], A. Kimura[3,4], M. Kitaguchi[1,7], J. Koga[8], S. Makise[8], Y. Niinomi[1], T. Oku[9,10], T. Okudaira[1,9], K. Sakai[3], T. Shima[11], H. M. Shimizu[1], H. Tada[1], S. Takada[12,9], S. Takahashi[13,9], Y. Tani[5], T. Yamamoto[1], H. Yoshikawa[11], and T. Yoshioka[14]

[1]Department of Physics, Nagoya University; [2]Center for the Exploration of Energy and Matter, Indiana University; [3]Nuclear Data Center, JAEA; [4]Neutron Science Section, Materials and Life Science Division, J-PARC Center; [5]Tokyo Institute of Technology; [6]KEK; [7]Kobayashi-Maskawa Institute for the Origin of Particles and the Universe, Nagoya University; [8]Department of Physics, Kyushu University; [9]Technology Development Section, Materials and Life Science Division, J-PARC Center; [10]Department of Beam Line Science, Ibaraki University; [11]Research Center for Nuclear Physics, Osaka University; [12]Institute for Materials Research, Tohoku University; [13]The Institute for Solid State Physics, the University of Tokyo; [14]Research Center for Advanced Particle Physics, Kyushu University

Advancing Neutron Imaging Techniques to Highest Resolution with Fluorescent Nuclear Track Detectors

1. Introduction

Neutron imaging (NI) is a non-destructive and non-invasive inspection technique with a wide range of applications in various scientific disciplines and technological applications. The fundamentals of this technique need to be improved, particularly in achieving micrometer-scale or finer resolution, which remains a challenging task.

Recently, we developed a high-resolution NI device utilizing fine-grained nuclear emulsions (FGNE) [1]. The NI of gadolinium-based gratings (grating slits with a periodic structure of 9 µm) and a Siemens star test pattern, were successfully performed. The calculated imaging resolution, based on grayscale optical images of the gadolinium-based grating with a periodic structure of 9 µm was 0.945 ± 0.004 µm [1]. Although FGNEs offer exceptionally high resolution, they are not reusable, and post-irradiation chemical processing is required after each neutron exposure.

To address this limitation, we investigated the potential of fluorescent nuclear track detectors (FNTDs) for high-resolution NI. FNTDs are luminescent solid-state detectors based on Al_2O_3:C,Mg crystals. Given that the key feature of FNTDs is their reusability, it was essential to examine their reusability before employing them for imaging applications. We presented an approach to perform optical bleaching under the required conditions for NI. It was concluded that FNTDs can be reused for imaging applications at least seven times [2]. After assessing the reusability, NI of a gadolinium-based grating with a periodic structure of 9 µm was performed using the FNTD-based NI method. The same grating was used in both the FGNE [1] and the novel FNTD-based method [3]. The grating structure was successfully resolved for the first time using the novel FNTD-based NI technique.

2. FNTD-based neutron imaging detector

The schematic of the FNTD-based neutron detector is shown in Figure 1(a). The proposed detector consists of an FNTD combined with a neutron converter. The converter is composed of a 0.4 mm-thick silicon substrate, which is used as the base of the converter. A 230 nm-thick enriched $^{10}B_4C$ layer was deposited on the silicon substrate using an ion beam sputtering machine at the Institute for Integrated Radiation and Nuclear Science of Kyoto University [4]. After the neutron converter was fabricated, it was combined with the FNTD, as shown in Figure 1(b). The FNTD-based neutron detector, consisting of the FNTD and converter, was then packed in air-tight laminated bags, as shown in Figure 1(c).

3. Neutron imaging experiments at BL05 at J-PARC

The NI of the grating was performed at the low-divergence beam branch [5] of BL05 in the Materials and Life Science Experimental Facility (MLF) at Japan Proton Accelerator Research Complex (J-PARC). The beam divergence in the horizontal and vertical directions was set to 0.3 and 10 mrad, respectively. The directions of the gadolinium-based grating slit, and the incident neutrons (black arrows) are shown in Figure 1(a). The neutron flux and beam power during the experiment were 2×10^6 n/cm^2/s and 0.7 MW, respectively, and the neutron irradiation time was set to 2.8 h to accumulate approximately 2×10^4 tracks per (100 µm)^2, which are the required conditions for NI.

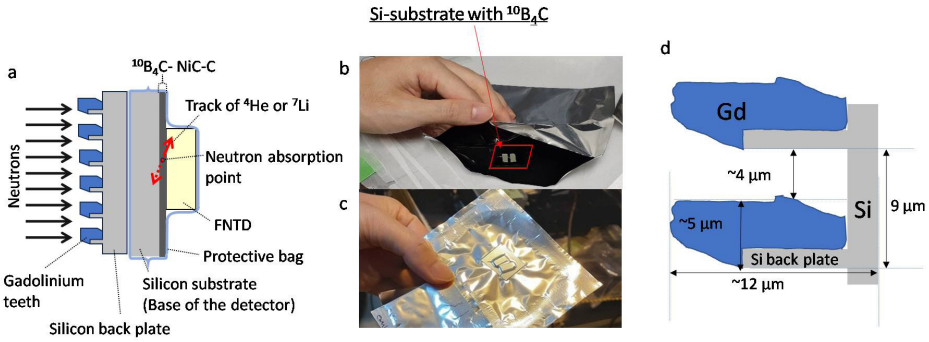

Figure 1. (a) Schematic layout of the neutron detector using an FNTD and a gadolinium-based grating with a periodic structure of 9 µm. (b) and (c) FNTD-based neutron detector: the FNTD combined with an enriched boron-based neutron converter, packed in a light- and air-tight laminated protective bag. (d) Schematic view of the two gadolinium teeth indicated as grating in the panel (a).

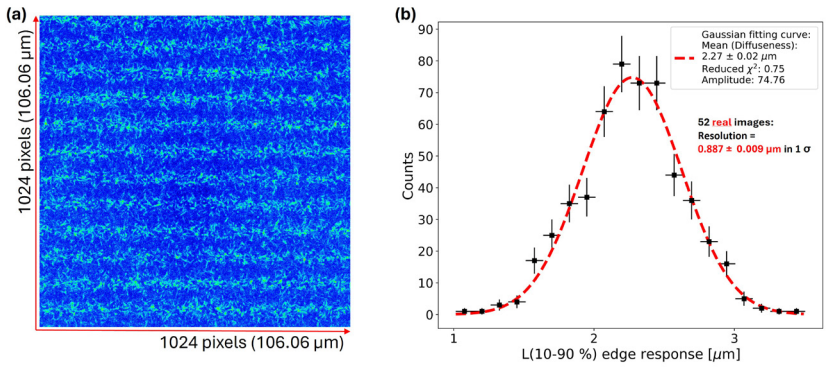

Figure 2. (a) Microscopic image of the FNTD showing the recorded tracks during neutron capture events through the gratings. (b) Distribution of the 10–90% edge response from 52 FNTD images. The dotted red line shows a Gaussian fitting curve. The mean value of the distribution of the 10–90% edge response (diffuseness) is 2.27 ± 0.02 μm when employing a Gaussian fitting function. The deduced 1σ 10–90% edge response (imaging resolution) is 0.887 ± 0.009 μm.

4. Results

After the NI experiment, the FNTD readout was conducted using high-resolution nondestructive readout systems based on confocal laser scanning microscopy (CLSM). Figure 2(a) shows the microscopic image of the FNTD using the CLSM. The dimensions and number of pixels in this image were 106.07 × 106.07 μm^2 and 1024 × 1024, respectively. The structure of the gadolinium grating, with a periodicity of 9 μm, was successfully resolved for the first time using the FNTD-based neutron detector. It was clearly visible as shown in Figure 2(a). Figure 2(b) is the distribution of the 10-90% edge response. The dotted red line in Figure 2(b) shows a Gaussian fitting curve. The mean value of the distribution of the 10-90% edge response (diffuseness) is 2.27 ± 0.02 μm when employing a Gaussian fitting function. The measured imaging resolution was 0.887 ± 0.009 μm, the highest imaging resolution achieved so far.

5. Summary

In this paper, we present a novel NI device based on FNTDs combined with a neutron converter layer formed using $^{10}B_4C$. Experiments were performed to analyze the NI of a gadolinium-based grating of a known shape. For the first time, a micrometer-structured grating slit with a periodic structure of 9 μm was successfully resolved. The NI with the FNTDs exhibited an unprecedented resolution of 0.887 ± 0.009 μm. We conclude that sub micrometer-scale spatial resolution can be achieved using the proposed FNTD-based NI technique.

The novel FNTD-based NI technique will be employed for several real-world applications such as biological samples, infrastructure materials and semiconductor devices with RIKEN Compact Neutron Source Systems (RANS) [6] and J-PARC. Along with exploring advanced applications using the proposed NI technique, we will continue our efforts to improve the fast readout system and to develop user-friendly reusability techniques for the FNTDs, based on optical bleaching and thermal annealing, which remain challenging tasks.

References

[1] A. Muneem *et al.*, J. Appl. Phys. **133**, 054902-1-16 (2023).
[2] A. Muneem *et al.*, Radiation Measurements. **158**, 106863-1-9 (2022).
[3] A. Muneem *et al.*, Scientific Reports. **15**, 2103-1-11 (2025).
[4] M. Hino, *et al.*, Nucl. Instrum. Methods Phys. Res. Sect. A **797**, 265-270 (2015).
[5] K. Mishima, *et al.*, Nucl. Instrum. Methods Phys. Res. Sect. A **600**, 342-345 (2009).
[6] Y. Otake, RIKEN Accelerator-driven compact neutron systems, EPJ Web of Conferences 231, 01009 (2020).

A. Muneem[1,2], J. Yoshida[1,3,4], T. R. Saito[1,5,6], H. Ekawa[1], M. Hino[7], K. Hirota[8], G. Ichikawa[8,9], A. Kasagi[1,10], M. Kitaguchi[11,12], K. Mishima[8,12], J-Un Nabi[13], and M. Nakagawa[1]

[1]High Energy Nuclear Physics Laboratory, RIKEN; [2]Neutron Beam Technology Team, RIKEN; [3]Department of Physics, Tohoku University; [4]International Center for Synchrotron Radiation Innovation Smart (SRIS), Tohoku University; [5]GSI, Germany; [6]Department of Physics, Saitama University;[7]Institute for Integrated Radiation and Nuclear Science, Kyoto University;[8]High Energy Accelerator Research Organization (KEK) ;[9]Japan Proton Accelerator Research Complex, J-PARC Center;[10]Graduate School of Artificial Intelligence and Science, Rikkyo University;[11]Department of Physics, Nagoya University;[12]Kobayashi-Maskawa Institute for Origin of Particles and the Universe (KMI), Nagoya University;[13]Department of Physics, University of Wah

Evidence of tuned anharmonicity in the thermoelectric material $Cu_{2-x}S$

1. Introduction

Cu_{2-x}(S, Se) is a well-known thermoelectric (TE) material that shows a high figure of merit (ZT ≈ 1.7).[1–5] The main reason for its high ZT is its very low thermal conductivity. However, according to previous reports[1–5], Cu_{2-x}(S, Se) shows an abnormal increase in lattice thermal conductivity with increasing Cu deficiency. At high temperatures, Cu_{2-x}(S, Se) maintains a single cubic structure over a wide composition range.[6] Therefore, Cu deficiency corresponds to Cu vacancy-type point

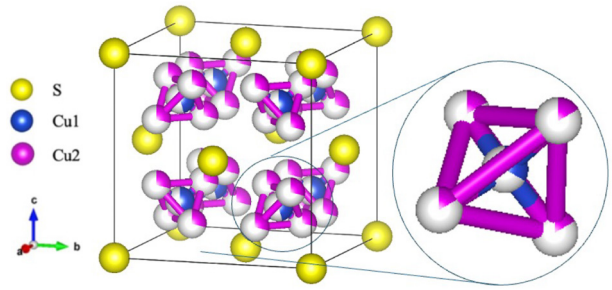

(a) Crystal structure of $Cu_{2-x}S$

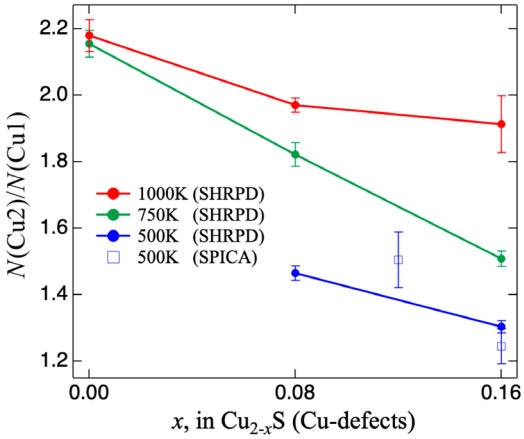

(b) The occupancy ratio of Cu1 and Cu2 sites: *N*(Cu2)/*N*(Cu1)

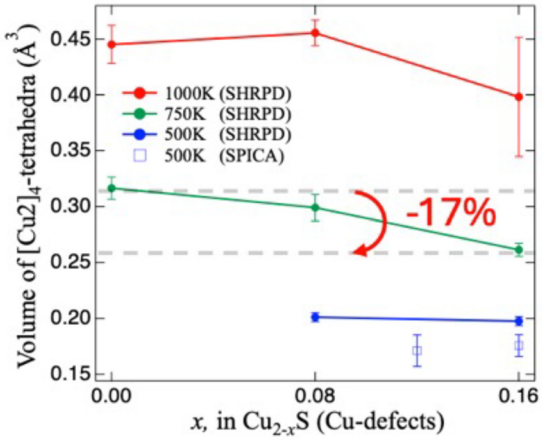

(c) The volume of the $[Cu2]_4$-tetrahedra

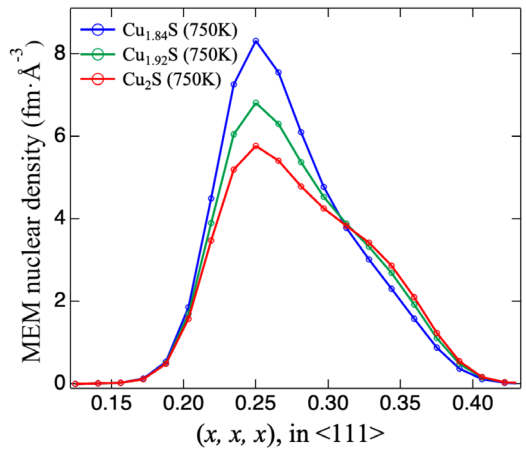

(d) One-dimensional MEM density along <111> around Cu atoms for $Cu_{2-x}S$

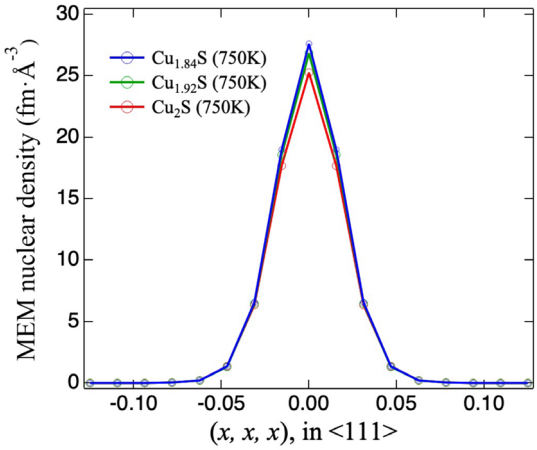

(e) One-dimensional MEM density along <111> around S atoms for $Cu_{2-x}S$

Figure 1. Crystal structure of $Cu_{2-x}S$ and structure analysis results

defects. Meanwhile, the lattice thermal conductivity (k) can be written as $k = (1/3)\sum Cvl = (1/3)\sum Cv^2t$, where C is the specific heat, and v, l, and t represent the phonon properties (velocity, mean free path, and lifetime). In general, point defects such as atomic vacancies in crystalline materials scatter phonons and reduce the lattice thermal conductivity, and such a strategy is often introduced intentionally to lower the thermal conductivity of TE materials.[7–9] In addition, Ref. 10 shows that the specific heat (C) of $Cu_{2-x}S$ decreases with increasing Cu deficiency. Both the phonon and heat capacity effects predict a decrease in lattice thermal conductivity with increasing Cu defects. For this reason, the abnormal trend of lattice thermal conductivity in Cu_{2-x}(S, Se) suggests that another mechanism is involved. We considered that this anomaly may be explained by a tuning in anharmonicity of atomic vibrations.

2. Experiments

Neutron diffraction (ND) experiments were performed on Cu-defect-controlled $Cu_{2-x}S$ powder samples in the high-temperature range (500–1000 K) at the BL08 SuperHRPD and BL09 SPICA of J-PARC MLF. Rietveld structure analyses were carried out using ND data obtained at the backscattering bank, which provides the highest resolution ($\Delta d/d$ = 0.04 and 0.09 % for SuperHRPD and SPICA). Maximum Entropy Method (MEM) analyses for nuclear density were conducted using high-statistics SuperHRPD data. From the MEM results, one-particle potentials (OPPs) were calculated.

3. Results and Discussion

3.1 Structure analysis

Rietveld refinement for $Cu_{2-x}S$ was conducted based on the $Fm\bar{3}m$ space group, in which S atoms form an fcc framework, and Cu atoms partially occupy the interstitial sites (Fig. 1a). One (or less) Cu atom is distributed over the Cu1 (8c, tetrahedral center) and Cu2 (32f, tetrahedral vertex) sites, forming tetrahedral units. Based on the refinement results, the ratio of the numbers of Cu atoms at the Cu2 and Cu1 sites and the volume of the $[Cu2]_4$ tetrahedra were calculated (Fig. 1b, c). With

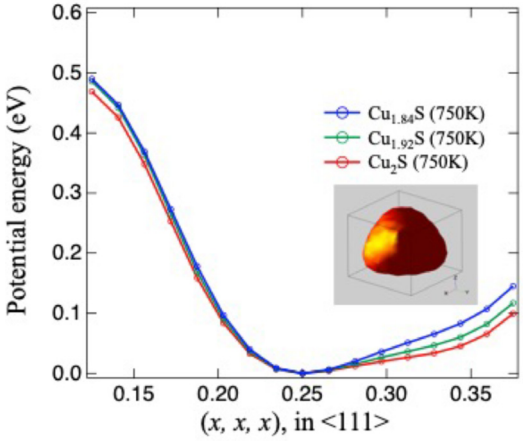

(a) 1D OPP of Cu (inset: 3D OPP of Cu)

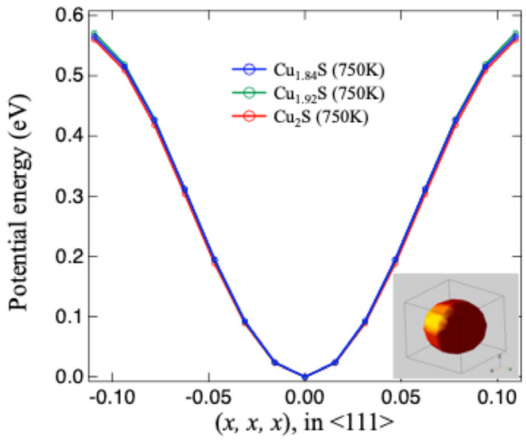

(b) 1D OPP of S (inset: 3D OPP of S)

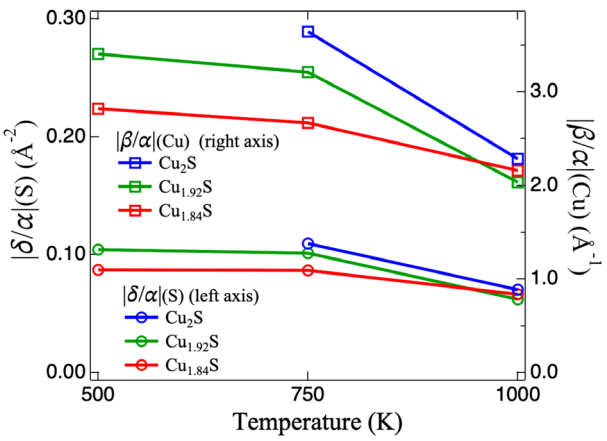

(c) Degree of Anharmonicities: |β/α|(Cu) and |δ/α|(S)

Figure 2. One particle potential (OPP) results

increasing Cu defect, Cu atoms become more concentrated at the Cu1 site, and the tetrahedral volume shrinks. The nuclear density distribution obtained from the maximum entropy method (MEM) shows a similar trend to the Rietveld results. (Fig. 1d, e) These structural changes strongly suggest that the local potential around the Cu atoms varies significantly.

3.2 One-particle potential analysis

To discuss the atomic potential directly and quantitatively, one-particle potentials (OPPs) were calculated from the MEM nuclear density using the Boltzmann distribution. (Fig. 2a, b) The OPPs of S are more harmonic, whereas those of Cu are more anharmonic, and as the Cu defect increases, the S potentials are almost unchanged, while the Cu potentials become steeper. The OPPs were fitted using the theoretical potential function [11]: $V = \frac{1}{2}\alpha(x^2 + y^2 + z^2) + \beta(xyz) + \gamma(x^2 + y^2 + z^2)^2 + \delta(x^4 + y^4 + z^4 - 3/5r^4) + \cdots$, and the harmonic ($\alpha$) and anharmonic ($\beta$, γ, δ) terms were obtained. In the lattice, heat is transferred through the vibrational motion of atoms, where a higher harmonic coefficient enhances it, while a higher anharmonic coefficient suppresses it. Therefore, discussing both coefficients together is an effective way to discuss heat transfer, and we defined the degree of anharmonicity as β/α for Cu and δ/α for S. (Fig. 2c) Both Cu and S show the highest degree of anharmonicity in Cu_2S, which decreases with increasing Cu defect. These trends of degree of anharmonicity successfully explain the unusual increase in lattice thermal conductivity in Cu_{2-x}(S, Se) induced by Cu defects.

4. Summary

We conducted ND on $Cu_{2-x}S$, which shows an unusual increase in lattice thermal conductivity with increasing Cu defect. Rietveld refinement was carried out assuming one S site and two Cu sites. The analysis revealed that, as the Cu defect increased, the Cu distribution, estimated from the volume of the $[Cu2]_4$ tetrahedra, decreased, and Cu occupancy became increasingly concentrated at the center. The OPP analysis demonstrated that the degree of anharmonicity is highest in Cu_2S and gradually decreases with increasing Cu defect.

Our results highlight that Cu defect can tune anharmonicity, providing new insight into the origin of the low lattice thermal conductivity in Cu_{2-x}(S, Se).

References

[1] He, Y. *et al*., Adv. Mater. **26**, 3974 (2014).
[2] Xiao, X.-X.*et al*., Chin. Phys. B **20**, 087201 (2011).
[3] Geng, Z. *et al*., J. Materiomics. **5**, 626 (2019).
[4] Yang, L. *et al*., Acta Mater. **113**, 140 (2016).
[5] Yu, B. *et al*., Nano Energy. **1**, 472 (2012).
[6] Okamoto H. *et al*., ASM International. Volume **3**, 176 (2016).
[7] Takeuchi, T. *et al*., Phys. Rev. B **74**, 054206 (2006).
[8] Dasgupta, T. *et al*., Phys. Rev. B **83**, 235207 (2011).
[9] Hu, L. *et al*., Adv. Funct. Mater. **24**, 5211(2014).
[10] Mansour, B. A., Tahoon, K. H. & El-Sharka, A. A. Phys. Stat. Sol. **148**, 423 (1995).
[11] Willis, B. T. M. Acta Cryst. A **25**, 277 (1969).

S. Song[1,2,3], T. Saito[1,2,3], S. Lee[1,2], M. Hagihala[1], Y. Ishikawa[4]. S. Torii[1,2], K. Mori[1,2,3], S Itoh[1,2,3], K. Lee[5], D. Cho[6], and T. Kamiyama[1,2,7,8]
[1]Neutron Science Section, Materials and Life Science Division, J-PARC Center; [2]Institute of Materials Structure Science, KEK; [3]SOKENDAI (The Graduate University for Advanced Studies); [4]Neutron Science and Technology Center, CROSS; [5]Pohang Accelerator Laboratory, POSTECH; [6]Department of Physics, Jeonbuk National University; [7]Institute of High Energy Physics, Chinese Academy of Sciences; [8]Spallation Neutron Source Science Center

Visualization of local structure and F-ion diffusion pathways in $Ca_{0.48}Ba_{0.52}F_2$ solid electrolyte

1. Introduction

Rechargeable batteries with high energy densities can be used in large-scale applications such as electric vehicles and residential energy storage systems. All-solid-state fluoride batteries (FBs) using diffusive fluoride ions have attracted considerable research attention as viable alternatives to commercial rechargeable batteries such as nickel-metal hydride batteries and lithium-ion batteries [1,2].

A wide electrochemical potential window and high ionic conductivity are two essential requirements for solid electrolyte materials. Thus, alkaline-earth metal fluorides, such as CaF_2, SrF_2, and BaF_2, have attracted considerable attention from researchers as solid electrolytes for all-solid-state FBs. In general, however, their ionic conductivities are relatively low. Meanwhile, the ionic conductivities of metastable CaF_2–BaF_2 compounds synthesized via high-energy mechanochemical milling have drastically increased by more than five orders of magnitude over the past decades [3]. In this study, we investigate the structural characteristics of the $Ca_{0.48}Ba_{0.52}F_2$ solid electrolyte by time-of-flight neutron diffraction (TOF-ND) experiments [4]. ND measurements are well suited for the accurate determination of positions and Debye–Waller factors of light atoms in the presence of heavy atoms.

2. Results and discussion

TOF–ND experiments were performed for $Ca_{0.48}Ba_{0.52}F_2$ at different temperatures, using the SPICA located at the J-PARC MLF [5]. The Rietveld refinement of the TOF-ND data for $Ca_{0.48}Ba_{0.52}F_2$ obtained at 573 K and the refined crystal structure are shown in Figs. 1 and 2, respectively. In Fig. 1, an excellent agreement is observed between the experimental and calculated intensities. To visualize nuclear density distributions and predict the conduction pathways of F^- ions in the $Ca_{0.48}Ba_{0.52}F_2$ structure, we utilized the maximum entropy method (MEM)-based application. Fig. 3 shows the nuclear density distribution on the (110) plane for $Ca_{0.48}Ba_{0.52}F_2$ at 573 K, which is drawn for the contour surface corresponding to the nuclear density of 0.01 fm $Å^{-3}$. Consequently, the nuclear density distribution related to F atoms coincides with the most probable conduction pathways of F^- ions: the "–F1–$_{□F}$–F1–" route.

Next, we calculated the atomic pair distribution

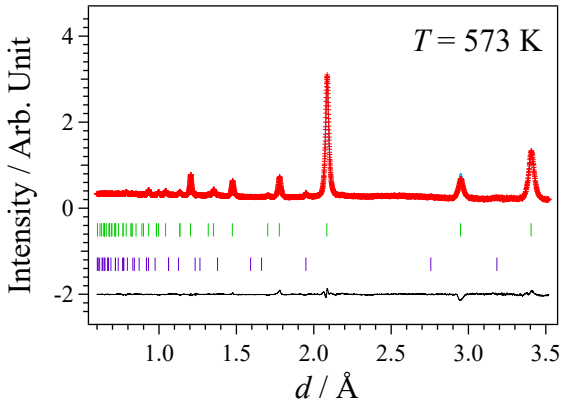

Figure 1. Rietveld refinement of the TOF–ND data for $Ca_{0.48}Ba_{0.52}F_2$ obtained at 573 K.

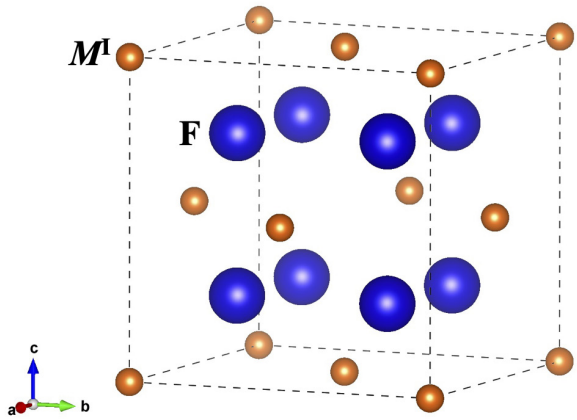

Figure 2. Refined crystal structure of $Ca_{0.48}Ba_{0.52}F_2$ obtained at 573 K. The atomic displacements of M^I (= $Ca_{0.48}Ba_{0.52}$; orange ellipsoids) and F (blue ellipsoids) are shown for the 80 % probability.

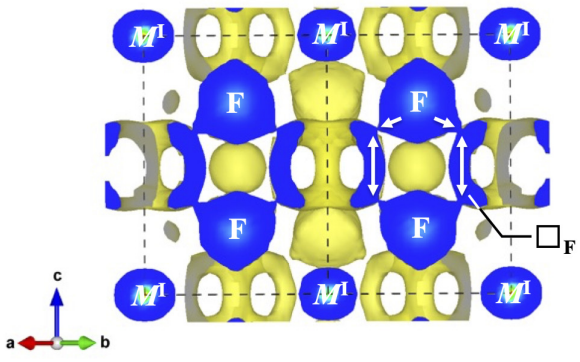

Figure 3. Three-dimensional nuclear density distribution on the (110) plane for $Ca_{0.48}Ba_{0.52}F_2$ at 573 K.

function, $g(r)$, of $Ca_{0.48}Ba_{0.52}F_2$ at 573 K (see Fig. 4). The atomic arrangement of $Ca_{0.48}Ba_{0.52}F_2$ obtained via reverse Monte-Carlo (RMC) modeling performed using the $g(r)$ data is shown in Fig. 5. Interestingly, fluctuations of Ca, Ba, and F atoms in the local structure are observed owing to the mixing of Ca with Ba. Fig. 6 exhibits an overlay of a sliced RMC cell (i.e., local atomic arrangements) and sliced MEM map (i.e., nuclear density distributions). In this figure, the diffusion pathways of F^- ions are represented by the "–F1–$_{\square F}$–F1–" network. According to the F^- diffusion mechanism established for $Ca_{0.48}Ba_{0.52}F_2$, the geometric frustration-induced positional disorder observed for F^- ions is one of the structural origins for the fast F^- ion conduction in $Ca_{0.48}Ba_{0.52}F_2$.

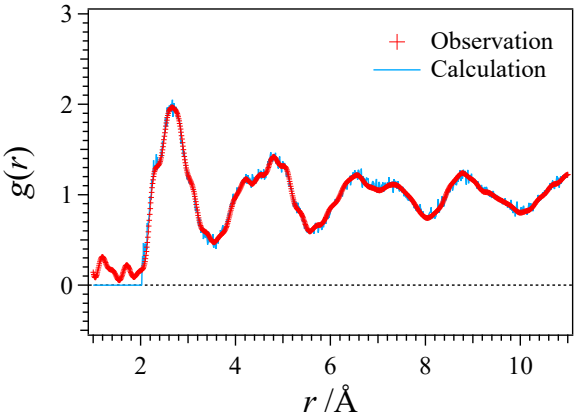

Figure 4. RMC modeling of $Ca_{0.48}Ba_{0.52}F_2$ using the neutron atomic pair distribution function, $g(r)$, at 573 K.

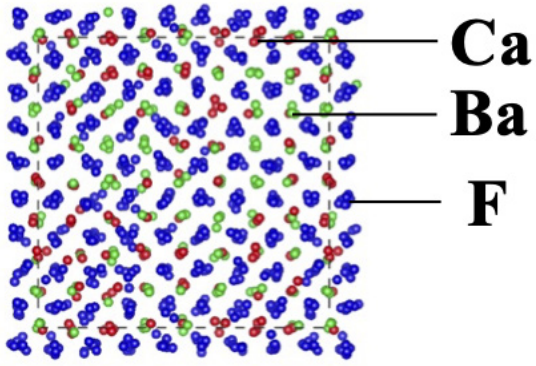

Figure 5. The three-dimensional atomic configuration of $Ca_{0.48}Ba_{0.52}F_2$ obtained via RMC modeling at 573 K.

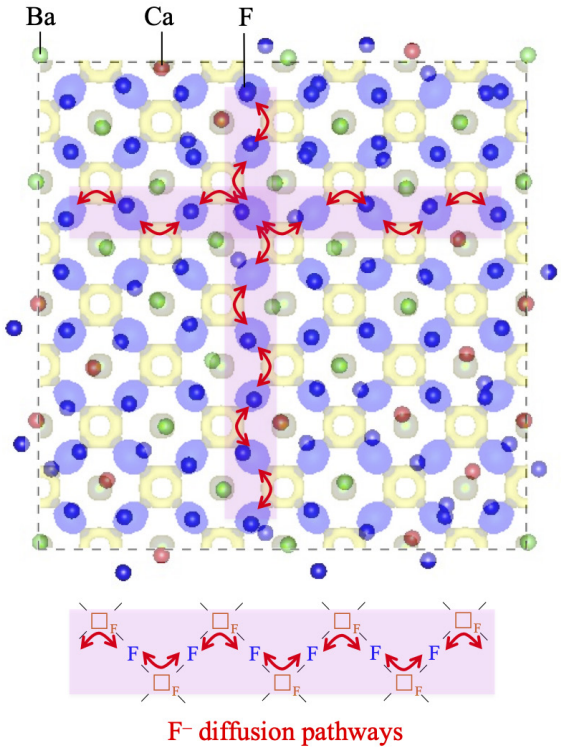

Figure 6. Schematic illustration of the F^- diffusion mechanism in the $Ca_{0.48}Ba_{0.52}F_2$ structure.

3. Conclusions

The "–F1–$_{\square F}$–F1–" diffusion pathways of fluoride ions in $Ca_{0.48}Ba_{0.52}F_2$ was identified via Rietveld refinement and a maximum entropy method. In addition, RMC modeling revealed the existence of geometric frustration-induced positional disorder with respect to Ca, Ba, and F atoms. The findings of this work may facilitate the development of solid electrolytes for next-generation all-solid-state rechargeable batteries.

References

[1] M.A. Reddy and M. Fichtner, J. Mater. Chem. **21**, 17059 (2011).
[2] A. Mohammad *et al.*, J. Mater. Chem. A **9**, 5980 (2021).
[3] B. Ruprecht *et al.*, J. Mater. Chem. **18**, 5412 (2008).
[4] K. Mori *et al.*, ACS Appl. Energy Mater. **7**, 7787 (2024).
[5] M. Yonemura *et al.*, J. Phys. Conf. Ser. **502**, 012053 (2014).

K. Mori[1,2,3], K. Sato[4], T. Ogawa[5], A. Kuwabara[5], S. Song[1], T. Saito[1], T. Fukunaga[4], and T. Abe[6]
[1]Institute of Materials Structure Science, KEK; [2]Neutron Science Section, Materials and Life Science Division, J-PARC Center; [3]Institute of Quantum Beam Science, Graduate School of Science and Engineering; [4]Office of Institutional Advancement and Communications, Kyoto University; [5]Nanostructures Research Laboratory, Japan Fine Ceramics Center; [6]Graduate School of Engineering, Kyoto University

Atomic-Scale Imaging of Oxygen in Ferroelectric $BaTiO_3$ using Neutron Holography

1. Introduction

Atomic-resolution holography is a powerful method for visualizing three-dimensional atomic configurations around specific elements in crystals [1,2]. Although this method was originally developed to determine the sites of dopant atoms embedded in materials, it has recently been found that the reconstructed atomic images are highly sensitive to atomic displacements. This sensitivity enables the evaluation of ionic polarizations in ferroelectric materials [3-5]. However, conventionally used technique, X-ray fluorescence holography, is insensitive to light elements, making it difficult to visualize O ions and evaluate their displacements in ferroelectric oxides such as $BaTiO_3$. Yet, understanding the displacements of both cations and anions is crucial for elucidating the microscopic origin of ferroelectricity.

Multiple-wavelength neutron holography (MNH), developed in 2017 [6], is a promising approach for visualizing O ions in ferroelectric materials, because neutrons are more sensitive to light elements than X-rays. This method employs the time-of-flight technique with pulsed neutrons, enabling the simultaneous acquisition of numerous holograms recorded at different incoming neutron wavelengths. Clear atomic images can then be reconstructed using Barton's multiple-wavelength algorithm [7]. Indeed, MNH has successfully produced images of fluorine ions in Eu-doped CaF_2 [6].

$BaTiO_3$ is one of the most representative ferroelectric materials. As shown in Fig. 1, it has a perovskite structure in which Ti and O ions are displaced, as revealed by previous X-ray and neutron diffraction studies [9, 10]. To demonstrate the feasibility of visualizing O ions and evaluating their displacements, we applied MNH to ferroelectric $BaTiO_3$ to reconstruct atomic images around Ti ions [11].

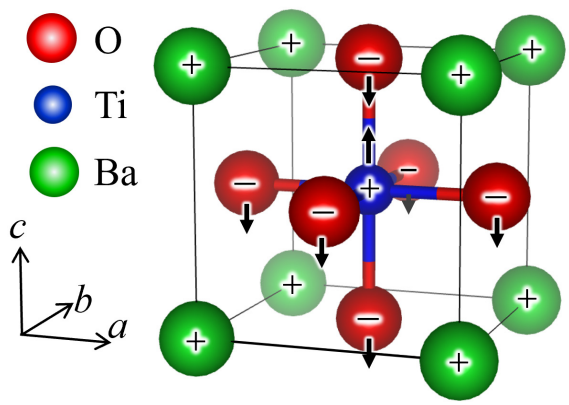

Figure 1. Crystal structure of $BaTiO_3$. The displacements of the Ti and O ions in the *c* direction is indicated by arrows. VESTA [8] was used for the structural visualization.

2. Experiments

MNH experiments were performed at BL10 of MLF at room temperature. We mounted a single crystal of $BaTiO_3$ with a size of $10\times10\times3\,mm^3$ on a two-axis (ω and φ) rotation stage. Prompt γ-rays were detected by a BGO ($Bi_4Ge_3O_{12}$) scintillation detector.

To extract γ-rays originating from Ti, the intensities in the range of 1230–1538 keV were integrated in the γ-ray spectrum. In this energy range, the absorption cross-section of Ba is approximately 10^{-3} times smaller than that of Ti, allowing γ-rays emitted from Ba to be neglected. The cross-section of O is even smaller by roughly one order of magnitude.

The ω and φ scan ranges were 10°–170° and 0°–360°, respectively, and the time-of-flight spectra of γ-rays were recorded for each ω and φ. The total measurement time for the full range of ω and φ was approximately 17 hours. To improve statistics, three scans were performed. Atomic image reconstruction was carried out using holograms obtained with incident neutron wavelengths from 0.63 to 1.04 Å.

3. Results and Discussion

Figure 2(a) shows the reconstructed atomic image around Ti in $BaTiO_3$. The red and blue circles indicate the expected positions of O and Ti ions, respectively, based on the average crystal structure. Distinct positive peaks appear at the nearest-neighbor positions corresponding to the O ions, demonstrating that the O ions can be observed using MNH. Additionally, strong negative peaks are found around $(\pm4, 0)$ and $(0, \pm4)$, corresponding to neighboring Ti positions. Because the neutron scattering length of Ti is negative, these negative peaks can be attributed to Ti ions.

Figure 2(b) presents the intensity profiles of the image shown in Fig. 2(a) in the ⟨100⟩ direction (dashed arrow). The profile is normalized to the Ti–Ti peak intensity. The calculated result based on the cubic $BaTiO_3$ structure is also shown. The Ti–O peak intensity derived from the cubic model is notably higher than that obtained in the MNH experiment, indicating the pres-

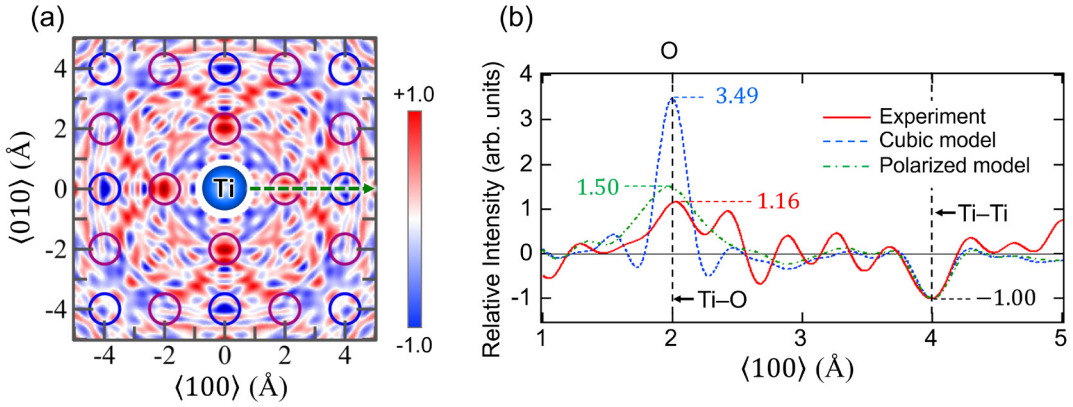

Figure 2. (a) Atomic image around Ti in $BaTiO_3$ reconstructed from the holograms obtained by the MNH experiments. Red and blue circles indicate the expected positions of O and Ti ions, respectively, based on the average structure. (b) Intensity profile of the images in (a) in the ⟨100⟩ direction indicated by dashed arrow. Here, the calculated results using cubic model and polarized model are also shown.

ence of ionic displacements of O and Ti, as illustrated in Fig. 1.

To evaluate the magnitude of the O ionic displacement relative to the Ti ion, we calculated the intensity of the neighboring O image as a function of the positional deviation σ_T expressed as

$$\sigma_T = \sqrt{\sigma_{Ti} + \sigma_O + \sigma_p},$$

where σ_O and σ_{Ti} are the mean square displacements of O and Ti atoms due to the thermal vibration, respectively, and σ_p denotes the sum of the displacement magnitudes of O and Ti ions. On the basis of the calculated σ_T dependence of the O image intensity and the experimentally obtained relative O image intensity of 1.16 (Fig. 1), σ_T was estimated to be approximately 0.23 Å [11]. Using σ_{Ti}=0.07 Å [10] and σ_O=0.15 Å [9], we obtain σ_p=0.16 Å. Using these values, we calculated holograms and reconstructed atomic images to plot the intensity profile as shown in the green dot-dashed line in Fig. 2(b). It is confirmed that the agreement with the experimental result is significantly improved by taking the ionic displacement into account as well as the thermal vibrations.

4. Conclusion and Future Perspective

We have successfully demonstrated that images of O ions can be reconstructed using MNH in ferroelectric $BaTiO_3$. From the intensity ratio of the O and Ti images, the difference between the Ti and O ionic positions in the polarization direction was evaluated to be 0.16 Å, showing that MNH is a useful technique for quantitatively evaluating the ionic polarization of ferroelectric materials including light elements. As mentioned in the Introduction, atomic-resolution holography is particularly powerful for clarifying local structures around dopants in materials. Therefore, doped ferroelectric systems such as Sm-doped $Pb(Mg_{1/3}Nb_{2/3})O_3$–$PbTiO_3$ [12] represent promising targets for future studies.

References

[1] K. Hayashi *et al.*, J. Phys.: Condens. Matter. **24**, 093201 (2012).
[2] K. Kimura, J. Phys. Soc. Jpn. **91**, 091005 (2022).
[3] W. Hu *et al.*, Phys. Rev. B. **89**, 140103 (2014).
[4] K. Kimura *et al.*, Phys. Rev. B. **104**, 144101 (2021).
[5] Y. Yamamoto *et al.*, Appl. Phys. Lett. **120**, 052905 (2022).
[6] K. Hayashi *et al.*, Sci. Adv. **3**, e1700294 (2017).
[7] J. J. Barton, Phys. Rev. Lett. **67**, 3106 (1991).
[8] K. Momma and F. Izumi, J. Appl. Cryst. **44**, 1272 (2011).
[9] J. Harada *et al.*, Acta Crystallogr., Sect. A **26**, 336 (1970).
[10] G. H. Kwei *et al.*, J. Phys. Chem. **97**, 2368 (1993).
[11] K. Yamakawa *et al.*, J. Phys. Soc. Jpn. **93**, 104601 (2024).
[12] F. Li *et al.*, Science. **364**, 264 (2019).

K. Kimura[1], K. Yamakawa[1], H. Nakada[1], K. Oikawa[2], M. Harada[2], Y. Inamura[2], K. Ohoyama[3], and K. Hayashi[1]
[1]*Department of Physical Science and Engineering, Nagoya Institute of Technology;* [2]*Neutron Science Section, Materials and Life Science Division, J-PARC Center;* [3]*Graduate School of Science and Engineering, Ibaraki University*

Development of a Compact *in-situ* ^{3}He Neutron Spin Filter at J-PARC

1. Introduction

A neutron polarization device using polarized ^{3}He gas (^{3}He neutron spin filter: ^{3}He NSF) produced by spin-exchange optical pumping (SEOP) has been developed at J-PARC [1]. The ^{3}He NSF can polarize neutrons across a wide energy range owing to the strong spin dependence of the neutron absorption cross-section of ^{3}He nuclei. However, the ^{3}He NSF becomes larger in size than other polarization devices because SEOP requires many components, including a ^{3}He glass cell (^{3}He cell), a static magnetic field (B_0 coil), a heater, and a laser system. Since the experimental space at MLF is limited, the *ex-situ* ^{3}He NSF, a system in which a ^{3}He cell is polarized offline and brought to the beamline has been used for user experiments at BL04, BL06, BL10, BL15, and BL21 [1]. The *ex-situ* ^{3}He NSF offers advantages of simplicity and compactness. However, ^{3}He polarization begins to decay once the ^{3}He cell is removed from the laser system. This decay leads to a decrease in data quality as neutron polarization and transmission decrease with ^{3}He polarization decay. Meanwhile, an *in-situ* ^{3}He NSF is a system where a laser system is integrated and thus can maintain ^{3}He polarization. This system was adopted at BL23 as a dedicated polarization device [2]. To expand the use of the *in-situ* ^{3}He NSF at various beamlines, downsizing of the system is necessary. Therefore, we have developed a new compact *in-situ* ^{3}He NSF to enhance polarized neutron experiments at MLF. Details can be found in Ref. [3].

2. Design and construction of the *in-situ* ^{3}He NSF

Some beamlines have a space of approximately 300 to 400 mm along the beam axis where a ^{3}He NSF can be installed. Therefore, this study aimed to downsize the system to fit within these installation spaces without any modification to the existing beamlines. The optical system that defines the dimensions of the laser shielding box was designed based on ray-tracing calculations, resulting in dimensions of 320 x 400 x 540 mm (length x width x height), as shown in Fig. 1. The fabricated *in-situ* ^{3}He NSF comprises a ^{3}He cell, laser source, optical system, laser shielding box, B_0 coil, and adiabatic fast passage nuclear magnetic resonance (AFP-NMR) system which can flip the ^{3}He spin direction. The ^{3}He cell, made of a boron-free aluminosilicate GE180 glass with an outer diameter of 35 mm, and a length of 50 mm was employed. The glass cell was filled with approximately 3 atm of ^{3}He at room temperature, 100 Torr of N_2 gas, and small amounts of Rb and K for hybrid SEOP [1]. An air-cooled, fiber-coupled infrared laser source was employed as the pumping laser. This laser source does not need to be placed inside the shielding box, enabling a more compact design. In addition to the 100 W pumping laser, the laser source can emit a 2 mW red pilot laser for optical alignment. As a result, this *in-situ* ^{3}He NSF can be installed at beamlines without requiring any modification to establish a new laser-controlled area. The laser light into the shielding box through a 10 m fiber cable is converted into circularly polarized light by internal optical systems and irradiated onto the cell from both sides. Quarter-wave plates can switch the circular polarization in synchronization with the AFP-NMR, allowing the ^{3}He polarization to be maintained for either spin state. This AFP-NMR system is contained inside the B_0 coil. The B_0 coil was designed using finite element simulations to optimize magnetic field homogeneity for achieving high ^{3}He polarization.

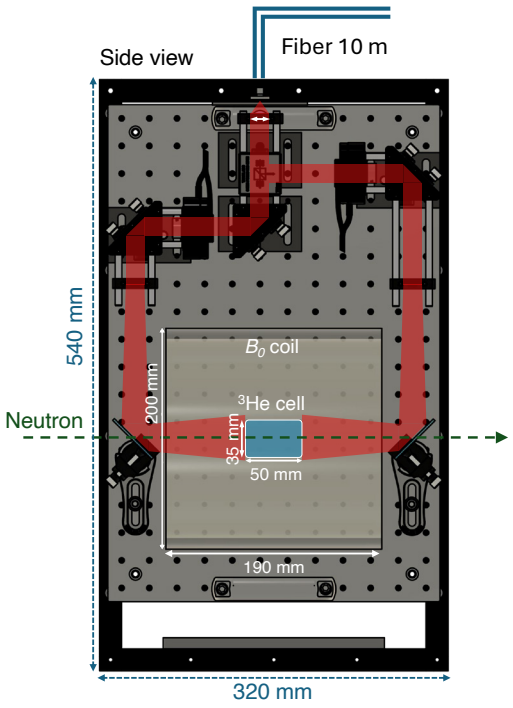

Figure 1. Schematic side view of the *in-situ* ^{3}He NSF. The red line shows the laser light path.

3. Experiments and results

The performance of the *in-situ* ^{3}He NSF was evaluated on NOBORU at BL10 and on SENJU at BL18.

In NOBORU, neutron transmission measurement was conducted to assess the ^{3}He polarization. The ^{3}He polarization was estimated from the ratio of transmitted neutron intensities between the polarized and unpolarized ^{3}He. Figure 2 shows the time dependence of the ^{3}He polarization measured every 15 min over 110 h and the AFP-NMR signal measured every 30 min. The average ^{3}He polarization over the period from 25 h to 130 h was 0.611 ± 0.005. The wavelength dependence of the neutron polarization and neutron transmission during saturated ^{3}He polarization is shown in Fig. 3. These results indicate that the developed *in-situ* ^{3}He NSF stably polarized neutrons over a wide energy range for an extended period.

In SENJU, a polarized neutron diffraction experiment was conducted using the *in-situ* ^{3}He NSF as the incident neutron polarizer and the (111) reflection of a Cu_2MnAl single crystal as the scattering neutron polarization analyzer (Fig. 4). The scattering intensities between spin-up and spin-down showed a clear difference and the flipping ratio was 13.1 ± 2.4 at 4.1 Å. This result demonstrates that the developed *in-situ* ^{3}He NSF can perform quantitative measurements in polarized pulsed neutron diffraction experiments.

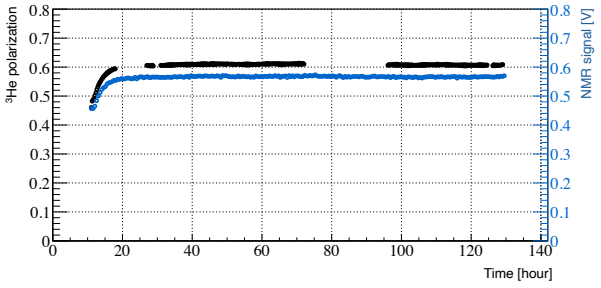

Figure 2. Time dependence of the ^{3}He polarization (black) and AFP-NMR signal (blue).

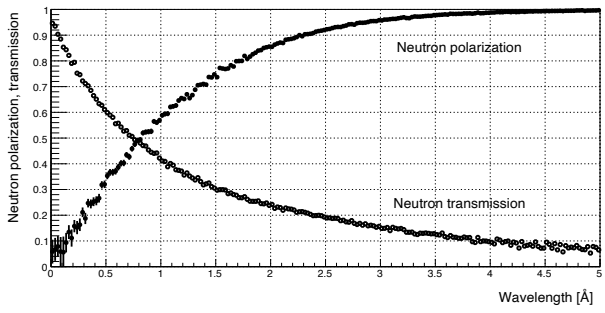

Figure 3. Neutron wavelength dependence of neutron polarization (open circles) and neutron transmission (dots) at saturated ^{3}He polarization.

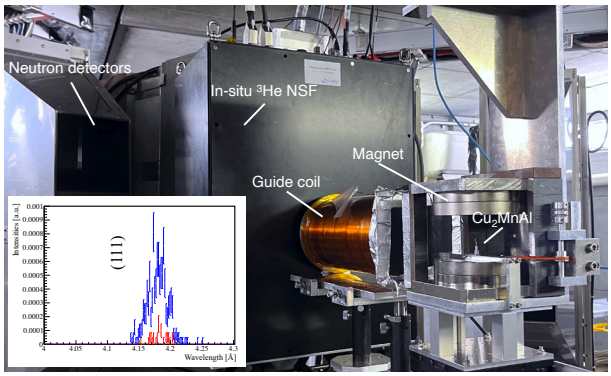

Figure 4. Photograph of setup on SENJU. The inset shows the (111) reflection of Cu_2MnAl. The red and blue lines represent the intensities of spin-up and spin-down neutrons, respectively.

4. Future Plans

Several applications based on this compact and versatile *in-situ* ^{3}He NSF are planned at various beamlines. For example, a dedicated *in-situ* ^{3}He NSF has been developed for nuclear physics experiments at BL04. In addition, magnetic holography experiments are planned at BL10. The utilization of this device on BL21 is also under consideration. Through these developments, the application of polarized neutrons at MLF is expected to make significant progress.

References

[1] T. Okudaira *et al.*, Nucl. Inst. and Meth. Phys. Res. A **977**, 164301 (2020).
[2] T. Ino *et al.*, J. Phys. Conf. Ser. **862**, 012011 (2017).
[3] S. Takahashi *et al.*, Nucl. Inst. and Meth. Phys. Res. A **1075**, 170410 (2025).

S. Takahashi[1,2], R. Kiyanagi[3], T. Okudaira[4,2], S. Takada[5,2], R. Kobayashi[2], M. Okuizumi[4], T. Ino[6], K. Asai[4], Y. Tsuchikawa[3], K. Oikawa[3], M. Harada[7], T. Ohhara[3], J. Suzuki[8], M. Fujita[5], Y. Ikeda[5], K. Kakurai[9,10], and T. Oku[2,11]

[1]*The Institute for Solid State Physics, the University of Tokyo;* [2]*Technology Development Section, Materials and Life Science Division, J-PARC Center;* [3]*Neutron Science Section, Materials and Life Science Division, J-PARC Center;* [4]*Department of Physics, Nagoya University;* [5]*Institute for Materials Research, Tohoku University;* [6]*Institute of Materials Structure Science, KEK;* [7]*Neutron Source Section, Materials and Life Science Division, J-PARC Center;* [8]*Neutron Industrial Application Promotion Center, CROSS;* [9]*Institute of Multidisciplinary Research for Advanced Materials, Tohoku University;* [10]*RIKEN Center for Emergent Matter Science;*[11]*Graduate School of Science and Engineering, Ibaraki University*

Direct Observation of Hydrogen-Bond Symmetrization in Ice by Neutron Diffraction up to 100 GPa

1. Introduction

Water exhibits an extraordinary diversity of crystalline structures depending on temperature and pressure. At least twenty distinct polymorphs of ice have been identified, and new forms continue to be discovered almost every few years. Among these, high-pressure ices provide a fascinating arena for studying fundamental aspects of hydrogen bonding under extreme conditions—an essential theme not only in condensed matter physics but also in planetary science.

In 1964, Kamb and Davis [1] determined the crystal structure of ice VII, one of the high-pressure polymorphs stable above 2 GPa. In their seminal work, they predicted that with increasing pressure, the lengths of O–H covalent bond and the H···O hydrogen bond in ice VII become closer and would eventually become equal at a certain pressure. This transition, known as hydrogen-bond symmetrization, corresponds to the situation in which the hydrogen atom sits exactly midpoint between two neighboring oxygen atoms. To the best of my knowledge, the paper by Kamb and Davis represents the earliest discussion of hydrogen-bond symmetrization induced by pressure.

Although the possibility of hydrogen-bond symmetrization was proposed more than half a century ago, experimental evidence did not emerge until the late 1990s. At that time, several groups conducted vibrational spectroscopic studies [2-4], including infrared absorption measurements, on ice VII under pressure. From these vibrational studies, the transition pressure was estimated to be around 60 GPa for H_2O ice, leading to the designation of the symmetrized phase as ice X. Interestingly, the corresponding transition pressure for D_2O ice was found to be much higher, approximately 70 GPa, highlighting a strong isotope effect. This difference has been explained in terms of quantum tunneling effect: the proton in H_2O, owing to its smaller mass, exhibit a large spread in their wavefunction, enabling them to more easily tunnel through the potential barrier separating two adjacent hydrogen sites. Consequently, the effective potential shape becomes symmetric at a lower pressure than in the case of deuterium.

In the late 2010s, several new experiments, such as high-pressure ^{1}H-NMR measurements and X-ray diffraction studies [5,6] of the compressibility, suggesting that the hydrogen-bond symmetrization might occur at different pressures than previously thought. However, these methods probed indirect signatures, such as changes in electronic or elastic properties, rather than directly visualizing the hydrogen positions. Consequently, reported transition pressures varied widely across the literature, ranging from 20 to 75 GPa. Rather than converging on a clear answer, the situation became increasingly ambiguous.

2. Neutron diffraction up to 100 GPa

After years of technical developments and optimization of experimental procedures, we finally achieved a major milestone in March 2021: the neutron diffraction patterns from ice VII at pressures exceeding 100 GPa. This was made possible by a combination of high brilliance neutron sources at J-PARC/MLF, newly designed opposed-anvil high-pressure cells [7], and finely collimated radial collimators [8] that minimizes background scattering.

Over the next few years, we dedicated extensive efforts to improving the quality of the diffraction data by enhancing signal-to-noise ratios and refining attenuation corrections. By December 2023, we obtained a complete and high-quality dataset suitable for quantitative structure refinement (Fig. 1). These measurements represent the highest-pressure neutron diffraction data ever recorded for an ice phase [9].

3. Hydrogen-bond symmetrization

Neutron diffraction provides three key structural parameters, which describe the spatial distribution of each atom around its mean position, often approximated by a Gaussian function.

Using these parameters, we reconstructed the deuterium probability density distribution along the O–O axis (Fig. 2). At lower pressures, the distribution of the distance between a deuterium and an oxygen atom exhibits two distinct peaks, corresponding to the two local minima between neighboring oxygen atoms. As pressure increases, these two peaks become closer. Above approximately 80 GPa, they merge into a single peak, indicating that the hydrogen atoms occupy a midpoint between two oxygens.

This transition from a bimodal to a unimodal hydrogen distribution constitutes the first direct

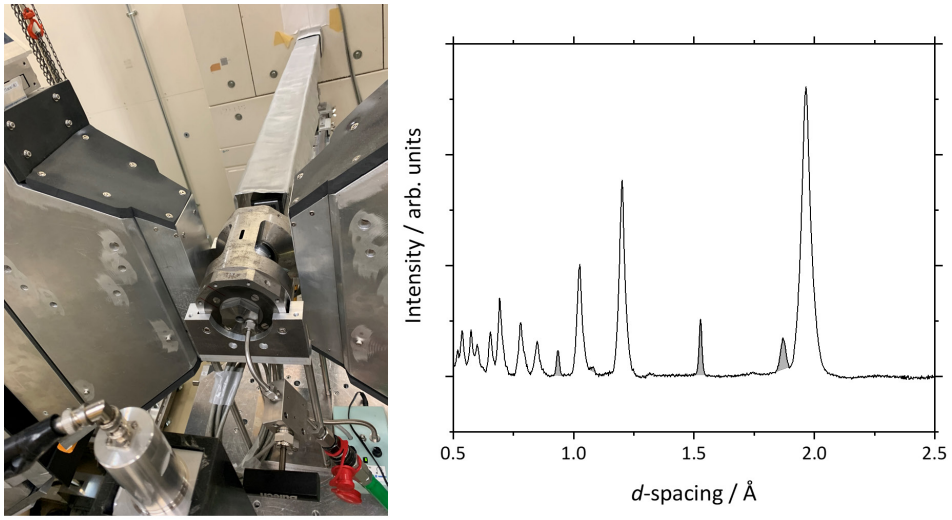

Figure 1. High-pressure apparatus installed at PLANET (left) and neutron diffraction pattern of ice X at 101 GPa (right). The shaded peaks are from ice and the others from diamond anvils.

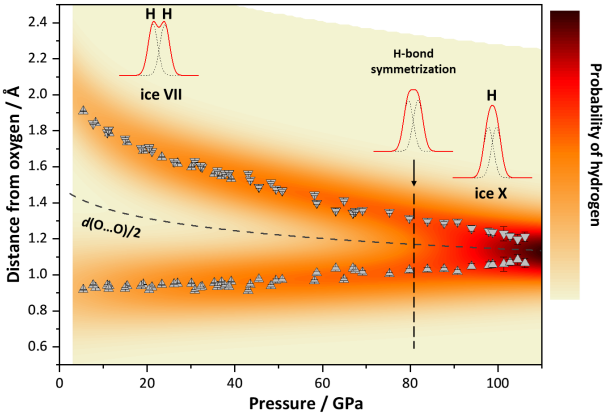

Figure 2. Pressure dependence of the distance and its distribution of a deuterium atom from the oxygen atom in ice obtained from high-pressure neutron diffraction experiments.

experimental observation of hydrogen-bond symmetrization in ice. Unlike previous spectroscopic or elastic property measurements, neutron diffraction provides an unequivocal structural proof: the hydrogen atoms come to occupy the position truly at the center of the O···O linkage in the oxygen framework of ice at ultrahigh pressure.

4. Implications and Outlook

From an experimental perspective, achieving neutron diffraction at pressures exceeding 100 GPa marks a technological breakthrough. The success of these experiments was made possible by the continuous development of high-pressure techniques at the J-PARC MLF BL11 PLANET beamline, which provides one of the world's most efficient neutron experiment platform for high-pressure research. The results also demonstrate the unique capability of neutron scattering in visualizing light atoms, especially hydrogen.

References

[1] B. Kamb and B.L. Davis, Proc Natl Acad Sci USA. **52**, 1433 (1964).
[2] A.F. Goncharov *et al.*, Science. **273**, 5272 (1996).
[3] K. Aoki *et al.*, Phys. Rev. B **54**, 22 (1996).
[4] Ph. Pruzan *et al.*, J. Phys. Chem. B **101**, 6230 (1997).
[5] T. Meier *et al.*, Nat. Commun. **13**, 3042 (2022).
[6] A.S.J. Méndez *et al.*, Phys. Rev. B **103**, 064104 (2021).
[7] K. Komatsu *et al.*, High Press. Res. **40**, 184 (2020).
[8] T. Hattori *et al.*, Nucl. Instrum. Methods Phys. Res. A **1059**, 168956 (2024) .
[9] K. Komatsu *et al.*, Nat. Commun. **15**, 5100 (2024).

K. Komatsu[1]
[1]*Graduate School of Science, The University of Tokyo.*

Experimental Verification of Altermagnet by Inelastic Neutron Scattering Technique

1. Introduction

The microscopic structures of magnets have traditionally been classified into two categories: ferromagnets, in which spins align parallel to each other (Fig. 1(a) top), and antiferromagnets, in which spins align antiparallel to each other (Fig. 1(b) top). Recently, however, a third class of magnets, known as altermagnets, has been proposed [1,2]. This new class emerged from the introduction of a novel concept—classifying magnets based on the symmetry that includes not only spin orientation but also the surrounding ligands structure. In antiferromagnets, the local environments around neighboring spins are identical. In contrast, in altermagnets (Fig. 1(c) top), the crystal environments surrounding oppositely oriented spins differ. For example, the local crystal structure (schematically represented by the gray diamond) surrounding the up spin indicated by the red arrow at the lower left does not coincide directly with that surrounding the down spin (blue arrow) at the upper left (or lower right). They overlap only after a 90° rotation. Magnets possessing such crystal symmetry—where the local environments of opposite spins do not coincide by translation alone but coincide upon rotation, while maintaining antiparallel spin alignment—are classified as altermagnets.

In this newly classified group of altermagnets, an intriguing physical state called the chiral magnon has been theoretically predicted. A chiral magnon is a quasiparticle capable of carrying spin current. Traditionally, chiral magnons in ferromagnets have attracted significant attention. However, from the viewpoint of magnonic device applications, ferromagnetic devices operate only at low frequencies (GHz range) (Fig. 1(a) bottom), which limits their performance. Moreover, because ferromagnets possess a finite magnetization, they inevitably generate stray magnetic fields, which are undesirable for device integration. In contrast, antiferromagnets are expected to operate at much higher frequencies (THz range) near Γ point ($q = 0$), which is accessible by light, but their magnon chirality completely cancels out (Fig. 1(b) bottom), making it impossible to sustain a net spin current. Consequently, realizing device operation based on antiferromagnons is difficult. In contrast, altermagnets combine the advantages of both ferromagnets and antiferromagnets. The magnons in altermagnets are theoretically predicted to exhibit chiral splitting as indicated by red and blue curves in Fig. 1(c) bottom. In other words the spin currents with opposite chiralities acquire different energies preventing cancellation and thereby enabling the generation of ultrafast spin currents. Thus, altermagnets represent a new class of materials that, despite having antiparallel spin alignment and zero net magnetization (like antiferromagnets, eliminating stray fields), still host chiral magnons akin to those in ferromagnets. Direct observation of magnons in altermagnets is therefore crucial—not only to verify whether a material truly exhibits altermagnetism, but also to explore its potential for magnonic device applications. Although many candidate altermagnetic materials have been proposed, magnons in such systems had not been experimentally observed until very recently.

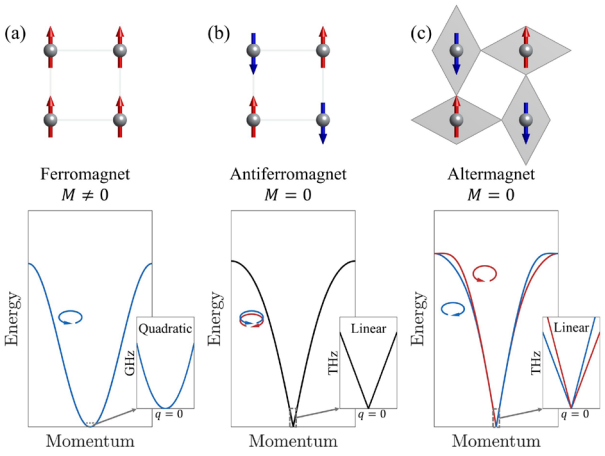

Figure 1. (a): Ferromagnetic, (b): Antiferromagnetic, (c): Altermagnetic spin structures (top), and the dispersion relations of magnons (bottom). M indicates magnetization. The red and blue rotating circles represent opposite chiralities (right- and left-handed).

2. Content of Research

The research group synthesized large, high-quality single crystals of MnTe, a candidate altermagnetic material, to observe its magnon dispersion. Mn ions are particularly suitable for neutron-scattering studies of magnetic excitations, and spin splitting characteristic of altermagnetism had already been reported in angle-resolved photoemission spectroscopy (ARPES) measurements. Therefore, MnTe was expected to be an ideal system for observing chiral magnon splitting.

Inelastic neutron-scattering experiments were

conducted using the High-Resolution Chopper Spectrometer (HRC) [3] at the Materials and Life Science Experimental Facility (MLF) of J-PARC. The HODACA spectrometer [4] at the JRR-3 research reactor was also employed for crystal characterization.

The observed neutron spectra are shown in Figs. 2(a) and 2(c). In Fig. 2(a), at excitation energies above E = 30 meV, a magnon splitting of approximately 2 meV (indicated by white circles) was detected [5]. In the low-energy, small-momentum region, the magnon dispersion rises linearly, resembling that of a conventional antiferromagnet. These features provide crucial evidence for altermagnetic behavior.

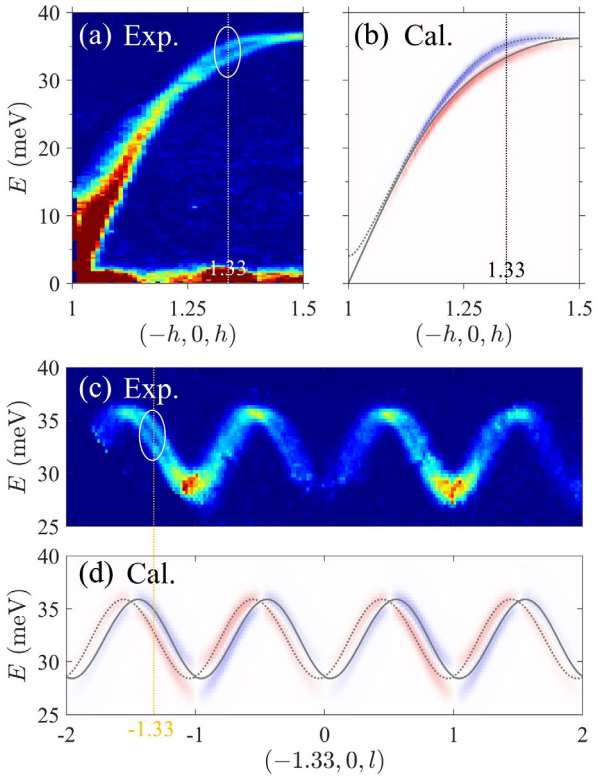

Figure 2. (a) & (c) Neutron spectra of MnTe. These show different momentum regions, but $h = 1.33$ in (a) and $l = -1.33$ in (c) represent the same momentum -1.33, 0, -1.33). At this momentum, a magnon splitting of approximately 2 meV was observed. (b) & (d) Calculated magnon chirality. Red and blue represent magnons with different chiralities. The gray solid and dashed lines indicate the calculated magnon dispersion.

Figure 2(c) displays the high-energy spectrum in a different momentum region, where alternating propagation of the split magnon branches along the momentum axis was clearly observed. The calculated magnon dispersions, shown as grey solid and dashed lines in Figs. 2(b) and 2(d), reproduce the experimental spectra with excellent agreement. When counter-clockwise and clockwise chiralities are represented in red and blue, respectively, the low-energy region appears colorless due to complete cancellation of chiralities, whereas at higher energies, the two magnons exhibit distinct chiralities—clearly visible as red and blue branches. The alternating pattern of chirality in Fig. 2(d) confirms the presence of chiral magnons capable of carrying spin current.

3. Future Prospects

Altermagnetic materials embody a new paradigm in magnetism. The experimental verification of chiral magnons presented in this study demonstrates their potential to generate spin current, offering a key step toward realizing high-speed and energy-efficient magnonic devices. This discovery establishes a foundation for future exploration of ultrafast spin transport phenomena and functional magnetic materials at the MLF.

References

[1] L. Šmejkal, J. Sinova, and T. Jungwirth, Phys. Rev. X **12**, 031042 (2022).
[2] L. Šmejkal, J. Sinova, and T. Jungwirth, Phys. Rev. X **12**, 040501 (2022).
[3] S. Itoh, T. Yokoo, S. Satoh, S. Yano, D. Kawana, J. Suzuki, and T. J. Sato, Nucl. Instrum. Methods Phys. Res., Sect. A **631**, 90 (2011).
[4] H. Kikuchi, S. Asai, T. J. Sato, T. Nakajima, L. Harriger, I. Zaliznyak, and T. Masuda, J. Phys. Soc. Jpn. **93**, 091004 (2024).
[5] Z. Liu, M. Ozeki, A. Asai, S. Itoh, and T. Masuda., Phys. Rev. Lett. **133**, 156702 (2024).

Z. Liu[1], M. Ozeki[1], S. Asai[1], S. Itoh[2,3], and T. Masuda[1,3]
[1]The Institute for Solid State Physics, The University of Tokyo; [2]Neutron Science Section, Materials and Life Science Division, J-PARC Center; [3]Institute of Materials Structure Science, KEK

Singular Continuous and Nonreciprocal Phonons in Quasicrystal AlPdMn

1. Introduction

Quasicrystals, a class of materials discovered four decades ago [1], present a profound challenge in condensed matter physics: they possess long-range order but fundamentally lack the translational symmetry that defines conventional crystals. This aperiodic structure gives rise to peculiar properties, including unusual electrical, thermal, and magnetic properties [2-4]. To understand these features, it is essential to resolve a long-standing issue: how do phonons propagate in these uniquely ordered, non-periodic lattices? Theoretical models predict that the breakdown of Bloch's theorem in quasicrystals should lead to singular continuous states [5], characterized by an infinite number of fine energy gaps, a signature of their self-similar structure. Earlier experiments using neutron were limited by energy resolution [6], preventing a definitive confirmation of these pseudo-gaps.

To address this issue, we performed inelastic neutron scattering study on the acoustic phonon modes of the icosahedral quasicrystal AlPdMn by using the TOF type backscattering spectrometer DNA (BL02) and cold-neutron disk chopper spectrometer AMATERAS (BL14) [7]. Both the DNA and AMATERAS are characterized by their low background, which facilitates the acquisition of clean $S(Q, \omega)$ data in the low-energy region. Specifically, AMATERAS permits the simultaneous collection of data with multiple E_i's and energy resolutions (ΔE). Meanwhile, DNA is a unique instrument, combining a coupled moderator with a pulse-shaping chopper to achieve μeV resolution in the meV energy range. By combining DNA and AMATERAS, we achieved various ΔE~0.004 meV and 0.015 meV with DNA and 0.05, 0.15, and 1.2 meV with AMATERAS. This capability allowed us to focus on hierarchical pseudogap structure especially at low-energy, small-momentum acoustic phonons, which reflect lattice dynamics on the larger length scales sensitive to the quasiperiodic order.

Figure 1(a) shows a contour map of phonon intensity at T=300 K around (0,2,2,0,-2,0) Bragg peak obtained using AMATERAS with ΔE of 0.015 meV. The phonon intensity drops discontinuously at several energies, which is clearly demonstrated in the Q-integrated phonon intensity in Fig. 1(b). In general, the intensity of acoustic modes in periodic lattices increases inversely proportional to energy. However, the acoustic mode

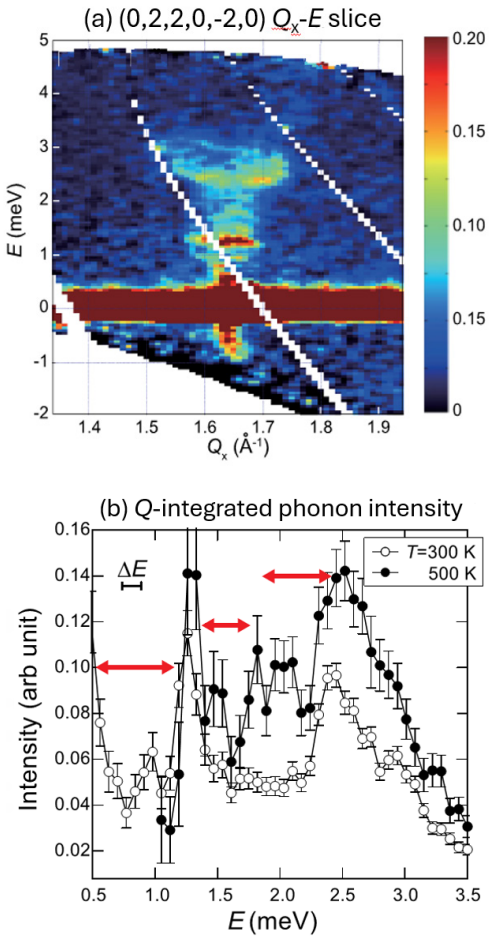

Figure 1. (a) Contour maps of phonon scattering intensity at T=300 K around (0,2,2,0,-2,0) Bragg peak. (b) Energy dependences of Q-integrated phonon intensity around the (0,2,2,0,−2,0) Bragg peak [7].

for the quasicrystal exhibits abrupt drops in intensity at several energies: 0.5–1.1, 1.3–1.75, and 2.2 meV. Furthermore, we observed hierarchical finer gap structure at lower energies with better energy resolutions of AMATERAS and DNA. A comparative analysis of these gap energies revealed a remarkable finding: they are scaled by the golden mean ($\tau = (1+\sqrt{5})/2$), the key parameter for the self-similar structure of icosahedral quasicrystals. The hierarchical gap structures with τ-scaling strongly provide the first direct evidence of the predicted singular-continuous states, marking a major breakthrough in the field of aperiodic lattice dynamics.

Furthermore, the best-resolution data (ΔE of 0.004 meV) from DNA revealed that the pseudo-gap structure vanishes in the extremely low-energy region below

0.06 meV. The lowest observed pseudo-gap corresponded to characteristic phonon wavelengths ranging from approximately 1000~2700 Å, which closely matches the structural coherence length (480~2000 Å derived from high-resolution X-ray diffraction measurements [8]. This observation links the structural perfection to its dynamic behavior, no pseudo-gaps for wavelengths beyond the coherence length of quasiperiodic order.

Beyond the hierarchical energy structure, we also uncovered a novel phenomenon: nonreciprocal phonon dynamics in quasicrystals. Figure 2(a) shows the energy slices of phonon scattering intensity around the (0,2,2,0,-2) Brag peak integrating energy range of 2.1~2.4 meV.

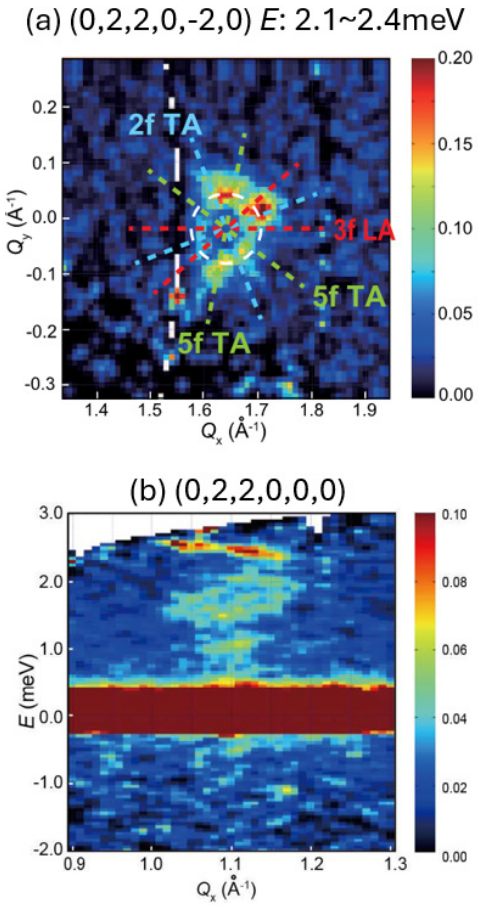

Figure 2. (a) Contour maps of phonon scattering intensity at T=300 K around (0,2,2,0,-2,0) Bragg peak for Q_x-Q_y slice. (b) Asymmetric phonon signal with respect to energy around (0,2,2,0,0,0) [7].

Suppression of the phonon intensity along specific directions as indicated by dotted lines can be explained by anisotropic pseudo-gaps. However, the phonon scattering intensity distribution was found to be highly asymmetric with respect to the Bragg point in Q-space, which is not seen in a periodic lattice. More significantly, we observed a pronounced asymmetry in intensity between the positive-energy and negative-energy sides around certain Bragg peaks, as shown in Fig. 2(b). Phonons are quasiparticles subject to Bose statistics, whose intensity is proportional to the Bose factor. Bose factors on the negative-energy side can be close to zero at low temperatures; however, the current data were measured at 300 K, which rules out such a scenario. The principle of detailed balance of scattering function $S(-Q,-\omega)=\exp(-\hbar\omega/k_BT)\,S(Q,\omega)$ guarantees that excitation at (Q,ω) should have a nearly equivalent signal at $(-Q,-\omega)$ at T=300 K and low energies. The current observation of the asymmetrical phonon intensity in energy can be related to the asymmetry in phonon intensity between Q and $-Q$, indicating characteristic non-reciprocal phonon in quasicrystals.

In summary, this research, powered by the superior resolution and low background of the AMATERAS and DNA, has discovered singular continuous states and nonreciprocal phonons in quasicrystals. Since phonons are key to thermal transport and thermoelectric performance, these distinctive characteristics in the phonons of quasicrystals can offer unique functions of quasicrystals not being available in periodic lattice.

References

[1] D. Shechtman *et al.*, Phys. Rev. Lett. **53**, 1951 (1984).
[2] P. Lanco *et al.*, J. Non-Cryst. Solids. **153**, 325 (1993).
[3] K. Edagawa and K. Kajiyama, Mater. Sci. Eng. **294**, 646 (2000).
[4] K. Deguchi *et al.*, Nat. Mater. **11**, 1013 (2012).
[5] A. Sütő, J. Stat. Phys. **56**, 525 (1989).
[6] M. De Boissieu *et al.*, J. Phys. Condens. Matter **5**, 4945 (1993).
[7] M. Matsuura *et al.*, Phys. Rev. Lett. **133**, 136101 (2024).
[8] J. Gastaldi *et al.*, Philos. Mag. **83**, 1 (2003).

M. Matsuura[1], J. Zhang[2], Y. Kamimura[2], M. Kofu[3], and K. Edagawa[2]
[1]*Neutron Science and Technology Center, CROSS;* [2]*Institute of Industrial Science, The Univ. of Tokyo;* [3]*Neutron Science Section, Materials and Life Science Division, J-PARC Center*

Adsorption Characteristics of Polymer Additives under Shear Condition in a Narrow Gap

1. Introduction

In recent years, the use of polymer additives in lubricants has become more commonplace, aiming to achieve low friction and high wear resistance in sliding surfaces under boundary lubrication conditions. Traditionally, the most common application of polymer additives in lubricants was as viscosity index improvers [1,2]. However, some viscosity index improvers also possess adsorption properties, and research has evaluated their performance as friction modifiers due to their ability to adsorb onto metal surfaces [3,4].

The adsorption structure of polymer additives has traditionally been difficult to elucidate, but is gradually becoming clearer with advances in surface and interfacial analysis techniques. Neutron reflectometry is a useful technique capable of quantitatively measuring the thickness and density of adsorption layers; specifically, the use of deuterated polymers enables clear visualization of the additive adsorption layer structure within base oils. Several studies have also been conducted on the adsorption structure of polymer additives [5-7].

On the other hand, very few studies have verified the effect of polymer additives under conditions of full fluid-film lubrication, specifically in high-shear conditions within a narrow gap. Consequently, the extent to which polymer additives adsorb under fluid lubrication and the characteristics they exhibit remain unclear. While polymer additives are generally expected to contribute to friction reduction under boundary lubrication conditions, understanding the fluid lubrication characteristics of oils containing polymer additives is critically important.

Therefore, this study investigated the adsorption characteristics of polymer additives in shear fields using neutron reflectometry techniques.

2. Polymer Additive Sample

For the adsorption characteristic study, a polymethyl acrylate (PMA)-based polymer additive was prepared. The chemical structure of PMA-based polymer additive is shown in Figure 1. PMA-based additives are among the most common polymer additives, with multiple reports describing improvements in friction properties achieved through their use [8-10]. In this study, a PMA-based polymer additive with a molecular weight of approximately 430,000 and a branched structure containing numerous polar groups was selected as the sample. Deuterated squalane ($C_{30}D_{62}$, displayed as "d-squ") was chosen as the base oil, and the polymer additive was dissolved at a concentration of 0.1 mass%.

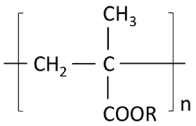

R: C1-C30 alkyl group

Figure 1. Chemical structures of PMA-based polymer additive for the study.

3. Neutron Reflectometry in Shear Field

In this study, to analyze the adsorption behavior of polymer additives under high shear conditions, a parallel-face viscometer with a narrow gap was installed on the neutron reflectometer SOFIA at J-PARC MLF. This allowed the acquisition of reflectivity profiles at the interface while applying shear. The substrate used was a 40×40×t5 Si block sputtered with a Cu coating approximately 30 nm thick. For specific details on the parallel-face viscometer mechanism, refer to [11,12]. Using neutron reflectometry, the interface structure between the upper surface of the lower disk (=Cu-sputtered Si block) and the sample oil was investigated while rotating the upper disk of the parallel-face viscometer. An upward force of 60 N was applied to the lower disk, with a gap length of approximately 2.3 μm. The neutron beam was incident from the side of the lower disk, and the reflectivity profile was obtained from reflections at the interface between the lower disk surface and the sample oil. The footprint was set to 2x10 mm to ensure the sample oil was confined within the outer ring region between the upper disk and the lower disk. Incidence angles were set at 0.3, 0.4, and 0.8°. The reflectivity profiles obtained at these angles were combined to derive a single reflectivity profile. Acquiring the single reflectivity profile took approximately 4 hours.

4. Results and Discussion

The experiments were conducted in the following order: (1) without lubricant, (2) after injecting sample oil into the gap and holding it stationary, (3) rotating at 100 rpm, (4) rotating at 60 rpm, (5) rotating at 20 rpm,

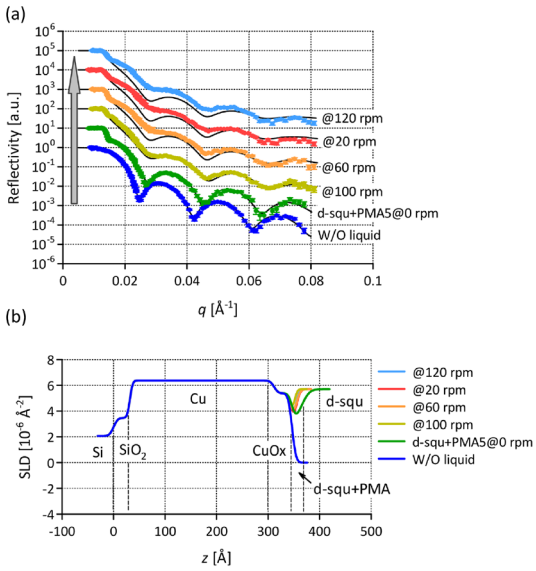

Figure 2. Neutron reflectometry results obtained by incorporating the parallel-face viscometer [13].

(6) stopping rotation (= stationary). The reflectivity profiles obtained under each condition are shown in Figure 2(a), and the SLD profiles estimated by optimally fitting these profiles are shown in Figure 2(b).

First, the reflectivity profile after sample oil injection in the stationary state and its corresponding SLD profile (second from the bottom) indicate that an adsorption layer up to 10 nm thick formed on the lower disk surface. Rotating the upper disk at 100 rpm reduced the adsorption layer thickness by approximately half. This phenomenon is consistent with observations in previous studies and is thought to result from the removal of some PMA molecules adsorbed on the surface due to shear forces. At this stage, the experimentally obtained reflectivity profile and the fitted curve agree well, indicating that the estimated SLD profile is valid. When the rotation speed of the upper disk was gradually reduced to 60, 20, and 0 rpm, no significant changes were observed in the SLD profile obtained from the optimal fitting. However, the discrepancy between the reflectivity profile and the fitting curve progressively increased. Neutron reflectometry is suitable for precise structural analysis perpendicular to the surface but is not well- suited for analyzing layers that exist in a non-uniform state within the plane. The changes in this reflectivity

profile obtained in this experiment do not correspond to changes in rotational speed but are attributed

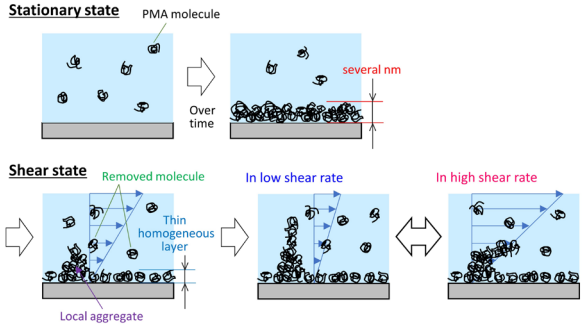

Figure 3. Illustration on adsorption behavior of adsorptive polymer additives [13].

to the gradual formation of an inhomogeneous layer over time. However, since the fringe pattern of the reflectivity profile itself did not change significantly even when the speed was varied, it can be inferred that a locally inhomogeneous layer formed while the thickness of the homogeneous layer remained essentially unchanged. Furthermore, the fact that the final profile at a rotation speed of 20 rpm is nearly identical to the profile at rest suggests that the formed adsorption layer remained on the surface even after rotation ceased. Finally, Figure 3 shows the behavior of the polymer additive inferred from these results.

Acknowledgements

Neutron reflectometry experiments at the Materials and Life Science Experimental Facility of the J-PARC was performed under a user program (Proposal No. 2022B0013).

References

[1] H. G. Müller, Tribol. Int. **11** 3, 189 (1978).
[2] M. J. Covitch, SAE Trans. **107**, 1881 (1998).
[3] J. Fan *et al.*, Tribol. Lett. **28** 3, 287 (2007).
[4] H. Spikes, Tribol. Lett. **60** 1, 5 (2015).
[5] J. B. Field *et al.*, Macromolecules. **25** 1, 434 (1992).
[6] Y. Song *et al.*, Macromolecules. **56** 5, 1954 (2023).
[7] N. Yamashita *et al.*, Tribol. Lett. **69** 2, 65 (2021).
[8] M. Müller *et al.*, Tribol. Trans. **49** 2, 225 (2006).
[9] M. Muraki *et al.*, Proc. Instit. Mech. Eng. Part J: J. Eng. Tribol. **224** 1, 55 (2010).
[10] M. Ueda *et al.*, Tribol. Int. **174**, 107756 (2022).
[11] T. Hirayama *et al.*, Lub. Sci. **32** 2, 46 (2020).
[12] N. Yamashita *et al.*, Sci. Rep. **13** 1, 18268 (2023).
[13] T. Hirayama *et al.*, Langmuir. **40** 12, 6229 (2024).

T. Hirayama[1], N. Yamashita[2], and M. Yamada[3,4]
[1]*Graduate School of Engineering, Kyoto University;* [2]*Dept. of Mechanical and System Engineering, Kyoto Institute of Technology;* [3]*Neutron Science Section, Materials and Life Science Division, J-PARC Center;* [4]*Institute of Materials Structure Science, KEK*

Water-Intercalated and Humidity-Responsive Lamellar Materials of Sodium Acrylate Random Copolymers

1. Introduction

Self-assembly and microphase separation of random, alternating, and brush (co)polymers attract attention for creating nanostructured materials with small domain spacing below 10 nm, as an alternative strategy using high χ–low N linear block copolymers [1, 2]. We have originally developed "pendant" microphase separation systems of amphiphilic random or alternating copolymers bearing hydrophilic poly(ethylene glycol) [2, 3], hydroxy [3, 4], and ionic [5, 6, 7] groups and hydrophobic alkyl groups for lamellar or nanostructured materials (Figure 1). By using the pendant self-assembly process, the domain spacing is controllable at a 0.1 nm level below 10 nm by the copolymer composition and side chains, and independent of the molecular weight and molecular weight distribution (MWD). Thus, common copolymers with broad MWD are also applicable to construct fine nanostructures.

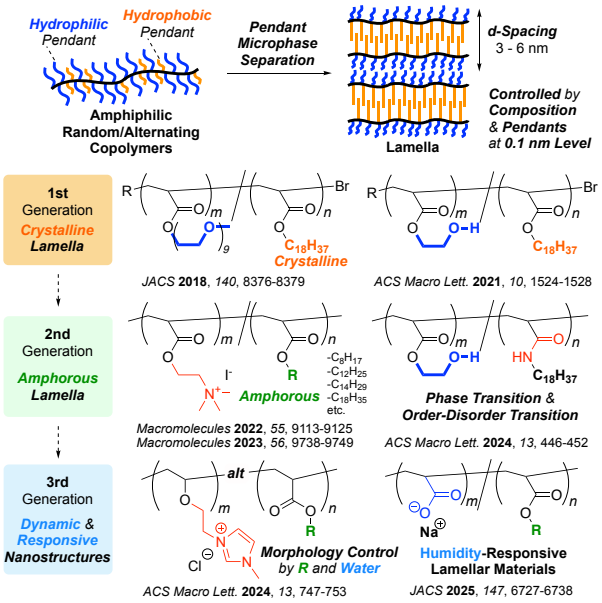

Figure 1. Design and pendant microphase separation of amphiphilic random/alternating copolymers into lamellar or nanostructured materials.

Water is ubiquitous on Earth and serves as an environment-friendly molecule in designing functional materials. Ionic (co)polymers have high affinity to water and often show hygroscopic properties. Focusing on the features, we examined water-assisted microphase separation of ionic random or alternating copolymers and successfully produced water-compatible and nanostructured materials. Importantly, the morphology and domain spacing can be controlled by not only polymer/pendant design but also the amount of absorbed water [6, 7].

Herein, we report water-intercalated and humidity-responsive lamellar materials obtained from the self-assembly of sodium acrylate (ANa)/alkyl acrylate (RA) random copolymers (Figure 2) [7].

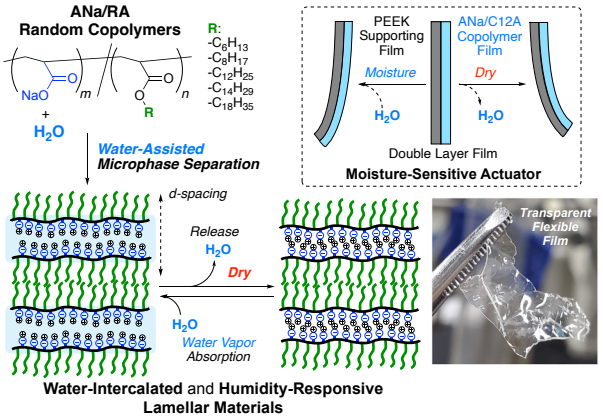

Figure 2. Water-assisted microphase separation of ANa random copolymers for water-intercalated and humidity-responsive lamellar materials [7].

2. Results and Discussion

ANa/RA random copolymers were synthesized by free radical copolymerization of *t*-butyl acrylate (tBA) and RA, followed by the post-modification of the tBA/RA copolymers with HCl and NaOH. Bulk ANa/RA random copolymers efficiently absorbed water via a water-vapor annealing process to form water-intercalated lamella. The phase separation depended on the weight fraction of the hydrophobic or hydrophilic segments including water. The domain spacing was tunable by the length of the hydrophobic groups, copolymer composition (ANa/RA molar ratio), and the amount of absorbed water.

For example, a bulk ANa/C12A (dodecyl acrylate) (5/5) random copolymer (M_n = 25600, M_w/M_n = 1.94) absorbed 19 wt% water therein (analyzed by TGA) via a water-vapor annealing in relative humidity (RH) 90% for 12 h. The number of H_2O per ANa unit was estimated to be ~5. As confirmed by SAXS, the water-absorbed sample formed lamella with 4.46 nm domain spacing. The bulk polymer becomes a flexible, transparent, and

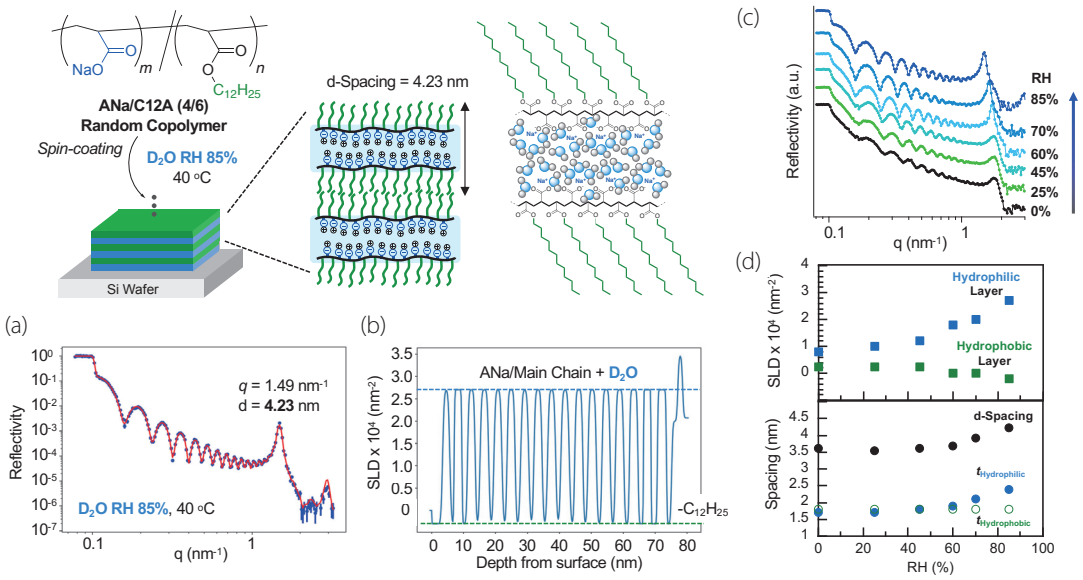

Figure 3. NR measurements of an ANa/C12A (4/6) random copolymer thin film on a silicon wafer. (a) NR profile (blue), the fitting curve (red), and (b) SLD profile of the thin film obtained in RH 85% at 40°C. (c) NR profiles of the thin film in RH 0, 25, 45, 60, 70, and 85% and (d) SLD, domain spacing, and layer thickness of the lamellar structures [7].

self-standing film (Figure 2), where the inner lamellar structure absorbs and releases water molecules to afford reversible expansion and contraction of the domain spacing at sub-1 nm level, responsive to humidity.

To clarify the lamellar structure in detail, the thin film of an ANa/C12A (4/6) random copolymer coated on a silicon wafer was analyzed by neutron reflectivity (NR, BL17, J-PARC) in RH 85% with D_2O vapor for neutron contrast at 40°C (Figure 3). The NR profile showed a sharp Bragg peak at q = 1.49 nm^{-1} originating from a layered lamellar structure parallel to the silicon wafer (d-spacing = 4.23 nm, Figure 3a). The multilayer consists of the hydrophobic phase of dodecyl groups and the hydrophilic phase of ANa/acrylate backbones and absorbed D_2O (Figure 3b).

NR measurements of an as-cast ANa/C12A (4/6) copolymer thin film by changing RH from 0% to 25%, 45%, 60%, 70%, and 85% with D_2O vapor revealed the following (Figure 3c,d): The thickness of the hydrophilic layer increased above RH 60%, into which D_2O molecules are selectively incorporated. The formation of the lamellar structure is promoted above RH 60% at 40°C.

3. Summary

We demonstrated that ANa/RA random copolymers absorbed water from outer environments to form small lamella consisting of the hydrophobic side chains and the hydrophilic ANa/main chains containing water. The double layer film of an ANa/C12A copolymer film and a PEEK supporting film was useful for a moisture-sensitive actuator, where the sub 1 nm-level humidity-response of the lamellar domain drives the macroscopic deformation of the film. This work would bring innovation in the design of water-compatible functional materials.

References

[1] C. Sinturel, F. S. Bates, M. A. Hillmyer, ACS Macro Lett. **4**, 1044 (2015).
[2] G. Hattori, M. Takenaka, M. Sawamoto, T. Terashima, J. Am. Chem. Soc. **140**, 8376 (2018).
[3] T. Ikami, M. Takenaka, H. Aoki, T. Terashima *et al.*, ACS Macro Lett. **10**, 1524 (2021).
[4] T. Ikami, H. Aoki, T. Terashima, ACS Macro Lett. **13**, 446 (2024).
[5] S. Imai, M. Takenaka, H. Aoki, T. Terashima *et al.*, Macromolecules. **55**, 9113 (2022).
[6] R. Sujita, H. Aoki, M. Takenaka, M. Ouchi, T. Terashima, ACS Macro Lett. **13**, 747 (2024).
[7] Y. Horiike, H. Aoki, M. Ouchi, T. Terashima, J. Am. Chem. Soc. **147**, 6727 (2025).

T. Terashima[1], Y. Horiike[1], and H. Aoki[2,3]
[1]*Department of Polymer Chemistry, Graduate School of Engineering, Kyoto University;* [2]*Institute of Materials Structure Science, KEK;* [3]*Neutron Science Section, Materials and Life Science Division, J-PARC Center*

Ferrimagnetic structure of the high-pressure state in α-Mn

1. Introduction

The elemental substance α-Mn possesses a highly complex crystal structure with 58 atoms per body-centered-cubic (bcc) unit cell, where Mn atoms occupy four distinct crystallographic sites. Magnetic moments order antiferromagnetically (AFM) below a Néel temperature (T_N) of 95 K. This AFM phase is confirmed by neutron diffraction, which reveals magnetic reflections at q = (0,0,1), consistent with a non-collinear magnetic structure in which each Mn site hosts a distinct magnetic moment [1,2].

The application of pressure rapidly suppresses T_N, which gives rise to a magnetic transition above 1.4 GPa with a transition temperature (T_A) of approximately 50 K. We recently discovered that this high-pressure phase exhibits a large anomalous Hall effect (AHE) and a weak ferromagnetic (WFM) character [3,4]. Notably, the anomalous Hall resistivity reaches approximately half the value of elemental Fe (a well-known ferromagnet), despite a significantly reduced spontaneous magnetization (~0.02 μ_B/Mn) compared to the individual Mn moments in the AFM phase. This large AHE is reminiscent of phenomena observed in non-collinear antiferromagnetic systems such as Mn_3Sn and Mn_3Ge, where Berry curvature is the driving mechanism. Since the AFM phase of α-Mn exhibits no AHE, a non-zero contribution from the Berry curvature is anticipated in the WFM phase, which arises from broken symmetry, like a ferromagnetic ordering with a magnetic propagation vector q = (0, 0, 0) [5].

To elucidate the magnetic structure of the WFM phase in α-Mn, we conducted single-crystal neutron-diffraction experiments under pressure.

2. Experimental

A large single crystal of α-Mn was grown using the Pb-flux method in a horizontal configuration. Neutron diffraction measurements were performed using the SENJU time-of-flight Laue diffractometer (BL18, MLF, J-PARC). Pressure up to 2.0 GPa was applied using a hybrid-anvil-type pressure cell [6]. The single-crystal sample, polished to a size of 1.0 × 1.0 × 0.4 mm^3, was mounted on the culet surface of the anvil with the $(0\bar{1}1)$ plane parallel to the surface and sealed with an aluminum alloy gasket along with the glycerol pressure transmitting medium. Pressure was determined at room temperature using the ruby fluorescence method. Magnetic and nuclear diffraction data were collected at six crystal orientations near the (*hkk*) reciprocal lattice plane. Data collection was performed at two key temperatures of 2.8 K and 60 K where the WFM and the paramagnetic phases are stable, respectively. Two wavelength bands of the second (λ = 4.4 ~ 8.8 Å) and 1.5 frames (λ = 2.2 ~ 6.6 Å) were used to increase the number of reflections available for analysis. The exposure time for each band was 4 and 6 hours, respectively. Temperature evolution was also measured from 2.8 K to 60 K with a shorter acquisition time. Data reduction and correction were performed using the STARGazer software.

3. Results and discussions

At 2.8 K, no additional intensity was observed except at the nuclear Bragg peak positions. *hkl* reflections with *h* = 2*n* (where *n* is an integer), which correspond to the nuclear Bragg peaks, exhibit a significant intensity increase compared to those at 60 K. This directly indicates that the magnetic structure in the WFM phase possesses the same symmetry as the atomic structure, characterized by a magnetic propagation vector q = (0, 0, 0).

Figure 1 represents the calculated and observed magnetic Bragg peak intensities at 2.8 K, represented by $|F_{\mathrm{mag}}|^2 = |F_{obs}(2.8\,\mathrm{K})|^2 - |F_{obs}(60\,\mathrm{K})|^2$, as magnetic peaks overlap with nuclear ones. A total of 23 reflections were observed, and the standard deviations are heavily influenced by the underlying nuclear Bragg peaks, which are typically much stronger than the magnetic signals.

Assuming nonzero magnetic moments on each

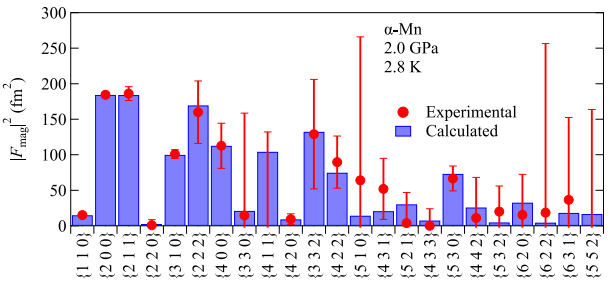

Figure 1. $|F_{\mathrm{mag}}|^2$ of magnetic reflections at 2.8 K. Error bars are shown by red lines. Blue bars represent the calculated intensities for the magnetic space group $I\bar{4}2'm'$ [7].

Mn site, the maximal magnetic space groups derived from the parent $I\bar{4}3m$ space group are rhombohedral $R3m'$, orthorhombic $Fm'm2'$, and tetragonal $I\bar{4}2'm'$. To identify the most plausible magnetic structure, we employed a least-squares refinement method that minimizes the R factor. Consequently, the $I\bar{4}2'm'$ magnetic space group exhibits the lowest R-factor, establishing it as the most likely candidate for the WFM phase in α-Mn.

Figure 2 illustrates the derived magnetic structure of α-Mn at 2.0 GPa. The refinement utilized 13 parameters, five of which were found to be statistically indistinguishable from zero within their error bars. Disregarding these negligible components, the magnetic moments at sites I (blue arrows), II (green arrows), III-1 (red arrows), and IV-1 (purple arrows) exhibit collinear alignment along the [001] direction. Conversely, the moments at sites III-2 (orange arrows) and IV-2 (magenta arrows) lie within the (001) plane. While the in-plane components cancel out, resulting in zero net moment within the (001) plane, a finite net moment remains along the [001] direction. This moment, amounting to $M_z = (-0.08 \pm 0.10)\mu_B$/Mn, is in good agreement with the spontaneous magnetization. Moreover, the magnetic moments obtained in this study agree well with the NMR resonance frequencies for sites I and II [8]. Conversely, the lack of corresponding NMR signals at sites III and IV, despite the nonzero magnetic moments in this study, suggests that the hyperfine coupling constant for these sites is significantly smaller than that for sites I and II. Since the emergence of a large AHE is highly dependent on the symmetry of the magnetic structure, the present result provides valuable constraints on the possible origins of the large AHE observed in high-pressure state of α-Mn. Furthermore, this work opens avenues for theoretical studies on the possible emergence of nonlinear charge transport phenomena in α-Mn under high pressure.

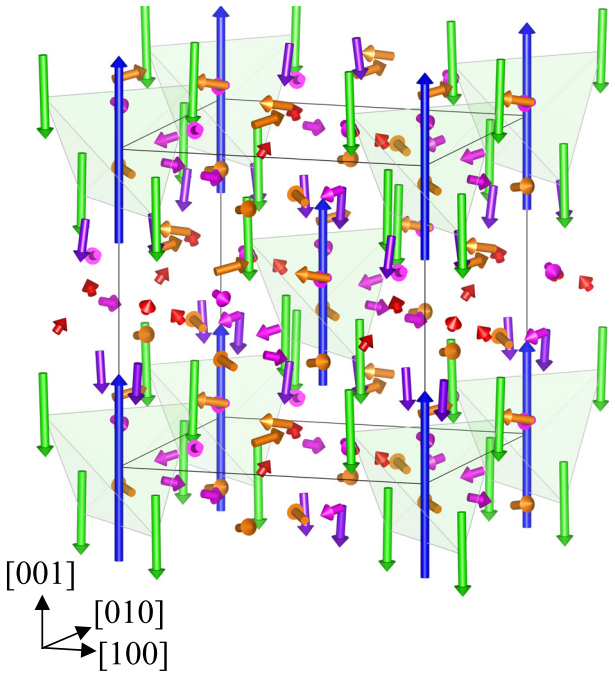

Figure 2. Magnetic structure of the WFM state of α-Mn determined at 2.0 GPa [7].

4. Conclusion

This study successfully identified that magnetic structure of the WFM state of α-Mn is ferrimagnetic by single crystal neutron diffraction experiments of a small sample (~0.4 mm^3) compressed with a hybrid-anvil pressure cell using SENJU diffractometer. The structure is dominated by large, antiparallel moments at site I (1.84 μ_B) and site II (0.83 μ_B). Importantly, nonzero magnetic moments (~0.3 μ_B) were also confirmed for sites III and IV.

References

[1] T. Yamada *et al.*, J. Phys. Soc. Jpn. **28**, 615 (1970).
[2] A. C. Lawson *et al.*, J. Appl. Phys. **76**, 7049 (1994).
[3] T. Sato *et al.*, JPS Conf. Proc. **30**, 011030 (2020).
[4] K. Akiba *et al.*, Phys. Rev. Res. **2**, 043090 (2020).
[5] Y. Yanagi *et al.*, Phys. Rev. B **107**, 014407 (2023).
[6] T. Osakabe *et al.*, J. Phys. Soc. Jpn. **79**, 034711 (2010).
[7] S. Araki *et al.*, Phys. Rev. B **110**, 094420 (2024).
[8] T. Ito *et al.*, J. Phys. Soc. Jpn. **90**, 085001 (2021).

S. Araki[1,2], K. Iwamoto[2], K. Akiba[1,2], T. C. Kobayashi[1,2], K. Munakata[3], K. Kaneko[4,5,6], and T. Osakabe[4]
[1]Department of Physics, Okayama University; [2]Graduate School of Natural Science and Technology, Okayama University; [3]Neutron Science and Technology Center, CROSS; [4]Materials Sciences Research Center, Japan Atomic Energy Agency; [5]Advanced Sciences Research Center, Japan Atomic Energy Agency; [6]Neutron Science Section, Materials and Life Science Division, J-PARC Center

In-situ neutron diffraction empowers the development of new titanium superelastic alloys

1. Introduction

Superelastic alloys, which can recover large strains through reversible stress-induced martensitic transformations, have attracted significant attention for applications in aerospace engineering, biomedical devices, and energy systems. However, realizing lightweight superelastic alloys that maintain reliable functionality under extreme temperature conditions—from cryogenic to high temperatures—has long been a challenge. Recently, we have developed a new titanium-based superelastic alloy (Ti–Al–Cr), representing a breakthrough toward this goal. This alloy exhibits outstanding superelasticity over an exceptionally wide temperature range from 4.2 K to 400 K (Fig. 1), far beyond the operational limits of conventional superelastic materials such as Ni–Ti [1]. In addition to potential applications in biomedical devices as a substitute for conventional superelastic alloys, the Ti–Al–Cr alloy shows great promise for space-exploration technologies, where materials must withstand severe thermal fluctuations. A representative example is the superelastic tire concept proposed by NASA, where such alloys could play an enabling role [2].

Developing such a high-performance superelastic alloy is far from trivial. In particular, understanding the martensitic transformation mechanisms that govern its superelastic behavior under extreme temperature and stress conditions presents exceptional challenges. Unlike conventional superelastic alloys, this Ti–Al–Cr alloy does not exhibit a thermally induced martensitic transformation upon cooling; instead, the transformation occurs only under applied stress, making structural analysis difficult. Moreover, the alloy shows an anomalous temperature dependence of transformation stress, raising questions about how its transformation pathway evolves with temperature. Addressing these challenges requires atomic-scale insights, for which in-situ neutron diffraction techniques demonstrate unparalleled power and precision.

2. Experimental

To clarify the martensitic transformation mechanisms responsible for the exceptional superelasticity of the Ti–Al–Cr alloy, in-situ neutron diffraction experiments were conducted at the Materials and Life Science Experimental Facility (MLF) of J-PARC. Two complementary diffractometers were utilized: the Extreme Environment Single Crystal Neutron Diffractometer (SENJU) and the Engineering Materials Diffractometer (TAKUMI) [3-5].

At SENJU, in-situ tensile tests were performed on a <110>-oriented single-crystal specimen using a time-of-flight Laue technique at room temperature. Diffraction data were collected at multiple static strain levels during loading and unloading, enabling precise determination of lattice parameters and crystal structures through *UB*-matrix analysis using the STARGazer software [6]. Complementary experiments at TAKUMI were carried out under cryogenic conditions to track the evolution of crystal structures during stress-induced martensitic transformation. Using a similar single-crystal specimen and dog-bone geometry, in-situ neutron diffraction patterns were recorded under controlled stress and strain states. The experimental setups for SENJU and

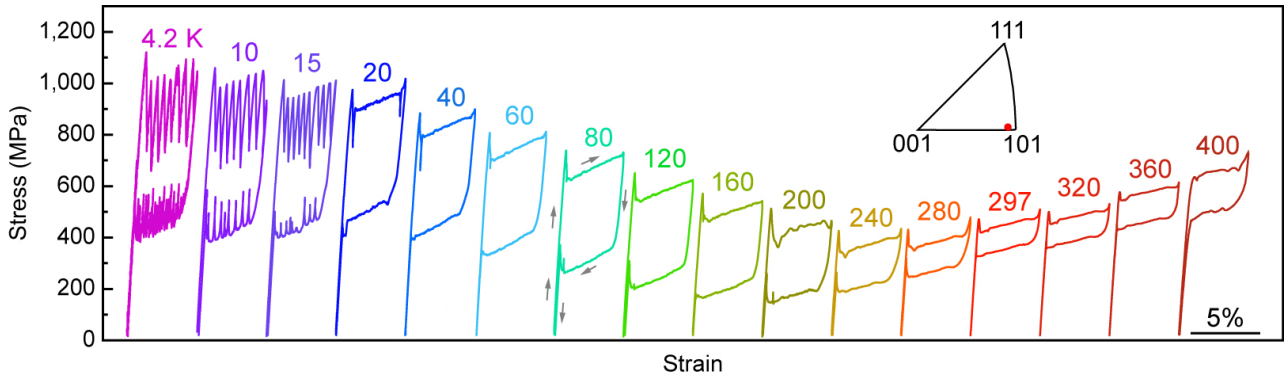

Figure 1. Stress–strain curves obtained from tensile tests at various temperatures for a near-<110>-oriented single-crystal Ti–Al–Cr specimen [1].

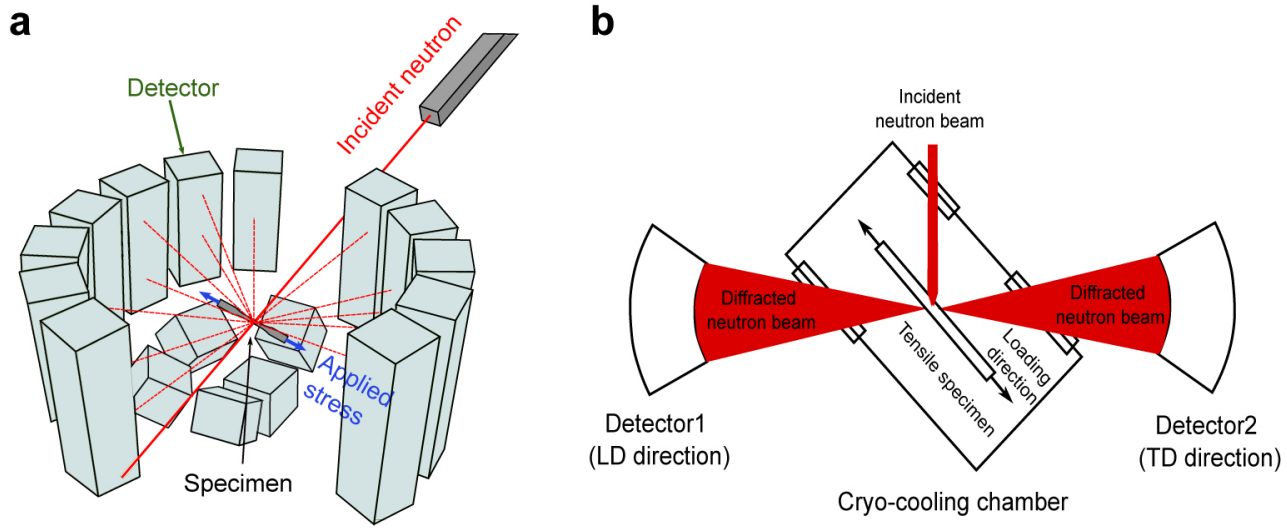

Figure 2. **a**, Schematic of the in-situ tensile testing setup at SENJU. **b**, Schematic of the in-situ tensile testing setup at TAKUMI [1].

TAKUMI are schematically shown in Fig. 2 [1].

3. Results and discussion

Results of in-situ single-crystal neutron diffraction measurements conducted at SENJU are shown in Fig. 3 [1]. The reconstructed two-dimensional reciprocal lattices revealed a distinct structural evolution from the untransformed parent phase to the stress-induced martensite phase (Figs. 3a and 3b). The parent phase was identified as having a B2-ordered cubic structure with a lattice parameter of $a = 3.22$ Å. Under tensile stress where the martensite phase is stabilized, the martensite phase was determined to possess an orthorhombic B19-type ordered structure, with lattice parameters $a = 2.94$ Å, $b = 4.90$ Å, and $c = 4.61$ Å. Simulated diffraction patterns based on these structural parameters reproduced the experimental results well, confirming the lattice correspondence between the two phases (Fig. 3c). Using lattice-deformation theory, the orientation-dependent transformation strain associated with the B2 → B19 transformation was calculated (Fig. 3d). The maximum recoverable strain was estimated to be about 8.7% under <001> compression and 7.6% under <110> tension, which is in excellent agreement with the experimentally observed superelastic strain. These results unambiguously demonstrate that the remarkable superelasticity in the Ti–Al–Cr alloy originates from a reversible B2–B19 martensitic transformation between ordered structures—a transformation type that, while known in Ni–Ti-based systems, has been newly realized in a Ti-based alloy system.

Figure 1 shows a positive temperature dependence of transformation stress above approximately 240 K, typical for superelastic alloys. Interestingly, at lower temperatures, the transformation stress of this Ti–Al–Cr alloy increases upon further cooling—a highly unusual behavior suggesting a possible change in the martensitic transformation mechanism. To investigate this, in-situ neutron diffraction experiments were conducted at TAKUMI. Tensile loading–unloading tests were performed at various cryogenic temperatures to capture the structural evolution during stress-induced transformation. The diffraction patterns revealed that the phase transformation pathway remained unchanged throughout the temperature range examined: the reversible transformation consistently occurred between the B2 parent phase and the B19 martensite phase, with no evidence of new or intermediate crystal structures. This finding ruled out the possibility that the anomalous stress–temperature dependence originates from a change in the transformation mechanism. Subsequent analysis indicated that the origin lies instead in the unusual lattice stability of the B2 parent phase at lower temperatures, which resists transformation despite cooling [1].

4. Summary

These findings not only reveal the microscopic origin of the outstanding and robust superelasticity in Ti–Al–Cr alloys but also underscore the indispensable role of neutron diffraction techniques in investigating materials under extreme stress and temperature conditions. The synergy between SENJU's high-precision single-crystal diffraction capability and TAKUMI's temperature-dependent structural analysis has proven

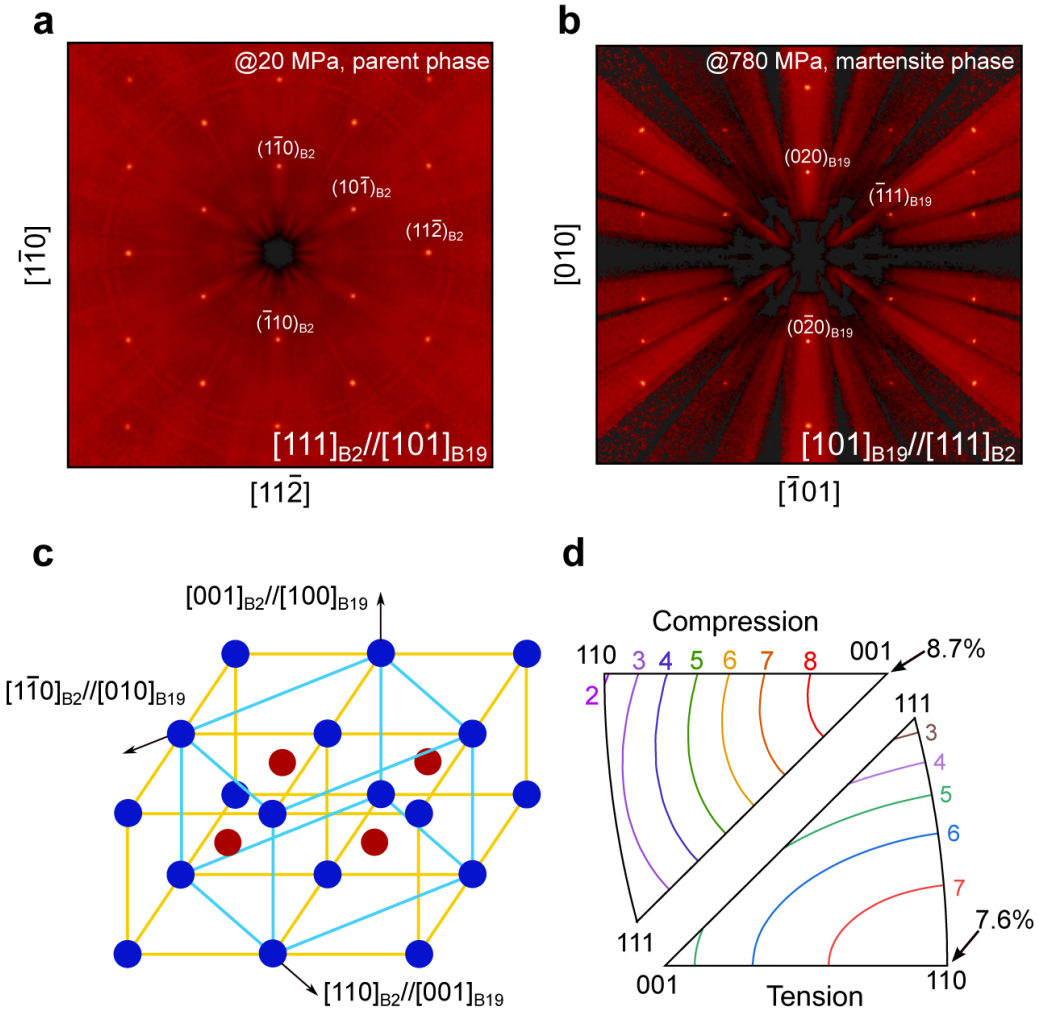

Figure 3. **a**, Two-dimensional neutron diffraction patterns collected before tensile loading, showing the B2 structure. **b**, Two-dimensional neutron diffraction patterns collected during tensile loading, revealing the B19 structure. **c**, Lattice correspondence between B2 parent (Orange) and B19 martensite (Blue) phases determined from the in situ neutron diffraction results. **d**, Calculated orientation dependence of transformation strain under tension and compression [1].

to be a particularly powerful approach for elucidating complex martensitic transformation phenomena. This work paves the way for the rational design of next-generation lightweight superelastic alloys capable of reliable operation in harsh environments—from biomedical devices to future space-exploration systems.

References

[1] Y. Song *et al.*, Nature. **638**, 965 (2025).
[2] https://technology.nasa.gov/patent/LEW-TOPS-99
[3] https://mlfinfo.jp/en/beamlines.html
[4] T. Ohhara *et al.*, J. Appl. Crystallogr. **49**, 120 (2016).
[5] S. Harjo *et al.*, Mater. Sci. Forum. **681**, 443 (2011).
[6] T. Ohhara *et al.*, Nucl. Instrum. Methods Phys. Res. A **600**, 195 (2009).

S. Xu[1,2], Y. Song[1,2], X. Xu[2], T. Omori[2], T. Kawasaki[3], R. Kiyanagi[3], S. Harjo[3], W. Gong[3], and R. Kainuma[2].
[1]*Frontier Research Institute for Interdisciplinary Sciences, Tohoku University;* [2]*Department of Materials Science, Tohoku University;*
[3]*Neutron Science Section, Materials and Life Science Division, J-PARC Center*

Order–Disorder Dichotomy in Li_3VO_4: Structural Origins of High-Power Performance

1. Introduction

The explosive growth of AI-data centers and edge-computing infrastructure has generated an unprecedented demand for energy-storage systems capable of delivering instantaneous, high-power output without sacrificing lifetime or safety. Conventional lithium-ion batteries, designed primarily for energy density, encounter kinetic bottlenecks under such extreme conditions. To transcend these limits, structural-disorder engineering has emerged as an attractive approach: deliberate cation mixing can activate new ion-transport pathways, suppress phase segregation, and enhance mechanical resilience [1].

Among oxide-type anodes, Li_3VO_4 (LVO) stands out for its broad voltage window (0.3–1.3 V *vs.* Li/Li^+), long cyclability, and inherent structural robustness. However, its ordered lattice exhibits sluggish Li-ion diffusion. Our prior studies revealed that inducing cation disorder between Li and V increases the Li-ion diffusivity by nearly two orders of magnitude, unlocking extreme rate capability while preserving structural stability [2,3]. However, the atomic origin of this phenomenon remained unresolved because Li positions could not be visualized by X-ray diffraction alone.

Here, we established a mechanochemical synthesis route to controllably generate a pure single-phase cation-disordered LVO and conducted a multimodal structural analysis integrating XRD, neutron diffraction at J-PARC MLF, XAFS, total-scattering/Pair-Distribution Function (PDF) analysis, and HR-TEM measurements. This comprehensive approach reveals, for the first time, how cation disorder evolves across multiple length scales and how it directly governs electrochemical kinetics in LVO crystal (Fig. 1) [4].

2. Multi-scale Characterization of Cation-disordered Crystal Structure

Progressive mechanochemical milling caused the systematic disappearance of XRD reflections below $2\theta \approx 30°$, corresponding to Li/V layer stacking, signifying the onset of cation disorder. To determine the full atomic configuration, we employed a complementary refinement strategy: XRD resolved the V sublattice, whereas time-of-flight neutron diffraction (J-PARC MLF BL20, iMATERIA) provided crucial sensitivity to the Li sublattice, otherwise invisible to X-rays.

Joint Rietveld refinement of the X-ray and neutron diffraction data yielded a wurtzite-type crystal structure model (S.G. $P6_3mc$), where Li and V statistically share identical cation sites. This description captured the long-range symmetry of the cation-disordered LVO but obscured local heterogeneity. As shown in Fig. 1, HR-TEM imaging disclosed a nanoscale mosaic of "colonies" of ordered domains embedded in a disordered matrix, revealing that partial cation ordering remains locally even after complete loss of long-range periodicity.

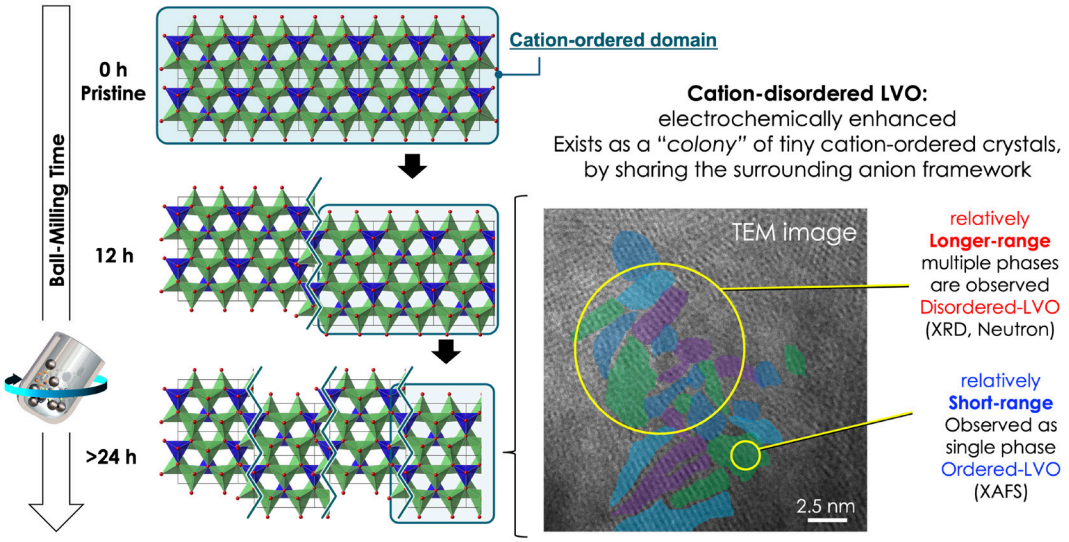

Figure 1. Overview of this study, representing that the size of the cation-ordered crystal domains is reduced by increasing ball-milling time. The TEM image displays the mechanochemically-treated cation-disordered LVO crystal, involving a "colony" of tiny cation-ordered crystals by sharing the surrounding anion framework.

V-K-edge EXAFS analysis confirmed nearly unchanged VO_4 coordination in both ordered and disordered samples, verifying that disorder originates mainly from cation mixing rather than anion distortion. PDF analysis with box-car refinement exposed the hierarchical nature of disorder: for interatomic distances shorter than ~8Å, the ordered $Pmn2_1$ model gives the best fit, while beyond this range the disordered $P6_3mc$ model dominates. Thus, the cation-disordered LVO embodies a dual-scale framework combining short-range order with long-range disorder.

This hierarchy can be rationalized by an antiphase-domain-boundary (APDB) model in which ordered sub-nanoregions are periodically interrupted by cation-swapping interfaces (Fig.2). Crucially, neutron diffraction data were indispensable for validating Li-site occupancy and quantifying the extent of cation mixing, establishing the atomic foundation of this model.

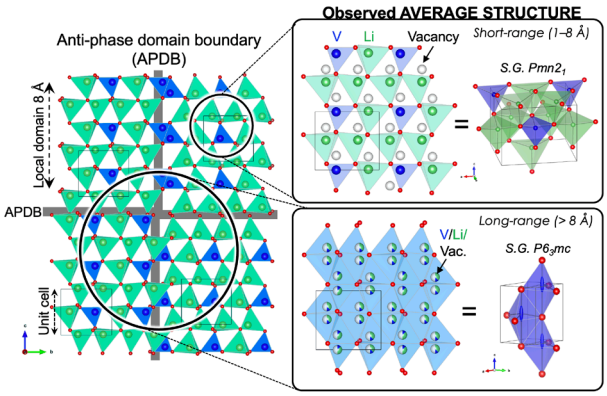

Figure 2. Schematic illustration for the cation-disordered LVO crystal structure by using multiple unit cells combined to represent a larger crystal structure. The structure averaged over interatomic distances greater than 8Å across the APDB, reflects the $P6_3mc$ structure, whereas averaging over distances less than 8Å retains the structure of the cation-ordered local domains.

3. Disorder-driven Electrochemical Kinetics

Electrochemical testing revealed that the mechanochemically produced cation-disordered LVO exhibits exceptional high-rate capability. At 50C-rate (72-s discharge), it maintains over 70% of its theoretical capacity, whereas ordered LVO retains less than 20%. Galvanostatic intermittent titration (GITT) and impedance analyses confirmed that the Li-ion diffusion coefficient rises by two orders of magnitude following disordering.

These findings highlight that cation disorder generates a network of low-barrier diffusion channels, leading to accelerated ion transport, suppressed stress concentration, and enhanced cycle stability. The study thus establishes a clear benefit of cation disorder in which controlled disorder is not an undesired defect but a functional state enabling high-power operation.

4. Future Works

Building on these insights, we have recently developed a spray-dry "quench" synthesis that enables one-step formation of cation-disordered LVO directly from solution precursors [5]. In this process, homogeneous precursor solutions are rapidly dried and crystallized within milliseconds, effectively freezing the disordered configuration. This approach provides the possibility of a scalable and controllable production route for various types of disordered structures.

Combining these synthesis methods with state-of-the-art structural characterization techniques—such as synchrotron total scattering, neutron diffraction, and local spectroscopy—will allow us to quantitatively reveal how atomic-scale disorder governs bulk electrochemical performance. Such integrated studies will deepen our understanding of the structure–performance relationship across multiple length scales. Ultimately, we aim to define what constitutes "beneficial disorder"—the kind of controlled structural randomness that enhances ion transport, structural stability, and reaction kinetics—and to establish the guiding principles for its design and manipulation in next-generation energy-storage materials.

References

[1] J. Lee *et al.*, *Science.* **343**, 519 (2014).
[2] E. Iwama *et al.*, *ACS Nano.* **10**, 5398 (2016).
[3] P. Rozier *et al.*, *Chem. Mater.* **30**, 4926 (2018).
[4] K. Matsumura *et al.*, *Small.* **20**, 2405259 (2024).
[5] K. Matsumura *et al.*, *ACS Energy Lett.* **10**, 2184 (2025).

K. Matsumura[1,2], P. Rozier[3,4], E. Iwama[1,2,5], K. Ohara[6], Y. Orikasa[7], W. Naoi[8], P. Simon[3,4], and K. Naoi[1,2,5]
[1]*Institute of Global Innovation Research, Tokyo University of Agriculture and Technology;* [2]*Department of Applied Chemistry, Tokyo University of Agriculture and Technology;* [3]*CIRIMAT, Université de Toulouse, CNRS;* [4]*Réseau sur le Stockage Électrochimique de l'Energie, RS2E FR CNRS 3459;* [5]*Advanced Capacitor Research Center, Tokyo University of Agriculture and Technology;* [6]*Faculty of Materials for Energy, Shimane University;* [7]*Department of Applied Chemistry, College of Life Sciences, Ritsumeikan University;* [8]*Division of Art & Innovative Technologies, K & W Inc.*

Structure and particle surface analysis of Li_2S-P_2S_5-LiI-type solid electrolytes synthesized by the liquid-phase method

1. Introduction

All-solid-state Li batteries have attracted significant attention owing to their several advantages over conventional organic liquid electrolyte batteries, such as higher safety, higher energy density, superior rate performance, and wider operational temperature range [1]. All-solid-state batteries use solid electrolytes not only in the separator layer but also in the cathode and anode layers, so the choice of solid electrolyte is crucial for the overall performance and safety of the battery. Various sulfide-based solid electrolytes have been reported to date, but we focused on the Li_2S-P_2S_5-LiI system, which is considered highly stable with respect to the negative electrode [2-6]. Our groups focused on the liquid-phase synthesis of Li_2S-P_2S_5-LiI for scaling up and lower cost. While it is anticipated that the surface state will differ depending on the synthesis method, research on the surface state of solid electrolyte particles and its impact on electrochemical properties is also scarce. In this study, Li_2S-P_2S_5-LiI solid electrolytes were synthesized by mechanical milling and liquid-phase shaking. The particle surface states of both synthesis routes were analyzed using neutron total-scattering experiments, because neutrons are sensitive to protons, including those in the organic solvent, more so than X-rays. As a result, the liquid-phase-synthesized sample exhibited an organic-solvent-derived, stable surface layer containing protons, which contributed to its high stability toward Li anodes [7].

2. Experiments

Li_2S-P_2S_5-LiI solid electrolytes were synthesized by mechanical milling and liquid-phase shaking, as previously reported [7]. DC polarization measurements were conducted using a charge–discharge measurement tool (BST-2004 H, Nagano) with a Li/solid electrolyte/Li symmetric cell that was prepared by attaching Li foil to both sides of the pelletized solid electrolyte; a current density of ± 0.3 mA cm^{-2} was applied with a charge and discharge time of 1 h. Neutron total scattering experiments were performed on $Li_7P_2S_8I$ solid electrolytes sealed in a V-Ni null scattering sample container (outer diameter: 3.0 mm, thickness: 0.1 mm) at 27 °C for an exposure time of 3.5 h using a NOVA neutron total scattering instrument (BL21 beamline) with a decoupled liquid hydrogen moderator using an incident flight path of 15 m and a scattered flight path of 1.2–1.3 m at the 90° detector bank ($0.008 < d\ (= 2\pi/Q = \lambda/(2 \sin \theta)) < 0.63$ nm) connected to a 800-kW spallation neutron source at the Japan Proton Accelerator Research Complex. Samples for all analytical experiments were prepared within an Ar-filled glove box and carefully transported to a vacuum chamber without exposure to air or moisture.

3. Results and discussion

DC polarization tests of the Li_2S-P_2S_5-LiI solid electrolytes were conducted to assess their stability toward Li. Li_2S-P_2S_5-LiI, synthesized by mechanical milling, exhibited a constant overvoltage of 20 mV, and a short circuit occurred after 20 h of DC polarization at room temperature (Fig. 1). In contrast, Li_2S-P_2S_5-LiI, synthesized by liquid-phase shaking, maintained a constant voltage in the range of 35–47 mV even after 1200 h of DC polarization at room temperature. Therefore, Li_2S-P_2S_5-LiI synthesized by liquid-phase shaking is more stable toward Li metal than that synthesized by mechanical milling, despite exhibiting a higher overvoltage, because of its lower ionic conductivity. Thus, Li_2S-P_2S_5-LiI synthesized via liquid-phase shaking is more suitable for all-solid-state Li-metal batteries. The electrochemical window test results of the liquid-phase shaking sample have been reported elsewhere [8].

Figure 2 shows the neutron diffraction patterns and PDFs of the Li_2S-P_2S_5-LiI solid electrolytes synthesized by liquid-phase shaking and mechanical milling. The neutron diffraction pattern of the former exhibited a higher background than that of the latter. In addition, a tendency for the intensity to decrease with decreasing lattice spacing d was observed only for the Li_2S-P_2S_5-LiI solid electrolyte synthesized by liquid-phase shaking, indicating that it included H^+ derived from the solvents. Thus, we could conclude that the solvent-derived organic surface layer formed on the Li_2S-P_2S_5-LiI solid-electrolyte particles acted as a solid-electrolyte interface (SEI) for the Li anode. To date, numerous studies on SEIs in organic-electrolyte batteries have been reported.

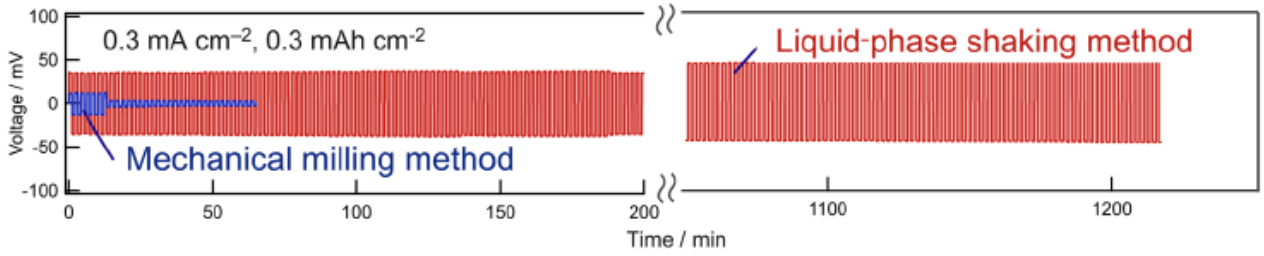

Figure 1. DC polarization test results of the Li_2S-P_2S_5-LiI solid electrolytes synthesized by mechanical milling and liquid phase shaking.

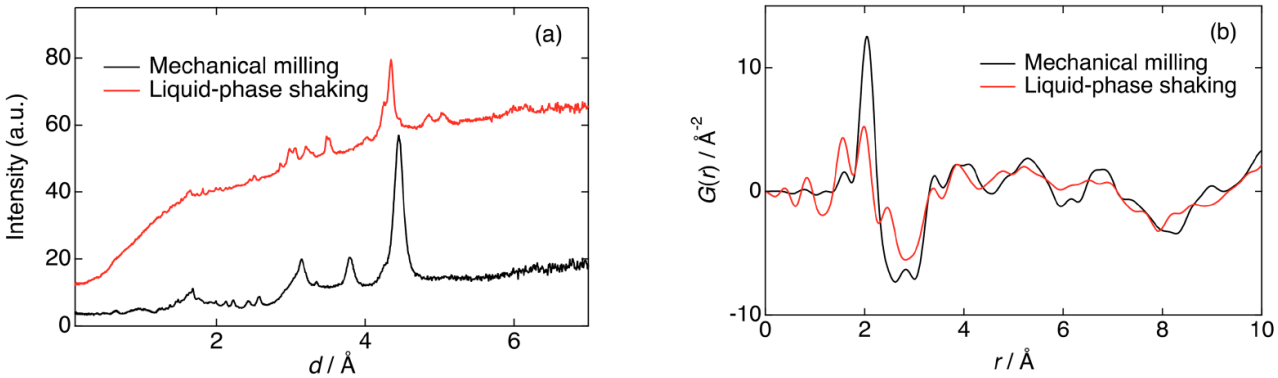

Figure 2. Neutron diffraction patterns (a) and PDF of Li_2S-P_2S_5-LiI solid electrolytes (b) synthesized by liquid-phase shaking and mechanical milling.

4. Conclusion

Li_2S-P_2S_5-LiI solid electrolytes synthesized by liquid phase shaking and mechanical milling were analyzed in terms of the particle surface states. Analyzing the particle surface states revealed that the sample synthesized by liquid-phase shaking showed the solvent-derived organic surface layer, including H^+ derived from the ethyl propionate solvent, whereas the mechanically milled sample did not. These surface layers were one of the factors that contributed to the high Li stability, a behavior similar to that observed in organic-electrolyte batteries. The neutron total-scattering experiments visualized the surface layer containing H^+ for the first time in Li_2S-P_2S_5-LiI solid electrolytes synthesized by liquid-phase shaking.

References

[1] Y. Kato *et al.*, Nat Energy. **1**, 4 (2016).
[2] S.J. Choi *et al.*, ACS Appl Mater Interfaces. **10**, 37 (2018).
[3] S. Spannenberger *et al.*, Solid State Ionics. **341**, 115040 (2019).
[4] S. Song *et al.*, Chem. Mater. **34**, 18 (2022).
[5] Z. Wu *et al.*, Ind. Eng. Chem. Res. **62**, 1 (2022).
[6] Z. Wu *et al.*, Chem. Eng. J. **442**, 136346 (2022).
[7] K. Hikima *et al.*, J. Solid State Electrochem., (2024).
[8] K. Hikima *et al.*, Solid State Ionics. **354**, 115403 (2020).

K. Hikima[1], K. Ikeda[2], and A. Matsuda[1]
[1]Toyohashi University of Technology; [2]Neutron Science and Technology Center, CROSS

Neutron Bragg Edge Spectroscopy for Developing Practical Magnetic Materials

1. Introduction

Currently, the most widely used probe for analyzing the internal magnetic structure of materials is neutron diffractometry. However, its application has been largely limited to fundamental research on magnetism. This is simply because traditional magnetic devices have consisted of homogeneous components made of ferromagnetic materials without any internal magnetic structure, and thus there has been no need to evaluate such internal structures/heterogeneity. As a result, neutron diffractometry has evolved as a "big science" technique capable of achieving high precision and high resolution, rigorously analyzing a limited number of carefully selected samples in response to the demands of fundamental magnetism research.

Recently, however, materials that exploit more complex microscopic magnetic structures—such as antiferromagnetism—have begun to play a key role in technological innovation. Additionally, in the pursuit of further performance improvement, magnetic devices that intentionally include or permit magnetic heterogeneity at the macroscale are now being employed. These changes in the field of applied magnetism indicate that evaluation of internal magnetic structures/ heterogeneity will become essential for the development of magnetic materials and devices in the future. In such developments, analytical techniques are often required to offer high throughput for composition and process optimization studies, as well as non-destructive imaging to enable verification after device integration or during operation. Here, the question arises: Can neutron diffractometry, which has successfully pursued precision and resolution, also address these new needs? If there are difficult cases, exploring alternative analytical methods could be worthwhile. In this study, from this perspective, we investigated the potential of neutron transmission spectroscopy [1-4].

2. Bragg edge spectroscopy and its applications

When neutron diffraction occurs at a certain wavelength, the transmission at that wavelength is expected to decrease. Figure 1 shows the transmission spectrum of a single crystal of holmium when neutrons are incident along the [001] direction, obtained at BL22 RADEN in J-PARC [4]. In this figure, a dip appears at the wavelength corresponding to the lattice constant c along the c-axis of hexagonal holmium at room temperature. Considering Bragg's diffraction condition ($2d \sin\theta = n\lambda$), this can be interpreted as a decrease in transmission due to backscattering ($\sin\theta = 1$) from the (002) planes with the interplanar spacing ($d = c/2$). As expected, clear signatures of diffraction appear in the transmission spectrum. When the same single crystal is cooled to 30 K, below the helical ordering temperature of holmium magnetic moments, new satellite dips ($0\ 0\ 2\pm\tau$) appear on both sides of the original dip in the spectrum, as shown by the blue curve in Figure 1. From τ, the periodicity of the helical magnetic order along the c-axis can

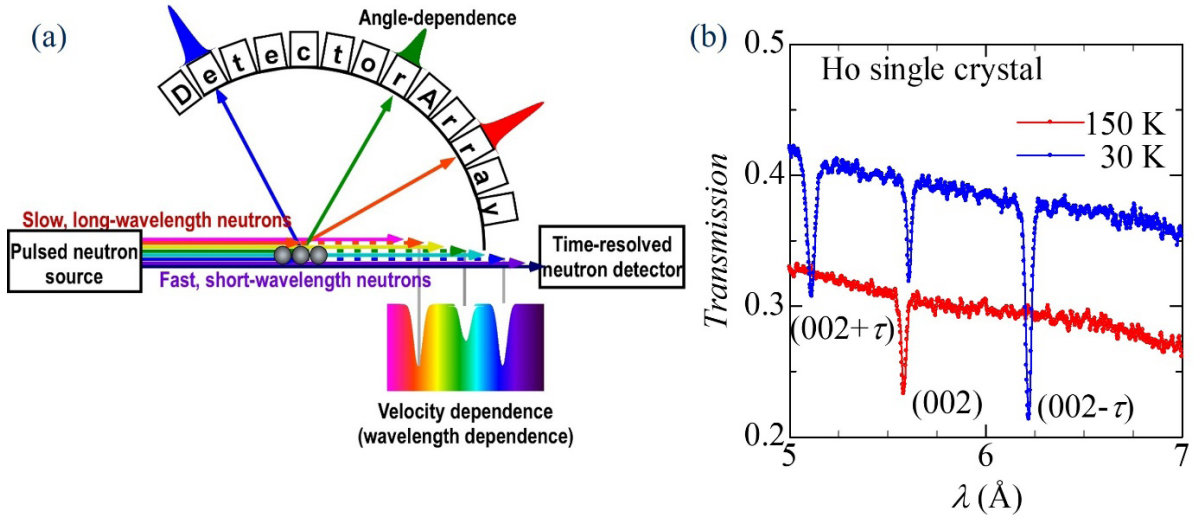

Figure 1. (a) Principle and (b) typical results of neutron transmission spectroscopy for a Ho single crystal © JAP2025 [4].

be estimated. In this way, similar to well-established neutron diffractometry, internal magnetic structure information can be acquired from the transmission spectrum.

As discussed above, the relationship between neutron diffractometry and transmission spectroscopy is analogous to that between dark-field and bright-field microscopy, both originating from the same physical phenomena. However, each method has its advantages and disadvantages, which should be considered when utilizing them. For example, magnetic backscattering from the (111) planes of a randomly oriented powder with magnetic moments of 1 μ_B arranged on an FCC lattice with a lattice constant of 0.35 nm is calculated to be about 30 fm^2 per atom. For a sample thickness of 1 cm, this corresponds to about 3% of the incident neutrons being scattered. If 10,000 neutrons are incident on a 1 cm^2 area of the sample, approximately 9,700 will transmit and be detected by a zero-dimensional counter with a 1 cm^2 aperture, resulting in a signal-to-noise ratio (S/N) of about 3. By contrast, in a diffractometer using a large-area detector with a solid angle coverage of 30 % (10^3–10^4 cm^2), about 100 neutrons are detected, yielding a S/N of approximately 10. Thus, in principle, neutron diffractometry offers a better signal-to-noise ratio than transmission spectroscopy for relatively small magnetic moments. Conversely, when the background level per unit detector area is high, transmission spectroscopy may have an advantage in terms of the signal-to-background ratio. In any case, neutron diffractometry is generally considered more suitable than transmission spectroscopy for strictly resolving internal magnetic structures in magnetic materials.

On the other hand, conventional neutron diffractometry measures the angular dependence of scattered neutrons; consequently the sample must be positioned at the center point of detectors arranged on a spherical surface. In contrast, in transmission spectroscopy, neutrons travel straight from the source through the sample to the detector. Therefore, if a large parallel beam is separated and arrayed using a mask with multiple holes and irradiates many samples simultaneously, and the transmission spectrum of each beam is measured by a detector array, it becomes possible to evaluate the internal magnetic structures of multiple samples in parallel. This is particularly advantageous for high-throughput measurements in in-situ environments where sample changers cannot be easily implemented. Moreover, using this principle, imaging of internal magnetic structures—previously achieved by scanning and measuring one point at a time with neutron diffraction—can now be performed via single-shot mapping. In other words, for applied magnetism, where high throughput optimization and non-destructive imaging are essential, transmission spectroscopy may offer advantages over neutron diffraction.

Based on these considerations, in this study, we applied multi-sample simultaneous transmission spectroscopy to the optimization of heavy rare-earth alloys as magnetic refrigeration materials for hydrogen liquefaction [5], and evaluated its practicality and challenges [3]. Furthermore, in-situ transmission spectroscopic imaging was employed to visualize the internal states of practical magnetic devices such as ferrite inductors [1] and electrical steel sheet cores [4] for power electronics, and its potential and limitations were investigated. The details are provided in the original paper, but promising results were obtained for all initial applications, suggesting future prospects for further development.

3. Summary

Addressing the challenges identified here will not be easy, but transmission spectroscopy is expected to play a vital role in data-driven optimization of magnetic materials and in the verification of magnetic devices after integration or during operation in the future.

References

[1] H. Mamiya, Y. Oba, N. Terada, K. Hiroi, T. Ohkubo, and T. Shinohara, Sci. Rep. **13**, 9184 (2023).
[2] H. Mamiya, Y. Oba, N. Terada, K. Hiroi, and T. Shinohara, IEEE Trans. Magn. **59**, 6500505 (2023).
[3] H. Mamiya, N. Terada, S.R. Larsen, N. Tsujii, K. Hiroi, T. Shinohara, and H. Sepehri-Amin, Phys. Rev. Res. **7**, 013233 (2025).
[4] H. Mamiya, N. Terada, K. Hiroi, T. Shinohara, and Hossein Sepehri-Amin, J. Appl. Phys. **138**, 143904 (2025).
[5] N. Terada and H. Mamiya. Nature Comm. **12**, 1212 (2021).

H. Mamiya[1], N. Terada[1], K. Hiroi[2], T. Shinohara[2], and H. Sepehri-Amin[1]
[1]*National Institute for Materials Science;* [2]*Japan Atomic Energy Agency*

Massive Dirac magnons in the three-dimensional honeycomb magnetic oxide $FeTiO_3$

1. Introduction

Topological magnons are found in magnetic crystals involving hexagonal loops such as 2D kagome lattices or 3D pyrochlores. Among them, the minimal band structures with two magnon modes are available in 2D honeycomb lattices. Similarly to the electronic band structure of graphene, these honeycomb ferromagnets exhibit crossings between two linearly dispersive magnon bands at the Dirac wave vectors $Q_{K/K'} = \pm(1/3,1/3)$. The associated magnons propagate effectively as relativistic massless particles and are thus called Dirac magnons in reference to the Dirac electrons in graphene [1]. These Dirac magnons may also become massive and topological when spin-orbit-coupling(SOC)-driven exchanges break the time-reversal symmetry and open the gap between the otherwise twofold degenerate modes [2,3]. Recent inelastic neutron scattering (INS) experiments observed finite gap openings larger than 1 meV at the bulk magnon Dirac points of van der Waals honeycomb ferromagnets CrI_3 and $CrGeTe_3$, suggesting that their edge states should exhibit gapless topological excitations [4-7]. Breaking of time-reversal symmetry in these compounds was attributed to antisymmetric Dzyaloshinskii-Moriya (DM) exchanges between the next-nearest neighbor (NNN) Cr^{3+} spins mediated by heavy ligands such as I or Te [8,9].

Although the symmetry of the honeycomb lattice does not allow the nearest-neighbor (NN) bonds to have finite DM exchanges, symmetric and anisotropic exchanges between them can also break the time-reversal symmetry. For example, bond-directional anisotropic exchanges have recently been used to explain Dirac magnons and nodal line dispersions observed in $CoTiO_3$ [10]. However, since the Co^{2+} spins are within the honeycomb planes, the Dirac magnons in $CoTiO_3$ remain gapless [10,11]. To break the time-reversal symmetry and open the Dirac gaps, it is necessary for the magnetic moments to tilt out of the honeycomb planes.

In this work, we investigated the Dirac magnons in $FeTiO_3$ which is isostructural to $CoTiO_3$ while replacing its quantum spins with large spins of Fe^{2+} ($3d^4$, $S = 1/2$). Although these two oxides also share the same antiferromagnetic (AFM) ordering with stacked ferromagnetic honeycomb layers, $FeTiO_3$ has spins oriented nearly perpendicular to the honeycomb planes contrary to $CoTiO_3$. Therefore, it is considered a likely candidate to exhibit a magnon gap opening at the Dirac point.

2. Experimental method

A large single crystal of $FeTiO_3$ was grown using the floating zone method in an image lamp furnace. To observe magnon excitations, the BL23 POLANO time-of-flight spectrometer at the Materials and Life Science Experimental Facility of the Japan Proton Accelerator Research Complex was used in the multiple incident energy mode with E_i = 11.57, 30.2 and 78.7 meV.

3. Results and Discussions

The magnon excitation spectra observed along selected high-symmetry plane crossing the AFM zone center are shown in the upper row of Fig. 1 [12]. At the 2D Brillouin zone center $Q_\Gamma = (0,0)$, a strong magnon mode appears around $\hbar\omega = 4.9$ meV and disperses upward in all directions in the honeycomb plane. This mode is ascribed to the two sublattice spins of the honeycomb ferromagnet fluctuating in-phase with respect to each other and thus called the acoustic magnon by analogy to acoustic phonons. Figure 1a shows that in the [h h] direction the acoustic magnon mode disperses up to ≈12 meV at the zone boundary $Q_M = (1/2,1/2)$. The other mode, ascribed to the out-of-phase spin fluctuations and thus called the optical magnon, is also visible continuing up to $\hbar\omega = 15.2$ meV at Q_Γ. This is the maximum energy of the magnon band. Notice that the scattering intensities are not equal between left and right half panels in Figs. 1c and 1d. Such intensity asymmetry is ascribed to the crystal structure of $FeTiO_3$ belonging to the rhombohedral $R\bar{3}$ space group and is also consistent with the fact that the sample used in this work consists of a single domain.

Upon close inspection, we notice apparent discontinuities in magnon dispersion at the Dirac point Q_K where the two magnon modes are expected to cross each other. These discontinuities are observed in Fig. 1a, b and d, respectively, suggesting a finite gap opening via avoided crossing. Since the magnon density of states will vanish at Dirac points, neutron scattering data may show gap-like features with intensity minima even when a true energy gap does not open. Therefore, to confirm the validity of the suspected gap

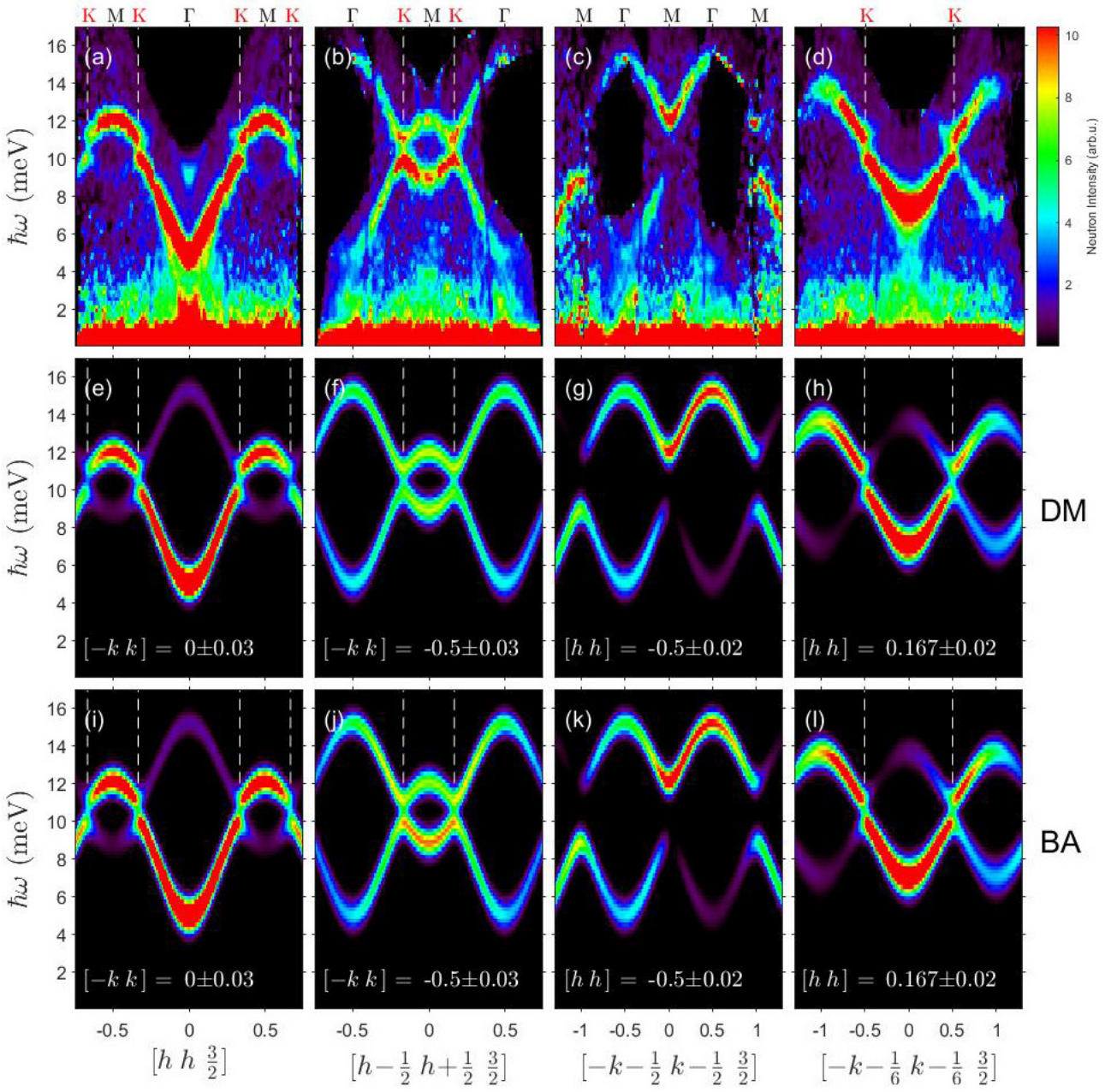

Figure 1. (a–d) The upper row shows INS spectra in the selected high-symmetry directions while (e–h) the middle and (i–l) the bottom rows show the linear spin wave calculations based on the DM model and BA model, respectively, discussed in the text. The letters on top of (a–d) mark the high-symmetry positions on the 2D Brillouin zone. All calculations are convoluted with the instrumental resolution, the sample mosaic distribution and an additional Gaussian broadening of a 0.8-meV full width half maximum. The vertical dashed lines indicate the Dirac points marked K.

opening, it is important to compare experimentally observed intensities with model calculations after being integrated over equal momentum widths. First, we checked the L-dependence of the scattering intensities at the Dirac point. The data clearly showed that two intensity maxima are separated by ≈ 1.2 meV with virtually no L dependence within the range up to $l = 6$. It is notable that the apparent separation is significantly larger than the energy resolution of 0.65 meV in full-width-half-maximum estimated at the energy transfer of $\hbar\omega = 10.5$ meV. By subsequently integrating the data over $0 \leq l \leq 6$ to improve the statistics, we also find that the upper and lower magnon modes clearly deviate from linear dispersion relations near the Dirac point. We therefore conclude that the Dirac magnons in $FeTiO_3$ are gapped and massive.

To quantitatively evaluate the Dirac magnon gap and deduce its origin, we set up the spin Hamiltonian including isotropic Heisenberg exchanges and additional SOC terms. We tested two models to account for

the SOC on the honeycomb lattice: (1) the NNN antisymmetric DM exchanges (DM model) and (2) the NN bond-directional anisotropic exchange (BA model) suggested for $CoTiO_3$ [12]. In the former DM model, the time- reversal symmetry between two sublattice excitations will be broken when the DM vector is parallel to the c axis. The middle and bottom panels of Fig. 1 show the model calculations using the DM model and the BA model, respectively, which produce almost identical results.

To test the plausibility of two considered models, we calculated the strength of exchange interactions using the OpenMX package based on the fully relativistic density functional theory. Fixing the magnetic moments along the direction parallel to the c axis, we obtained isotropic Heisenberg exchange, for example, $J_1 = 1.00$ meV as well as the out-of-plane DM exchange $|\vec{A}| = 0.03$ meV. However, the bond-directional anisotropic exchange anisotropy was found to be negligible. Therefore, we finally conclude that the DM exchange is responsible for the magnon gap opening at the Dirac points.

4. Summary

We investigated the magnon excitations of the three-dimensional honeycomb magnet $FeTiO_3$ with spins oriented nearly parallel to the c axis. Our INS experiment reveals a finite gap opening of $\Delta_K = 1.2$ meV at the in-plane Dirac crossings, which appears independently of the out-of-plane wave vectors. Using the linear spin-wave and DFT calculations, we find that the antisymmetric DM exchange between NNN Fe^{2+} spins is responsible for the Dirac gap opening. Based on these observations and analysis, we conclude that the Dirac magnons in $FeTiO_3$ are massive and topological. Our work demonstrates that Fe^{2+} ions of the honeycomb oxide can have a sufficiently strong spin-orbit coupling to establish topological spin excitations on honeycomb lattices.

References

[1] J. Fransson *et al*., Phys. Rev. B **94**, 075401 (2016).
[2] F. D. M. Haldane, Phys. Rev. Lett. **61**, 2015 (1988).
[3] C. L. Kane and E. J. Mele, Phys. Rev. Lett. **95**, 226801 (2005).
[4] L. B. Chen *et al*., Phys. Rev. X **8**, 041028 (2018).
[5] L. B. Chen *et al*., Phys. Rev. X **11**, 031047 (2021).
[6] F. Zhu *et al*., Sci. Adv. **7**, eabi7532 (2021).
[7] L. B. Chen *et al*., Nat. Commun. **13**, 4037 (2022).
[8] S. A. Owerre, J. Phys.: Condens. Matter **28**, 386001 (2016).
[9] S. K. Kim *et al*., Phys. Rev. Lett **117**, 227201 (2016).
[10] M. Elliot *et al*., Nat. Commun. **12**, 3936 (2021).
[11] B. Yuan *et al*., Phys. Rev. X **10**, 011062 (2020).
[12] J.-H. Chung *et al*., Sci. Rep. **15**, 5978 (2025).

J.-H. Chung[1], K. Shin[1], T. R. Yokoo[2,3,4,5], D. Ueta[2,3,4], M. Imai[6], H.-S. Kim[7], D. H. Kiem[8], M. J. Han[8], and S.-I. Shamoto[2,6,9,10]
[1]*Department of Physics, Korea University;* [2]*Institute of Materials Structure Science, KEK;* [3]*Neutron Science Section, Materials and Life Science Division, J-PARC Center;* [4]*Department of Advanced Studies, The Graduate University for Advanced Studies;* [5]*Graduate School of Science and Technology, University of Tsukuba;* [6]*Advanced Science Research Center, Japan Atomic Energy Agency;* [7]*Department of Semiconductor Physics, Kangwon National University;* [8]*Department of Physics, Korea Advanced Institute of Science and Technology;* [9]*Neutron Science and Technology Center, CROSS;* [10]*Department of Physics, National Cheng Kung University*

Non-destructive depth-selective quantification for carbon contents in steel using lifetime of muon

1. Introduction

Steel is one of the most important materials for human beings, for example, it is the main structural component in almost all modern buildings and essential in cars and railroads. Steel mainly comprises Fe, with an atomic number of 26, and smaller amounts of other elements. Among them, C, an element with an atomic number of 6, is important for determination of the properties of steel. Generally, steel containing a relatively large amount of C of up to 1 wt.% is hard but brittle, but that containing a small amount of C is relatively soft and tough. Thus, the C content is important for understanding the properties of steel. Currently, a destructive chemical analysis involving the combustion of steel is used to analyze the amount of C in the steel. In this method, steel is decomposed at high temperatures and the emitted CO_2 gas is quantified using infrared absorption. Non-destructive bulk analysis methods have never been developed.

In recent years, non-destructive analytical methods using muon beams have been developed, and this method has been applied to archaeological artifacts, extraterrestrial samples, and Li-ion batteries [1-3]. A muon has the same negative charge and a mass of 207 times larger than that of an electron. The muon decays to a high-energy electron (up to 50 MeV) and two neutrinos, with a lifetime of 2.2 μs in a vacuum. When a muon stops in a material, it is captured by an atom. The captured muon immediately transitions into the muon 1s atomic orbit, emitting characteristic X-rays (muonic X-rays), and finally, the muon decays into an electron or is absorbed by a nucleus of the atom.

However, the application of this method to steel sample is difficult because the low-energy muonic X-rays from light elements, such as carbon, are interfered by the Compton scattering background signal of high-energy X-rays from heavy elements. In this study, we propose an innovative analytical method, non-destructive and position-selective carbon analysis method for steel using a muon beam [4].

2. Principle of Elemental Analysis Method by Muon Lifetime

In this study, we propose an element quantification method that measures the lifetimes of muons based on the electrons formed via muon decay. Since the processes of muon decay into electron and absorption into the nucleus compete, the total lifetime of the muon decreases when a muon forms a muonic atom. As a result, the apparent lifetime of the muon is <2.2 μs, with unique values for each element, e.g., 2.0 μs in C and 0.21 μs in Fe [5]. Therefore, identifying the atoms capturing the muons is possible by measuring their lifetimes.

This method has three advantages. First, the muon capture probability of each element depends on the composition of the muon capturing material, and multi-elemental analysis is possible. Second, the muon lifetime in a heavy element is short, and it is rapidly absorbed into the nucleus, whereas that in a lighter element is longer. As a result, the electrons formed via decay of the muons captured by light elements are continuously emitted, even after all muons captured by the heavy elements have decayed. This suggests that small amounts of light elements may be identified by measuring the components with long lifetimes. Finally, it is possible to perform non-destructive depth-profile analysis by controlling the incident muon energy.

We established non-destructive and position selective C analysis method using muon lifetime analysis [4].

3. Experimental

The muon experiment was conducted in the D1 experimental area of the Muon Experimental Facility (MUSE) of MLF, J-PARC as Proposal No. 2019A0281, 2020A0193 and 2021B0387. We prepared standard steel samples with carbon contents of 30 ppm (regarded as pure Fe in this study) 0.42 %, and 4.46. We also prepared a layered sample with carbon contents of 0.51 %, 0.20 %

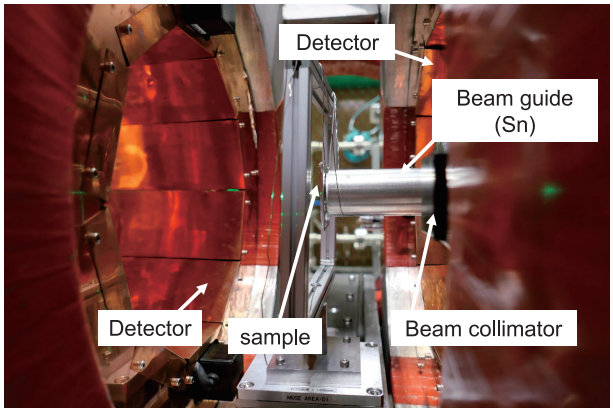

Figure 1. Image of the experimental setup.

Table 1. Comparison of the C contents determined using the muon and chemical analyses.

Incident muon momentum (MeV/c)	Estimated muon stoppage depth (mm)	C contents determined via muon analysis (%)	C content determined via chemical analysis (%)
46	1.21	0.50 ± 0.02	0.51
40	0.73	0.19 ± 0.01	0.20
32	0.35	1.12 ± 0.03	1.03

and 1.03% with thickness of 0.5 mm in each.

We performed muon irradiations for these samples and emitted electrons were measured by the large-solid angle electron detection system equipped in the D1 area. The muon lifetime spectrum could be obtained by determining the difference between the accelerator operation and muon detection times. The photo of experimental setup is shown in Figure 1.

4. Results and Discussion

Figure 2 shows the lifetime spectrum of the steel containing 0.42%. The two peaks at approximately 7448 and 8048 ns correspond to the muon arrival times. Four components – Fe, C, air, and a background with a long lifetime – were considered in analyzing the muon lifetime spectrum. The intensity of each component (Fe, C, air and background) against time is expressed by a simple exponential function. The lifetime of each component was taken from the literature value [5], except for background component of 20 μs.

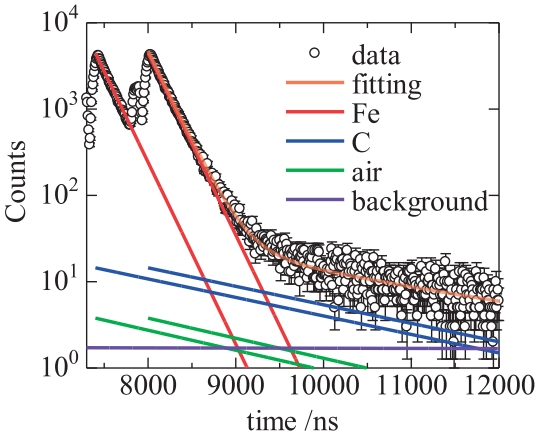

Figure 2. Muon lifetime spectrum of a C content of 0.42 wt.% steel.

First, we constructed a calibration curve using standard samples of pure Fe, 0.42% and 4.46%. The calibration curve showed a linear relationship, indicating that the carbon concentration can be determined from the ratio of captured muon (C/Fe).

To evaluate the performance of depth-selective analysis, muon irradiation experiments with momentum of 32, 40 and 46 MeV/c were conducted for the layered sample. When muons were introduced into the sample at an energy of 32 MeV/c, the average depth of muon stoppage was calculated as 0.35 mm from the surface. Using 40 and 46 MeV/c muons, the average depths of muon stoppage were estimated as 0.73 and 1.21 mm, respectively.

The results of depth-selective analysis are shown in Table 1. The analysis values using muon reproduced the C concentration in each steel layer, as determined via chemical analysis. In conclusion, using muon lifetime measurements, we successfully determined the sub-percent C content in steel without sample destruction.

References

[1] K. Shimada-Takaura *et al.*, J. Nat. Med. **75**, 532 (2021).
[2] T. Nakamura *et al.*, Science. **379**, eabn8671 (2022).
[3] I. Umegaki *et al.*, Anal. Chem. **92**, 8194 (2020).
[4] K. Ninomiya *et al.*, Sci. Rep. **14**, 1797 (2024).
[5] T. Suzuki *et al.*, Phys. Rev. C **35**, 2212 (1987).

K. Ninomiya[1], M. K. Kubo[2], M. Inagaki[3], G. Yoshida[4], I. Chiu[5], T. Kudo[6], S. Asari[6], S. Sentoku[2], S. Takeshita[7,8], K. Shimomura[7,8], N. Kawamura[7,8], P. Strasser[7,8], Y. Miyake[7,8], T. U. Ito[9], W. Higemoto[9,10], and T. Saito[11]

[1]Natural Science Center for Basic Research and Development, Hiroshima University; [2]Division of Natural Sciences, International Christian University; [3]Institute for Integrated Radiation and Nuclear Science, Kyoto University; [4]Radiation Science Center, KEK; [5]Materials Sciences Research Center, Japan Atomic Energy Agency; [6]Graduate School of Science, Osaka University; [7]Muon Science Section, Materials and Life Science Division, J-PARC Center; [8]Institute of Materials Structure Science, KEK; [9]Advanced Science Research Center, Japan Atomic Energy Agency; [10]Department of Physics, Tokyo Institute of Technology; [11]National Museum of Japanese History

Measuring and Analyzing Positive and Negative Muon-induced Soft Errors in 12-nm FinFET and 28-nm Planar SRAM Devices

1. Introduction

Soft errors present a significant challenge to the reliability of modern information systems. When cosmic rays interact with electronic devices at ground level, they can induce bit flips and transient malfunctions—collectively known as soft errors. Historically, these soft errors were attributed mainly to nuclear reactions between secondary cosmic-ray neutrons and silicon. However, as semiconductor technologies continue to scale, evidence suggests that muons are becoming an increasingly important contributor.

Studies by B. D. Sierawski *et al.* [1] demonstrated that positive muon–induced soft errors occur in CMOS SRAMs fabricated in 65 nm, 45 nm, and 40 nm nodes, with the error rate increasing as feature size shrinks. N. Fert *et al.* [2] further reported positive muon–induced single-event upset (SEU) cross sections in FinFET devices. Later pioneering works [3, 4] examined 65-nm bulk and SOI SRAMs under negative muon irradiation, revealing that negative muons produce much larger SEU cross sections than positive muons because of muon-capture reactions. Subsequent experiments evaluated negative muon–induced SEUs in 28-nm [5] and 20-nm [6] SRAMs. Nevertheless, no studies have yet reported negative muon irradiation results for FinFETs. To elucidate the muon contribution to the overall soft-error rate (SER), it is therefore essential to investigate the effects of negative muons on FinFET technologies.

2. Experiment

Muon irradiation experiments were conducted at MUSE using 12-nm FinFET and 28-nm bulk planar SRAMs. The 12-nm device contained four types of SRAMs with a total capacity of 28.3 Mbits, while the 28-nm device incorporated two SRAM types totaling 18.9 Mbits. Figure 1 illustrates the experimental setup, which comprised a collimator, a plastic scintillator, and a board-mounted chip positioned upstream of the muon beam.

The threshold charge required to flip a stored bit—known as the critical charge—depends on the operating voltage of each SRAM. To examine this dependence, we applied supply voltages of 0.30V, 0.56V, and 0.69V to the 12-nm chip, and 0.62V, 0.77V, and 0.90V to the 28-nm chip. Bit upsets are most likely when muons stop near the SRAM transistors, where they deposit significant energy and induce negative-muon capture reactions. To observe how the SEU cross section varies with muon energy, the momentum of the irradiation beam was systematically adjusted.

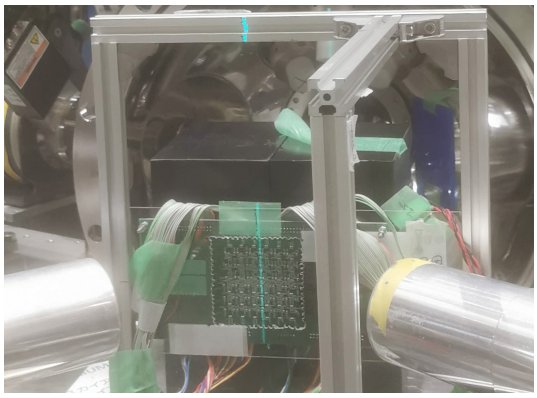

Figure 1. Experimental system seen from the downstream side. Reprinted with permission from [7].

3. Results

Momentum scans were performed for both the 12-nm and 28-nm devices to evaluate their SEU cross sections. Figure 2 shows the dependence of the SEU cross section on muon momentum for positive and negative muons at supply voltages of 0.69V (12 nm) and 0.77V (28 nm), respectively. Data for positive-muon irradiation of the 12-nm device are not shown, as no upsets were

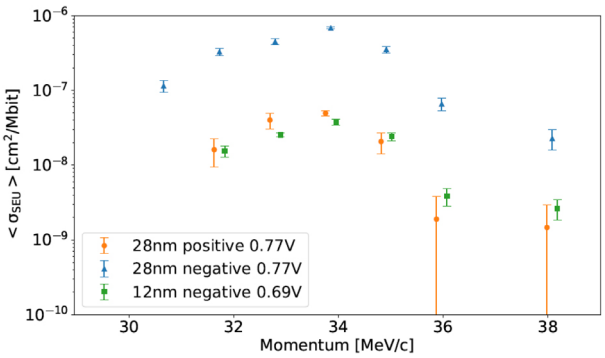

Figure 2. Positive and negative muon momentum dependence of SEU cross section; 12-nm and 28-nm SRAM chips operated at voltages of 0.69V and 0.77V, respectively. Reprinted with permission from [7].

detected during a one-hour exposure to 33.9 MeV/c positive muons.

The SEU cross sections reached their maximum around 33.9 MeV/c for both the 12-nm and 28-nm devices, which is determined by the package and chip structures. In both cases, the SEU cross section induced by negative muons exceeded that of positive muons by more than an order of magnitude at the peak momentum. This observation suggests that direct ionization is not the primary mechanism responsible for SEUs in these technologies. The critical charges of the 12-nm and 28-nm SRAMs are sufficiently large that the majority of through-passing muons cannot generate enough charge to induce bit upsets.

4. Conclusion and Future Plans

In this study, the SEU cross sections of 12-nm FinFET and 28-nm bulk planar SRAM devices were measured under both positive and negative muon irradiation. The results revealed that negative muons induced SEU cross sections more than an order of magnitude higher than those caused by positive muons in both technologies. This pronounced difference indicates that direct ionization is not the dominant mechanism responsible for SEUs in either process. Instead, the relatively large critical charge values of the 12-nm and 28-nm SRAMs suggest that through-passing muons do not generate sufficient charge to cause bit upsets; rather, the observed SEUs are mainly attributed to negative-muon capture reactions occurring when muons stop within the device.

However, the above discussion mainly applies to muons that stop within the device. In contrast, high-energy muons, which are several orders of magnitude more abundant, can traverse the device without stopping. If the SEU cross section for such muons from direct ionization is nonzero, their cumulative effect could significantly influence the overall SEU rate. To fully understand muon-induced effects on VLSI chips under terrestrial conditions, high-energy muon irradiation experiments are required.

Future work will also aim to establish a closer correlation between simulation results and experimental data to clarify the underlying physical mechanisms. Simulations for positive muon irradiation were successfully conducted for both 12-nm and 28-nm devices, with most results accurately reproduced using conventional methods [8]. In contrast, for negative muons, the involvement of multiple nuclear species with widely varying linear energy transfer (LET) values makes accurate reproduction of experimental results more challenging. Further investigation is needed.

5. Acknowledgements

This work was supported by the Grant-in-Aid for Scientific Research (S) from Japan Society for the Promotion of Science (JSPS) under Grant JP19H05664 and Grant 24H00073.

References

[1] B. D. Sierawski, *et al.*, IEEE Trans. Nuclear Science. **57**(6) (2010).
[2] N. Seifert, *et al.*, in IEEE International Reliability Physics Symposium (IRPS) (2015).
[3] W. Liao, *et al.*, IEEE Trans. Nuclear Science. **65**(8) (2018).
[4] S. Manabe, *et al.*, IEEE Trans. Nuclear Science. **65**(8) (2018).
[5] W. Liao, *et al.*, in Proc. International Reliability Physics Symposium (IRPS) (2019).
[6] T. Kato, *et al.*, IEEE Trans. Nuclear Science. **68**(7) (2021).
[7] Y. Gomi, *et al.*, Proc. European Conference on Radiation and Its Effects on Components and Systems (RADECS) (2023).
[8] Y. Gomi, *et al.*, IEEE Trans. Nuclear Science. **72**(8) (2025).

M. Hashimoto[1] and Y. Gomi[1]
[1]*Graduate School of Informatics, Kyoto University*

Absence of Magnetic Order in Altermagnet Candidate RuO_2

1. Introduction

The recent theoretical prediction of a third type of magnetism, known as *altermagnetism*, has attracted considerable attention due to its potential applications in next-generation spintronic devices. This form of magnetism exhibits properties intermediate between those of conventional ferromagnets and antiferromagnets. Ruthenium dioxide (RuO_2, rutile structure) has been proposed as a possible metallic altermagnet. Although RuO_2 has long been known as a Pauli paramagnetic metal, recent neutron diffraction and resonant X-ray scattering experiments have reported an antiferromagnetic (AFM) order—an essential requirement for altermagnetic order [1,2].

However, the reported magnetic moment on Ru, $|\boldsymbol{m}_{Ru}| = 0.05\,\mu_B$, is close to the detection limit for these experimental techniques. Therefore, independent verification using alternative probes is crucial.

2. Experimental and Simulation

We investigated the magnetic ground state of a high-quality single crystal of RuO_2 (residual resistivity ratio RRR > 1500) using muon spin rotation and relaxation (μSR) technique. The μSR measurements were performed in both zero and longitudinal fields across a temperature range of 5-400 K using ~100% spin polarized μ^+ beam (~4 MeV), employing the ARTEMIS spectrometer installed in the S1 area at MLF, J-PARC.

First-principles density functional theory (DFT) calculations were carried out using *Quantum ESPRESSO* to estimate the muon stopping sites. A 3×3×3 rutile supercell + one hydrogen was optimized within the generalized gradient approximation using the Perdew–Burke–Ernzerhof functional with an energy cutoff of 60 Ry, 3×3×4 *k*-mesh and a on-site Coulomb interaction U = 2 eV for Ru 4*d* orbital in the nonmagnetic state. Atomic positions were relaxed until the maximum force was below 1×10^{-3} Ry/Bohr.

3. Results and Discussion

Figure 1(a) displays the temperature evolution of zero-field (ZF)-μSR spectra [3]. No precession signal characteristic of magnetic order is detected, implying the absence of a uniform internal magnetic field, B_{loc}, at the presumed muon stopping site(s). As shown in Fig. 1(b), the observed slow relaxation at 5 K is completely suppressed by applying a weak longitudinal field (LF) of 1 mT, indicating that B_{loc} is quasistatic and excludes the possibility that motional narrowing could average B_{loc} to zero.

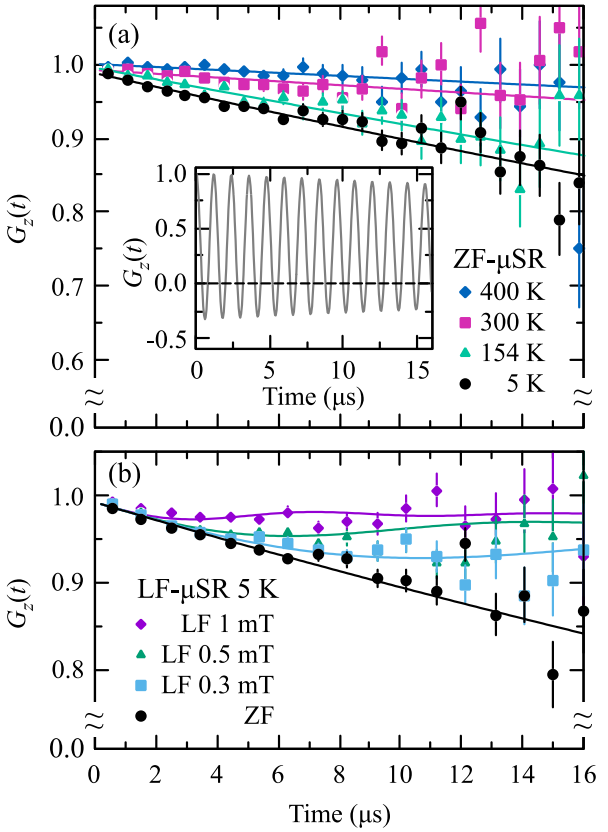

Figure 1. (a) Temperature dependence of the ZF-μSR spectra, and (b) external field dependence of LF-μSR spectra at 5 K in single-crystalline RuO_2. Solid lines represent the best fit to the data using Eq. (1). Inset: the simulated μSR procession signal expected for the AFM order proposed in previous studies (see text).

The curve fits of the spectra were performed using the following function:

$$A_0 G_{(t)} = A_1 G_{KT}(\lambda, B_{LF}, t),$$
$$G_{KT}(\lambda, 0, t) = \frac{1}{3} + \frac{2}{3}(1 - \lambda t)\exp(-\lambda t), \quad (1)$$

where $G_{KT}(\lambda, B_{LF}, t)$ is the static Lorentzian Kubo-Toyabe function with λ being the relaxation rate, B_{LF} is the external magnetic field. As shown in Fig. 1, the temperature dependence of ZF spectra and LF spectra at 5 K are well reproduced by the Eq. (1). We found that the A_1 value remains nearly constant across the temperature range of 5-400 K, being almost identical to the maximal

value of the spectrometer. This indicates the absence of muonium formation (a neutral H like state) and rules out the occurrence of any fast depolarization components due to magnetic order beyond the time resolution of the spectrometer.

Before concluding the absence of AFM order, however, certain pitfalls must be addressed. In antiferromagnets, high-symmetry interstitial sites can exist where dipolar fields from magnetic ions cancel. For the reported AFM structure [1,2], this occurs at the 4*d* = (0, 0.5, 0.25) and 8*j* = (0.25, 0.25, 0.25) positions. If muons occupy such sites, the μSR spectra would remain insensitive to magnetic ordering. Hence, identifying the likely muon sites and assessing their sensitivity to B_{loc} is essential.

Figure 2 represents the optimized defect structure involving hydrogen (H) as pseudo-muon obtained from the DFT calculations, illustrating the most stable site, labeled Site1, where the H atom forms an OH-like bond. When H was fixed at the high-symmetry 8*j* and 4*d* positions, the total energies were approximately 2.1 and 1.4 eV higher than that of Site1, respectively, ruling out muon localization at those cancellation sites.

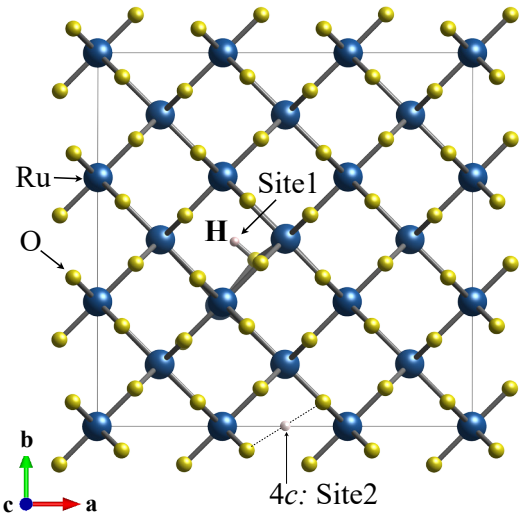

Figure 2. Local structure around the hydrogen (H) atom used to mimic a muon RuO_2, obtained by structural optimization within 3x3x3 supercell. Site1 denotes the most stable position, where the H atom forms an OH-like bond. Site2 corresponds to the center of the tunnel along the *c*-axis [4*c* site, (0.5, 0, 0)].

Because the muon mass is roughly one-ninth that of H, the effect of zero-point energy (E_0), which was neglected in the static DFT calculation, should be taken into account. If E_0 exceeds the potential barrier around Site1, the muon could instead reside near the center of the *c*-axis channel, referred to as Site2 [4*c*: (0.5, 0, 0)], as depicted in Fig. 2.

Dipolar field calculations based on the AFM configuration reported in [1] yield B_{loc} = 6.17 mT at Site1 and 5.96 mT at Site2, corresponding to muon precession frequencies of 0.84 and 0.81 MHz, respectively. The expected oscillation at Site1 is shown in the inset of Fig. 1(a). No such oscillation was observed experimentally over the entire 5-400 K range.

As the $\boldsymbol{m}_{Ru}$ has been reported to deviate slightly from the *c*-axis [2], we performed additional simulations of B_{loc} considering arbitrary orientations of $\boldsymbol{m}_{Ru}$. The results indicate that B_{loc} does not vanish at either Site1 or Site2 for any assumed direction of $\boldsymbol{m}_{Ru}$.

Alternatively, if one interprets the slow relaxation observed in the 5 K spectrum as a part of precession arising from an extremely small B_{loc}, the upper bound of the ordered moment can be estimated. Fitting the data with

$$G_z(t) = \frac{1}{3} + \frac{2}{3}\cos(\omega_{loc}t), \qquad (2)$$

where $\omega_{loc} = \gamma_\mu B_{loc}^{exp}$ and $\gamma_\mu/2\pi$ = 135.539 MHz/T, gives $B_{loc}^{exp} = 5.9(2)\times10^{-2}$ mT. Comparing this with the calculated B_{loc} = 5.96 mT for Site2 yields an upper limit of $|\boldsymbol{m}_{Ru}| = 4.8\times10^{-4}\,\mu_B$, significantly smaller than the previously reported 0.05 μ_B.

Taken together, these results indicate that the antiferromagnetic order suggested in earlier reports is unlikely to exist in bulk RuO_2.

References

[1] T. Berlijn *et al.*, Phys. Rev. Lett. **118**, 077201 (2017).
[2] Z. H. Zhu *et al.*, Phys. Rev. Lett. **122**, 017202 (2019).
[3] M. Hiraishi *et al.*, Phys. Rev. Lett. **132**, 166702 (2024).

M. Hiraishi[1,2,3], H. Okabe[4,2,3], A. Koda[2,3], R. Kadono[2,3], T. Muroi[5], D. Hirai[6], and Z. Hiroi[5]
[1]*Graduate School of Science and Engineering, Ibaraki University;* [2]*Muon Science Section, Materials and Life Science Division, J-PARC Center;* [3]*Institute of Materials Structure Science, KEK;* [4]*Institute for Materials Research, Tohoku University (IMR);* [5]*Institute for Solid State Physics, University of Tokyo;* [6]*Department of Applied Physics, Graduate School of Engineering, Nagoya University*

First successful acceleration of positive muons

1. Motivation

Muons, elementary particles akin to electrons but roughly 200 times heavier, have garnered great attention in modern physics. Despite their fleeting lifetime of 2.2 microseconds, muons serve as powerful probes for exploring phenomena beyond the Standard Model of particle physics, while also finding applications across diverse scientific and engineering domains.

One of the most intriguing properties of the muon is its anomalous magnetic moment, denoted as g–2. For a spin-½, point-like particle, g is theoretically expected to be exactly 2 at the leading order, but quantum field effects introduce small deviations through higher-order loop corrections involving virtual particles.

Another closely related quantity is the muon's electric dipole moment (EDM). Although the Standard Model predicts an extraordinarily small EDM, numerous Beyond-Standard-Model theories foresee values that could fall within the sensitivity range of ongoing or future experiments.

To achieve precise determinations of g–2 and EDM, high-quality muon beams characterized by high polarization and low emittance are indispensable. Emittance, which represents the spread of particles in phase space, is typically large in conventional muon beams derived from pion decay, thus constraining measurement accuracy.

To overcome these limitations, the experimental collaboration proposed a pioneering approach—cooling muons to dramatically suppress beam emittance [1]. However, conventional cooling techniques such as stochastic or electron cooling, effective for protons and ions, are unsuitable for muons due to their extremely short lifetime.

2. Experiment

The team implemented a unique method utilizing ultra-slow muons [2]. The concept, outlined in Figure 1, begins with a surface muon beam that is stopped within a specially prepared silica aerogel target. Inside the target, muons reduce their energy to thermal energy. Some muons capture electrons to form muonium atoms—hydrogen-like systems composed of a positive muon and an electron. A portion of these atoms escapes from the target surface into the vacuum. When illuminated by a precisely tuned deep-ultraviolet laser

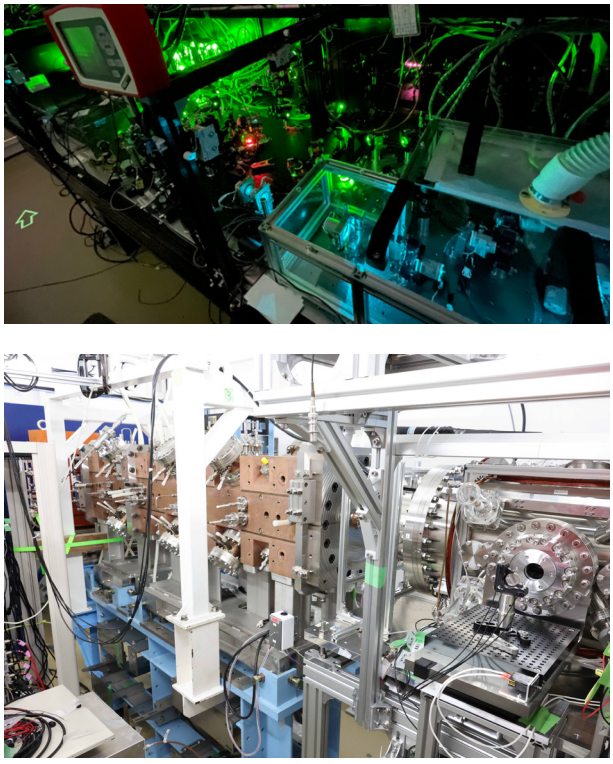

Figure 2. (top) The 244~nm laser system. (bottom) The cold muon source and the RFQ.

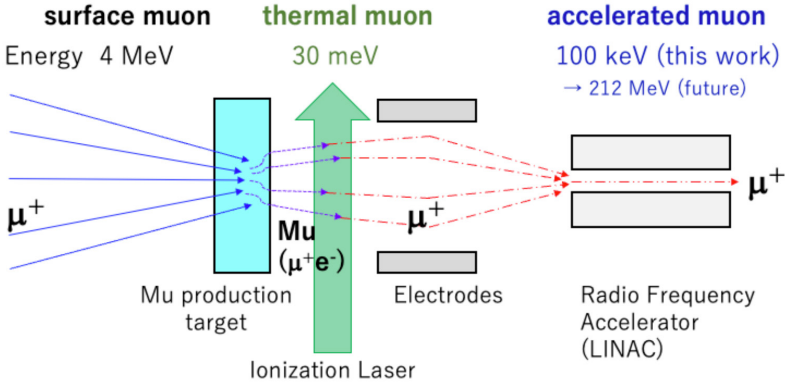

Figure 1. Concept of positive muon cooling and acceleration.

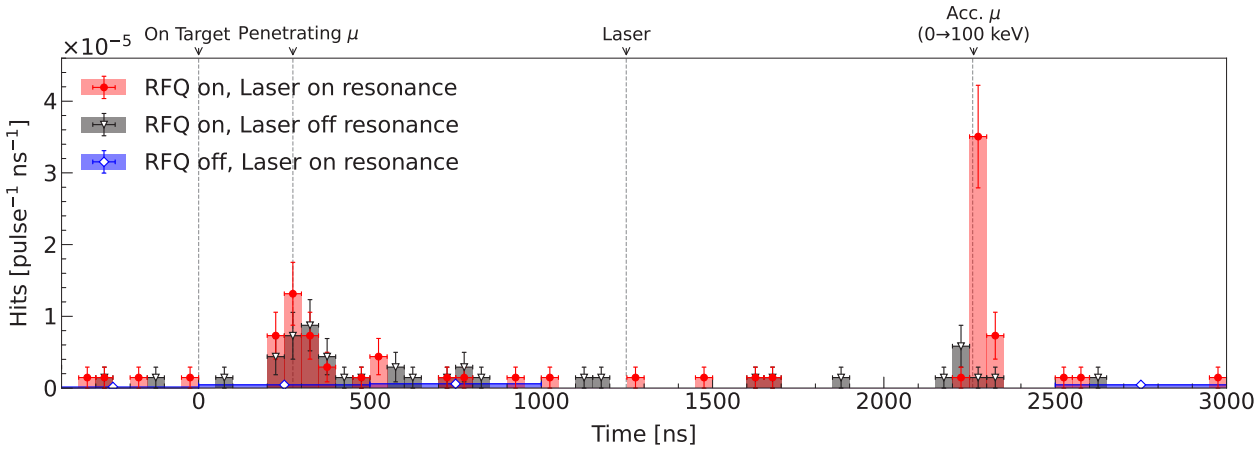

Figure 3. The measured time-of-flight distribution at the detector after the RFQ and a bending magnet.

pulse (Figure 2, top), the electron is stripped away, releasing the muon as a slow particle with thermal energies.

The emitted ultra-slow muons are extracted through electrostatic fields and focused by electric lenses before being injected into a radio-frequency quadrupole (RFQ) linear accelerator (Figure 2, bottom). The RFQ accelerates the muons to 100 keV. This process was successfully demonstrated at the S2 experimental area of J-PARC MLF in 2024—marking the world's first successful radio-frequency acceleration of cooled positive muons [3].

Beam characterization involved beam-profile monitors and time-of-flight (TOF) measurements (Figure 3). A distinct peak in the TOF distribution, corresponding to the arrival of accelerated muons, appeared only when the laser frequency was properly tuned and the RFQ was energized. The observed TOF values matched simulation predictions, confirming the beam's identity and energy.

Additionally, beam emittance was evaluated through Q-scan measurements, wherein the magnetic field strength of quadrupole magnets was varied to study changes in the downstream beam size. The measured emittance was 0.85π mm·mrad (horizontal) and 0.32π mm·mrad (vertical)—a reduction of about 200-fold and 400-fold, respectively, relative to the uncooled surface muon beam. These results demonstrated a significant enhancement in beam performance.

3. Summary and Future Plans

The first-ever radio-frequency acceleration of positive muons at J-PARC represents a milestone in accelerator and beam technology. This achievement stems from years of cross-disciplinary research spanning beamline development, laser engineering, muonium target fabrication, and precision diagnostics. The success marks the beginning of a new chapter in experimental physics, heralding a broad spectrum of future scientific opportunities with accelerated muons.

References

[1] M. Abe *et al.*, PTEP, **2019**, 053C02 (2019).
[2] K. Nagamine *et al.*, Phys. Rev. Lett. **74**, 4811 (1995).
[3] S. Aritome *et al.*, Phys. Rev. Lett. **134**, 245001 (2025).

S. Aritome et al.[1,2,3,4,5,6,7,8,9,19,11,12,13,14,15,16],
[1]*Muon Science Section, Materials and Life Science Division, J-PARC Center;* [2]*Graduate School of Science, University of Tokyo;* [3]*High Energy Accelerator Research Organization;* [4]*Research Institute for Interdisciplinary Science, Okayama University;* [5]*Institute of Science and Technology, Niigata University;* [6]*Graduate School of Science, Nagoya University;* [7]*Kobayashi-Maskawa Institute for the Origin of Particles and the Universe, Nagoya University;* [8]*Graduate School of Science and Engineering, Ibaraki University;* [9]*Department of Chemistry, Laboratory for Advanced Spectroscopy and Imaging Research (LASIR), University of British Columbia;* [10]*Japan Atomic Energy Agency (JAEA);* [11]*Research Center of Advanced Particle Physics, Kyushu University;* [12]*Department of Physics and Astronomy, University of Victoria;* [13]*TRIUMF, Vancouver;* [14]*Faculty of Science, Kyushu University;* [15]*School of Physics, Peking University;* [16]*State Key Laboratory of Nuclear Physics and Technology*

A Neutrino Experiment at J-PARC MLF : JSNS^2

1. Introduction

A neutrino experiment at J-PARC MLF, the JSNS^2 (J-PARC Sterile Neutrino Search at J-PARC Spallation Neutron Source) experiment, was proposed in 2013 [1] to investigate short-baseline neutrino oscillations caused by the sterile neutrino, a phenomenon suggested by the results of several previous experiments [2–5]. This phenomenon cannot be explained by the standard neutrino oscillation model, thus the observation of this phenomena makes a breakthrough the particle physics if exists.

The JSNS^2 experiment installs a 50-ton liquid scintillator detector on the third floor of the MLF, at a baseline of 24 m from the neutrino source [6]. The neutrino source is a liquid-mercury target designed to withstand a 1 MW proton beam. Although it is originally constructed as a spallation neutron source for material and life science studies, the mercury target simultaneously produces a large amount of (anti)neutrinos. JSNS^2 especially utilizes (anti)neutrinos from muon decay at rest ($\mu^+ \rightarrow e^+ + \nu_e +$ anti $\nu\mu$) to search for sterile neutrinos. Protons are accelerated to 3 GeV by the Rapid Cycling Synchrotron at J-PARC and impinge on the mercury target. The beam operates at 25 Hz with two 100 ns width bunches separated by 600 ns, providing excellent temporal separation between signal and background. The designed 1 MW beam power was achieved in 2024. The measured number of muons produced per proton at the target is 0.48±0.17 as determined via the $^{12}C(\nu_e, e^-)^{12}$Ng.s. reaction (CNgs) [7], which is about an order of magnitude higher than that in the KARMEN experiment [8] using ISIS facility in UK owing to the higher proton energy. If short-baseline anti $\nu\mu \rightarrow$ anti ν_e neutrino oscillations occur, the signal is detected through the inverse beta decay (IBD) reaction, anti $\nu_e + p \rightarrow e^+ + n$, in the liquid scintillator. The target scintillator contains 0.1 % Gd by volume, enabling neutron capture after thermalization, which releases ~8 MeV γ-rays with a mean capture time of ~30 μs. The prompt signal from the positron and the delayed signal from Gd capture form a coincidence signature. The most severe background arises from cosmogenic neutrons, which can mimic this coincidence through recoil protons (prompt) and captured γ-rays (delayed) [9]. To suppress such backgrounds, 10% di-isopropylnaphthalene (DIN, $C_{16}H_{20}$) was dissolved into the Gd-LS during 2021–2022.

DIN enhances pulse-shape discrimination (PSD) performance for prompt candidates. A dedicated PSD algorithm utilizing full waveform information and a log-likelihood ratio method was developed to further reduce neutron-induced backgrounds [10]. Commissioning data were collected in 2020 [9], and physics data have been accumulated since 2021. Despite annual installation and dismantling of the detector and scintillator at MLF, no significant degradation of the scintillator performance has been observed. In total, JSNS^2 accumulated 4.8×10^{22} protons on target (POT) from 2021 to 2024.

Further details on the detector setup can be found in Ref [6].

2. Results

From here, the scientific results from the JSNS^2 experiment are shown.

2.1 Sterile neutrino search

A careful analysis on the sterile neutrino search is necessary due to the importance of the results. Neutrino experiments usually employ the underground or at least the shallow environments to reduce the cosmogenic backgrounds, however JSNS^2 is the overground experiment. The scheduled timing from accelerator of the beam and the veto layer of the detector reduces the background drastically, however the cosmogenic neutrons completely mimic the IBD signals, resulting they are the most important background after the event selections. The typical number of neutron background after the event selection is ~1000 events in 2022 data, however the number of signal events with LSND best fit (suggested with the highest probability) is less than 2. The current PSD performance of the JSNS^2 is good to separate positron signals from the neutron background using the waveforms of PMTs in a event. The rejection power of the neutrons is 99.7 % while the efficiency of the positrons is estimated to be 83 % The signal-to-noise ratio after the PSD application is 1.6-to-3. Using this powerful tool, other improvements and the blind analysis, the first search result will be shown soon within 2025.

2.2 $^{12}C(\nu_e, e^-)^{12}$Ng.s. measurement

The muon decay at rest also provides the electron neutrinos. Using the cross section measurements of this $^{12}C(\nu_e, e^-)^{12}N_{g.s.}$ reaction from other experiments [11,12], we can measure the electron neutrino flux. This reaction gives two sequential coincidence signals with

the electrons as the prompt signal, and the positrons from the beta decay of $^{12}N_{g.s.}$ with the maximum energy of 16.3 MeV and 15.9 ms decay time. This is crucial measurement of the sterile neutrino searches, especially estimation for the anti $\nu\mu$ flux, i.e. number of oscillated IBD events because the production rates of parent particles, pions, muons and kaons of (anti)neutrinos with 3 GeV protons hitting the mercury target have not been measured. Note that the sources of both ν_e and anti-ν_μ are the same: decay-at-rest plus-charged muons. See details of the measurement in [7]. The importance of this measurement is as follows: (1) The JSNS^2 detector can measure the neutrinos with a few 10 MeV. (2) The mercury target creates the neutrinos from muon decay-at-rest source. (3) The neutrino flux (and the parent muons) is consistent with the simulation of hadron models within 1.2 sigmas, it is about 10 times larger than that of KARMEN [7]. This results using 2021-2022 data are utilized for the sterile neutrino analysis to estimate the number of IBD events.

2.3 Kaon Decay At Rest Neutrinos (KDAR)

J-PARC MLF provides the unique opportunity to measure the monochromatic energy (~236 MeV) neutrinos since the hits of 3 GeV protons to the mercury target create K^+ mesons, and $K_{\mu2}$ decay sequentially. The monochromatic energy neutrinos give the deep insights for the nuclear physics since there have never been such experiments using the real "monochromatic energy neutrinos" like the electron scattering measurements. The muon neutrino produced by $K_{\mu2}$: ($K^+ \rightarrow \mu + \nu_\mu$) has the quasi-elastic interaction in the liquid scintillator ($\nu_\mu + n \rightarrow \mu^- + p$). The KDAR signal also has the two sequent signals which consist of the prompt made by the muons and the protons, and of the delayed made by the Michel electrons decayed from μ^-. These suppress the background detection, resulting the ~80% of purity. The backgrounds are dominated by the interactions of other neutrinos. The detector effects can be removed from the observed energy of the prompt signal using MC (we say this as "unfolding"), and it gives full information of the KDAR neutrino interaction. The s- and p-shells effects are observed after this unfolding. Details of the measurements can be seen in [13].

3. Acknowledgements

We deeply thank the J-PARC for their continuous support, especially for the MLF and the accelerator groups for providing an excellent environment for this experiment. We acknowledge the support of the Ministry of Education, Culture, Sports, Science and Technology (MEXT) and the JSPS grants-in-aid: No. 16H06344, No. 16H03967, No. 23K13133, No. 24K17074, No. 20H05624 and 25H00649, Japan

References

[1] M.Harada, *et al.*, arXiv:1310.1437 (2013).
[2] C.Athanassopoulos, *et al.*, Phys. Rev. Lett. **77**, 3082 (1996).
[3] V. V. Barinov, *et al.*, Phys. Rev. C **105**, 065502 (2022).
[4] A. A. A. Arevalo, *et al.,* Phys. Rev. Lett. **121**, 221801 (2018).
[5] G. Mention, M. Fechner, T. Lasserre, T. A. Mueller, D. Lhuillier, M. Cribier, and A. Letourneau, Phys. Rev. D **83**, 073006 (2011).
[6] S.Ajimura, *et al.,* Nucl. Instrum. Methods. A **1014**, 165742 (2021).
[7] T.Dodo, *et al.*, Phys. Rev. D **112**, 032012 (2025).
[8] B. Armbruster, *et al.*, Phys. Rev. D **65**, 112001 (2002).
[9] Y.Hino, *et al.*, Eur. Phys. J. C **82**, 331 (2022).
[10] T.Dodo, *et al.*, Prog. Theo. Exp. Phys. 2025, 023H02 (2025).
[11] R. Maschuw *et al.*, Prog. Part. Nucl. Phys. **40**, 183 (1998).
[12] L. B. Auerbach *et al.*, Phys.Rev. C **64**, 065501 (2001).
[13] E.Marzec, *et al.,* Phys. Rev. Lett. **134**, 081801 (2025).

T. Maruyama[1,2] for JSNS[2] collaboration
[1]*Institute of Particle and Nuclear Studies, KEK;* [2]*Neutrino Section, J-PARC Center*

Neutron Source

Neutron Source Section

1. Operational overview

The beam operation for the user program in fiscal year 2024 started on April 8th with beam power of 990 kW, equivalent to 1 MW (the highest recorded), at the outlet of the 3GeV rapid cycling synchrotron (RCS) (950 kW at the MLF) and continued until May 29th. The first 1 MW long-term stable operation could be achieved and the press release was produced (https://www.j-parc.jp/c/en/press-release/2024/05/31001348.html). From May 29th, the beam power decreased to 900 kW due to a budget shortfall caused by soaring electricity costs. Moreover, from June 5th, the beam power was further decreased to 830 kW due to a change of the accelerator mode of the Main Ring (MR). The beam operation of MLF ended on June 24th due to a water detection issue in the Helium Vessel. The maintenance work for the long outage then began.

When the MLF beam operation started on December 9th after the long outage, the monitoring value of the radioactivity at the MLF exhaust tower showed a tendency to be higher than normal and the beam operation was suspended. It was suspected that the sealing performance of the mercury pipe flanges, which were fastened during the replacement of the mercury pump, was insufficient. Therefore, we improved the remote handling method and work procedures, and successfully replaced the metal O-rings on the mercury pipe flanges. After resuming beam operation on April 7th, normal monitoring results from the MLF exhaust tower were observed, allowing the 900 kW proton beam user program to start on April 15th.

The availability of the beam operation for the user program before the long outage in FY2024 was 82.1 % but MLF was out of the operation in the latter half of FY2024.

2. Maintenance work overview

As previously mentioned, the long outage at MLF started on June 24th. On July 18th, the used mercury target vessel, which was in operation from 2018 to 2019, was transported from MLF to the storage building (the so-called RAM building), where a total of 7 used target vessels were stored at that time. The water detection trouble in the Helium vessel was investigated and the cause was presumed to be the slight humid air inflow. Therefore, countermeasures were implemented to prevent this.

On September 9th, specimens were cut out successfully from the fore front wall of the used target vessel which was operated for the long-term user program with the highest beam intensity recorded of 950 kW. The maximum damage depth on the specimens was measured and the full beam power (1 MW) for the next two-year operation of the target vessel was decided.

In September, a trouble at the power manipulator which remotely loosens and tightens bolts of the target vessel occurred. After investigation, it was found that the cause of the trouble was a failure of an electrical device. The power manipulator could be operated normally by replacing the electrical device, resulting in three weeks delay. After that, the used mercury target vessel was replaced with a new one successfully on October 21st. The new one has the improved structure of the mercury flow channel with the split bubbler generator like the previous target vessel used during 2023 and 2024.

For the first time since the MLF operation began, the mercury circulation pump (Fig. 1) was also replaced successfully from November 5th to 8th. In parallel, periodic voluntary inspections of the cryogenic circulation system were conducted in accordance with the

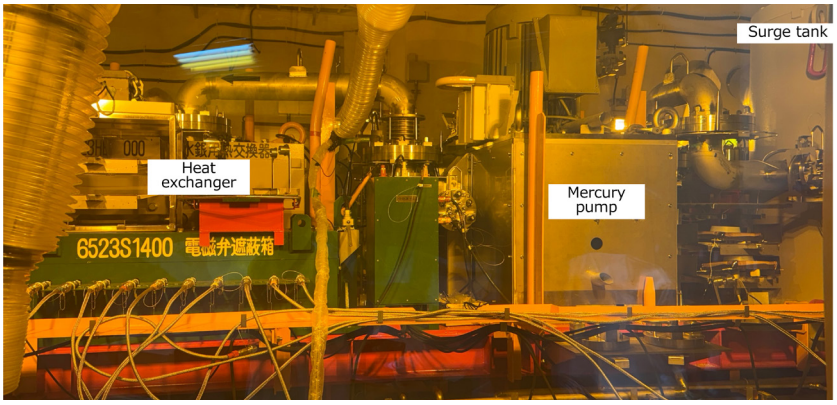

Figure 1. The mercury circulation pump on target trolley in hot cell room.

Figure 2. The remote handling practices at HENDEL building (uncontrolled area).

High Pressure Gas Safety Law and it was confirmed that there were no major troubles.

After the maintenance works ended and the MLF beam operation started, it was found that there were signs of unusual radioactive material during the proton beam tuning from December 9th. It was suspected that the sealing performance of the mercury pipe flanges, which were fastened during the replacement of the mercury pump, was insufficient. Therefore, we repeatedly practiced remote-handling works to fasten the pipe flanges properly using mockups and improved the remote control method and work procedures (Fig. 2). Finally, the metal O-rings on the mercury pipe flanges were successfully replaced.

The remote handling test of the moderator and reflector assembly was conducted using a spare assembly, as in the previous year. An assembly consists of three moderators, a reflector and a shielding plug, and only the used moderators and reflector are replaced, while the shielding plug is reused, similar to the proton beam window. Because the operating lifetime of a moderator and reflector assembly is relatively long, 30,000 MWh, equivalent to 8 years at 1 MW, the previous remote handling operation was conducted during the commissioning period before the MLF beam operation began more than 10 years ago. As the remote handling with the irradiated moderators and reflector will be planned three years later, enough preparation and practices would be conducted in order to avoid any troubles.

M. Harada[1], K. Sakai[1], and K. Haga[2]
[1]*Neutron Source Section, Materials and Life Science Division, J-PARC Center;* [2]*Materials and Life Science Division, J-PARC Center*

Application of Indentation Technique to Material Degradation Evaluation in the Mercury Target Vessel for Spallation Neutron Sources

1. Introduction

The mercury target vessel in the materials and life science experimental facility is a multi-walled structure with a water shroud surrounding the mercury vessel. This design prevents leakage of mercury even if the mercury vessel fails. Each vessel is subjected to irradiation damage from incident protons and generated neutrons. The irradiation damage is one of main factors determining the lifetime of the mercury target vessel [1]. Furthermore, each vessel is subjected to approximately 10^4 thermal stress cycles due to beam trips. The mercury vessel additionally is subjected approximately 10^9 dynamic stress cycles due to pressure waves caused by the instantaneous heating of the mercury. These loads contribute to material fatigue degradation [2]. Therefore, we will evaluate the material degradation of the used mercury target vessels.

The Spallation Neutron Source (SNS) in Oak Ridge National Laboratory uses similar mercury target vessels and has conducted tensile tests for each vessel under various irradiation intensities, load conditions, and temperature histories [3,4]. However, considering the difference in beam energy between J-PARC (3 GeV) and SNS (1 GeV), as well as the difference in hydrogen and helium gas generation that will affect post-irradiation strength degradation. It is crucial to independently evaluate the material degradation of the mercury target vessel used in J-PARC. Therefore, we plan to apply the indentation technique. We proposed a method for identifying constants in material constitutive equation representing mechanical properties by applying inverse analysis including numerical experiments simulating indentation tests [5].

In this study, we applied the mechanical property evaluation method using indentation tests to ion-irradiated materials that simulate proton and neutron irradiation damage. The material degradation due to irradiation was evaluated. We compared and discussed the applicability of this method with the evaluation data from SNS, which was estimated to be at the same irradiation dose, considering the scatter in the evaluated properties.

2. Materials and experiments

The material evaluated in this study for the mercury vessel is 316L stainless steel. Small plate specimens with dimensions of 3 mm x 6 mm x 0.5 mm were used. Ion irradiation with ion beams of 12.0 MeV nickel and 1.0 MeV helium at a temperature of 673 K was conducted at Takasaki Ion Accelerators for Advanced Radiation Application. The depth profile of atomic displacement damage by nickel ions and helium ion concentration were determined using TRIM code [6]. In the irradiated area with a depth of ~2.6 μm, the displacement damage intensity increased with increasing depth. It reached the maximum value at a depth of ~2 μm. Two irradiated specimens were prepared with the maximum displacement damage intensities of 5 and 35 dpa. The term dpa denotes the average number of displacements per atom caused by irradiation. The maximum injection rate of the helium ions was 50 appm/dpa.

The indentation tests were conducted 10 times on the unirradiated and irradiated areas of the specimen surface using a dynamic ultra-microhardness tester (Shimadzu, DUH-211S). A conical indenter with a tip radius of approximately 5 μm was used. The maximum indentation load was set to 14.7 mN.

3. Methods for evaluating material degradation

Based on the load-depth curve obtained in the indentation tests, the mechanical properties of the ion-irradiated region were evaluated using the following procedure.

(1) Identification of constants in material constitutive equation

Three constants in the Swift-type constitutive equation representing the stress – strain curve were identified by the inverse analyses using Kalman filter combined with numerical experiments in the indentation technique. Because there is a distribution of damage in the depth direction within the irradiation area, the damage area of the finite element model (FEM) was divided into four layers in this study, and then constants of each layer were identified.

(2) Numerical experiments of tensile tests

Numerical experiments of tensile test were conducted based on the constants identified for each layer using FEM. The model was based on the geometry of the specimen used in the tensile test.

4. Results and discussions

The numerical experimental results of the tensile test using the identified constants of the fourth layer of two irradiated specimens are shown in Fig. 1. The yield stress and tensile strength increase, while the uniform elongation decreases with increasing displacement damage intensity. Figure 2 shows the total elongation evaluated based on the internal stress state of the specimen. The total elongation gradually decreased with increasing displacement damage intensity, but no further change was observed beyond approximately 10 dpa. This tendency is consistent with the tensile test results for irradiated materials within the range of the scatter. It is expected that similar results will be obtained for the used mercury target vessel at J-PARC. The evaluation results and previous tensile tests exhibit significant scatter. Systematic data were collected through indentation tests, and the lifetime is evaluated statistically.

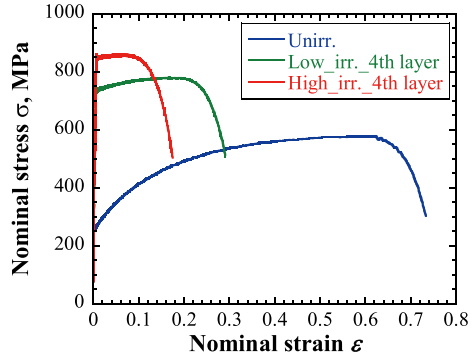

Figure 1. Stress -strain curves of unirradiated area and 4th layer of irradiated area

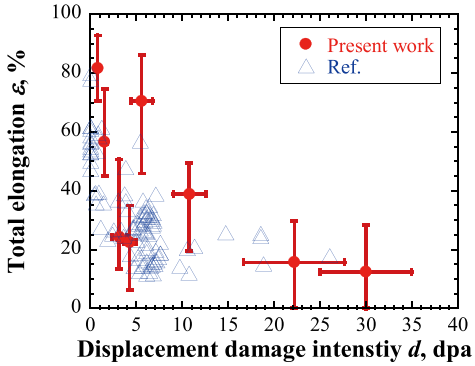

Figure 2. Relationship between total elongation and displacement damage intensity. Circle dots indicate results of present work and triangular dots indicate reference results [3,4].

Previous SNS results reflect the combined effects of temperature history and fatigue due to repeated loading. For specimens irradiated at 9 dpa, the total elongation at 164°C decreased to approximately one-quarter of the value at room temperature [7]. Considering the operational temperature of the mercury target vessel, which reaches approximately 150°C, it is necessary to consider the lifetime considering the temperature effect in comparison with the indentation results obtained at room temperature. Cold-worked materials simulating irradiation showed a softening tendency up to approximately 10^4 cycles, followed by hardening beyond 10^7 cycles [8]. Since the frequency of dynamic stress application differs between the mercury vessel and the water shroud, comparing the mechanical property evaluation results of the two vessels is expected to clarify the effects of repeated loading on material properties.

5. Conclusions

To evaluate the material degradation of the mercury target vessel due to irradiation, the application of the indentation technique was investigated using ion-irradiated materials that simulate proton and neutron irradiation damage. The total elongation decreased with increasing the displacement damage intensity. This trend is consistent with previously reported material degradation behaviors observed in tensile tests using small specimens considering the scatters in the data. We plan to evaluate the material degradation of each vessel to present a realistic and reasonable lifetime.

References

[1] S. Ishikura, M. Futakawa *et al.*, JAERI-Tech. **2004-028**, 15 (2004).
[2] M. Futakawa *et al.*, Nucl. Instrum. Methods Phys. Res. A **562**, 676 (2006).
[3] D. A. McClintock *et al.*, J. Nucl. Mater. **450**, 130 (2014).
[4] D. A. McClintock *et al.*, J. Nucl. Mater. **545**, 152729 (2021).
[5] T. Wakui *et al.*, Mater. **17**, 5925 (2024).
[6] S. Hamada *et al.*, J. Nucl. Mater. **258-263**, 383 (1998).
[7] J. L. Puzzolante *et al.*, J. Nucl. Mater. **283**, 428 (2000).
[8] Z. Xiong *et al.*, Procedia Eng. **101**, 552 (2015).

T. Wakui[1], S. Saito[2], and M. Futakawa[3]
[1]Neutron Source Section, Materials and Life Science Division, J-PARC Center; [2]Nuclear Transmutation Division, J-PARC Center; [3]J-PARC Center

Neutron Science

Neutron Science Section

1. User program

In fiscal year 2024, 147 of 301 proposals for 2024A and 113 of 321 for 2024B were approved as general neutron experiments. The Promotion for Industrial Use and the Priority Use for National Projects were also admitted as a new proposal category. For the Long-term proposals, six proposals were applied, of which three were approved. In addition, four ongoing proposals will continue into the next period, and two completed projects were reviewed.

In 2024, the MLF experienced several issues that resulted in the loss of many experimental days. Consequently, a large number of experiments were forced to be postponed, causing considerable disruption not only for visiting users but also within the MLF facility. Most of these experiments are planned to be carried over to the next round, 2025A.

2. Instruments update

The following devices were updated in 2024.

2-1. New detectors

A new scintillation detector system has been installed at the backward detector bank of Super-HRPD (BL08) to enable single crystal diffraction measurement. The two-dimensional ^{6}Li glass scintillator with a single pixel size of 6 x 6 mm^2 provides high spatial resolution, which is sufficient for detecting sharp Bragg spots from single crystals. At the SENJU (BL18) diffractometer, newly developed area detectors with 128 x 192 pixels, far surpassing the conventional detector 64 x 64 pixels, have been installed to capture sharp Bragg spots from single crystals (see Fig. 1). Two detectors were installed in 2024, a total of nine detectors will be planned. This extension will not only expand the detection area but also enable highly efficient measurements without gaps between detector banks.

2-2. New sample environments

Measurements of samples under various physical conditions, such as low and high temperatures, pressure, magnetic fields, and electric fields, are essential for elucidating the key parameters that govern material properties. To meet user demands, a wide variety of sample environment devices is considered an essential facility resource. To support a wide range of temperature measurements, high-temperature furnaces were developed for iMATERIA (BL20), DNA (BL02), and HRC (BL12),

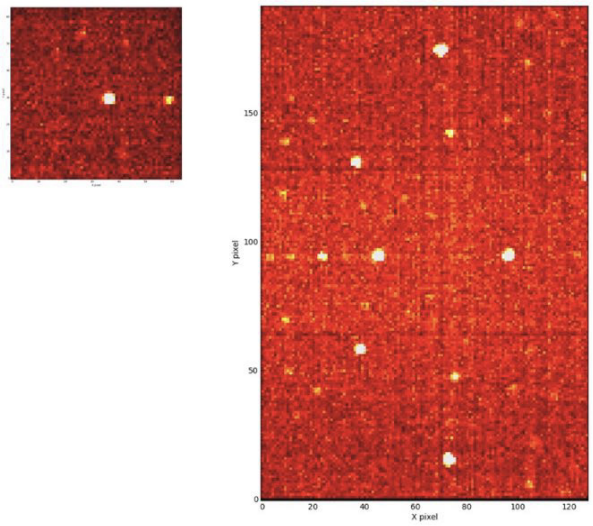

Figure 1. Comparison of diffraction patterns from the standard sample ($12CaO \cdot 7Al_2O_3$) observed with conventional detector (left) and the new detector (right). The detector area has increased significantly.

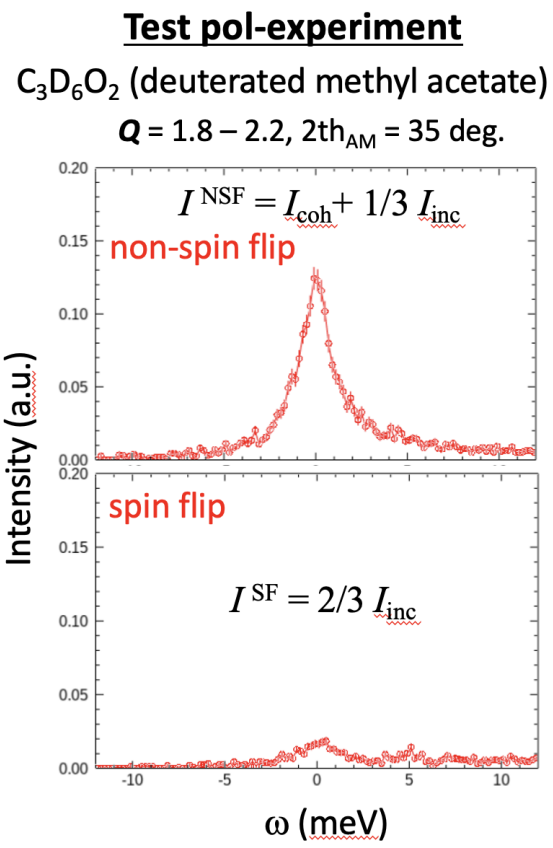

Figure 2. Polarized neutron-diffraction measurements for deuterated methyl acetate $C_3D_6O_2$ at POLANO (BL23). The separation of coherent and incoherent scattering can be achieved by independently conducting spin-flip and non-spin-flip measurements.

capable of reaching up to 700 K, 590 K, and 800 K, respectively. Additionally, a newly developed rheometer has been introduced for neutron reflectometry at SOFIA (BL16).

2-3. Neutron polarization

We have worked for several years to implement neutron polarization analysis using a pulsed neutron source. POLANO (BL23) is one of the instruments at MLF designed for inelastic measurements with polarized neutrons. After a long period of development and fabrication, all polarization and magnetic devices components were installed on the POLANO by 2023. The on-beam polarization commissioning started in 2024. Figure 2 shows the first data obtained from a liquid sample of deuterated methyl acetate ($C_3D_6O_2$). The non-spin flip and spin-flip datasets exhibit a significant difference in scattering processes, due to their differing scattering cross-sections.

3. Meetings and Education

The Neutron Science Section organized and contributed to the meetings listed below. These activities promoted active exchange of ideas and strengthened collaboration.

(1) Joint ESS-J-PARC & SAKURA Workshop (June 10-12, 2024, at J-PARC Research Building)

Participants exchanged opinions about the cooperative relationship between ESS and J-PARC. Presentations were delivered by researchers from both sides under the SAKURA Mobility Program which supports institutional exchange. Through this workshop, both facilities shared concrete directions to further strengthen their cooperation.

(2) The Annual Meeting on Industrial Application for Neutron (July 11-12, 2024, at Akihabara Convention Hall)

This annual event is organized in response to industry demand for research utilizing neutron and muon beams provided by MLF and JRR-3. The program featured 22 oral presentations and 72 posters, with 247 participants attending on-site and 135 joining online.

(3) The 4th J-PARC Symposium 2024 (October 15-17, 2024, at Mito City Civic Center)

The MLF-related sessions addressed six topics: carbon neutrality; advances in experimental techniques and analysis methods; quantum devices and topological materials; circular economy and environmental sustainability; life science innovation; and future plans for overseas neutron and muon facilities. The symposium featured 93 oral presentations and 290 poster presentations, with approximately 400 domestic and international researchers participating in lively discussions.

(4) The 8th Neutron and Muon School (December 9-13, 2024 at J-PARC)

The program aims to broaden the foundation of neutron and muon research by offering students and young researchers opportunities to learn directly from experts about the characteristics and experimental methods of neutrons and muons. After the lectures, participants were divided into small groups for hands-on training using instruments at MLF and JRR-3. There were 31 participants on-site and 72 registered for the online lecture. (Fig. 3)

Figure 3. Participants of the Neutron and Muon School receiving hands-on training from a BL21 beamline staff. (©IMSS)

(5) Quantum Beam Science Festa 2024 (March 12-14, 2025 at Tsukuba International Congress Center)

On the first day of the 16th MLF Symposium, participants discussed the current status of the MLF and its future roadmap.

4. Publications and Awards

In 2024, research utilizing the MLF neutron beamlines resulted in 207 scientific publications, 19 of which were featured in press releases. In addition, 16 prizes were awarded. The following three achievements highlight contributions made by the Neutron Science Section.

- The 22nd Young Researcher Award, The Japanese Society for Neutron Science
"*Research on Novel Physical Properties in Ce Compounds*", D. Ueta (BL12)
- The 22nd Young Researcher Award, The Japanese Society for Neutron Science
"*In Situ Pulsed Neutron Diffraction Study on the Mechanism of Mechanical Properties of Advanced Structural Materials*", T. Yamashita (Former Post Doc. BL19)
- International Magnesium Science & Technology Award for Excellent Paper of the Year
"*Strengthening of αMg and long-period stacking ordered phases in a Mg-Zn-Y alloy by hot-extrusion with low extrusion ratio*", S. Harjo, W. Gong, K. Aizawa, T. Kawasaki, M. Yamasaki (BL19)

M. Nakamura[1], T. Yokoo[1,2], and A. Sano[1,2]
[1]*Neutron Science Section, Materials and Life Science Division, J-PARC Center;* [2]*Institute of Materials Structure Science, KEK*

BL01: 4D-Space Access Neutron Spectrometer 4SEASONS

1. Introduction

4SEASONS is a direct-geometry time-of-flight neutron spectrometer for thermal neutrons, and one of the Public Beamlines in the MLF [1]. In 2024, 15 General Use (GU) proposals, 2 New User Promotion (NUP) proposals, one CROSS Development Use proposal, and one Instrument Group Use proposal were approved. One reserved proposal was granted beamtime. However, for ten of these proposals, the allocated beamtimes were fully or partly transferred to the next fiscal year due to unexpected long shutdowns of the facility. 85% of the GU and NUP proposals were submitted by international users. 72% of the submitted proposals were in the field of magnetism, while the rest targeted phonons and other atomic vibrations. 10 peer-reviewed papers were published.

2. Instrument upgrade

Detectors: We have been updating the detector electronic modules (NEUNET) to enable the pulse-width-and-height limitation function [2]. Last year, we purchased new NEUNET boards with this function (Fig. 1) and confirmed that the positions along the detectors were resolved correctly [3]. This year, we carried out a long-term stability test in two ways—we repeated three-minute counting of neutrons more than 1000 times, and we kept counting neutrons for three days. As a result, we found that the kicker counts are occasionally missing in the recorded data, and the frequency of this phenomenon depends on the neutron intensity. This problem may be caused by a bug in the FPGA program, and we are discussing with the vendor how to fix it.

Figure 1. NEUNET boards in the 4SEASONS control cabin. Silver and black boards are new and old NEUNETs, respectively.

Sample Environment: 4SEASONS is equipped with a top-loading and a bottom-loading (BL) GM refrigerator for cooling samples. The BL refrigerator provides a lower background environment thanks to the absence of vacuum chambers. However, this year, we prepared an outer vacuum chamber (OVC) for the BL refrigerator (Fig. 2). This was motivated by a problem with the cryopump used to achieve a sufficiently high vacuum for the operation of the refrigerator in the scattering chamber. With the OVC, we can maintain a high vacuum around the sample and run experiments even when the high-vacuum pumping system malfunctions. The OVC will also be useful for offline precooling of samples before the experiment to save the sample cooling time.

Figure 2. The bottom-loading GM refrigerator with the outer vacuum vessel at 4SEASONS.

4SEASONS utilizes an oscillating radial collimator to reduce scattering from sample environment devices [4,5]. The collimator blades are made of cadmium-plated aluminum. We planned to replace the Cd blades with boron-based blades to improve performance at high energies above the cut-off energy for the neutron absorption by cadmium. The new boron-based blades

were made of Kapton® films painted by ^{10}B on both sides. As a result of the on-beam test at 4SEASONS, however, we found that the new blades produce higher background than the Cd blades. We have now reverted to the original Cd blade and are investigating the cause of this elevated background.

New Device: Boron is a typical neutron-absorbing material that is widely used in the neutron-shielding components of neutron scattering instruments. Glues are commonly used to form boron into the desired shapes and dimensions. However, neutron scattering by hydrogen in glues degrades the shielding performance of boride absorbers. Accordingly, we used thermal spray coating to deposit natural B_4C powders onto aluminum plates and characterized the resulting coatings. The obtained thickness of the coatings and estimated volume fraction of boron in them are similar to those of an existing Fermi chopper slit. The neutron scattering measurements at 4SEASONS revealed that the reflection of neutrons on the surface of the thermal-spray-coated plate is less intense than that on the Fermi chopper slit coated with a ^{10}B-epoxy mixture, especially at low neutron energies. The latter feature was attributed to the hydrogen-free nature of the thermal spray coating and should be advantageous for neutron-shielding components.

Acknowledgments

We thank K. Inoue, W. Kambara, and H. Tanaka for their support and advice. The instrumentation works described here were supported by the engineers of the Neutron Science Section and the Technology Development Section of the MLF.

References

[1] R. Kajimoto *et al.*, J. Phys. Soc. Jpn. **80**, SB025 (2011).
[2] S. Sato *et al.*, J. Neutron Res. **24**, 427 (2022).
[3] R. Kajimoto *et al.*, MLF Annual Report 2023, 72 (2024).
[4] M. Nakamura *et al.*, JPS Conf. Proc. **8**, 036011 (2015).
[5] M. Nakamura *et al.*, Physica B **551**, 480 (2018).

R. Kajimoto[1], M. Nakamura[1], K. Kamazawa[2], Y. Inamura[1], K. Iida[2], S. Hayashida[2], and M. Ishikado[2]
[1]Neutron Science Section, Materials and Life Science Division, J-PARC Center; [2]Neutron Science and Technology Center, CROSS

Current Status of BL02 DNA in 2024

1. Introduction

DNA is a TOF type backscattering spectrometer utilizing Si crystal analyzers, installed at Materials and Life Science Experimental Facility (MLF), the Japan Proton Accelerator Research Complex (J-PARC) [1,2]. DNA employs a pulse-shaping chopper to extract neutrons with sharp temporal structure from the broad pulses produced by the coupled moderator, enabling μeV-order energy resolution over a meV-order energy transfer range. DNA achieves a signal-to-noise ratio ~10^5, facilitating studies across diverse research fields, including those involving materials with small scattering cross-sections or limited sample quantities of samples (on the order of milligrams).

In 2024, the BL02 team composition changed with the appointment of Dr. Tamatsukuri as a deputy responsible and the addition of Dr. Murasaki to the DNA member. In 2024, DNA contributed to 12 peer-reviewed publications, consistent with the DNA's average output in recent years. These publications covered a diverse range of research areas, including bio-matter, water dynamics, hard matter, functional materials, proton conduction, soft matter, and food. Notable outcomes included two press releases highlighting research on the lattice dynamics in a quasicrystal and fast proton conduction in polymer membranes. Dr. Fumiya Nemoto received the Encouragement Award from the Japan Neutron Science Society for his work on structure formation in liquid-crystalline soft matter, which incorporated neutron scattering data from DNA. Additionally, Dr. Jin Shimada, successfully completed his doctoral degree from Osaka University in 2024 with a dissertation entitled "Thermodynamic and electrochemical properties in semiclathrate hydrate systems for thermal storage technology" including DNA data.

2. User Program in the periods 2023B and 2024A

In 2024, DNA received 17 General Proposals (GP) for the 2023B period and 19 for the 2024A period. Of these, 16 GPs (including one New User Promotion proposal) were approved for 2023B, and 8 GPs were approved for 2024A. The ratio of approved to requested beamtimes was 65 % for 2023B and 45 % for 2024A, corresponding to the competition rates of 1.1 and 2.4, respectively.

Due to the target-related issues between November 2023 and January 2024, as well as in June 2024, six experiments were carried over to subsequent periods. In May 2024, a malfunction of the pulse-shaping chopper prevented high-resolution measurement for one month (described in the next section); during this period, high-flux measurements were conducted for four reserved proposals until the chopper was repaired. Additionally, two Long Term Program (LTP) proposals ran at DNA during the 2023B and 2024A periods.

3. Beamline activities

[Development of sample environment]

To expand the accessible temperature range at DNA, a compact high-temperature furnace compatible with the oscillating radial collimator at BL02 has been under development in recent years. This furnace is designed to enable studies of solid-state ionic conductors, such as oxygen ion conductors, which require sample temperatures up to 1000°C that are unattainable with the standard GM cryostat. In June 2024, the first user experiment utilizing this furnace was successfully conducted, reaching a temperature of 860 °C.

In addition to the furnace development, a new superconducting magnet suitable for BL02 has been developed to broaden the scope of magnetism research. In 2024, the magnet successfully achieved its design specification of 3.5 T maximum magnetic field. Additionally, a dedicated oscillating radial collimator has been developed to minimize background scattering when using this magnet. Although efforts are ongoing to reduce the magnet's helium consumption, which is currently higher than desired, the system is expected to be available for user experiments in the 2026 experimental cycle.

[Radiation exposure reduction]

At DNA, the high neutron flux essential for efficient data collection causes significant radioactivation of samples and their containers, preventing immediate sample replacement after experiments and necessitating a waiting period for radiation levels to decay. To address this issue, an automatic sample changer was installed [3]. In 2024, the system was further enhanced with a second automatic sample exchange stick to improve data collection efficiency. Additionally, a mobile lead-glass window was introduced (Fig.1), which reduces gamma-ray exposure by approximately 20% and facilitates safer sample handling procedures.

[Aging problem]

The pulse-shaping chopper is a key component for high-resolution measurements at DNA, consisting of

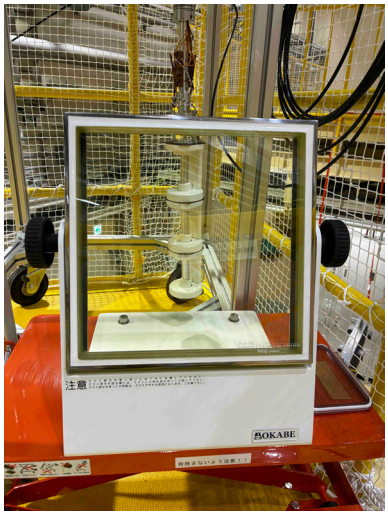

Figure 1. The lead-glass window through which the sample components of the elevating automatic sample changer are visible.

three high-speed choppers. On May 7, 2024, the resolver, that detects the phase, of the No. 3 high-speed chopper malfunctioned, rendering the high-resolution mode (ΔE~4 μeV) unavailable. While repair options were explored, experiments compatible with the high-flux mode (ΔE~15 μeV), which does not require the pulse-shaping chopper, were conducted. The resolver was replaced on May 22, 2024, and high-resolution mode operation was restored on June 5, 2024.

Additionally, following the target failure and subsequent shutdown on June 24, the resolver of the No. 1 chopper also malfunctioned on June 26. This resolver was replaced during the beam shutdown period. The original resolvers installed during construction are coil-based, and failures occur when the coils develop breaks. Replacement with coil-free resolver units is currently under consideration to improve the reliability of DNA experiments.

Since 2021, damaged Si(111) analyzer mirrors have been systematically replaced. The deterioration of these mirrors, including cracking and detachment from the aluminum base, was attributed to oxidation of the gadolinium back-coating used as a neutron absorber. To overcome this issue, Gd_2O_3 has been adopted as the neutron absorber in new Si(111) analyzers. In 2024, the damaged Si(111) analyzer mirror at bank #17, covering a scattering angle range of $-40.5° < 2\theta < -31.5°$, was successfully replaced with a Gd_2O_3-backcoated mirror. Additionally, a Gd_2O_3-backcoated mirror was newly installed at bank #18 (covering $-52.5° < 2\theta < -43.5°$) to enhance signal statistics in the lower Q region. Replacement of the remaining Gd-backcoated analyzer mirrors will continue in subsequent periods.

In 2023, deterioration of the ^{3}He position-sensitive detectors (PSDs) was observed, attributed to degradation of the CF_4 quench gas. Consequently, a new detector design without CF_4 quench gas was developed in 2024, and replacement of one of the existing PSDs was initiated. However, it was determined that the logic programmed into the field-programmable gate array (FPGA) of the NeuNET data processing board also required updating to accommodate the new detectors. The FPGA logic in the NeuNET board is currently being optimized, and the new PSD systems will be installed along with the updated NeuNET boards upon completion of this work.

[Other activities]

In December 2024, three students—two from the University of Tokyo and one from China—participated in the Neutron and Muon School 2024. During their training at BL02, they studied instrument design principles and performed quasi-elastic neutron scattering (QENS) analysis on water dynamics in Nafion®, utilizing data collected in the previous year.

4. Future Plans

We will continue to work on the development of sample environment and addressing aging problems. Furthermore, an oscillating pulse-shaping chopper is under development to improve data statistics and provide adjustable energy transfer ranges. Advanced analysis methods, including Bayesian estimation incorporating Poisson statistics, are also being developed.

References

[1] K. Shibata *et al.*, JPS Conference Proceedings. **8**, 036022 (2015).
[2] Y. Kawakita *et al.*, EPJ Web of Conferences. **272**, 02002 (2022).
[3] T. Tominaga *et al.*, JPS Conference Proceedings. **33**, 011095 (2021).

M. Matsuura[1], Y.Kawakita[2], T. Yamada[1], T. Tominaga[1], H. Tamatsukuri[2], K. Ohuchi[1], R. Murasaki[1], and H. Nakagawa[2,3]
[1]Neutron Science and Technology Center,CROSS; [2]Neutron Science Section, Materials and Life Science Division, J-PARC Center; [3]Materials Sciences Research Center, JAEA

Current Status of BL03 iBIX

1. Introduction

The IBARAKI Biological Crystal Diffractometer, iBIX, is one of the two diffractometers constructed by the Ibaraki Prefecture Government (iBIX and iMATERIA), and iBIX is installed at the BL03 beam port of the spallation neutron source of the Materials and Life Science Experimental Facility (MLF) of the Japan Proton Accelerator Research Complex (J-PARC) [1,2,3]. The following features of iBIX are designed for protein crystals, the chief target material, which posses large unit cell parameters and are fragile to gamma-ray irradiation: a curved arrangement of the neutron guide mirrors in order to prevent gamma-rays contamination in the direct beam and finely pixelized two-dimensional detectors of 0.52 mm pitch in x and y directions. iBIX has elucidated atomic positions of hydrogen nuclei in many crystals, and thereby has revealed hydrogen-bonding, protonation and hydration structures in biological macro-molecules, organic compounds and polymers [4].

iBIX participated in BINDS (Basis for Supporting Innovation Drug Discovery and Life Science Research) since FY2022 [5], and crystal structure analysis of protein crystals by neutron diffraction is receiving support from BINDS. FY2024 is the second year since the operation organization of iBIX and iMATERIA was transferred from Ibaraki University to the Neutron Industrial Application Promotion Center, CROSS. This article presents the current status of iBIX.

2. Development and maintenance

The current specification of iBIX is shown in Table 1.

Table 1. Specifications of iBIX

Moderator	Coupled
Wavelength of incident neutron	0.7~4.0 Å (1st frame) 4.0~8.0 Å (2nd frame)
Beam intensity Just before chopper Specimen position	 2.7×10^9 n/s/cm^2/MW 2.9×10^8 n/s/cm^2/MW
L_1	40 m
L_2	491 mm
Solid angle by a total of 34 detectors	20% for 4π
Diffraction angle 2θ	15.5~168.5 deg
Detection area per detector	133×133 mm^2
Pixel size of a detector	0.52×0.52 mm^2
Sample environment	Gas flow type cooling system (100~400 K for N_2) Heater system for polymers (300~600 K) Tensile loading system for polymers (0~200 N, 0~90 mm, 1~100 μm/sec)

[Motorized incident beam slit system]

Energy dispersive Laue diffraction at MLF using Time of Flight (ToF) method enables observation of the three-dimensional reciprocal space without rotation of the specimen. This is one of the superiorities against measurements with monochromatic x-rays. Although energy dispersive Laue diffraction is also achievable using white X-ray, energy resolution of X-ray detectors is limited to several percent. On the other hand, spallation neutron of 25 Hz at MLF, which corresponds to 40,000 μs of interval to the next injection, is measurable within ~1 μs of error.

The fine three-dimensional measurement of the reciprocal space by energy dispersive Laue diffraction at MLF promises the realization of nondestructive three-dimensional analysis with only two directions of pixelized irradiation data. Whereas the concept of this method will be reported in our future paper, this approach needs an incident beam slit enabling the pixelized scanning of the incident beam. Therefore, a motorized incident beam slit system was purchased and its control program and attachments to install the slit system on iBIX were developed.

A motorized cross slit screen (Huber, 3002.30M) was purchased, and the standard tungsten blades for X-rays were replaced with SUS304 blades which are customized to attach Cd plates (see Fig. 1). Each of the four blades is independently motorized and controlled by a four-channel stepper motor controller (TSUJICON, UPM4C-01). By replacing a standard collimator with the slit system, the motorized slit system can be installed easily (see Fig. 2). The customized blades, attachments to install the slit system to BL03, and the system controlling program were prepared by a BL03 operation team member TS.

Since the beamtime was severely limited in FY2024 due to hardware trouble at the upper stream near the mercury target, application of the slit system will be reported in FY2025.

[Repair of the cryogenic cooler]

The gas flow type cryogenic cooler system tabulated in Table 1 was purchased from Japan Thermal Engi-

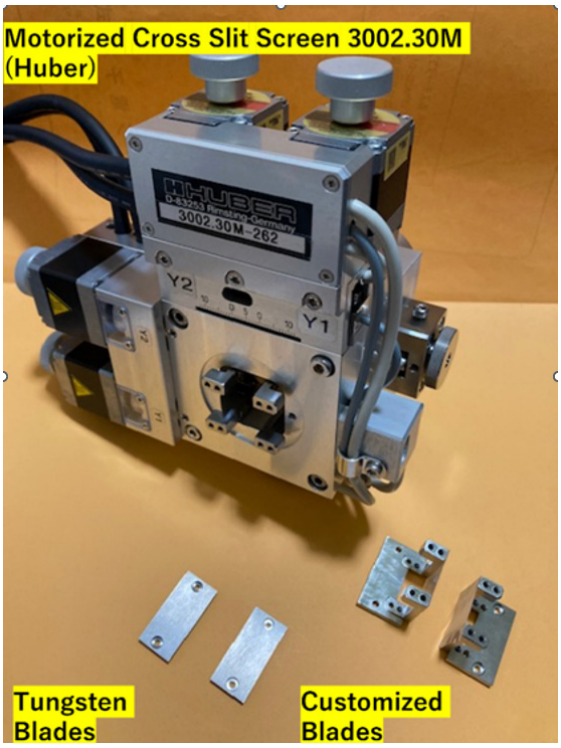

Figure 1. A Motorized Cross Slit Screen 3002.30M (Huber) and the two types of blades: the preinstalled tungsten blades for X-rays and the customized SUS304 blades to attach Cd plates for neutrons.

neering Co. Ltd. nearly 14 years ago. One of the constituents of the system, nitrogen gas supplier using pressure swing adsorption (PSA), went out of order in December. Since we had another stand-alone PSA type nitrogen gas supplier, we made an operation to bring the gas supplier under control of the system controller. The helium compressor of the cryogenic system was also overhauled in FY2024. Since the manufacturer of the cryogenic system went bankrupt in FY2023, we are also planning to upgrade and replace the controller system within one or two years.

T. Sakakura[1], H. Sugiyama[1], and K. Kusaka[1]
[1]*Neutron Industrial Application Promotion Center, CROSS*

Figure 2. The Motorized Cross Slit Screen 3002.30M (Huber) installed at iBIX.

3. Future Plans

Without losing the functions designed for protein crystallography, we are planning to develop and introduce new functions for polycrystals. As for maintenance, a controller of the cryogenic system is now under designment for future upgrades.

References

[1] I. Tanaka *et al.*, Nucl. Instrum. Methods Phys. Res. A **600**, 161-163 (2009).
[2] T. Hosoya *et al.*, Nucl. Instrum. Methods Phys. Res. A **600**, 217-219 (2009).
[3] T. Ohhara *et al.*, Nucl. Instrum. Methods Phys. Res. A **600**, 195-197 (2009).
[4] K. Kusaka *et al.*, J. Synchrotron Rad. **20**, 994 (2013).
[5] https://www.binds.jp/.

Implementation of an in-situ SEOP system at BL04, ANNRI

1. Introduction

The Accurate Neutron-Nucleus Reaction measurement Instrument (ANNRI) is installed at beamline No. 4 of the Materials and Life Science Experimental Facility (MLF) and was constructed for the purpose of measuring neutron-induced nuclear reactions. ANNRI is equipped with Ge, NaI, and $LaBr_3$ detectors for detecting gamma rays emitted from neutron capture reactions, as well as Li-glass detectors for neutron transmission measurements. Using these detectors, measurements of neutron capture cross sections, total cross sections, and elemental analyses—of critical importance in reactor design and radiation science—have been carried out [1,2,3]. More recently, measurements of angular correlations in nuclear reactions have also been conducted, aiming at studies of time-reversal symmetry violation using nuclear reactions [4,5].

With the growing diversity of users, there has been an emerging demand for experiments utilizing polarized neutrons. Therefore, in collaboration with the Spin Filter Team of the Technology Development Section, efforts have begun to introduce a ^{3}He spin filter [6] into ANNRI as a neutron polarization device. At first, ^{3}He gas was polarized by laser pumping (spin exchange optical pumping, SEOP) outside the beamline and subsequently transferred to the beamline for experiments (ex-situ operation). The installation of the spin filter enabled measurements of the spin dependence of angular correlations in neutron capture reactions [7,8] and determination of the spin states of excited nuclei through measurements of the circular polarization of the emitted gamma rays [9]. However, in the ex-situ operation, the polarization gradually decayed once the cell was introduced into the beamline, limiting the operation time to about two days before replacement of the cell was required.

2. The installation of the in-situ SEOP system

To enable the long-term and stable use of polarized neutrons, a new SEOP system capable of in-situ ^{3}He polarization directly on the beamline has been developed by the Spin Filter Team [10]. A new in-situ SEOP system derived from this design and optimized for ANNRI has been introduced on the beamline. Figure 1 shows a top view of the ANNRI beamline. The

Figure 2. The photograph after installing the in-situ SEOP system.

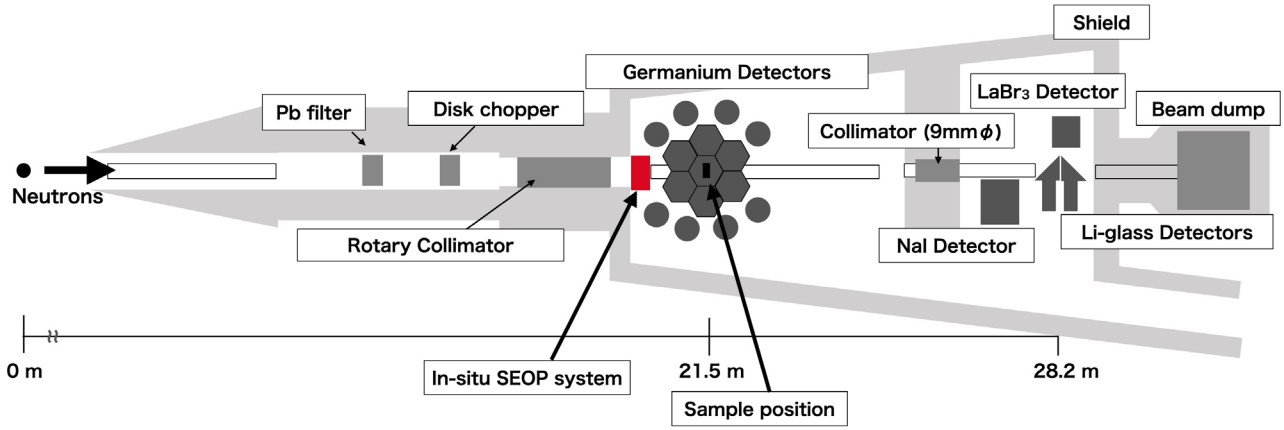

Figure 1. The top view of the ANNRI beamline.

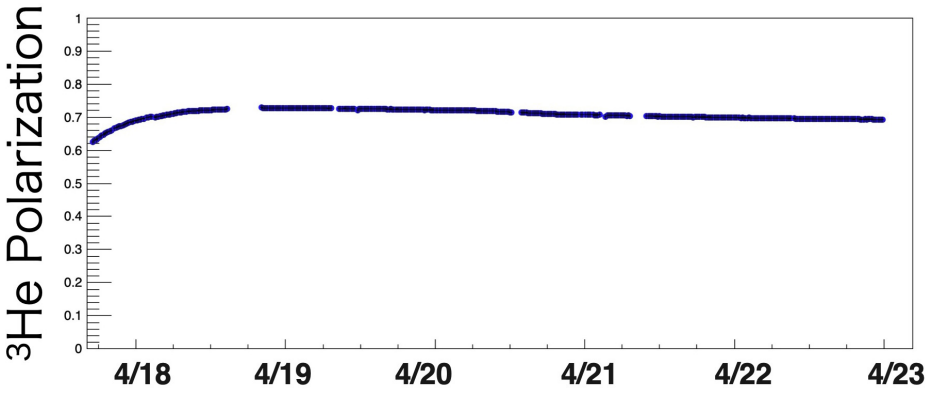

Figure 3. Time dependence of the ^{3}He polarization.

in-situ SEOP system was installed in the limited space between the rotary collimator and the array of Ge detectors. Figure 2 presents a photograph of the setup after installing the in-situ SEOP system. Guide coils were installed inside the duct connecting the SEOP box to the sample position located at the center of the Ge detector array, in order to maintain the neutron polarization during transport. This configuration enables measurements of nuclear reactions induced by polarized neutrons. Figure 3 shows the monitored ^{3}He polarization over time. The results demonstrate that a stable polarization can be maintained over extended periods.

3. Summary

Through collaboration with the Spin Filter Team, a new in-situ SEOP system has been successfully implemented at ANNRI, allowing for the stable use of polarized neutrons over extended periods. In the near future, it is expected that this setup will be actively utilized for nuclear physics experiments and nuclear data measurements. Furthermore, to enhance the neutron polarization, particularly for neutrons in the several eV energy region, development of ^{3}He cells with a larger effective gas thickness is currently in progress. These upgraded cells are planned to be installed in the beamline in subsequent stages.

References

[1] A. Kimura *et al.*, J. Nucl. Sci. Technol. **49**, 708 (2012).
[2] Y. Toh *et al.*, Annal. Chem. **93**, 9771 (2021).
[3] S. Endo *et al.*, Nucl. Sci. Eng. **198,** 786 (2024).
[4] T. Okudaira *et al.*, Phys. Rev. C **97**, 034622 (2018).
[5] J. Koga *et al.*, Phys. Rev. C **105**, 054615 (2022).
[6] T. Okudaira *et al.*, Nucl. Instrum. Methods Phys. Res. A **977**, 164301 (2020).
[7] T. Yamamoto *et al.*, Phys. Rev. C **105**, 039901 (2022).
[8] S. Endo *et al.*, Phys. Rev. C **105**, 039901 (2022).
[9] S. Endo *et al.*, Eur. Phys. J. A **59**, 288 (2023).
[10] S. Takahashi *et al.*, Nucl. Instrum. Methods Phys. Res. A **1075**, 170410 (2025).

S. Endo[1,2], S. Hayashi[3], S. Kawamura[3], A. Kimura[1,2], R. Kobayashi[4], T. Oku[4], T. Okudaira[3], M. Okuizumi[3], and S. Takada[4,5]
[1]Nuclear Data Center, JAEA; [2]Neutron Science Section, Materials and Life Science Division, J-PARC Center; [3]Department of Physics, Nagoya University; [4]Technology Development Section, Materials and Life Science Division, J-PARC Center; [5]Institute for Materials Research, Tohoku University

Status of Fundamental Physics Beamline BL05 (NOP) in 2024

1. Introduction

Neutron Optics and Physics (NOP/ BL05) at the MLF in J-PARC is a beamline for studies in the field of fundamental physics. The beamline is divided at the upstream into three branches, the so-called Polarized, Unpolarized, and Low-Divergence branches, used in different experiments in a parallel way [1,2].

Neutron lifetime measurements are conducted at the Polarized beam branch with a spin flip chopper. Pulsed ultra-cold neutrons (UCNs) by a Doppler shifter are available at the Unpolarized beam branch. At the Low-Divergence beam branch, the search for an unknown intermediate force is performed by measuring neutron scattering with nano particles. The beamline is also used for the R&D of optical elements and detectors.

2. Measurement of the neutron lifetime

The decay of neutrons is closely related to the mechanism of the synthesis of elements in the universe and to particle physics. The neutron lifetime has been measured in two ways: 1) by counting the incident neutrons and the protons from neutron beta decay (beam method) and 2) by storing UCNs in a container and determining the neutron lifetime according to the disappearing time (storage method). Currently, the lifetime determined via the former method is 888.0 ± 2.0 s, and that for the latter is 878.4 ± 0.5 s, with a difference of 9.5 s (4.6σ) [3]. This discrepancy is called the "neutron lifetime puzzle" and has remained unsolved for nearly 20 years. The smaller decays compared with the disappearance suggest that neutrons are lost owing to decay into dark matter or collisions with dark matter. In general, different methods are needed to validate the experimental results, as utilizing the same experimental methods may lead to the same mistakes. Using the polarization beam branch at NOP/BL05, an experiment was conducted via a different method, in which instead of protons, electrons were measured from the neutron beta decays. The first lifetime result was published in 2020 as $898 \pm 10\,(stat.)\,^{+15}_{-18}\,(syst.)$ s, which is consistent with both the beam and bottle methods [4]. A spin-flip chopper (SFC), which shapes the neutron beam into bunches, was replaced with a larger one in 2020, and the intensity was increased by 3 times [5]. Commissioning began in 2021, and physics run for the neutron lifetime began after the SFC was tuned. The higher intensity of the neutron beam after the SFC upgrade made it possible to achieve total statistics of 1.7 s. Analysis of the background estimation and the determination of efficiency are also in progress. After the evaluation of the systematic uncertainties is completed, we will publish the results in a paper.

The main source of systematic uncertainties is the undefined background. To address this, we are developing a new apparatus for measuring the neutron lifetime (LiNA experiment [6] shown in Fig. 1), where a solenoid magnetic field of approximately 0.6 T is applied to a time projection chamber (TPC) to effectively discriminate β-decay events from other electron events, significantly improving the signal-to-noise (S/N) ratio.

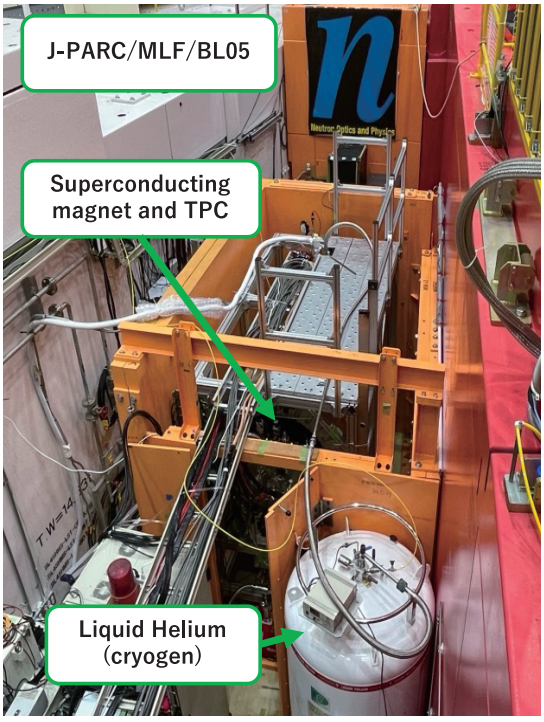

Figure 1. Photograph of the apparatus of the LiNA experiment set at the BL05 beamline.

Since 2020, a superconducting solenoid has been operational along the beamline, enhancing TPC performance as expected. We have installed and are commissioning the superconducting magnet. This approach not only enhances event identification but also reduces the measurement time by half, aiming for an uncertainty of 1 s because of the decreased environmental background.

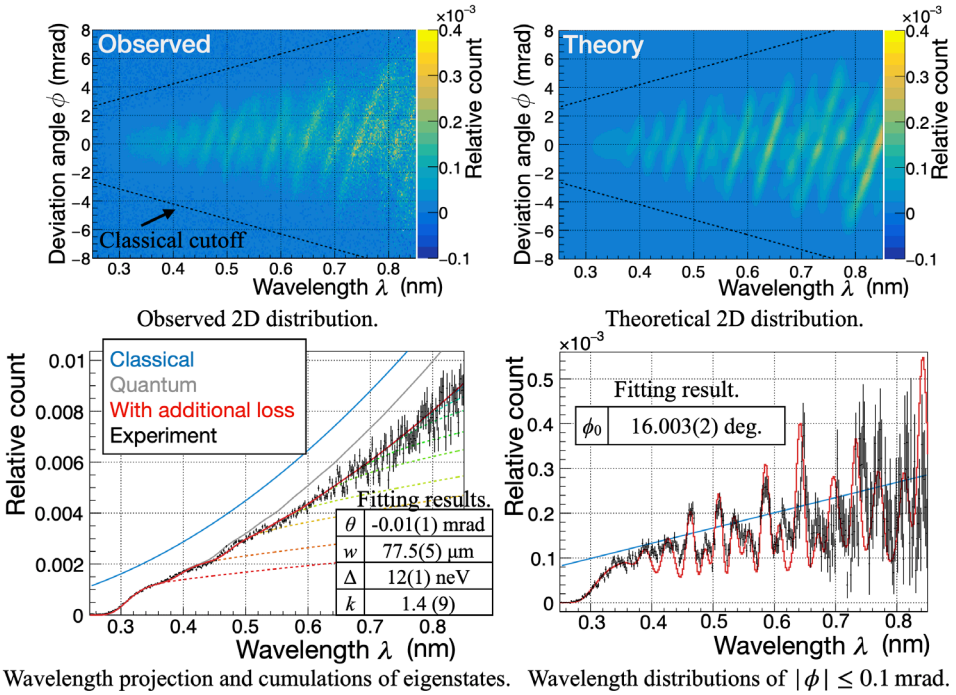

Figure 2. (Top Left and Right) Observed and theoretical distributions of neutron whispering gallery, respectively. (Bottom Left) Wavelength distribution of the neutron whispering gallery. The colored dashed lines illustrate the contribution of n ≤ 1, 2, … states to the red curve. The theoretical curves use best-fit parameters. (Bottom Right) Wavelength distributions with the deviation angle in −0.1 mrad ≤ ϕ < 0.1 mrad [8].

3. Measurement of neutron whispering gallery states using a pulsed neutron beam

When neutrons propagate while reflecting off a cylindrical potential barrier, they can take quantized states due to the centrifugal force. This phenomenon is called neutron whispering gallery [7]. For a neutron velocity of 1000 m/s and a curvature radius of 25 mm, the centrifugal acceleration reaches 4 x $10^6 g$, with a quantum state length scale of 40 nm. Precise measurements enable tests of the equivalence principle in quantum mechanics, quantum mechanics in non-inertial frames, surface potential characterization, and searches for short-range interactions.

We performed the neutron whispering gallery measurement at NOP/ BL05, which has 40 times neutron intensity compared to ILL (where previous experiments were performed). We successfully measured the neutron whispering gallery with a highly polished SiO_2 concave mirror [8]. The result of 5 hours exposure at the best incident condition is shown in Fig. 2. The observed and theoretical distributions are in good agreement with each other after we introduce an additional loss, which may be due to the surface waviness of the mirror. A 1.3 % discrepancy (in the angle span of the mirror measured by the mirror surface, the beam geometry, and the interference fringe fitting) exceeds uncertainties and is attributed to deviations in mirror edge shape. Fitting suggests an ideal sensitivity for the acceleration by centrifugal force as 10^{-4}.

References

[1] K. Mishima *et al.*, Nucl. Instrum. Methods Phys. Res. A **600**(1), 342-345 (2009).
[2] K. Mishima, Hamon **25**(2), 156-160 (2015).
[3] R.L. Workman *et al.* (Particle Data Group 2022), Prog. Theor. Exp. Phys. **2022**, 083C01 (2022).
[4] K. Hirota *et al.*, Prog. Theor. Exp. Phys. **2020**, 123C02 (2020).
[5] K. Mishima *et al.*, Prog. Theor. Exp. Phys. **2024**, 093G01 (2024).
[6] N. Sumi *et al.*, Nucl. Instrum. Methods Phys. Res. A **1045**, 167586 (2023).
[7] V.V. Nesvizhevsky *et al.*, Nat. Phys. **6**, 114 (2010).
[8] G. Ichikawa and K. Mishima, Phys. Rev. D **111**, 082008 (2025).

K. Mishima[1,2] and G. Ichikawa[2] on behalf of NOP collaboration
[1]*RCNP, Osaka University;* [2]*Institute of Materials Structure Science, KEK*

BL06: Commissioning Status of Village of Neutron Resonance Spin Echo Spectrometers (VIN ROSE)

1. Introduction

The neutron spin echo (NSE) technique represents a sophisticated variant of inelastic and quasi-elastic neutron spectroscopy [1]. A principal advantage of NSE is that its energy resolution remains intrinsically decoupled from the incident neutron energy spectrum; consequently, the method accommodates moderately monochromatic beams (typically 10–15% in $\Delta\lambda/\lambda$). Furthermore, because NSE directly yields intermediate scattering functions, it is exceptionally well-suited for investigating slow relaxation dynamics in condensed matter. Consequently, high-intensity, high-energy-resolution NSE spectrometers have been extensively developed and implemented [2].

Since 2011, Kyoto University and the High Energy Accelerator Research Organization (KEK) have engaged in a collaborative effort to construct beamline BL06. This facility integrates two different modalities of resonance neutron spin echo (NSE) spectrometry: a Modulated Intensity by Zero Effort (MIEZE) instrument and a Neutron Resonance Spin Echo (NRSE) instrument, achieved by bifurcating the beam via dual curved supermirror guide tubes [3]. The incorporation of neutron resonance spin flippers (RSFs) facilitated a significant reduction in the physical footprint of the apparatus, thereby permitting the contiguous installation of both spectrometers within the radiation shielding enclosure [4].

The user program at BL06 commenced partially utilizing the MIEZE spectrometer during the 2017B proposal cycle, whereas the high-resolution NRSE spectrometer remains in the commissioning phase and utilization of polarized neutron is partially possible [5].

This report presents the operational status at BL06 as of fiscal year 2024.

2. Commissioning status at BL06 in FY2024

While most of user programs were cancelled due to the neutron target malfunction in FY2024, the spectrometer's detection systems have been upgraded; specifically, the obsolete RPMT detectors [6] were replaced by a flat-panel photomultiplier tube (FP-PMT) system [7] employing a ^{6}Li-glass scintillator, thereby enabling the expansion of the detector array and improving measurement efficiency. The details of the detector system are described in the following section.

Some fundamental and preliminary experiments were conducted with the NRSE beamline, namely, developments of focusing super mirrors, neutron spin interference experiments, detector tests, etc.

3. Multidetector system for MIEZE

A Flat-panel and Resistor type PMT (FRP) system developed for a two-dimensional position-sensitive neutron detector was used at BL06. Flat-panel-type MA-PMT assembly (Hamamatsu Photonics K.K., H12700A-03) and enriched lithium 6 glass scintillators (Scintacor, G20) with 0.2 - 0.8 mm thickness were adopted as the FRP system. DAQ is performed by routing signals from these detectors through NeuNET and GateNET modules [8]. The NeuNET module has been upgraded by adopting FPGA device, where 4 FRP detectors can be connected to one board. 16 detectors have been currently prepared in operation.

4. Summary

In this report, the status of BL06 VIN ROSE in FY2024 were summarized. As the neutron source had some trouble, the utilization of the beamline was very limited, and we concentrated exclusively on the upgrade and optimization of the equipment without using neutron beam. We prepared the multidetector system for the MIEZE spectrometer, which will contribute significantly to the experimental efficiency.

References

[1] F. Mezei ed., Neutron Spin Echo, Lecture Notes in Physics (Springer, Berlin) **128**, (1982).
[2] B. Farago *et al.*, Neutron News **26**, 15 (2015).
[3] M. Hino *et al.*, J. Nucl. Sci. Tech. **54**, 1223 (2017).
[4] M. Hino *et al.*, Phys. Procedia. **136-141**, 136 (2013).
[5] https://mlfinfo.jp/en/bl06/
[6] K. Hirota *et al.*, Physica B **385**-**386** 1297 (2006).
[7] S. Satoh, Hamon **27**, 8 (2017).
[8] S. Satoh *et al.*, Nucl. Instrum. Methods Phys. Res. A **600**, 103(2009).

H. Endo[1,2], M. Hino[3], and T. Oda[4]
[1]Neutron Science Division, Institute of Materials Structure Science, KEK; [2]Neutron Science Section, Materials and Life Science Division, J-PARC Center; [3]Institute for Integrated Radiation and Nuclear Science, Kyoto University; [4]The Institute for Solid State Physics, The University of Tokyo

BL08: Status Report on SuperHRPD for 2024

1. Introduction

In FY 2024, the BL08 beamline experienced a long-term suspension of beam operation due to trouble with the MLF neutron source. As a result, only eight general proposals and part of the S-type project 2024S05 were carried out. The breakdown of general proposals was as follows: two room-temperature measurements, three low-temperature measurements, and three high-temperature measurements.

One of the high-temperature sample environments available at BL08 is the cryofurnace. During this fiscal year, we performed maintenance and improvements to enhance the high-temperature performance of the cryofurnace, as described in this report. In addition, we report on the preparation status for single-crystal measurements planned under the S-type project.

2. Improvement of Temperature-Control Accuracy of the Cryofurnace at High Temperature

The cryofurnace, fully implemented in SuperHRPD starting in FY 2021, provides a temperature range from 4.2 K to 800 K within a single sample environment [1,2].

In the initial implementation, temperature tracking of samples at high temperatures was unstable, indicating the need to optimize the temperature sensing system. The sensor originally used was a PT-103 platinum resistance thermometer manufactured by Lake Shore Cryotronics Inc., embedded in a hole within the heater block on the sample center stick. However, under high-temperature conditions, the sample chamber is maintained under vacuum, resulting in insufficient thermal contact between the embedded sensor and the heater block, which prevented accurate and prompt measurement of the sample temperature. To address this issue, we switched to a screw-mount PT-103-AM type sensor, which provides improved thermal contact with the heater block. This modification significantly enhanced the precision and responsiveness of temperature measurements.

Figure 1 shows the temperature variation of the lattice constant for the standard NIST silicon powder sample along with readings from each temperature sensor. The lattice constants were obtained by Rietveld refinement at each sensor temperature. The values from the PT-103-AM are closer to the reference curve than those from the PT-103. In addition, improved temperature tracking corresponding to heater output was observed during measurements, enabling stable and accurate temperature control under high-temperature conditions.

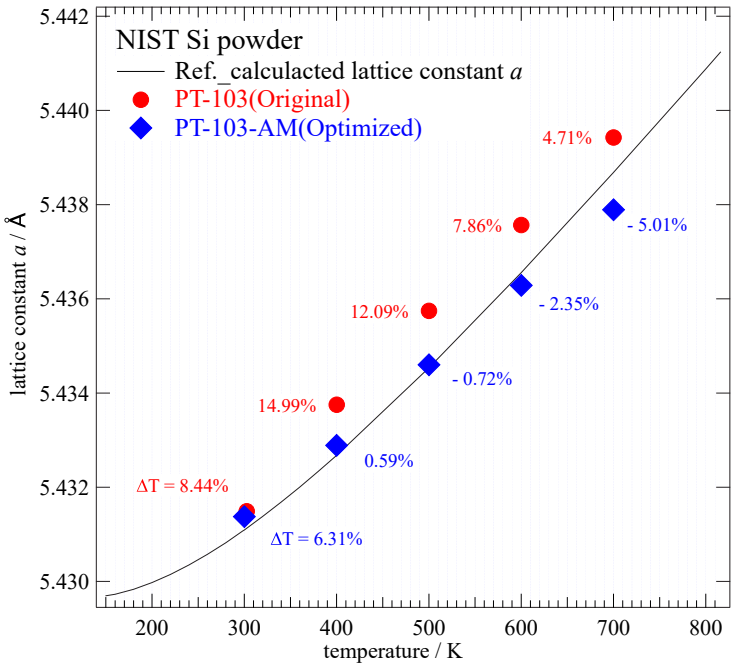

Figure 1. Relationship between lattice constants of standard samples and temperature sensor values. The optimized temperature sensor values (blue filled squares) are approaching the reference curve [3]. The value ΔT at each plot point represents the temperature difference from the lattice constant of the reference curve expressed as a percentage.

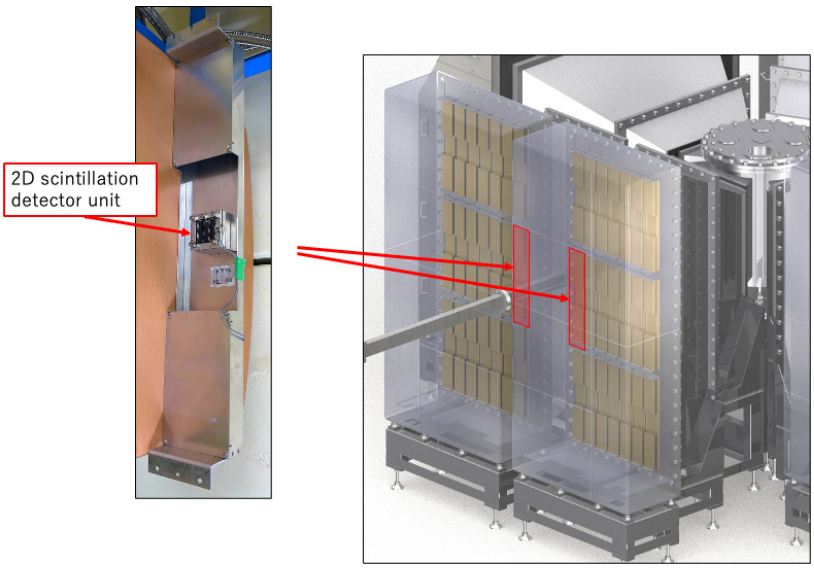

Figure 2. (Left) A scintillation detector unit installed in the detector frame. (Right) The area of the SuperHRPD's backward detector bank under consideration for replacement with scintillation detectors. One unit of the scintillation detector is a lithium glass-type two-dimensional detector with a detection area of 50 mm × 50 mm and a pixel size of 6 mm × 6 mm.

3. Preparation for Single-Crystal Measurements

As part of the S-type project, a new initiative has been launched to extend the super-high-resolution neutron diffraction technology developed for the SuperHRPD to single-crystal measurements. While this diffractometer has demonstrated outstanding performance in powder diffraction experiments, this new effort aims to further enhance its capability for the precise measurement of single-crystal diffraction peaks, which require higher angular resolution and detector accuracy.

To achieve this goal, part of SuperHRPD's backward detector bank will be replaced with a newly developed two-dimensional scintillation detector system (see Figure 2). This upgrade is expected to significantly improve spatial resolution and detection efficiency, enabling more accurate and detailed data collection for single-crystal studies.

As an initial step, a mounting frame for the scintillation detector units has been designed and fabricated. The frame has the same dimensions as the existing PSD detector box, ensuring compatibility and allowing easy installation in the SuperHRPD system. Currently, one scintillation detector unit has been completed. The basic performance of this detector will be verified in FY 2025, along with planned single-crystal diffraction measurements, to evaluate detector performance and confirm improvements in data precision.

In the next phase, we plan to replace the left and right maximum-angle detector boxes with detector frames that can accommodate scintillation units. We will then gradually increase the number of installed units. Through these efforts, this project aims to establish super-high-resolution single-crystal measurement capabilities using the SuperHRPD.

4. Summary

High-temperature conditions were established with the cryofurnace. Optimization of the temperature sensor improved both the accuracy of sensor readings and the actual sample temperature.

Furthermore, the scintillation counter for single crystals, planned for the S-type project, has been completed and is currently being adjusted and tested under beam operation.

References

[1] S. Torii *et al.*, MLF Annual Report 2020, 94-95 (2021).
[2] S. Torii *et al.*, MLF Annual Report 2021, 97-99 (2022).
[3] Y. Okada and Y. Tokumaru, J. Appl. Phys. **56**(2), 314-320 (1984).

S. Torii[1,2], G. Kitahara[1,2], S. Yamauchi[1,2], and K. Mori[1,2]
[1]*Neutron Science Section, Materials and Life Science Division, J-PARC Center;* [2]*Institute of Materials Structure Science, KEK*

Current Status of BL09 SPICA in FY2024

1. Introduction

The special environment powder diffractometer (SPICA) located at BL09 of J-PARC MLF (see Fig. 1) was founded by the New Energy and Industrial Technology Development Organization (NEDO), together with the High Energy Accelerator Research Organization (KEK) and Kyoto University. In the NEDO projects (i.e., RISING (FY2009 – 2015), RISING2 (FY2016 – 2020) [1], and RISING3 (in progress; FY2021 – 2025) [2]), SPICA is dedicated to structural investigations for the next-generation rechargeable batteries, as well as commercial lithium-ion batteries. SPICA was designed and developed to achieve a high resolution ($\Delta d/d$) of 0.08% with high intensity [3]. To realize the high $\Delta d/d$, SPICA has been situated at approximately 50 m from the neutron source system. SPICA focuses on neutron diffraction experiments under special environments, especially in charge-discharge operations (i.e., *operando* measurements). In addition, an annex building for SPICA (next to the 1st experimental hall of J-PARC MLF) was built to prepare samples for neutron diffraction experiments, assemble rechargeable batteries, and conduct their charge-discharge evaluations before and/or after *operando* measurements. Currently, SPICA is widely used in various experiments, particularly in the field of battery science [4–10].

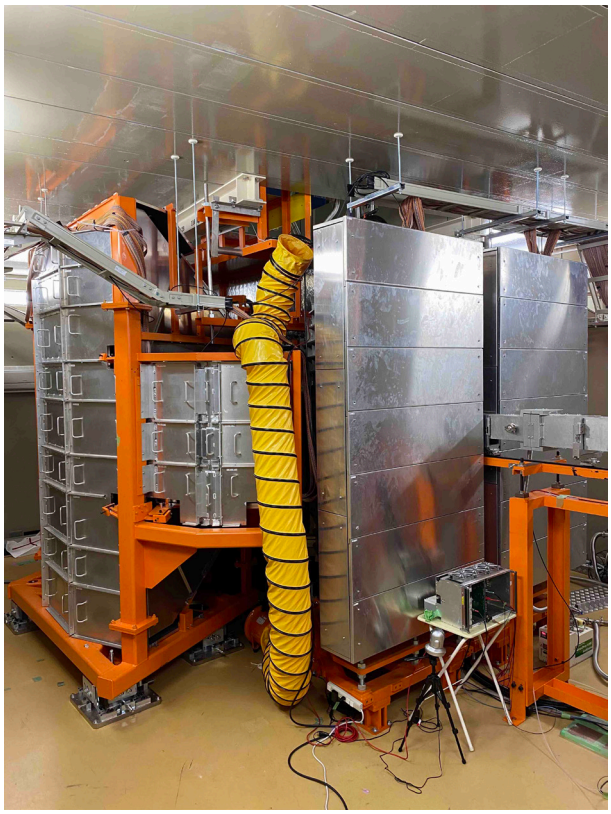

Figure 1. BL09 special environment powder diffractometer (SPICA).

2. Specifications of SPICA

SPICA was installed at BL09, which has the thin side of a decoupled poisoned moderator with the best time resolution (or the shortest pulse at full width in half maximum (FWHM) region) of all MLF moderators. The neutron intensity on the thin side is weaker than that on the thick side (i.e., BL18, 19, and 20 in the 2nd experimental hall); however, the thin side has the advantage of a symmetrical peak profile, which can be used to extract strain information in the samples. The primary flight path from the moderator to the sample position (L_1) is 52 m, and the secondary flight path from the sample position to the detectors (L_2) is approximately 2 m. An elliptical supermirror guide gradually changes the mirror coating from $m = 3$ to 6 toward the sample position, making it efficient to increase the number of neutrons at the sample position. SPICA utilizes 1568 ^{3}He gas-filled one-dimensional position- sensitive detectors (PSDs) with a diameter of 1/2 inch and an active length 0.60 m from a total of 0.67 m. The detector banks are formally grouped according to the scattering angle (2θ): backscattering bank ($150° \leq 2\theta \leq 175°$), high-angle multi-purpose bank ($120° \leq 2\theta \leq 150°$), 90-degree multi-purpose bank ($60° \leq 2\theta \leq 120°$), low-angle multi-purpose bank ($10° \leq 2\theta \leq 60°$), and small-angle bank ($5° \leq 2\theta \leq 15°$). In particular, the detectors in the multipurpose bank ($10° \leq 2\theta \leq 150°$) have been placed continually on a cylindrical locus approximately 2 m from the sample position. The $\Delta d/d$ value was evaluated for each bank: $\Delta d/d = 0.12\%$ for the backscattering bank, $\Delta d/d = 0.47\%$ for the 90-degree multi-purpose bank, and $\Delta d/d = 1.27\%$ for the low-angle multipurpose bank. The chopper rotated at a frequency of 25 Hz, which was the same as the repetition rate of the proton beam injection. The natural bandwidth of the SPICA is 2.9 Å. Three single-disc choppers were used for bandwidth selection to prevent frame overlapping and operated at 6.25 Hz to 25 Hz repetition to select bandwidths.

3. Relocation of the ^{3}He-gas neutron monitor

Relocation of the ^{3}He-gas neutron monitor was conducted during the summer. In Fig. 2(a), the ^{3}He-gas neutron monitor had been placed between the four-quadrant slits in the concrete blocks. The ^{3}He-gas

(a)

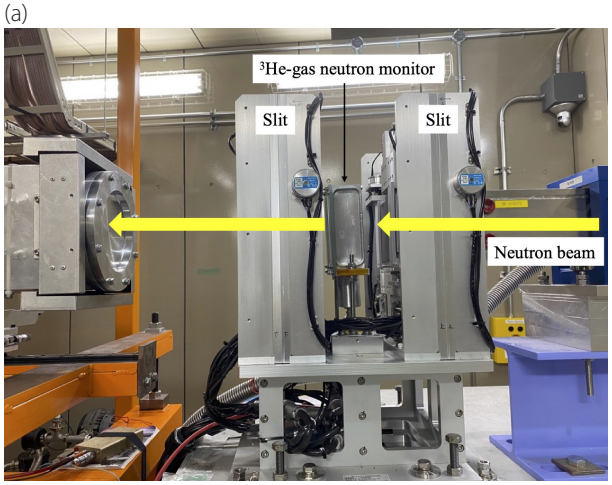

(b)

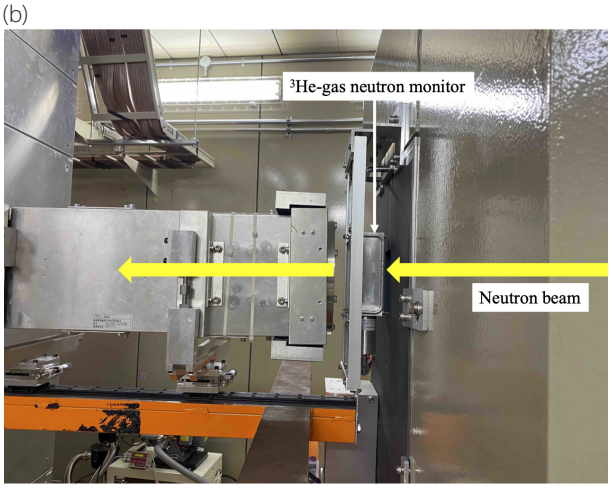

Figure 2. Relocation of the ^{3}He-gas neutron monitor: (a) before and (b) after installation.

neutron monitor was replaced from inside to outside of the concrete blocks, as shown in Fig. 2(b). We have confirmed to be able to measure monitor spectra at the current position.

References

[1] https://www.rising.saci.kyoto-u.ac.jp/rising2/
[2] https://www.rising.saci.kyoto-u.ac.jp/en/
[3] M. Yonemura *et al.*, J. Phys. Conf. Ser. **502**, 012053 (2014).
[4] Y. Kato *et al.*, Nat. Energy. **1**, 16030 (2016).
[5] S. Taminato *et al.*, Sci. Rep. **6**, 28843 (2016).
[6] K. Mori *et al.*, ACS Appl. Energy Mater. **3**, 2873 (2020).
[7] K. Mori *et al.*, ACS Appl. Energy Mater. **7**, 7787 (2024).
[8] F. Takeiri *et al.*, Nat. Mater. **21**, 325 (2022).
[9] K. Kino *et al.*, Appl. Phys. Express. **15**, 027005 (2022).
[10] Y. Izumi *et al.*, Adv. Energy Mater. **13**, 2301993 (2023).

K. Mori[1,2,3], K. Namba[1], F. Song[1,2], T. Kawamura[3], S. Song[1,2], T. Saito[1,2], and S. Torii[1,2]
[1]Institute of Materials Structure Science, KEK; [2]Neutron Science Section, Materials and Life Science Division, J-PARC Center; [3]The Graduate University for Advanced Studies (SOKENDAI)

BL10: NOBORU

1. Introduction

We continue to study a temporal change in neutronic performance for long-term stable neutron source operation under increasing proton beam power up to 1 MW. This year, stable operation at a beam power of approximately 940 kW was kept until late June; however, subsequent problems in the neutron source led to the cancellation of the remaining scheduled user programs for the year. At NOBORU, nine general-use proposals, one long-term proposal and two project-use proposals were carried out.

This year, in addition to the routine fixed-point observations, we conducted test diffraction experiments at 90° and 170° detector banks using a B_4C collimator (with 1 mm wide × 5 mm high aperture) placed 30 mm away in front of the sample. Using this incident beam collimator and a 1 mm gauge-length radial collimator for the 90° detector bank, we measured several Japanese sword samples by neutron diffraction. We also measured the same samples by neutron diffraction using the same incident beam collimator and a coarse collimator for the backward detector bank.

2. Experiment

We measured four cut pieces of Japanese swords: Hiromasa-1, Hiromasa-2, Yoshiie, and Yoshihira, from left to right in Fig. 1(a). Their cutting edges were secured on a cadmium plate with aluminum tape. For each sample, diffraction data was obtained at five locations with 1 mm intervals as shown in Fig. 1(a).

The instrument parameters for converting the measured time-of-flight (*TOF*) to *d*-spacing, as well as the initial parameters for the profile function, were determined using silicon powder diffraction data analyzed with Z-Rietveld software (ver. 1.1.4). In the Rietveld refinement of the pearlite phase of the swords, a two-phase analysis was conducted using cubic α-iron and cementite (Fe_3C). The composition of cementite was assumed to be stoichiometric, and initial structural parameters were referred to the values given in literature [1].

3. Results

Figure 2 shows the enlarged Rietveld refinement patterns for the 90° (a) and 170° (b) diffraction data of the second region from the left of Hiromasa-1. While the measurements were intended to be taken from the same location, the gauge volumes differ between each measurement, as illustrated in Fig. 1. Despite the better resolution and statistics of the backward diffraction data, the diffuse sample background results in a little worse fit for the cementite phase. Table 1 summarizes the reliable factors, goodness of fit, and mass ratio of the cementite phase. The resultant mass% of the car-

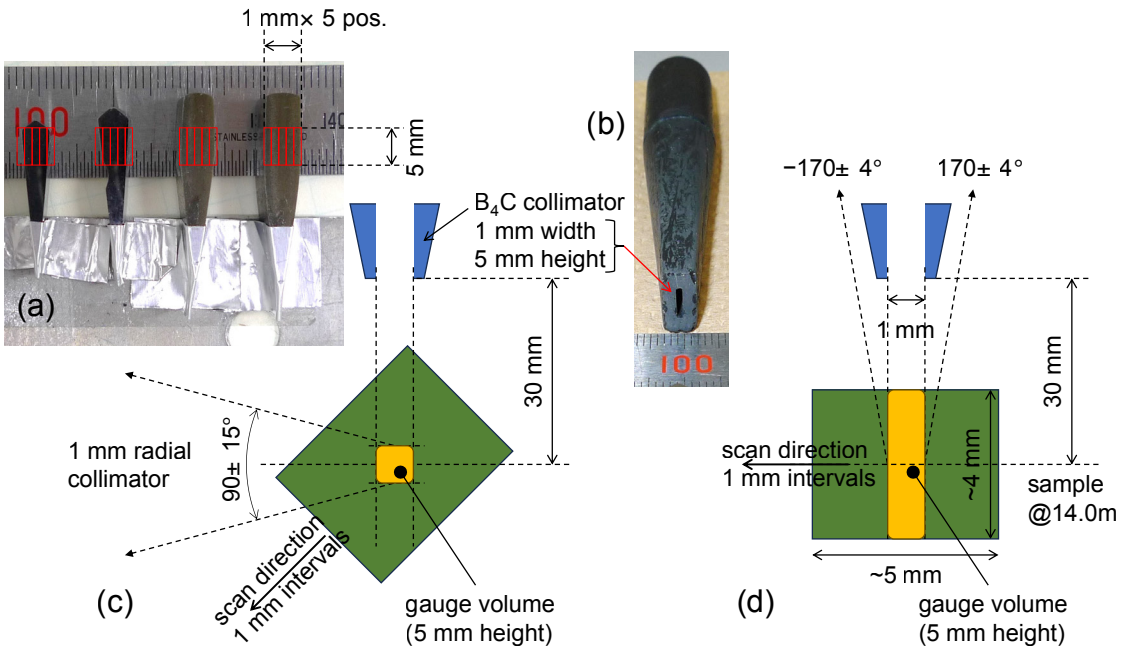

Figure 1. (a) Cut pieces of the Japanese sword. (b) B_4C collimator. Schematic top view of the 90° (c) and 170° (d) diffraction experiments.

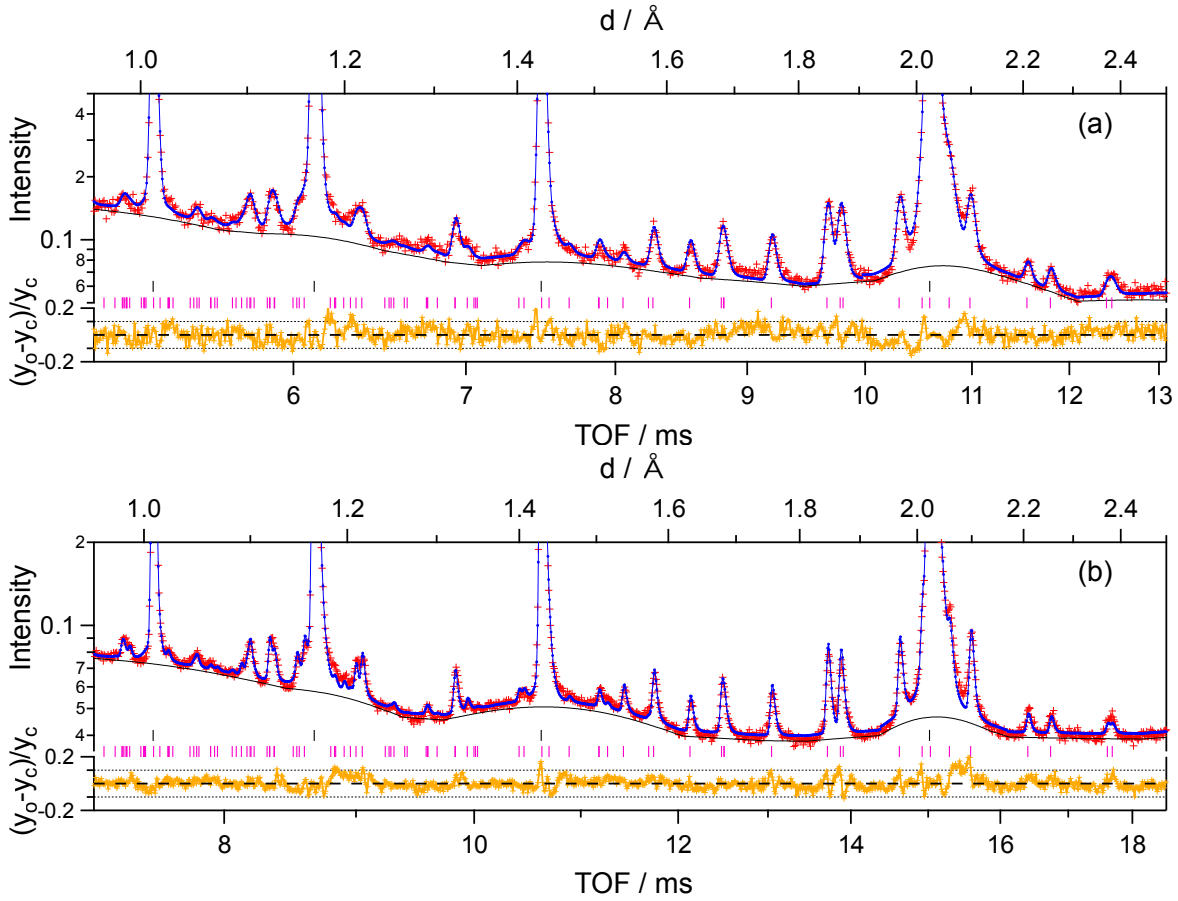

Figure 2. Enlarged Rietveld refinement pattern of the 90° (a) and 170° (b) diffraction data. The black and pink vertical tick marks indicate the Bragg peak positions of α-iron and cementite, respectively.

Table 1. Reliable factors (R_{wp} and R_B), goodness of fit (S^2), mass ratio, and resultant mass% of C of the second position of Hiromasa-1.

Det. angle, beam power × time	R_{wp} (%)	R_B of Fe_3C (%)	S^2	mass ratio of Fe_3C	mass% of C
90°, 1700 kWh	4.2822	15.5921	2.6058	0.0695(16)	0.465(10)
170°, 940 kWh	3.8505	15.7927	4.9051	0.0619(6)	0.414(4)

bon content at the position 2 of Hiromasa-1 is ca. 0.47 % and 0.41 % for the 90° and 170° diffraction experiments, respectively. At the targeted surface position in these diffraction data, the Electron Probe Micro Analyzer map shows approximately 0.4 mass% carbon. Thus, the carbon content estimated from the 90° data analysis appears to be slightly overestimated. We are currently advancing analyses of other measurement data positions in both diffraction experiments.

4. Conclusion

We plan to improve the accuracy of carbon content estimation in steel by systematically collecting and analyzing neutron diffraction data using Japanese sword test pieces with known carbon contents.

References

[1] I. G. Wood *et al.*, J. Appl. Cryst. **37**, 82-90 (2004).

K. Oikawa[1]
[1]*Neutron Science Section, Materials and Life Science Division, J-PARC Center*

Developments at BL11 PLANET

1. Modifying the vacuum chamber of Mito system

In PLANET, radial collimators are routinely used to remove unwanted Bragg peaks from sample surrounding materials, such as a heater and anvils[1]. This is essential for accurate structural analysis of crystals and, in particular, liquids. To date, three pairs of radial collimators with diffraction gauge length of 3.0 mm, 1.1 mm, and 0.5 mm have been manufactured [2]. In actual experiments, one of them is used, depending on the sample size. However, in the experiments using a low-temperature and high-pressure press "Mito System"[3], only the radial collimators with a gauge length of 3.0 mm are available because the vacuum chamber of the Mito system interferes with the radial collimators with other diffraction gauge lengths. This causes a big problem when collecting the data at pressures above 5 GPa where sintered double toroidal anvils with a smaller sample size are employed. To resolve this issue, the side panels of the vacuum chamber of the Mito system were reworked to reduce the width of the vacuum chamber. (Figure 1).

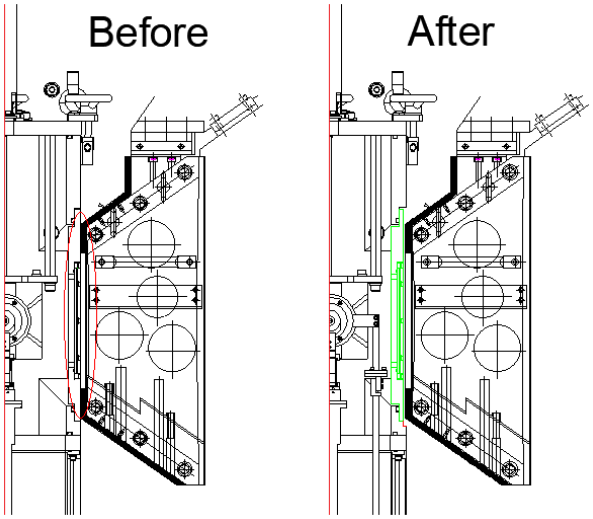

Figure 1. Vacuum chamber of Mito system before (Left) and after the modification (Right).

Besides this modification, the vacuum chamber of Mito system underwent an overhaul to remove contamination caused when a radioactive sample was blown out during a previous experiment. After cleaning, the chamber was assembled and its cooling performance was tested. The temperature change during cooling is shown in Figure 2. The results indicate that the cooling

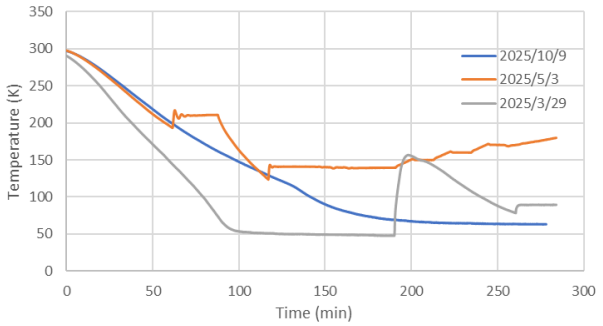

Figure 2. Comparison of cooling history (Blue: this study, Orange and gray: previous studies). The abrupt temperature increases observed at multiple locations in past experiments were attributed to temperature control by a heater to maintain the constant temperature for diffraction experiments.

performance after overhaul was essentially equivalent to that during the previous operation on May 3, at least within the temperature range down to 200 K. On the other hand, it differs from that of March 29. It is known that the cooling rate strongly depends on the applied pressure because the thermal conduction from the cold finger becomes more efficient when the sample (& gasket) is in close contact with the anvil. For a detailed comparison, another test using a compressed sample is required.

2. PDF analysis of crystals under high pressures

To date, procedures and software for analyzing the pair distribution function (PDF) of liquids under high pressure have been developed and routine analysis is now possible at PLANET.

In recent years, demands for PDF analysis of crystalline materials have been increasing because the PDF analysis can reveal subtle shifts in atomic positions and the resulting violation of the crystalline symmetry that cannot be detected by standard Rietveld analysis. However, applying PDF analysis to crystalline materials is not straightforward because the crystalline samples are always compressed with a liquid pressure transmission medium (PTM) to avoid Bragg peak broadening and the scattering from the PTM is superimposed on the sample data.

The intensity profiles of a PTM (4:1 deuterated methanol ethanol mixture) were collected at the same pressures as the sample measurements and subtracted from the sample data by multiplying a correction factor, taking the difference in the amount of PTM in

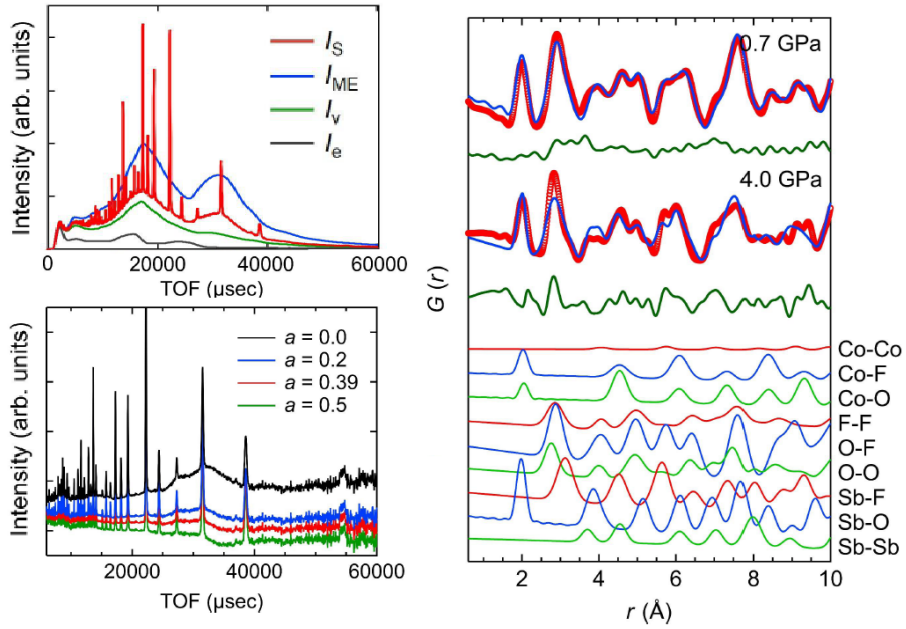

Figure 3. (Left upper) Raw data of a sample, an empty cell, a PTM, and a vanadium pellet. (Left lower) PTM fraction dependence of normalized sample intensity. (Right upper) Comparison of the observed $G(r)$ with that simulated assuming cubic symmetry. Red: experiment, Blue: simulation, Green: the difference. (Right lower) Pair correlation of each atom in the simulated $G(r)$. (Courtesy of Dr. Shimono)

the sample chamber into account. The normalized sample intensity was obtained by the equation,

$$i = \frac{(I_{Sample} - I_{Empty}) - a(I_{ME} - I_{Empty})}{I_{Vanadium} - I_{Empty}}.$$

Here, I_{Sample}, I_{Empty}, I_{ME}, and $I_{Vanadium}$ represents the observed intensities in the measurements of the sample, an empty cell, a PTM, a vanadium pellet, respectively. a is the factor related to the amount of PTM in the sample chamber. The representative results on a mixed anion compound, $Co_3Sb_4O_6F_6$ are shown in Figure 3[4]. The scattering from the PTM is successfully subtracted and $G(r)$ of the sample was obtained. The $G(r)$ obtained by this methods is well reproduced by that simulated assuming the cubic symmetry previously reported for the crystal[5].

References

[1] T. Hattori *et al.*, Nucl. Instrum. Methods Phys. Res. A **780**, 55 (2015).
[2] T. Hattori *et al.*, Nucl. Instrum. Methods Phys. Res. A **1059**, 168956 (2024).
[3] K. Komatsu *et al.*, High Press. Res. **33**, 208 (2013).
[4] S. Shimono *et al.*, (in prep.)
[5] S. Paul *et al.*, J. Mol. Struct. **1321**, 140006 (2025).

T. Hattori[1], A. Sano-Furukawa[1], S. Machida[2], J. Abe[2], Y. Sakai[2], and N. Okazaki[2]
[1]Neutron Science Section, Materials and Life Science Division, J-PARC Center; [2]Neutron Science and Technology Center, CROSS

High Resolution Chopper Spectrometer HRC

1. Introduction

The High Resolution Chopper Spectrometer (HRC) is being operated at BL12 in the MLF under the S-type project of IMSS, KEK, and the IRT project of ISSP, the University of Tokyo, to study dynamics in condensed matter. The activities of the HRC project in FY2024 are summarized in this report.

2. Instrumentation

There have been significant developments concerning the detectors. One development involved recovering the ^{3}He gas from previously broken detectors and purchasing eight new detectors. The second development was a change in the detector arrangement for the small-angle bank as shown in Fig. 1. Previously, the small-angle bank detectors for the HRC were arranged in two rows to prioritize detection efficiency, but this only covered a limited angle of 0.6° to 5.1°. Following an evaluation of the detection efficiency, the arrangement was changed to a single row. This new configuration now covers a scattering angle of 0.6° to 10° and makes it possible to explore the first Brillouin zone of typical materials at an incident energy E_i = 100 meV. Accompanying this change, a new incident collimator was created. Since the background noise has a significant impact in the low angle scattering range, a collimator with a narrower slit width is required. The conventional cadmium collimator had a hardness issue that necessitated a long collimator, which in turn restricted the cryostats that could be used. Therefore, a new gadolinium collimator was created to be compatible with all cryostats.

There has also been progress concerning the T0 chopper. The T0 chopper control system was designed over 15 years ago and had two problems: the program was complex, and components were difficult to obtain. To address this, a new control board was created in the FY2024. The plan is to develop the program over the next 2-3 years and then replace the old board once the new program is complete. The T0 chopper itself was also replaced. At HRC, the two T0 choppers are regularly swapped and maintained. This was the fourth replacement, and the blade surface, which receives the beam, showed advanced activation, measuring a dose of 530 μSv/h.

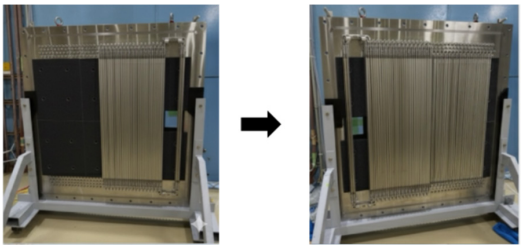

Figure 1. Modification of Detector Arrangement.

In the computing environment, two new functions have been implemented in the control program YUI and the analysis program HANA. When venting the vacuum chamber of HRC, it takes 20 minutes to start the dryer for compressed air. Previously, this operation was performed manually on-site, but remote and sequential operation functions of the dryer have now been added to YUI, improving the efficiency of sample changes. Furthermore, the NXSPE format is now available as an additional intensity histogram file.

3. Scientific Results

The magnetic structure of the helical magnet $GdRu_2Ge_2$ was successfully analyzed using high-energy, high-resolution neutron scattering, which led to the discovery of multiple topological magnetic orders, including magnetic skyrmions [1]. Analyzing magnetic structures in Gd compounds is typically challenging due to extremely large neutron absorption cross section of Gd. However, we exploited the fact that Gd absorption drops sharply when the neutron incident energy exceeds approximately 100 meV, and performed high-energy neutron scattering measurements at 150-200 meV. By combining this comprehensive neutron data with polarization analysis from resonant X-ray scattering, we identified that the magnetic phases, which change under an external magnetic field, are multiple magnetic skyrmion lattices of different symmetries, as well as a new magnetic order called the meron-antimeron lattice, characterized by a half-integer topological number.

The ground state of Ce_5Si_3, which is expected to exhibit geometric frustration due to the formation of Shastry-Sutherland lattice (SSL), was investigated. Previous heat capacity measurements suggested a spin dimer ground state for the Ce2 site. By inelastic neutron scattering(INS) experiments, there observed four crystalline electric field (CEF) excitations, determining the CEF levels for both Ce1 and Ce2 sites [2]. The magnetic moment of the Ce2 site was found to lie in the in-plane direction. Crucially, low-energy magnetic excitation with dispersion was observed around 0.6 meV at 0.3 K, due to the spin dimer formation. The

dispersion could not be explained by the conventional SSL model, possibly indicating unique features of SSL in 4f-electron systems. This suggests a possible splitting of the excited pseudo-triplet state due to the Ce1 site internal field or inter-layer interaction, which warrants further investigation.

The magnetism of the spin-1/2 pyrochlore antiferromagnet $Na_3Co(CO_3)_2Cl$ was investigated using multiple experimental techniques, including synchrotron X-ray diffraction and INS. Frustrated antiferromagnets like pyrochlores, where magnetic interactions conflict, are expected to exhibit peculiar magnetic states rather than conventional magnetic order upon cooling. The INS experiment observed two prominent CEF excitations at 34.6 and 44.8 meV [3]. Multiple experimental results confirmed that at low temperatures, the Co^{2+} ions possess a pseudo spin-1/2 degree of freedom with uniaxial anisotropy in their ground state. Advancing research on Co^{2+} containing pyrochlores like this compound is expected to experimentally elucidate the ground state of spin-1/2 pyrochlore antiferromagnets.

The magnetic structure and excitations of the two-dimensional triangular-lattice Heisenberg antiferromagnets *h*-(Lu,Y)MnO_3 and *h*-(Lu,Sc)FeO_3, which are known for spin-reorientation and multiferroic properties were investigated. Using neutron diffraction and INS, it was confirmed that two irreducible representations are necessary to accurately describe their magnetic structures. The spin wave dispersions were analyzed to derive the spin Hamiltonian. As shown in Fig. 2, *h*-$Lu_{0.47}Sc_{0.53}FeO_3$ showed flat dispersion along the c-axis, whereas *h*-$Lu_{0.3}Y_{0.7}MnO_3$ displayed clear c-axis dispersion, suggesting interlayer interaction in the latter [4]. Critically, the study showed spin reorientation can occur even in *h*-$Lu_{0.47}Sc_{0.53}FeO_3$ without interlayer coupling, challenging conventional understanding. Furthermore, the multiferroic mechanisms were found to differ, despite similar structures.

An INS study was performed on the Néel-type skyrmion host GaV_4Se_8. This material exhibits a structural transition at T_s = 4 K and a cycloidal spin structure below T_c = 18 K, where a triangular skyrmion lattice (SkL) is stabilized by a critical field. The INS experiment observed a spin wave excitation band energy of 8 meV

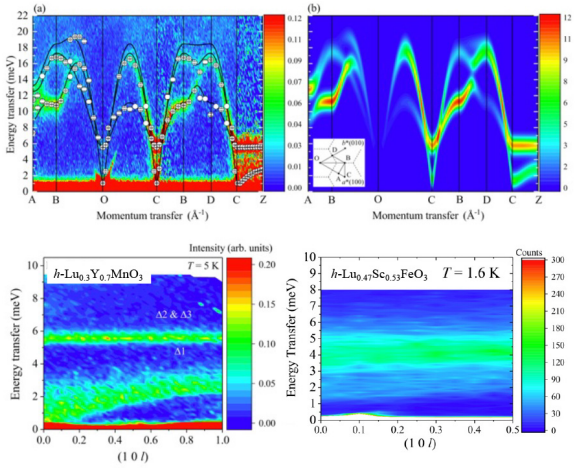

Figure 2. (a) Spin-wave dispersion relation of the *h*-$Lu_{0.3}Y_{0.7}MnO_3$. The lines are obtained by fitting. (b) Calculation of the dynamical structure factor using linear spin-wave theory [4]. (c) Spin wave dispersion of *h*-$Lu_{0.3}Y_{0.7}MnO_3$(left) and *h*-$Lu_{0.47}Sc_{0.53}FeO_3$(right) along the interplane direction.

[5]. This was approximated using an isotropic Heisenberg spin Hamiltonian and linear spin-wave theory, considering a V_4 molecular form factor. Compared to GaV_4S_8, GaV_4Se_8 shows a stronger isotropic interaction and negligible single-ion anisotropy, consistent with theoretical calculations. This suggests an enlarged SkL temperature regime, with the SkL's high critical fields attributed to the small single-ion anisotropy and strong Dzyaloshinskii-Moriya interactions.

A study by INS on single crystals of the altermagnetic candidate MnTe successfully observed the theoretically predicted altermagnetic magnon bands [6]. The details are covered in the Research and Development Highlights section of this report, under the title: "Experimental Verification of Altermagnet by Inelastic Neutron Scattering Technique."

References

[1] H. Yoshimochi *et al.*, Nat. Phys. **20**, 1001 (2024).
[2] D. Ueta *et al.*, Phys. Rev. B. **109**, 205127 (2024).
[3] K. Nawa *et al.*, J. Phys.: Condens. Matter. **36**, 495801 (2024).
[4] S. Yano *et al.*, Phys. Rev. B. **110**, 134444 (2024).
[5] Z. Liu *et al.*, J. Phys. Soc. Jpn. **93**, 124707 (2024).
[6] Z. Liu *et al.*, Phys. Rev. Lett. **133**, 156702 (2024).

D. Ueta[1,2], T. Masuda[3,2], S. Itoh[1,2], T. Nakajima[3], T. Yokoo[1,2], K. Ikeuchi[1,2], S. Asai[3], H. Saito[3], S. Yano[4], H. Kikuchi[3] D. Kawana[3], R. Sugiura[3], T. Asami[3], Z. Liu[3], S. Yamauchi[1,2], T. Seya[1,2], H. Ohshita[1,2], N. Yabe[5], and H. Tanino[3]
[1]*Neutron Science Section, Materials and Life Science Division, J-PARC Center;* [2] *Institute of Materials Structure Science, KEK;* [3]*The Institute for Solid State Physics, The University of Tokyo;* [4]*National Synchrotron Radiation Research Center;*[5] *Technology Development Section, Materials and Life Science Division, J-PARC Center*

BL14: AMATERAS

1. Introduction

AMATERAS is a cold-neutron disk-chopper spectrometer designed to study the dynamical properties of atomic, molecular, and magnetic systems in the cold to sub-thermal energy range, with high efficiency and flexible resolution [1, 2]. In recent years, high competition rate has become one of our major issues. To address this by improving the efficiency of experiments, the instrument group has promoted upgrades and automations of various components. In FY2024, we conducted commissioning of the top-loading ^{3}He cryofurnace and improved the background in the low- scattering-angle region. One of the instrument group members, S. O.-Kawamura, was seconded to MEXT in July 2024 and is scheduled to return in July 2025. Furthermore, another member, M. Kofu, moved to The Institute for Solid State Physics, University of Tokyo in January 2025, and has partly continued to work as a BL14 member after the transfer.

2. User program

In the 2024A round, 34 general proposals (short-term) were submitted to AMATERAS, and nine of them were approved. 11 general proposals including one long-term proposal and one project proposal were carried out in this round from April to June 2024. However, one approved general proposal could not be performed due to the interruption of beam operation at the end of June. In the 2024B round, we accepted four general proposals from 35 submitted proposals. The number of the accepted proposals is smaller than in usual rounds because of a temporary shortage of manpower. These experiments were carried over to the next round due to issues related to the neutron source. In FY2024, 67% of the general proposals performed were in the field of magnetism. Nine peer-reviewed papers were published during this fiscal year.

3. Instrument upgrades

At AMATERAS, users from a wide range of research fields require various sample environments for their experiments, such as a simple closed-cycle refrigerator (CCR), ^{3}He cryostat, dilution refrigerator, magnet, and so on. To reduce both the time to replace sample environments and the workload of beamline staffs, we purchased a top-loading ^{3}He cryofurnace in 2022 and have continued its commissioning and improvement since then. This cryofurnace is a cryogen-free system equipped with a pulse-tube cryocooler and a one-shot ^{3}He cooling system. We adopted a top-loading design, so-called load-lock system, and aim to cover a wide temperature range from 0.3 K to approximately 800 K by using low-temperature, middle-temperature and high-temperature sample sticks.

To evaluate its performance under actual beamline conditions, we conducted comprehensive commissioning with the ^{3}He cooling system of the cryofurnace, including a full cooling cycle, assessment of the lowest achievable temperature, holding-time measurement, and establishment of the sample exchange procedures for this load-lock system, by installing the cryofurnace on the vacuum scattering chamber of AMATERAS. The system reliably reaches approximately 0.3 K, which is consistent with the lowest temperature for typical one-shot ^{3}He cryostats, and maintains this temperature for about two days. Due to the characteristics of the dry-type ^{3}He cryostats, it takes a long time to cool the ^{3}He stage, where the sample is mounted, from relatively high temperature ($T \geq 80$ K) to the low temperature region, including initial cooling. It takes roughly one and a half days to cool from room temperature to the lowest temperature (Fig. 1). We will consider this issue for the efficient use of users' beamtime. This cryofurnace is equipped with a goniometer stage that allows rotation of the entire cryofurnace. We performed rotation measurement tests using the cryofurnace mounted on this goniometer stage as part of the commission-

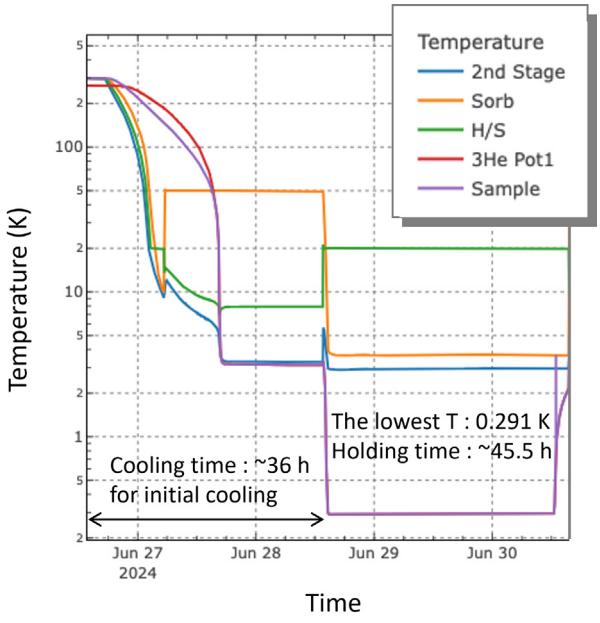

Figure 1. Example of the cooling test on the ^{3}He cryofurnace.

ing process. We plan to introduce this system for users' experiments while continuing further upgrades.

We have taken background-reduction measures on AMATERAS. Although most background originating from the sample environment, the vacuum scattering chamber, and other components had already been reduced, residual background remained near the direct-beam region, which was especially enhanced after extending a guide tube downstream of the monochromating chopper in FY2021. To address this issue, we implemented the background-reduction measures shown in Fig. 2, which include masking the upstream section of the get-lost tube with Cd and installing short vanes around it. As the result, the spurious scattering near direct-beam region was successfully suppressed (Fig. 3). Given the significant improvement, we plan to replace the interim vane with a permanent one next year.

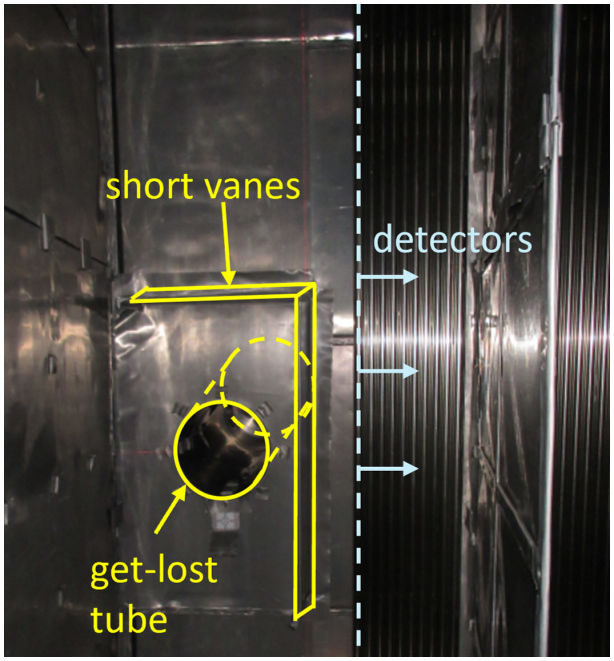

Figure 2. Background-reduction measures around the get-lost tube.

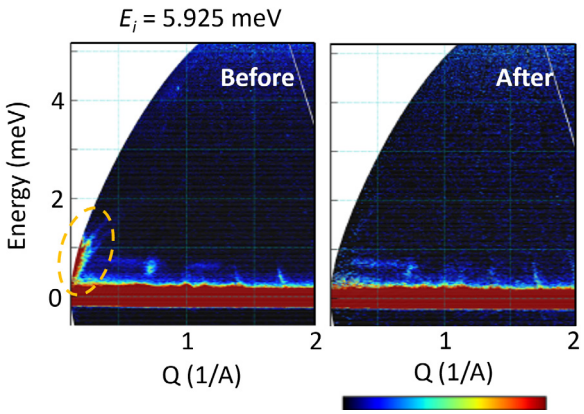

Figure 3. Measurement results of vanadium before and after the background-reduction measures.

4. Future Plans

We purchased new supermirror guide tubes in this fiscal year. We plan to replace the guide tubes in the upstream half of the beamline with the new ones in FY2025 to increase the neutron flux. Furthermore, we will continue the commissioning and upgrades of the ^{3}He cryofurnace so that it can be utilized as a standard sample environment on AMATERAS.

References

[1] K. Nakajima *et al.*, J. Phys. Soc. Jpn. **80**, SB028 (2011).
[2] K. Nakajima, RADIOISOTOPES. **66**, 101 (2017).

S. Ohira-Kawamura[1], M. Kofu[1,2], N. Murai[1], Y. Inamura[1], M. Nirei[1], P. Piyawongwatthana[1], D. Wakai[1,3], and K. Nakajima[4,1]
[1]Neutron Science Section, Materials and Life Science Division, J-PARC Center; [2]The Institute for Solid State Physics, The University of Tokyo; [3]NAT Corporation; [4]Materials Sciences Research Center, JAEA

Development of Sample Environment Devices at BL15

1. Introduction

The small- and wide-angle neutron scattering instrument TAIKAN (BL15) [1] is widely utilized in various research fields, including polymers, colloids and nanoparticles, biomolecules, battery materials, magnetic materials, and metals and alloys. Furthermore, BL15 TAIKAN enables efficient measurements over a length scale from approximately 0.1 to several hundred nanometers, leading to strong demand for simultaneous in situ measurements under varying sample environments. To address these needs, we have advanced the development of new sample-environment devices, upgrades to existing systems, and improvements to their control software.

In this article, we introduce three recently developed and implemented devices: a velocity-velocity gradient (1–2) plane shear cell, a power control system for Hydrogen fuel cells, and a 7 T cryomagnet.

2. Development of a 1–2 Plane Shear Cell

Rheological measurements are widely used for evaluating viscoelastic behavior in many industrial materials. By performing simultaneous measurements using a rheometer and small-angle neutron scattering, Rheo-SANS is a powerful technique for directly elucidating the correlation between macroscopic viscoelastic behavior and nanoscale structures. At BL15, the Rheo-SANS system [2] has been successfully applied to diverse fluid materials, including surfactant [3], polymer, inorganic, and clay suspensions [4]. However, a system for evaluating the characteristics of structural changes in the direction perpendicular to the flow velocity had not been developed.

Therefore, we developed a 1–2 plane shear cell [5] that allows measurements with a neutron beam incident perpendicular to the shear flow, as shown in Figure 1. As shown in the inset of Figure 1, the sample-irradiated region of this cell has a spatial width of 1.5 mm. Using a beam width of approximately 0.5 mm enables studies of the velocity-gradient dependence (1–2 direction) of the structures formed by the fluid. The sample temperature is controlled using a circulating water bath. In addition, we have been developing the software, allowing remote operation from IROHA2 [6].

2. Development of a Power Control System for Hydrogen Fuel Cells

A hydrogen fuel cell generates electricity through the electrochemical reaction between hydrogen and oxygen in air, producing only water as a byproduct. It consists of an anode, cathode, and electrolyte, which together facilitate the flow of protons and electrons. By using neutron scattering with hydrogen/deuterium (H/D) contrast variation, it is possible to reveal the structure of the electrolyte membrane and the distribution of water in the fuel cell.

Therefore, we developed the hydrogen fuel cell power control system shown in Figure 2. This system uses both deuterium and hydrogen gases and is equipped with two water tanks, one each for the hydrogen and air gas lines, thereby enabling H/D contrast variation SANS measurements during the power operation of a full cell. The system is currently undergoing commissioning, and software development is planned to enable control from the BL15 instrument system.

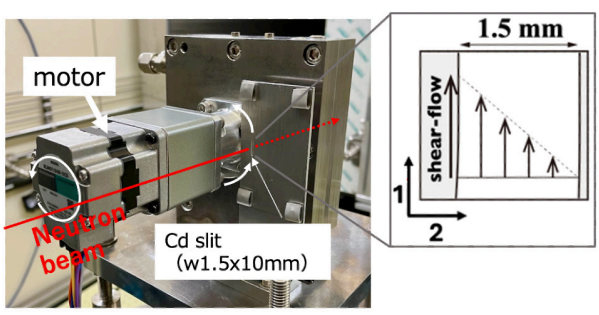

Figure 1. Photograph of the 1–2 plane shear cell and a schematic illustration of the shear flow imposed on the sample within the measurement area

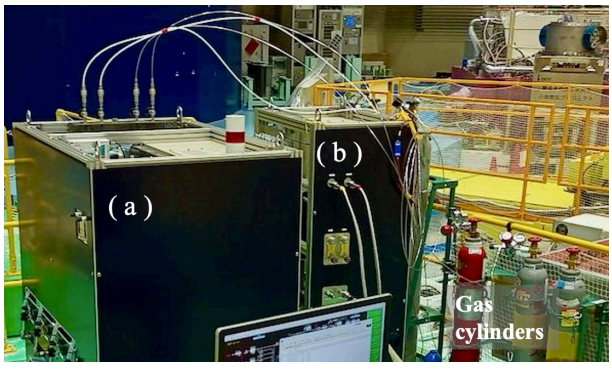

Figure 2. Photographs of the power control system for hydrogen fuel cell cells: (a) gas supply unit with temperature and humidity control; (b) exhaust hydrogen gas dilution unit

3. Development of a 7 T Cryomagnet

Electromagnets applying high magnetic fields to samples are one of the most widely used sample environment devices in neutron scattering experiments. At BL15, research experiments using superconducting cryomagnets have been continuously conducted to investigate magnetic materials [7].

To further advance research in such field, a new 7 T transverse-field magnet with an asymmetric magnetic field distribution, designed to avoid a zero-field region along the neutron beam path, has been installed at BL15, as shown in Figure 3.

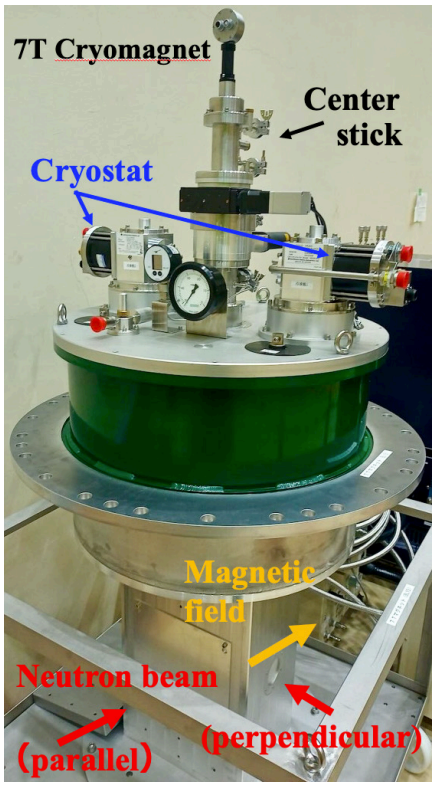

Figure 3. Photograph of a transverse-field 7T cryomagnet manufactured by Cryogenic Ltd.

By changing the incident beam direction, experiments can be performed with the magnetic field oriented either parallel or perpendicular to the neutron beam. Although the cryomagnet is currently under commissioning, the system allows measurements under magnetic fields of up to ±7 T (bipolar) and at temperatures between 0.3 and 300 K using a ^{3}He refrigerator.

4. Future Plans

At BL15, we carry out experiments that utilize the unique characteristics of neutrons and actively develop sample environment equipment, including the devices introduced here, to accommodate the diverse research needs of users from various fields. We will continue to promote the development of innovative experimental tools to further enhance research capabilities and support a wide range of neutron scattering studies.

References

[1] S. Takata *et al.*, JPS Conf. Proc. **8**, 036020 (2015).
[2] H. Iwase *et al.*, Journal of Colloid and Interface Science. **538**, 357-366 (2019).
[3] T. Sugahara *et al.*, Langmuir. **36**, 4695-4701 (2020).
[4] H. Iwase *et al.*, Langmuir. **37**, 6435-6441(2021).
[5] H. Iwase *et al.*, J. Appl. Cryst. **58**, 1407-1416 (2025).
[6] H. Hasemi *et al.*, JPS Conference Proceedings, Vol. 41. Proceedings of 11th International Workshop on Sample Environment at Scattering Facilities (2024).
[7] Y. Nii, *et al.*, Nat. Commun. **6**, 8539 (2015).

S. Takara[1], K. Hiroi[1], K. Ohishi[2], H. Iwase[2], Y. Kawamura[2], and T. Morikawa[2]
[1]Neutron Science Section, Materials and Life Science Division, J-PARC Center; [2]Neutron Science and Technology Center, CROSS

BL16: Neutron Reflectometry for Functional Interfaces

1. Introduction

SOFIA is a horizontal-type neutron reflectometer at Beamline 16 (BL16) in MLF. SOFIA provides an advantageous capability for investigating free surfaces (liquid-air and liquid-liquid interfaces), enabling measurements with the sample kept horizontal over the full Q_z-range, and has therefore been widely utilized for interfacial studies, particularly in soft-matter science. Benefiting from the high neutron intensity at J-PARC and efficient TOF-based measurements, SOFIA enables neutron reflectometry (NR) with relatively short data acquisition times.

In FY2024, SOFIA focused on (i) user programs, (ii) instrumental upgrades toward multi-incident-angle neutron reflectometry (MI-NR), and (iii) the development of advanced sample environments to further enhance time-resolved and operando interfacial studies.

2. Key Instrumental Achievements

2.1 Double-Disc-Chopper System

The double-disc chopper system at SOFIA was modified to improve robustness and neutron shielding performance, supporting extended measurement modes toward multi-incident-angle neutron reflectometry (MI-NR). In the previous setup, insufficient neutron shielding of the chopper discs limited the reliable use of double-frame measurements.

To address this issue, new chopper discs fabricated from borated aluminum and coated with Gd_2O_3 paint were developed and installed in collaboration with the neutron optics group at PSI. Transmission measurements confirmed that neutron intensity above approximately 0.2 nm was sufficiently suppressed ($<10^{-5}$), enabling stable double-frame operation (Fig. 1).

As a result, double-frame measurements became accessible not only for MI-NR-related studies but also for standard reflectometry experiments, thereby increasing the availability of time-resolved measurements and providing a technical basis for subsequent MI-NR demonstration experiments.

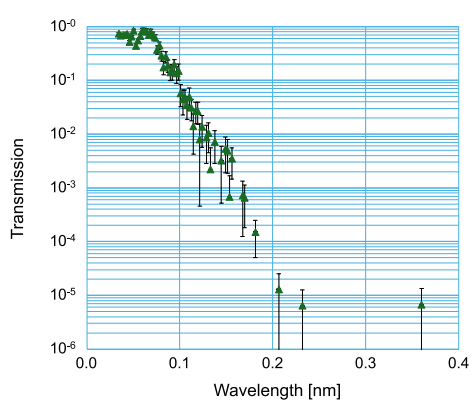

Figure 1. Transmission performance of the upgraded double-disc chopper.

2.2 Multi-Incident-Angle Neutron Reflectometry (MI-NR)

In the present SOFIA setup, the accessible Q_z-range is limited by the available wavelength band, requiring multiple incident angles to cover the full Q_z-range of reflectivity. To overcome this limitation and to improve efficiency for time-slicing measurements, SOFIA has been undergoing an upgrade toward a multi-incident-angle neutron reflectometer (MI-NR) in combination with focusing optics [1]. This approach aims to enable simultaneous coverage of a wide Q_z-range with enhanced beam intensity, which is essential for operando and time-resolved measurements.

After the installation of key components, a proof-of-principle demonstration toward MI-NR was performed at SOFIA in FY2024. Simultaneous reflectivity measurements were implemented using two detectors, enabling data acquisition at multiple incident angles within a single measurement sequence. As a reference sample, deuterated polystyrene (dPS) thin films with a thickness of 30 nm, which are routinely used at SOFIA as a standard sample, were measured to evaluate the feasibility of MI-NR measurements. Reflectivity profiles obtained at two different incident angles were successfully acquired simultaneously with a 30 min exposure at 100 kW beam power, which corresponds to just a 3 min exposure at 1 MW. Although the statistical quality was limited, the feasibility of MI-NR measurements at SOFIA was successfully demonstrated (Fig. 2). To the best of our

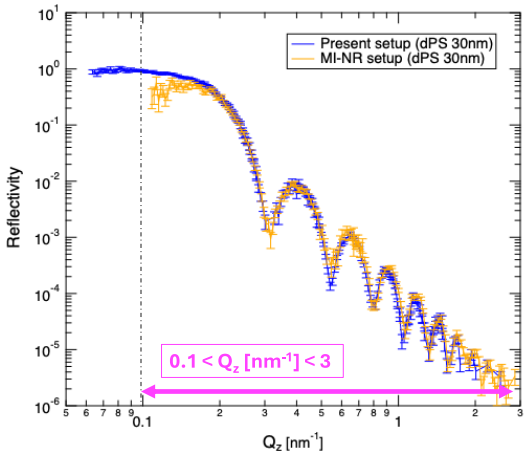

Figure 2. Proof-of-principle demonstration of MI-NR.

knowledge, this demonstration achieved the world's widest single-shot Q_z-range, covering $0.1 < Q_z\ [nm^{-1}] < 3$. We expect that the accessible Q_z-range will be further extended by higher statistical accuracy.

Through the installation, it turned out that the first manufactured focusing mirrors did not meet the expected performance due to fabrication-related issues, which leads to the blurring of the beam. New mirror pairs are currently under production. Our goal is to complete the final MI-NR installation at SOFIA and begin user operation by the end of 2027.

3. Sample Environment Development

3.1 Rheometer for NR measurement (Rheo-NR)

A rheometer system with a rotary cone plate (AMETEK Brookfield RST-CC) was successfully installed and operated, enabling NR measurements under steady shear flow (Fig.3). This sample environment allows in-situ investigation of interfacial structures of soft matter systems, and is applicable to studies in non-equilibrium physics, tribology, and food science.

Using this setup, a surfactant-water mixture exhibited surface-specific structural behavior distinct from that observed in the bulk [2]. The formation of an interfacial structure on a silicon substrate and its growth process under shear flow were found to depend on the increment rate of the applied shear rate.

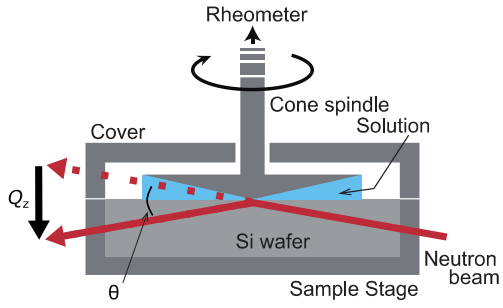

Figure 3. Experimental geometry for rheo-NR measurement.

3.2 Temperature-Controlled Stage with Integrated Humidity Control

A new temperature-controlled stage was developed for SOFIA using high-temperature Peltier elements, covering a temperature range from –20 to 180°C. This represents a significant extension compared with the previously available stage, which was limited to approximately 120°C. The new stage incorporates an integrated humidity control system based on temperature regulation of an internal water bath. The temperature control performance was successfully validated, and the system has been fully integrated into the SOFIA instrument control system.

4. Scientific Outcomes

During the 2024A cycle, 13 general proposals, 2 Multi-Probe (MP) proposals, and 1 long-term proposal were carried out at SOFIA. In addition, 17 peer-reviewed publications and 2 press releases were produced using data obtained at SOFIA. Among the resulting scientific outputs, one representative example is highlighted below to illustrate the capabilities of SOFIA.

4.1 Organization of malonamides from the interface to the organic bulk phase [3]

To clarify the relationship between extractant aggregate structures and solvent extraction performance, NR at SOFIA was employed in combination with small-angle X-ray scattering (SAXS) to investigate the supramolecular organization of amphiphilic malonamide extractants in the organic bulk phase and at the liquid-liquid interfaces. The combined analysis revealed that aggregates formed in the organic bulk phase mainly influence the metal ion selectivity through a size-recognition effect, while interfacial structures govern the kinetics of metal transfer across the liquid-liquid interface. Differences in the separation behavior of Pd(II) and Nd(III) were observed depending on the organic solvent used, such as toluene or heptane, reflecting the sensitivity of aggregate structures to solvent conditions. These results demonstrate the complementary roles of bulk and interfacial supramolecular organizations in solvent extraction processes and highlight the capability of NR to elucidate interfacial structures that are difficult to access using bulk-sensitive techniques alone.

References

[1] N. L. Yamada, *et al.*, J. Appl. Crystallogr. **53**, 1462-1470 (2020).
[2] F. Nemoto *et al.*, J. Chem. Phys. **161**, 164902 (2024).
[3] C. Micheau *et al.*, J. Mol. Liq. **401**, 124372 (2024).

Masako Yamada[1,2], Norifumi L. Yamada[1,2], Fumiya Nemoto[3], Takuya Hosobata[4], and Uwe Filges[5]
[1]Neutron Science Section, Materials and Life Science Division, J-PARC Center; [2]Institute of Materials Structure Science, KEK; [3]National Defense Academy; [4]RIKEN Center for Advanced Photonics; [5]PSI Center for Neutron and Muon Sciences

Development of a Focusing Supermirror for GISANS Measurements at SHARAKU Reflectometer

1. Introduction

The neutron reflectometer SHARAKU, installed at BL17 in the MLF, has been employed for the nanostructure analysis of the surface and interfaces in thin films on a wide variety of research fields, such as polymer [1,2] and magnetic samples [3]. Measurements have been carried out at SHARAKU on specular reflection (along Q_z) and off-specular scattering (in the Q_xQ_z plane). However, grazing-incidence small-angle neutron scattering (GISANS) experiments have not been performed yet due to a shortage of beam intensity. Hence, an implementation of GISANS at SHARAKU would extend its capability into the Q_yQ_z plane effectively. At a pulsed neutron beamline, one performs a GISANS measurement with a wide-band beam, analyzing neutron wavelength using the time-of-flight method (TOF-GISANS). It is therefore essential to develop focusing devices that function over a broad range of wavelengths and enhance the beam intensity at SHARAKU. To this end, we have developed a one-dimensional focusing neutron supermirror.

2. Beam Line Setup and Mirror Specifications

The focusing supermirror is of one-dimensional elliptical shape, with its two foci positioned at the first slit (S1) and at the detector surface of SHARAKU, as illustrated in Fig. 1. S1 narrows an incident beam vertically and defines the initial focal spot. The beam is extracted slightly downward by auxiliary slits. The focusing mirror reflects the extracted neutrons upward and converges them vertically onto the second focal spot on the detector surface. Specifications of the focusing mirror are listed in Table 1. When the focusing mirror is not used, the beam is collimated by S1 and the second collimating slit (S6), drawn horizontally.

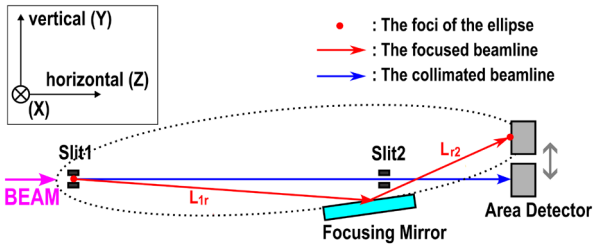

Figure 1. Geometry of neutron focusing and slit collimation. The dotted curve represents the ellipse according to which the mirror surface is figured. Note that scales and gradients are significantly exaggerated to facilitate visualization.

Table 1. Specifications of the focusing supermirror

the ellipsoid $(z/a)^2 + (y/b)^2 = 1$ $(z,y) = (a\cos\theta, b\sin\theta)$	$a = 5525$ mm, $b = 79.63$ mm, $\theta = 72.59$~$76.89°$
1st focus to mirror	$L_{1r} = 6980$ mm
mirror to 2nd focus	$L_{r2} = 4070$ mm
incident angle	~ 0.856°
supermirror	NiC/Ti, m=4
substrate surface	roughness: 0.183 nm RMS
	figure error(*): 188.7 nm PV
substrate	400 x 50 mm^2, fused quartz

(*) Deviation of the fabricated surface from the designed one.

3. Performance Test

We carried out a performance test of the focusing supermirror at SHARAKU, comparing the focused beam spot with an optimally collimated spot at the detector position.

The experimental setup of the performance test is schematically depicted in Fig. 2. Beam slits other than S6 were placed in accordance with the figure for the focusing geometry while, in the collimating geometry, all slits were aligned along the horizontal beamline. The focusing supermirror was placed 7430 mm from S1 at a nominal incident angle of 0.88°, slightly different from the designed position shown in Table 1 due to a technical problem in the experiment. The spots at the detector were observed using a multiwire-type proportional counter (MWPC) whose pixel size is 0.5 mm × 0.5 mm and spatial resolution 1.8 mm. [4,5]

Figure 3 shows two-dimensional images of the focused and collimated spot. Neutrons of 0.22 to 0.88 nm in wavelength were collected. The two images have similar spot shapes, but the scale on the color bars suggests that the focusing mirror enhanced the intensity twentyfold. The spot sizes are more extensive than our expectation of 1 mm in height and 2 mm in width. This could arise from (1) the finite spatial resolution of the MWPC detector, (2) the mispositioning of the focusing supermirror, and (3) the figure error of the elliptic surface of the supermirror. This report does not discuss measured spot sizes in detail.

The wavelength distributions of neutron intensity in the two beam spots are compared in Fig. 4, along with the intensity ratio. We found that neutrons with a wavelength greater than 0.225 nm are efficiently re-

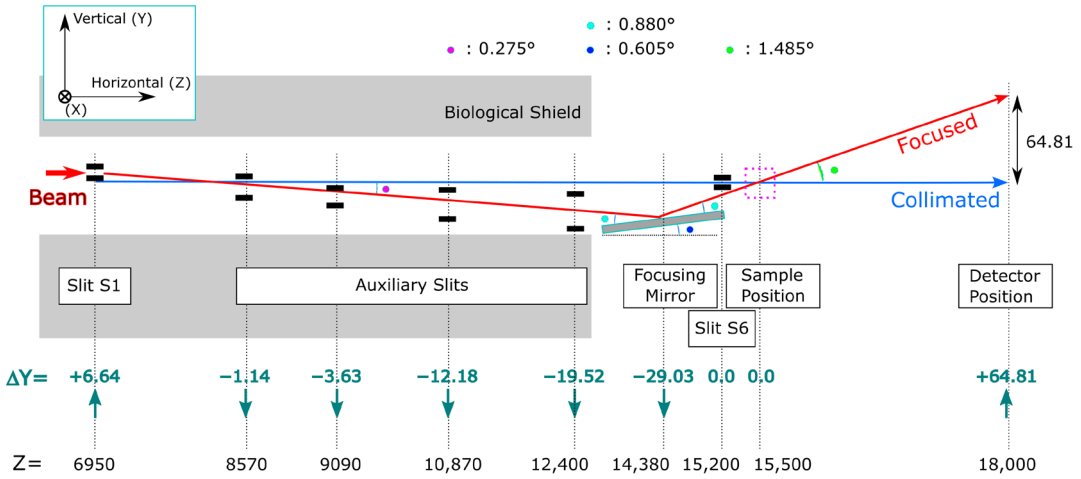

Figure 2. The setup of the performance test. The unit of digits is mm. ΔY denotes the vertical position of the focused beamline at each component, measured from the collimated (horizontal) beamline, with an accuracy of less than 0.1 mm. The blue-green arrows indicate upward/downward displacements from the horizontal line. Z represents the distance from the neutron source with an accuracy of ±1 mm. In this experiment, no sample was placed at the sample position.

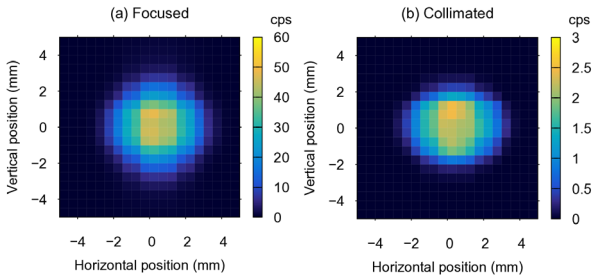

Figure 3. Two-dimensional images of (a) the focused spot and (b) the optically collimated spot.

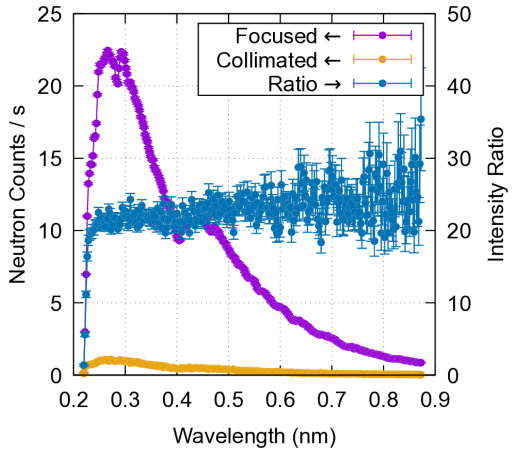

Figure 4. The intensities at the focused spot and the collimated one, and their ratio of dependence on neutron wavelength. Neutrons with a wavelength <0.22 nm were chopped upstream of the focusing-mirror position.

flected and focused by the supermirror, demonstrating that the mirror functions with an *m* value of 3.9 at the nominal incident angle of 0.88°. The intensity gain was ≳20 for a wavelength >0.23 nm.

4. Summary

We have developed a focusing supermirror for GISANS measurement at SHARAKU. A performance test demonstrated that the mirror enhances neutron intensity at the spot on the detector twentyfold compared with the optimum beam collimation, while maintaining the S/B ratio of the spot at 500. We have a plan to develop multiple focusing mirrors to enhance the intensity and S/B ratio. For details of the development and the experiment, refer to [6].

References

[1] R. Sujita *et al.*, ACS Macro Lett. **13**, 747 (2024).
[2] M. Kawano *et al.*, Macromolecules. **57**, 6625 (2024).
[3] T. Hanashima *et al.*, Appl. Phys. Express. **17**, 035002 (2024).
[4] K. Toh *et al.*, Nucl. Instrum. Methods Phys. Res. A **726**, 169 (2013).
[5] K. Toh *et al.*, J. Instrum. **9**, C11019 (2014).
[6] D. Yamazaki *et al.*, Quantum Beam Sci. **9**, 20 (2025).

D. Yamazaki[1], R. Maruyama[1], H. Aoki[2,3], T. Hanashima[4], K. Akutsu[4], N. Miyata[4], S. Kasai[4], and K. Soyama[5]
[1]*Neutron Instrumentation Section, Materials and Life Science Division, J-PARC Center;* [2]*Neutron Science Section, Materials and Life Science Division, J-PARC Center;* [3]*Institute of Materials Structure Science, KEK;* [4]*Neutron Science and Technology Center, CROSS;* [5]*Materials and Life Science Division, J-PARC Center*

Status of SENJU 2024

1. Introduction

SENJU is a TOF single-crystal neutron diffractometer designed for precise crystal and magnetic structure analyses under multiple extreme environments, such as low-temperature, high-pressure, and magnetic-field, as well as for taking diffraction intensities of small single crystals with a volume of less than 1.0 mm^3 down to 0.1 mm^3 [1]. Since the operation of SENJU started in 2012, our instrument group has carried out continuous commissioning and upgrades.

In 2024, we installed two large area detectors with a fan-like arrangement, and updated the data processing software, STARGazer-Online. In addition, we also report on the purposes of the instrument beam-time for SENJU.

2. Conceptual design of fan-like detector arrangement

The area detector is one of the most essential components of a single-crystal neutron diffractometer, and the evolution of the detector directly improves the performance of the diffractometer. SENJU features extensive detector coverage, owing to the 41 detectors equipped—each with a sensitive area of 256 × 256 mm—arranged around a central vacuum sample chamber. This configuration, combined with the white neutron beam provided by the MLF, enables efficient three-dimensional reciprocal space measurements. However, gaps between adjacent detectors can reduce measurement efficiency and complicate data acquisition.

To address these limitations and further enhance performance, a new generation of detectors has been developed. These detectors are six times larger than the original ones, 512 mm width and 718 mm height, and feature an asymmetric frame design, in which one edge is narrower than the others. This design allows for a novel "fan-like" arrangement, where the detectors are positioned in a circular configuration similar to the original layout but with slight overlaps between adjacent detectors (Fig. 1) [2]. This significantly reduces the gaps. In 2024, two of the new detectors have been installed, replacing nine of the original units (Fig. 2). Test measurements with a standard sample crystal

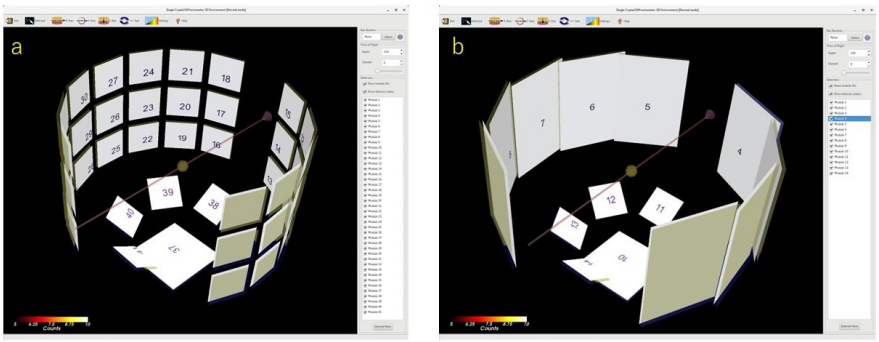

Figure 1. The initial detector arrangement of SENJU (left) and the conceptual design of the "fan-like" detector arrangement (right).

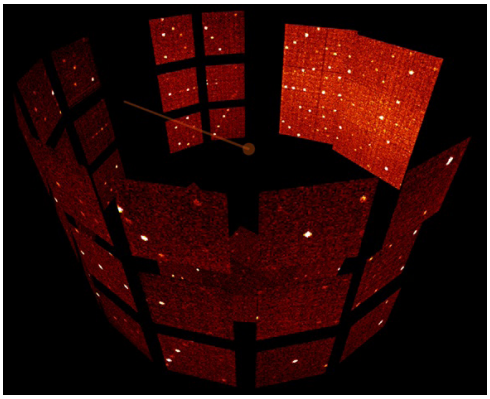

Figure 2. Diffraction image of a standard sample at SENJU with two large detectors.

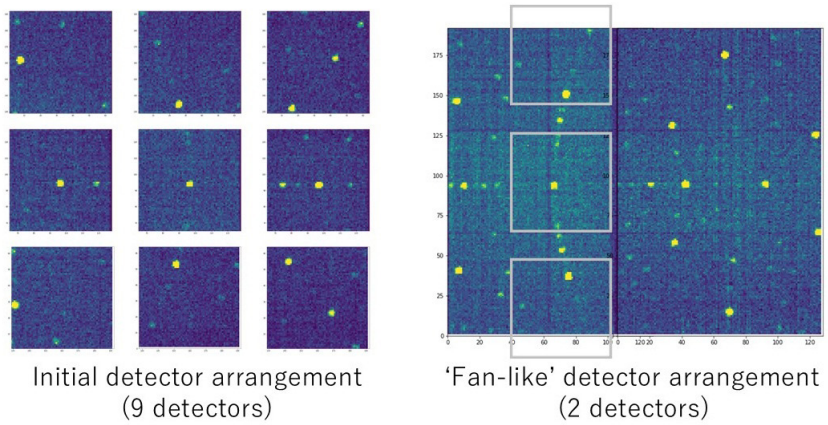

Figure 3. Diffraction image of a standard sample at the removed nine detectors (left) and the newly installed two detectors (right).

have demonstrated that the new detectors enable gapless measurement of diffraction images (Fig.3) and facilitate a more intuitive visualization of reciprocal lattices.

This detector upgrade project is now ongoing as a multi-year plan. The measurement efficiency of SENJU is expected to double with this upgrade.

3. Upgrading of STARGazer-Online

STARGazer-Online (SGO) is a remote data processing and data-visualization application for SENJU that works on web browsers such as Firefox, Chrome, and Safari. We have been continuously upgrading SGO to keep up with the latest scientific research.

The first stage of the data processing at SENJU is finding possible Bragg peaks from the diffraction data for the following UB matrix determination. Accurate selection of diffraction peaks in this stage is essential to ensure precise structure analyses. However, some data may be compromised by signals from the sample environment devices near the sample. Consequently, the quality of the measured data must be meticulously examined manually before they are used for structure analyses. Given the vast volume of data, manual inspection of each dataset is impractical, thereby necessitating the development of an efficient data-checking tool.

To efficiently assess the quality of each peak, a method utilizing an autoencoder has been developed. The autoencoder initially encodes an input image and subsequently decodes the encoded representation to reconstruct the original image. Since the autoencoder is trained to encode and decode a single, clean reflection, the input and reconstructed images will match only when a single, clean image is provided as input. To quantify the similarity between the two images, Euclidean distance and cosine similarity metrics are employed. Finally, the observed data can be effectively discriminated using these measures.

The autoencoder was embedded in the first data processing stage of SGO.

4. Use of the instrument beam time

In 2024, the instrument beam time was used mainly for measurements of standard samples to calibrate the accurate detectors' positions, and a vanadium-nickel alloy for calibration of detector efficiency in addition to the on-beam test of the newly installed large detectors.

References

[1] T. Ohhara *et al.*, J. Appl. Cryst. **49**, 120 (2016).
[2] T. Ohhara *et al.*, MLF Annual Report 2023 (2024).

T.Ohhara[1], R. Kiyanagi[1], A. Nakao[2], K. Munakata[2], Y. Ishikawa[2], K. Moriyama[2], I. Tamura[3], K. Kaneko[1], T. Nakamura[4], K. Toh[4], K. Sakasai[4], and T. Hosoya[4,5]

[1]Neutron Science Section, Materials and Life Science Division, J-PARC Center; [2]Neutron Science and Technology Center, CROSS; [3]New Research Reactor Promotion Office, JAEA; [4]Neutron Instrumentation Section, Materials and Life Science Division, J-PARC Center; [5]Graduate School of Science and Engineering, Ibaraki University

Research Trends and Highlights in TAKUMI

1. Introduction

TAKUMI is a neutron diffractometer dedicated to engineering materials science, installed at beamline 19 of the Materials and Life Science Experimental Facility (MLF) at J-PARC. High-precision research has been conducted across a wide range of materials, from fundamental studies to applications nearing practical implementation. These include investigations into microstructural evolution during cooling and heating, deformation behavior over a temperature range from 15K to 1373K in structural and functional materials, microstructural changes during thermo-mechanical processing, and residual stress mapping in engineering components—all yielding outstanding results. These achievements have been made possible by the high quality of diffraction patterns, which enable detailed analysis of Bragg peaks to extract critical structural information such as internal stress, phase composition, dislocation density, and texture. Furthermore, a variety of sample environment devices have been developed and utilized to support these advanced experiments.

2. Research trends

TAKUMI operated stably throughout FY2024, and the experiments of the accepted proposals were carried out to the extent permitted by the available beam time. Statistics of the experiments categorized by experiment and material type (based on allocated beam time), and by principal investigator (PI) affiliation (based on proposal numbers) are shown in Fig.1. Low-temperature loading experiments accounted for 57% of total beam time, maintaining the high level observed in the previous year (60%). Approximately half of the experiments focused on steel materials, indicating a renewed interest in steel, which had temporarily declined due to the rise of high-entropy alloys. This trend suggests that steel is regaining its former prominence in materials research. Notably, more than half of the experimenters were from overseas institutions, reflecting strong international interest in J-PARC and TAKUMI. In contrast, industrial utilization remains relatively low.

Thanks to the contributions of our users and collaborators, 30 peer-reviewed original research papers and 6 proceedings papers based on TAKUMI data were published in 2024. Additionally, numerous oral and poster presentations were delivered at domestic and international conferences, workshops, and seminars. A press release was issued for a study on ultrafine-grained stainless steel [1], which was subsequently featured in four newspapers. Three papers utilizing TAKUMI data received prestigious awards: the *Acta Materialia, Inc. Acta Student Award*, the *Sawamura Award* from the Iron and Steel Institute of Japan, and the *International Magnesium Science & Technology Award – Excellent Paper of the Year*. Furthermore, one user was honored with the *Young Scientist Award* from the Japan Society for Neutron Science, recognizing the impact of research conducted using TAKUMI.

3. Some highlights

Thanks to our users and collaborators, the scientific quality and practical relevance of our 2024 publications have been exceptionally high. However, due to limited space, only a few selected highlights are presented below.

(1) "Martensitic transformation-governed Lüders deformation enables large ductility and late-stage strain hardening in ultrafine-grained austenitic stainless steel at low temperatures" by W. Mao et al. [1]

This study reveals that ultrafine-grained (UFG) 304

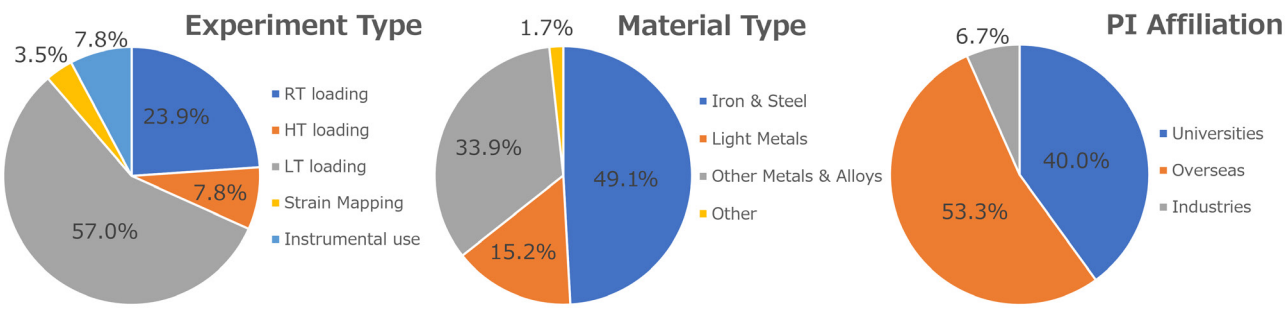

Figure 1. Experiment statistics for FY2024 categorized by experiment and material type (based on allocated beam time) and by principal investigator (PI) affiliation (based on proposal numbers).

austenitic stainless steel exhibits exceptional mechanical performance at cryogenic temperatures, defying the typical ductility loss caused by deformation-induced martensitic transformation. Using in-situ neutron diffraction and digital image correlation, the authors found that as temperature decreases from 295 K to 77 K, the deformation mechanism transitions from a cooperative mode involving dislocation slip and martensitic transformation to one dominated by martensitic transformation during the Lüders deformation. This shift delays plastic deformation in both austenite and martensite, preserving strain-hardening capacity for the subsequent uniform deformation. As a result, the UFG 304 steel maintains a remarkable elongation of 29% and achieves a tensile strength of 1.87 GPa at 77 K. The findings suggest a promising strategy for designing high-strength and high-ductility materials by controlling deformation modes in ultrafine-grained structures.

(2) "Contributions of multimodal microstructure in the deformation behavior of extruded Mg alloys containing LPSO phase" by K. Hagihara et al. [2]

This study investigates the deformation mechanisms of extruded magnesium alloys containing long-period stacking ordered (LPSO) phases. Using in-situ neutron diffraction and crystal plasticity simulations, the authors reveal that multimodal microstructures—comprising worked grains, recrystallized grains, and LPSO phases—enable both high strength (~390 MPa) and large elongation (~14%). The LPSO phase enhances work-hardening through kink-band strengthening and anisotropic slip behavior. A new concept, "Anisotropic Mechanical property-Induced Ductilization (AMID)," is proposed to explain how mechanical anisotropy in multiphase alloys contributes to improved ductility.

(3) "Strain analysis by neutron diffraction on Nb_3Sn strands in ITER central solenoid conductors of short and long twist pitch" by T. Suwa et al. [3]

This study investigates internal strain in Nb_3Sn strands within ITER central solenoid (CS) conductors using neutron diffraction. Comparing long twist pitch (LTP) and short twist pitch (STP) designs, the authors found that STP conductors effectively suppress strand bending and compressive strain, which are key factors in critical current degradation. Neutron diffraction measurements revealed that STP conductors not only prevent performance loss but also slightly improve current sharing temperature (T_{cs}). The findings support STP as a promising design for enhancing durability and performance in fusion magnet applications.

References

[1] W. Mao, *et al.*, *Acta Mater.* **278**, 120233 (2024).
[2] K. Hagihara, *et al.*, *Int. J. Plast.* **173**, 103865 (2024).
[3] T. Suwa, *et al.*, *Supercond. Sci. Technol.* **38**, 015008 (2024).

S. Harjo[1], T. Kawasaki[1], W. Gong[1], and T. Ito[1]
[1]*Neutron Science Section, Materials and Life Science Division, J-PARC Center*

Status of the IBARAKI Materials Design Diffractometer (BL20, iMATERIA)

1. Introduction

The IBARAKI Materials Design Diffractometer (iMATERIA) [1] at J-PARC was constructed to promote industrial applications of neutron scattering [2]. It offers both high intensity and resolution ($\Delta d/d \approx 0.15\%$), enabling multiscale analysis of materials—from crystalline and atomic structures of batteries and fuel cells to textures of steels and polymers. With four detector banks and a broad *d*-spacing range (0.07–3,000 Å), iMATERIA allows simultaneous measurements under various environments. Since 2008, over 700 industrial projects (≈60% of all MLF proposals) have been conducted through annual public calls. Beyond serving as an industrial gateway, iMATERIA supports advanced studies that drive material innovation.

2. Operando Neutron Diffraction of Lithium-Ion Batteries

Rechargeable batteries are essential devices for achieving carbon neutrality, and progress in lithium-ion battery (LIB) technology requires direct observation of lithium behavior in electrodes and solid electrolytes under operating conditions. With the recent power upgrade at J-PARC, short-time operando measurements have become feasible, enabling time-resolved diffraction of laminated cells. However, refinement of hundreds of sequential datasets can result in unphysical convergence, particularly for weak or overlapping phases. To overcome this, we employed the upgraded Z-Rietveld 2.0 [3], which allows parameter constraints during automated multiphase refinements of several hundred datasets.

The tested cell consisted of an NCM523 cathode ($LiNi_{0.6}Co_{0.2}Mn_{0.2}O_2$ mixed with acetylene black, carbon, and PVDF in a 100:3:3:3 ratio) on Al foil and a graphite anode on Cu foil. The electrolyte was 1 mol/L $LiPF_6$ in EC/EMC (3/1) with VC_2, and the laminated cell (10 stacked layers) was sealed in an aluminum film. Operando neutron diffraction was conducted using a V-foil compression jig under a constant current of 4.18 mA (0.025C). Time-resolved data were collected every 240 s at the backscattering bank and analyzed with Z-Rietveld 2.0.

Including both (001)- and (110)-oriented graphite phases significantly improved fitting accuracy. The refined results showed that certain graphite and Li-intercalated phases remained unchanged during charging, suggesting their relation to cell degradation (Fig. 1). The evolution of *c*-axis lengths and phase fractions revealed anisotropic Li extraction between (001) and (110) orientations. For the NCM523 cathode, lattice parameters followed known trends, while Li occupancies varied smoothly and nearly linearly with the state of charge, implying higher accuracy. These results demonstrate that graphite orientation and nonuniform structural evolution strongly influence electrochemical performance and degradation mechanisms.

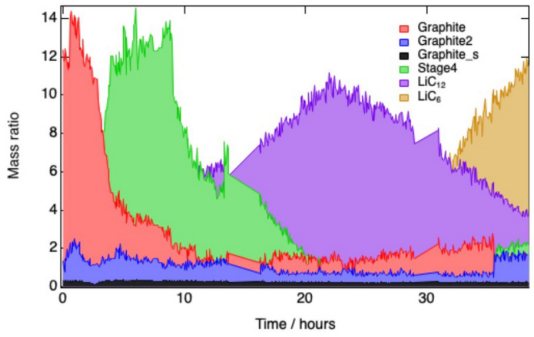

Figure 1. Mass ratio changes of each phase of the negative electrode active material in lithium-ion batteries during charging.

3. High-Temperature Compression and Dislocation Evolution in Copper

In-situ neutron and X-ray diffraction are powerful tools for analyzing microstructural evolution during deformation. However, tensile testing often causes localized fracture, limiting high-strain observations. To address this, we developed an in-situ neutron diffraction technique under compression using a vanadium alloy jig that is transparent to neutrons and mechanically robust at high temperatures. Compression testing avoids fracture, enabling measurements up to large strains.

Experiments on Cu–Zn alloys showed that under tension, dislocation multiplication was similar at room temperature and 573 K, whereas compression exhibited clear temperature dependence (Fig. 2) [4]. In pure copper, high-temperature compression caused stress oscillations corresponding to alternating work hardening and softening, synchronized with cyclic changes in dislocation density. Texture analysis indicated that softening was associated with dynamic recovery and recrystallization. By improving the time resolution to 5 s, we achieved real-time texture analysis during deformation.

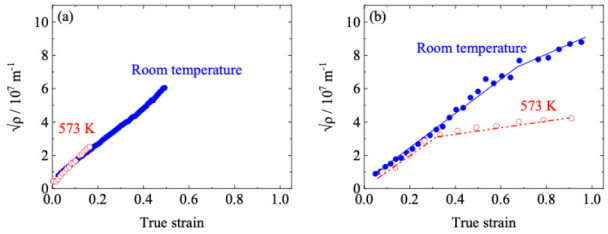

Figure 2. Change in the square root of dislocation density with true strain for Cu-Zn alloy specimens at room temperature and 573 K (a) tensile and (b) compressive deformation.

These results represent the world's first simultaneous measurement of texture evolution and dislocation density under high-temperature compression using iMATERIA. Dislocation densities derived from neutron diffraction, combined with the Bailey–Hirsch equation, successfully reproduced the observed temperature dependence of flow stress and stress oscillations. The dislocation hardening coefficient decreased with increasing temperature, indicating fewer dislocation interactions due to enhanced climb recovery. A {110} texture developed during compression and weakened at higher temperatures. These findings clarified the microscopic mechanisms underlying stress oscillations in metals at elevated temperatures, linking flow stress variations to dislocation multiplication and recovery, providing insights for predicting strength in high-temperature forming processes.

4. Spin Contrast Variation

For soft-matter and polymer studies, we are developing a spin contrast variation (SCV) method as part of the "Advanced Multicomponent Small-Angle Scattering" project. Unlike costly deuteration, SCV controls contrast through dynamic nuclear polarization (DNP), transferring electron-spin polarization to hydrogen nuclei under a low temperature and a strong magnetic field. Using radicals such as 2,2,6,6-tetramethylpiperidine 1-oxyl (TEMPO) and TEMPOL, the technique is applicable to both hydrophobic and hydrophilic systems.

Our setup achieves 1.2 K under reduced helium pressure and a 7 T magnetic field using a superconducting magnet. The system maintains airtight contact with the BL20 vacuum chamber, enabling stable low-temperature operation. Collaborative experiments with industrial partners (Panasonic, Sumitomo Rubber Industries, NOK) were performed in May 2024 using this SCV instrument.

Previous small-angle scattering studies on hu-man hair used deuterated samples to highlight intermediate filament contrasts. In the present study, we performed SCV experiments on hair immersed in light water and subsequently dried. The scattering profiles (Fig. 3) display a characteristic peak near q = 0.06 Å^{-1}, corresponding to the correlation between intermediate filaments com-posed of keratin coiled-coils embedded in a matrix. The intensity dependence on spin polarization differed markedly from that of deuterated samples, suggesting that water distribution in both the matrix and keratin domains strongly affects scattering contrast. Quantitative analysis of this polarization dependence is underway to refine the previously reported 40% deuteration ratio for amide-bound hydrogens in keratin coiled-coils [5].

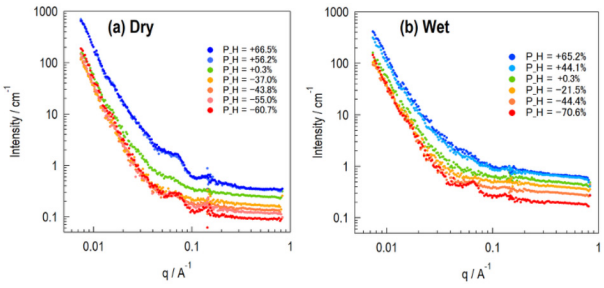

Figure 3. DNP-SANS profiles of hair fibers (a) dried after immersion in light water, (b) immersed in light water.

Through continued collaboration with industrial partners, the SCV system has enabled on-beam DNP measurements at BL20 without technical interruption. The insights obtained from these experiments are expected to advance structural studies of moisture absorption and desorption in hair fibers, contributing directly to the development of next-generation high-performance hair dryers and related consumer technologies.

References

[1] T. Ishigaki *et al.*, *Nucl. Instrum. Methods Phys. Res. A* **600**, 189-191 (2009).
[2] S. Koizumi *et al.*, *Hamon*. **34**, 89-96 (2024).
[3] R. Oishi *et al.*, *Nucl. Instrum. Methods Phys. Res. A* **600**, 94-96 (2009).
[4] S. Karasawa *et al.*, *Mater. Trans.* **66**, 871-877 (2025).
[5] Y. Noda *et al.*, *J. Appl. Cryst.* **56**, 1015-1031 (2023).

K. Ikeda[1], T. Ishigaki[1], Y. Noda[1,2], S. Sato[1,2], S. Koizumi[1,2], and J. Suzuki[1]
[1]*Neutron Industrial Application Promotion Center, CROSS;* [2]*Faculty of Engineering, Ibaraki University*

Status of the High Intensity Total Diffractometer (BL21, NOVA)

1. Introduction

NOVA, the High Intensity Total Diffractometer at J-PARC MLF, remains the most intense powder diffractometer in the facility, optimized for total scattering measurements and the analysis of the atomic Pair Distribution Function (PDF). NOVA's capabilities are crucial for studying materials across various research fields, including liquids, amorphous materials, locally disordered crystalline materials, and samples with incommensurate magnetic structures.

This year's major development focused on enhancing our data analysis platform through a productive collaboration with Rigaku Corporation. This partnership was initiated to upgrade the post-measurement data correction and analysis environment distributed to users, aiming to provide high-quality data seamlessly to both academic and industrial researchers.

2. Updating the Data Analysis Platform in collaboration with Rigaku

Our collaboration with Rigaku centered on integrating new and improved correction functions into the data reduction software, specifically targeting the challenges inherent in high-quality total scattering data analysis. The goal was to improve the efficiency and accuracy of corrections in the Fourier transform of *S(Q)* data.

The key improvements integrated into the software include:

2-1. Improved Ripple Removal Correction

The ripple (or low-*r* noise) correction is essential, especially for crystalline materials, where conventional methods struggled to reproduce the measured *S(Q)* or required computationally complex processes.

- **New Approach:** The improved method calculates the correction curve $\gamma(Q)$ directly, bypassing the inverse-Fourier-transform (*G(r)*) and Fourier-transform (*S'(Q)*) steps for the portion of the data being corrected [1].
- **Performance Improvement:** Utilizing this new method, the correction can be completed in a single step, reducing the processing time by approximately

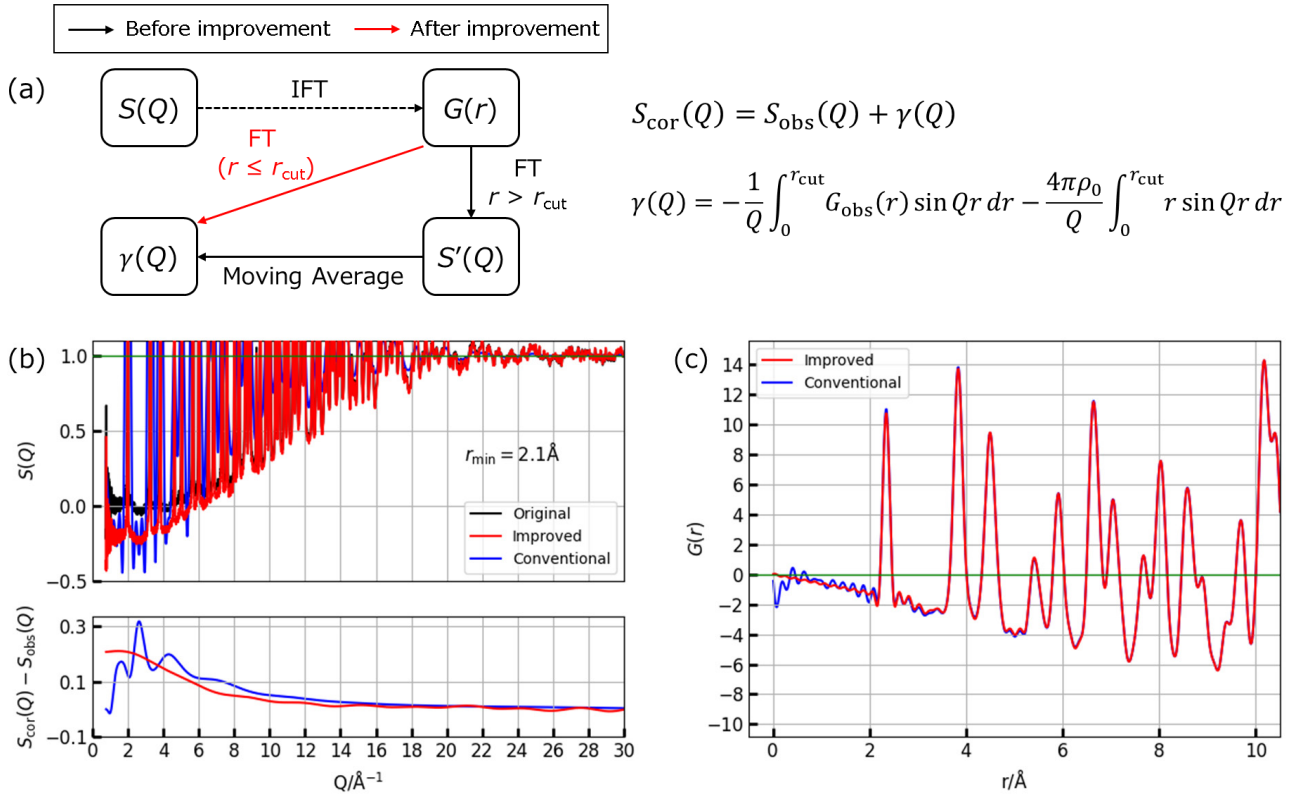

Figure 1. Overview of Ripple Removal Correction (a), comparison of the improved method (red) and conventional method (blue) for neutron total scattering data (in 90° bank in NOVA) using NIST Si640d in *S(Q)* (b) and *G(r)* (c).

two-thirds compared to the repetitive process of the conventional method (e.g., 0.12 s vs 0.37 s for powder diffraction data with NIST Si640d).

- **Result Quality:** The revised approach successfully removes artifacts in the corrected *S(Q)* and eliminates the unrelated oscillations on the low-*r* side of the *G(r)* profile, providing a cleaner and more accurate result.

3. Future Outlook and Synergistic Research

The ongoing goal is to enable more user-friendly analysis and provide feedback for experiments. It also contributes to the complementary use of neutron and X-ray scattering, as precise structural evaluation often requires data from both probes, particularly when studying correlations involving light elements such as hydrogen and lithium, or transition metals.

- **Software Integration:** To ensure a smooth workflow for users and enable at-a-time processing from neutron data reduction to *G(r)* creation, we are actively developing a graphical user interface (GUI) that integrates NOVA data reduction software, nvaSq and nvaGr [2-4]. This enables convenient feedback from experimental data confirmation to experimental planning.
- **Simultaneous Fitting:** We plan to expand the platform to enable end-to-end processing, similar to Rigaku's SmartLab Studio II (SLSII) software [5], covering the entire workflow from *G(r)* creation to local structure analysis such as Reverse Monte Carlo (RMC) modeling.

This collaboration with Rigaku is a positive model for facility-industry partnership, demonstrating how sharing the common goal of "seamlessly obtaining high-quality data" can rapidly accelerate development by pooling specialized knowledge and expertise. With NOVA providing high-quality data for short- and medium-range structure analysis in a short time, and the upgraded software ensuring efficient and accurate data processing, the platform is now significantly more robust for the user community.

References

[1] M. Yoshimoto, K. Omote, *J. Phys. Soc. Jpn.* **91**, 104602 (2022).
[2] T. Otomo *et al.*, KEK Progress Report. **2021-1 M**, 48 (2021).
[3] T. Otomo *et al.*, KEK Progress Report. **2012-4 M**, 27 (2012).
[4] K. Suzuya, RADIOISOTOPES. **60**, 63 (2011) (in Japanese).
[5] web page of the SLSII.

T. Honda[1,2,3], M. Yoshimoto[4], H. Ohshita[1,5], and T. Otomo[1,2,3]
[1]Institute of Materials Structure Science, KEK; [2]Neutron Science Section, Materials and Life Science Division, J-PARC Center; [3]Graduate Institute for Advanced Studies, The Graduate University for Advanced Studies, SOKENDAI; [4]Rigaku Holdings Corporation; [5]Neutron Instrumentation Section, Materials and Life Science Division, J-PARC Center

Development of Neutron Spin-Echo Imaging Method at RADEN

1. Introduction

Magnetic imaging method is one of the energy-resolved imaging methods, alongside Bragg-edge imaging and resonance absorption imaging methods. At BL22 RADEN, two types of magnetic imaging, polarimetry method and phase imaging method, are provided a wide dynamic range for sample magnetic field integral values, and the available magnetic field integral values for these methods are 10 to 10^4 [G·mm] and $>10^3$ [G·mm], respectively. They have contributed to achievements in various study fields, including the magnetic fields generated by motors and transformers, magnetic domains in electromagnetic steel sheets, and the magnetization process of NdFeB magnets [1-5]. However, the conventional methods mentioned above could not measure weak magnetic field integral values below 10 [G·mm], and thus could not accept the requirements for weak magnetic field measurement. In this magnetic field region, visualization of current density distributions in lithium-ion batteries and fuel cells could be a research target. In lithium-ion batteries, lithium plating during charging on the anode surface leads to performance degradation, but the specific mechanism by which it affects current density remains unclear. In fuel cells, managing water movement during power generation is important for stable power generation, and research using neutron imaging to visualize water movement has already been carried out; however, the relationship between water movement during power generation and current density has not been clarified. For further improvement of the performance of these industrially important devices, the measuring current density distribution is an essential research theme that cannot be avoided.

2. Neutron Spin-Echo Imaging

To enable these measurements, we developed a novel measurement technique for weak magnetic field visualization at BL22 RADEN. In the magnetic field integral below 10 [G·mm], the precession angle of the neutron spin is small, making it difficult to measure the magnetic field from changes in the transmission intensity from the neutron spin analyzer. To solve this problem, we focused on the neutron spin-echo (NSE) method. The NSE method has a phase shifter coil, which operates independently of the sample magnetic field and rotates neutron spins. Consequently, the observed neutron intensity is expressed as follows,

$$I = N\frac{1+\cos\Phi}{2}. \quad (1)$$

N is the number of neutrons, and the phase Φ includes the magnetic field integral along the neutron flight path, expressed as $\Phi = m\gamma\lambda BL / h$. Here, m, γ, λ, and h are the neutron mass, gyromagnetic ratio, wavelength, and Planck constant, respectively. B is the magnetic field along the neutron flight path, L is the flight path length, and BL is the magnetic field integral value. When the magnetic field integral value B_sL_s due to the magnetic sample is added, the B_sL_s is added as $\Phi' = m\gamma\lambda(BL + B_sL_s) / h$. The difference $\Delta\Phi$ between Φ' and Φ can be seen to give the sample magnetic field integral value as shown in the following equation.

$$\Delta\Phi = \Phi' - \Phi = \frac{m\gamma\lambda B_S L_S}{h} \quad (2)$$

The advantage of the NSE method is that it enables quantitative evaluation of the sample magnetic field integral value from the phase shift $\Delta\Phi$. This technique is expected to allow measurement of weak magnetic field integral values below 10 [G·mm], which was difficult to achieve with conventional methods. Therefore, we installed an NSE instrument at BL22 RADEN.

Figure 1 shows a photograph of the NSE instrument. Within the guide field coil, designed to avoid depolarization of the neutron spins, the system consists of spin flipper 1 (SF1), a phase shifter coil (PS), spin flipper 2 (SF2), and spin flipper 3 (SF3), arranged from upstream. Mezei-type flippers are employed for SF1 to SF3. The sample position is upstream of SF3. Since the beam size of polarized neutrons at BL22 RADEN is 50 mm square, the SF1-3 and PS coils were designed to

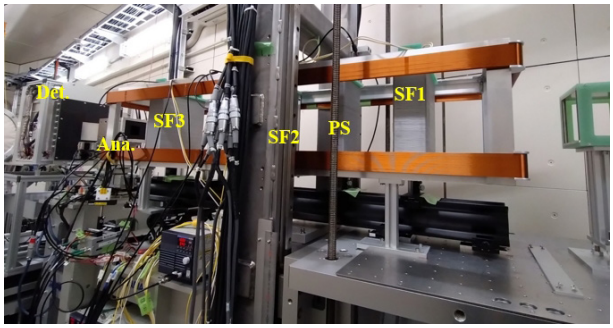

Figure 1. The photograph of the NSE instrument installed at BL22 RADEN.

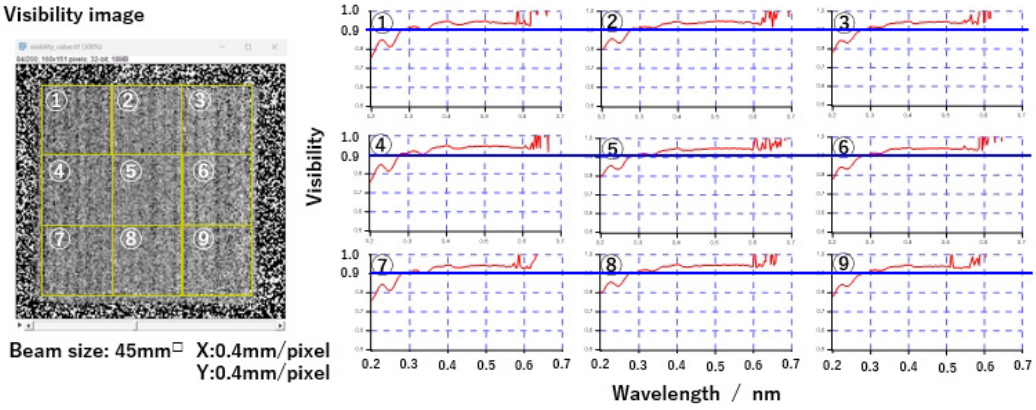

Figure 2. The beam area was divided into nine, and the visibility (neutron polarization) was evaluated for each area.

ensure high magnetic field uniformity (ΔB < 0.0005 G) within the beam region.

3. Demonstration

Demonstration using a neutron beam was carried out at BL22 RADEN (proposal No. of 2023I0022 and 2024C0010). In this experiment, a μNID detector was used [5]. To confirm the uniformity of the magnetic field within the beam region, an important aspect of coil design, the distribution of visibility (neutron polarization) of echo signal was evaluated. Figure 2 shows the direct beam measurement results. The beam size was 45 mm square and pixel size was 0.4 mm square. The beam area was divided into nine regions. The wavelength dependence of the visibility profiles for each area is shown. High visibility over 0.9 was obtained in the wavelength range longer than 0.3 nm. Since the wavelength dependence of visibility in each region showed nearly the same profiles, and highly uniform results were achieved across all nine regions.

Figure 3 shows the side and front views of the sample, as well as a schematic of aluminum wires of the sample. We tried to measure the magnetic field induced by the current when a 0.3 A current was applied to each aluminum wire in the same direction. The graph shown in the bottom-right of Figure 3 shows the line profile of the y-direction magnetic field integral value, $B_y L_s$, of the sample, where B_y and L_s are the y-direction of magnetic field and the thickness of the sample, respectively. As a result, we were able to measure a weak magnetic field integral less than 10 [G·mm]. Compared with the polarimetry method, the sensitivity to weak magnetic field has improved by approximately one order of magnitude.

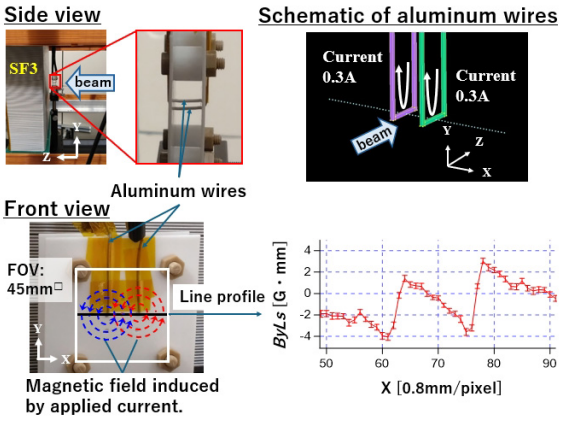

Figure 3. Side and front view of the sample, and the schematic of aluminum wires are shown. The bottom-right is measurement result of the magnetic field induced by applied current.

As a future update plan, we will install a magnetic shield to improve magnetic field uniformity for further improvement sensitivity to weak magnetic fields.

References

[1] T. Shinohara, *et al*, J. Phys.: Conf. Ser. **862**, 012025 (2017).
[2] M. Sales, *et al*., Sci. Rep. **8**, 2214 (2018).
[3] K. Hiroi, *et al*., JPS Conf. Proc. **22**, 011030 (2018).
[4] K. Hiroi, *et al*., Physica B: Condensed Matter. **551**, 146-151 (2018).
[5] T. Shinohara, *et al*., Rev. Sci. Instrum. **91**, 043302 (2020).

H. Hayashida[1], T. Shinohara[2], J.D. Parker[1], T. Kai[2], Y. Matsumoto[1], Y. Tsuchikawa[2], Y.H. Su[2], K. Oikawa[2], Y. Nagai[1], and Y. Kiyanagi[3]
[1]*Neutron Science and Technology Center, CROSS;*[2]*Technology Development Section, Materials and Life Science Division, J-PARC Center;*
[3]*Hokkaido University*

BL23: Polarized Neutron Spectrometer POLANO

1. Introduction

POLANO is a new spectrometer being constructed in MLF with polarization analysis capability [1-5]. Polarization analysis technique in the field of inelastic neutron scattering was formerly developed in the end of the 1960s and early 1970s for reactor-based neutron sources. At that time, a new generation of high-flux neutron reactors became available, which resulted in a resurgence of interest in polarization methods. The first new technique to appear was one-dimensional polarization analysis in 1969 [6]. After many years of the success of experiments involving reactor-based polarization, application of the polarization method to accelerator-based neutron source (pulse neutron) was commenced [7].

The polarization methods for reactor-based and accelerator-based neutron sources are, in principle, similar but there are also significant differences in terms of techniques. The POLANO was designed to realize polarization analysis in inelastic neutron scattering up to an energy (100 meV) higher than that reached in the reactor-based. The construction of the POLANO was initiated in 2013, prior to which, we had many discussions about the project, designs, technical issues and several other items. The major part of the construction of the instrument was completed by 2016, and received the first neutron beam in 2017. In the end of 2019, the general user programs were conducted with unpolarized neutron together with R&D of magnetic devices. Finally, most of the polarization components have been installed on the beam line in 2023 and polarization commissioning has been commenced.

2. Instrument Update

One of big issues in instrumentation at the POLANO is Fermi chopper. It is a device for monochromatizing incoming neutron energy being indispensable for the direct geometry chopper spectrometers. For a reasonable chopper is required as 600 Hz of rotational speed and 1 micro sec of phasing accuracy, that is highly advanced technology [8]. The Fermi chopper at POLANO used in most of experiments are with the condition of rather high frequency in order to gain much higher energy resolution. Firstly, designed Fermi chopper (Type-I) after several years in use encountered several problems, serious loosing phasing control, a large dip structure of unknown cause in the time evolution of rotation signal (see Fig.1(C)). Many of tests to find the reasons and figure out specific causes have been done so far. Main problems on the rotor have now been solved after all. At the same time, brand new chopper (Type-II) was manufactured as seen in Fig.1(A) and (B). Thus, we can safely continue the POLANO operation.

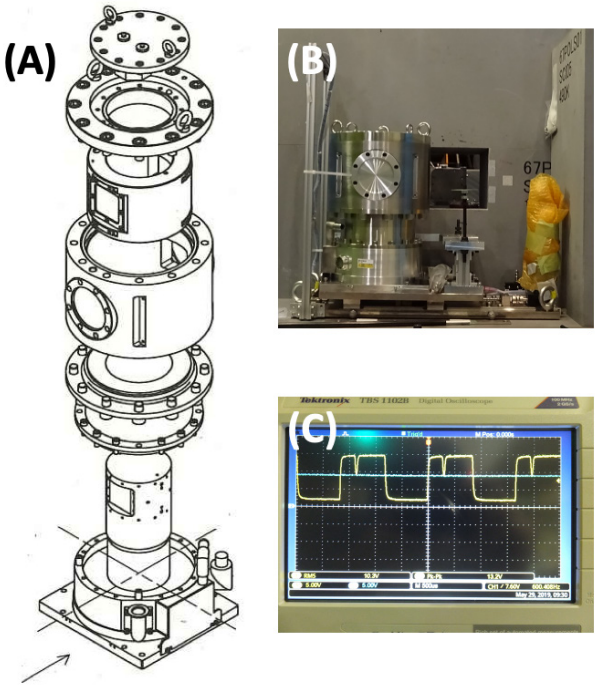

Figure 1. Newly manufactured Fermi chopper (Type-II). (A) The drawing of the Fermi chopper. (B) The chopper installed in the POLANO beam line. (C) Time evolution of the rotation signals (yellow line) for Type-I chopper in oscilloscope showing a deep dip hitting a comparator level in light blue.

Focusing on user use of the POLANO spectrometer, sample environment (SE) devices can be one of key items for a successful experiment. We have made lots of our effort to introduce new SE and to keep maintaining/up-grading the SE devices. Top-loading type refrigerator, which is main device for POLANO experiments was carefully tuned about controlling the heater power and sensor temperatures to obtain more stable temperature on the sample. A 7 T-magnet used as a common device in MLF is also available for POLANO experiments. B_4C liners in sample vacuum chamber where the magnet accommodates were totally refurbished to contain even large SE devices such as a cryo-magnet. Moreover, ^{3}He sorption refrigerator cooling down to 0.3 K is now in service sharing with the other instrument HRC.

These variety of SE devices enable us to widely control external physical parameter investigating wide field of science.

Computing on POLANO is updated. Some of new device modules working on YUI device controlling system are crucial to control and keep watching the status all of devices. For visualizing and analyzing the obtained data, total program HANA is used in our system. So called angle-scan, that is a series of scattering angle measurements rotating the sample step-by-step is one of typical scans for investigating 4-dimensional momentum Q and energy E space. This kind of measurement yields an enormous data set even for single scan. We renewed a HANA PC to high-end machine for handling such a big data. A set of 24 core CPU, 192 GB unified memory and 4 TB SSD storage is now available for users.

3. Scientific Outcome

Firstly, high-energy polarization inelastic scattering is one of our goals. Obviously, the polarization measurements can make the neutron scattering technique fruitful and used in wide field of research from fundamental physics to material sciences. The POLANO is a highly sophisticated polarization inelastic instrument. In the first phase of the polarization scheme, spin exchange optical pumping (SEOP) is used as a polarizer combined with 5.5 Qc bending analyzer mirror that enables the polarimetry measurement up to 42 meV of final neutron energy. A commissioning of the polarization system on POLANO, namely, SEOP polarizer, all of the magnetic systems, and a package of analyzer mirror, was finally initiated. In Fig. 2, an NMR signal monitoring the polarization of ^{3}He spins in a SEOP glass cell. Since our SEOP system has been designed as so-called "*in-situ* SEOP" system, where the spin polarization basically always been checked the neutron polarization while experiments. It will take around 20 hours to almost fully polarized the ^{3}He spins in a SEOP cell, and evaluated a ratio of spin polarization about 83% which is good enough to reasonably polarize neutron spins.

All of the polarization devices accommodated in the beam line were checked and on beam commissioning was initiated. Since the arrangement of analyzer mirror is quite limited in the scattering plane as around 18 degrees, it is necessary to adjust the analyzer position at an interesting scattering angle by rotating the analyzer. The first spin-flip (SF) and non-spin-flip (NSF) signals at scattering angle 40˚ are depicted in Fig. 3. The left in Fig. 3 is the 2D arranged detector array with the neutron spin condition up-up before and after the sample. On the other hand, the right figure shows down-up spin configuration intensities. It was successfully observed large differences in the intensity. This could be the first step to separately observe scattering processes between SF and NSF processes in materials, being enable to distinguish microscopic origin of physical parameters (degrees of freedom).

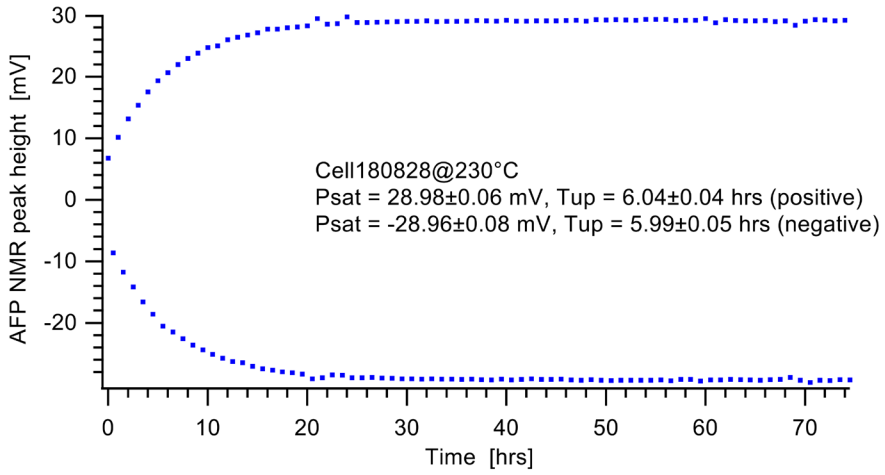

Figure 2. Time revolution of the NMR signal checking a polarization of ^{3}He spins in a SEOP cell. The up and down alternating signals by spin flip are clearly observed. After around 20 hours, the NMR signals are almost saturated corresponding the ^{3}He spin polarization is also completed. The NMR signal value can be translated as 80% of ^{3}He spins, which is rather deserved polarization for polarimetry experiments.

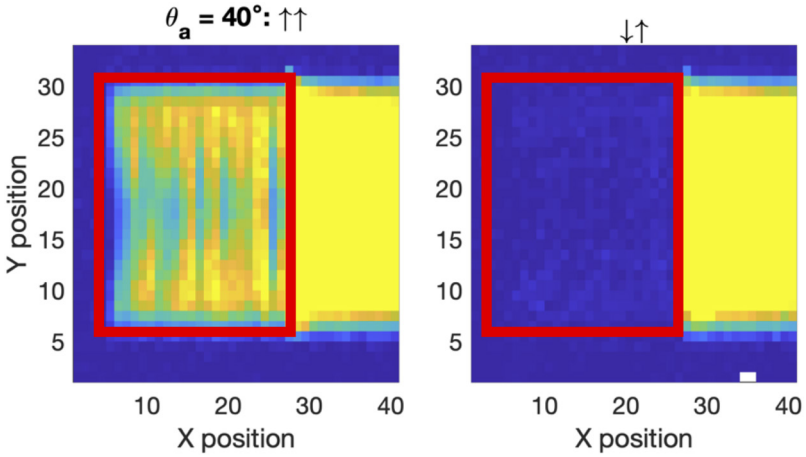

Figure 3. The first polarization measurement at POLANO spectrometer. The neutron spin up-up signals are illuminating at the detectors through super mirror analyzer (left). On the other hand, only few signals have been detected for down-up signals (right).

4. Future Plans

Now we plan to continue the polarization tests. Further tuning and calibrations of devices are indispensable for successful polarization experiments. New computing codes totally different from unpolarized experiment so far are also crucial for analyzing polarimetry. As well as above mentioned overall polarization device commissioning, practical polarization measurements with real samples will be scheduled. I'm trying to study a feasibility of low-energy polarimetry on quasi elastic measurements or low-lying excitations to begin with.

References

[1] T. Yokoo, *et al.*, J. Phys. Soc. Jpn. **82**, SA035 (2013).
[2] K. Ohoyama, *et al.*, J. Phys. Soc. Jpn. **82**, SA036 (2013).
[3] T. Yokoo, *et al.*, Journal of Physics Conf. Series **502**, 012046 (2014).
[4] T. Yokoo, *et al.*, EPJ Web of Conferences. **83**, 03018 (2015).
[5] T. Yokoo, *et al.*, AIP conference proceedings. **1969**, 050001 (2018).
[6] R. Moon, *et al.*, Phys. Rev. **181**, 920 (1969).
[7] J. R. Stewart *et al.*, J. Appl. Cryst. **42**, 69 (2009).
[8] S. Itoh, K. Ueno, T. Yokoo, Nucl. Instr. and Meth. **A661**, 58 (2012).

T. R. Yokoo[1,2,3,4], S. Itoh[1,2,3], K. Ikeuchi[1,2,3], D. Ueta[1,2,3], T. Ino[1,2,3], S. Yamauchi[1,2], N. Kaneko[1], H. Ohshita[1,2], G. J. Nilsen[5], K. Nemkovskiy[5], N. de Souza[6], T. Oku[2], H. Hayashida[7], M. Fujita[8], and M. Ohkawara[8]

[1]Institute of Materials Structure Science, KEK; [2]Materials and Life Science Division, J-PARC Center; [3]Materials Structure Science, The Graduate University for Advanced Studies, SOKENDAI; [4]Graduate School of Science and Technology, University of Tsukuba; [5]ISIS Neutron and Muon Source, Rutherford Appleton Laboratory; [6]Australia's Nuclear Science and Technology Organization; [7]CROSS; [8]IMR, Tohoku University

A large area, rectangular position-sensitive scintillation neutron detector for upgrade of SENJU

1. Introduction

SENJU is a time-of-flight Laue neutron diffractometer constructed in the Materials and Life Science Experimental Facility in the Japan Proton Accelerator Research Complex [1]. SENJU started its operation in 2012 with the original 37 detectors [2]. Most detectors are arranged cylindrically around the sample. Major detector upgrades have been in progress in SENJU. Although some new replacement detectors have been introduced to the instrument [3], there remain significant physical gaps between detectors. These gaps cause large unscanned regions in the reciprocal space, resulting in inefficient data collection. Ideally, such physical gaps should be eliminated. One simple solution is to replace the original "small area" detectors with larger ones. In this paper, the prototype detector that was designed for the SENJU upgrade is presented, followed by some experimental results.

2. A prototype detector

Figure 1 shows a photograph of the prototype detector. Table I summarizes the detector specifications. The prototype detector is made based on ^{6}Li:ZnS scintillator and wavelength-shifting fiber technology. The detector has a neutron-sensitive area of 512 × 768 mm^2 with a pixel size of 4 × 4 mm^2. The neutron-sensitive area is six times larger than the original detector (two times larger in the x-direction and three times larger in the y-direction). The filling factor, defined as a ratio of the neutron-sensitive area to the detector surface, has been improved from 0.73 to 0.85. The 128 WLS fibers are arranged in a regular pitch of 4 mm to make a fiber array for x-coordinate and 192 fibers for y-coordinate. These fiber arrays are sandwiched between flat scintillator screens. The ^{6}Li:ZnS(Ag) screens, purchased from SCINTACOR Co. Ltd., were adopted. The thicknesses of the two scintillator screens are 0.25 mm (upstream) and 0.45 mm (downstream) relative to the WLS fiber arrays. The scintillation light generated in the nuclear reaction of ^{6}Li(n,α)T in one of the scintillator screens is collected by the WLS fibers. To maximize the light collection, both ends of each WLS fiber are connected to a photomultiplier tube (PMT). Multi-anode PMTs (H8804) purchased from HAMAMATSU PHOTONICS K. K. were used. The pixel position of the incident neutron is determined by taking the coincidence of the WLS fibers that were lit in the x and y directions. If the scintillation light is detected across several pixels, the pixel with the maximum detected light intensity is determined as the detection pixel.

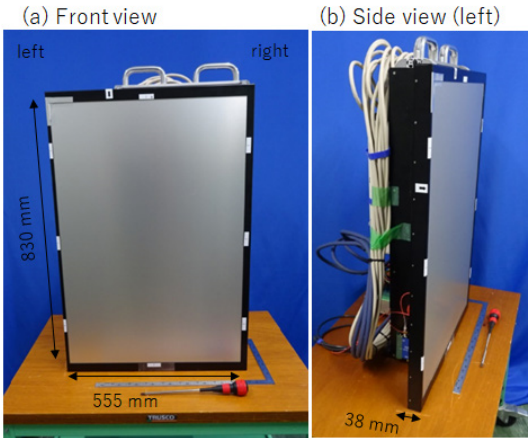

Figure 1. Photograph of the prototype detector.

Table 1. Detector specification [4]

Item	Prototype detector
Neutron-sensitive area	512 x 768 mm^2
Pixel size	4 x 4 mm^2
No. of pixel	24576
No. of electronics channel	128(X) + 192(Y)
Physical size	555^{W} x 830^{L} x $163(38)^{D}$ mm^3
Power dissipation	100 W
Weight	45 kg

3. Experimental results

The basic detector performance was examined by using a pulsed neutron beam at NOBORU at the J-PARC MLF. The position linearity was evaluated over the detector area by scanning a collimated beam that has a size of 1 x 1 mm^2. The incident beam positions were reproduced well without significant deviations both in x and y directions, confirming a good position linearity of the prototype detector.

Figure 2 shows count uniformity measured by using a ^{252}Cf neutron source. The emitted neutrons from the ^{252}Cf were thermalized in the graphite block and the detector was located at a distance of 1850 mm from the source to illuminate the detector uniformly.

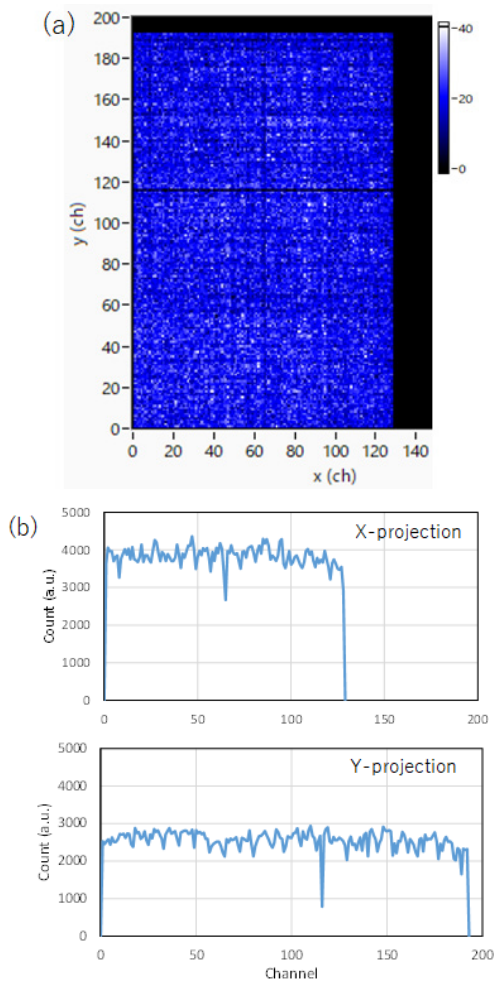

Figure 2. Count uniformity measured with a ^{252}Cf source. (a) Count distribution, and (b) projection of the x and y projection of the data [4].

The detector reproduced uniform neutron distribution well over the detective area. A large count dip occurred at the y channel 116 (Fig. 2 (a)). This dip could be attributed to either fiber breakage or malfunction in the photon counting electronics. In addition to that, small count dips appeared regularly at every 8 channels both in the x and y projections (Fig. 2(b)). These count variations were attributed to the gain variation in the pixel of the multi-anode PMT. Figure 3 shows the count histograms of the x and y projection data. By fitting the histograms with a Gaussian function, the uniformity of the counts was evaluated as a standard deviation. They are 5.9% and 6.9% for x and y projection data. These count variations originated from variations in factors

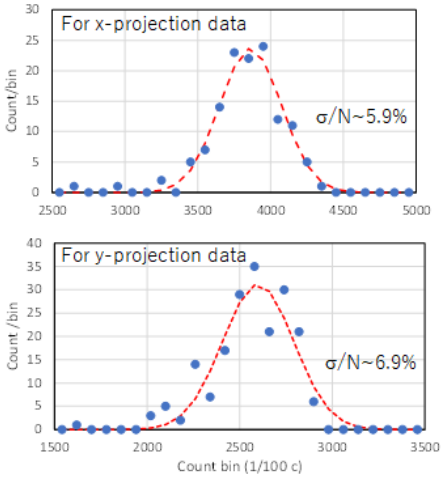

Figure 3. Count histograms for x and y projection data [4].

for each channel, such as neutron absorption rate, light collection efficiency, PMT gain. It should be noted that these position-dependent variations in neutron sensitivity can be calibrated, so they are acceptable for the diffraction measurements at SENJU. The prototype detector exhibited a detection efficiency of 43±3 % for a neutron with a wavelength of 2.1 Å. A ^{60}Co gamma-ray sensitivity was less than 10^{-7}. This detector performance is acceptable for use in the beamline.

4. Conclusions

A large area, rectangular position-sensitive scintillation neutron detector was successfully developed for the single crystal neutron diffractometer SENJU at J-PARC MLF. The detector specifications were specifically designed to fulfill the requirements for the instrument upgrade. Based on prototype results nine beamline detectors have been produced. Two detectors have been installed in SENJU and a feasibility study is being conducted.

References

[1] T. Ohhara, *et al.*, J. Appl. Cryst. **49**, 120 (2016).
[2] T. Kawasaki, *et al.*, Nucl. Instrum. & Meth. A **735**, 444 (2014).
[3] T. Nakamura, *et al.*, JPS Conf. Proc. **33**, 011097 (2021).
[4] T. Nakamura, *et al.*, Presented at J-PARC symposium, Tsukuba, Japan, Oct. 2024

T. Nakamura[1], K. Toh[1], R. Kiyanagi[2], T. Ohhara[2], and K. Sakasai[1]
[1]*Neutron Instrumentation Section, Materials and Life Science Division, J-PARC Center* [2]*Neutron Science Section, Materials and Life Science Division, J-PARC Center*

Sample Environment

1. Activities in JFY2024

Table 1 shows the frequency of the experiments in which the MLF sample environment equipment was used in JFY 2024.

Table 1. Frequency of the experiments in which the MLF sample environment equipment was used in JFY 2024

Name of equipment	No. of experiments
7T superconducting magnet	5
^{4}He cryostat	3
^{3}He cryostat	5
Dilution refrigerator	3
Humidity control system	3
Pulsed magnet system	1

2. Development of a low temperature device for the 7T superconducting magnet.

So far, in the conventional operation of the 7 T superconducting magnet, the achievable lowest temperature at the sample stage was 4 K. However, several users have requested to obtain lower temperatures below 2 K. To meet this requirement, we developed a new sample stick, where heat transfer directly took place between the cooling source and the sample as shown in Figure 1. While the 7T superconducting magnet is used, the specific part of the variable temperature insert (VTI) is cooled down to 1.5 K. Therefore, we expect that the temperature at the sample stage can be lowered below 4 K, and close to 1.5 K, by improving thermal conduction. In the new sample stick, a thermal contact was introduced to the original resin stick. The thermal contact is covered by tin-coated copper mesh and is placed at the coldest part in the VTI. It is connected to the sample stage by a copper rod so that the sample temperature can reach much lower. Using the new sample stick, the temperature at the sample stage reached 3.5 K (3.5 ± 0.3 K).

For further improvement, copper wires were added between the thermal contact and the sample stage.

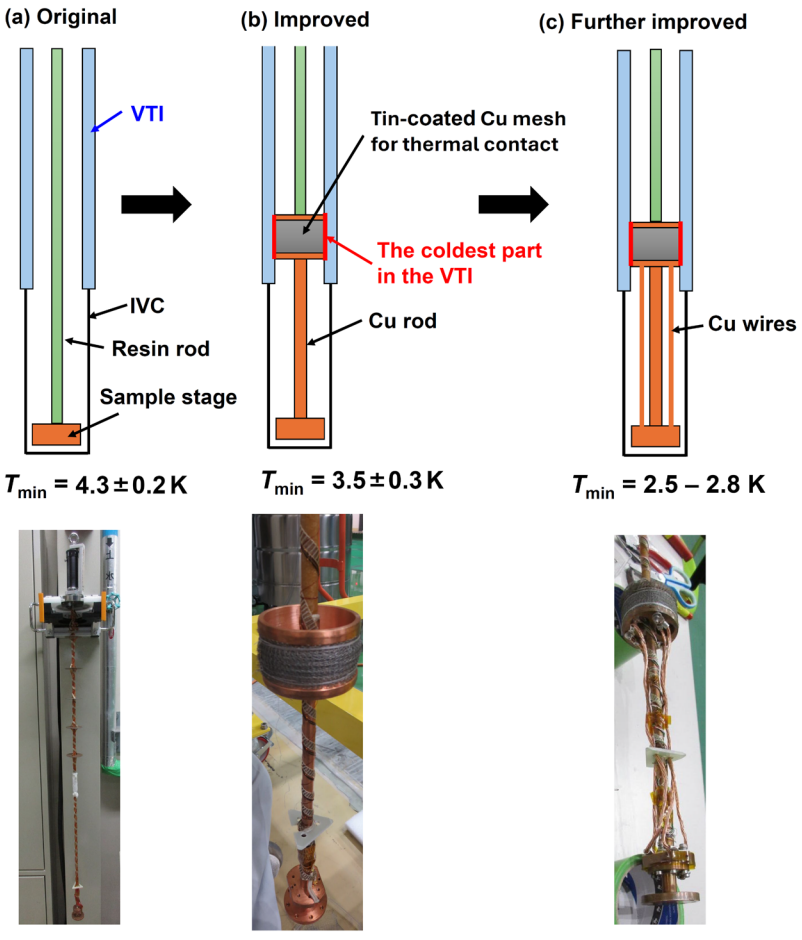

Figure 1. Improvement of the sample stick for the 7T superconducting magnet.

Using the sample stick, the temperature at the sample stage reached 2.5-2.8 K. We are now trying to achieve lower temperatures below 2 K.

3. Pulsed magnet

In this fiscal year, the maximum magnetic field of the pulsed magnet reached 40 Tesla. Figure 2 shows an example of the current waveform of the coil. It produces 40.5 T with the peak current of 7.8 kA. The pulse width at half the peak is 3.0 ms, and the rise time from zero to peak is 2.0 ms.

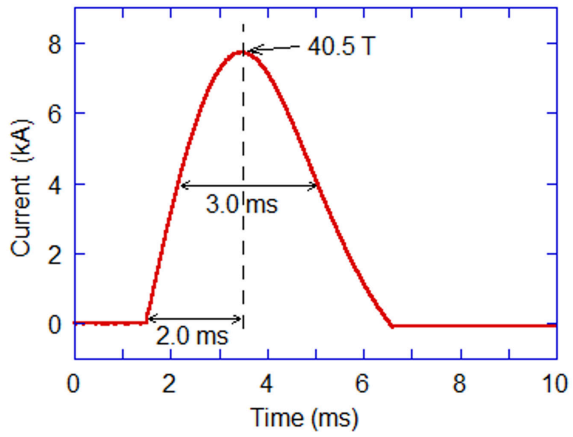

Figure 2. Example of the current waveform of the pulsed magnet.

A longer-pulsed magnet system with the pulse width of approximately 0.5 sec was used in the neutron scattering experiment of the triangular lattice antiferromagnets $CuFe_{1-x}Ga_xO_2$ (x = 0- 0.035) under the magnetic field up to 15 T [2]. We plan to improve the coils and the capacitor bank of the longer-pulsed magnet system to generate up to 20 T.

In recognition of many years of technological development and achievements related to pulsed magnets, the team received the Technology Award from the Japanese Society for Neutron Science (Figure 3) [1].

Figure 3. Dr. Watanabe (J-PARC Center), Associate Professor Narumi (Osaka University), and Professor Nojiri (Tohoku University) were awarded the Technology Award from the Japanese Society for Neutron Science.

4. ISSE Workshop 2024

The 12th International Workshop on Sample Environment at Scattering Facilities (ISSE Workshop 2024) took place at Båstad, Sweden, from September 15th to 20th, 2024. This workshop is held biennially and is organized by neutron/synchrotron facilities in the world that belong to the International Society for Sample Environment (ISSE) [3]. 114 engineers, technicians and scientists engaged in sample environment work participated in the event. 54 oral presentations, including online talks, and 36 poster presentations were given during the workshop. We exchanged information on new techniques related to sample environment and enjoyed interaction and fruitful discussion. The 13th edition will be held in USA in 2026.

References

[1] https://www.jsns.net/award-new
[2] T. Nakajima *et al.*, Phys. Rev. Research. **6**, 023109. (2024).
[3] S. Ohira-Kawamura *et al.*, Neutron News. **34**, 2 (2023).

Y. Sakaguchi[1], R. Takahashi[2], M. Ishikado[1], M. Watanabe[2], S. Zhang[1], Y. Yamauchi[3], S. Ishimaru[3], H. Arima-Osonoi[1], S. Takata[2,4], Y. Su[2], T. Morikawa[1], K. Ohuchi[1], S. Yamauchi[4,5], S. Ohira-Kawamura[2,4], and T. Oku[2]

[1]Neutron Science and Technology Center, CROSS; [2]Technology Development Section, Materials and Life Science Division, J-PARC Center; [3]NAT Corporation; [4]Neutron Science Section, Materials and Life Science Division, J-PARC Center; [5]Institute of Materials Structure Science, High Energy Accelerator Research Organization (KEK)

Instrument Control System at MLF

1. Introduction

A software framework IROHA2 [1,2] was developed to monitor, control and manage measurements for neutron and muon experiments at the MLF. As IROHA2 is used on numerous beamlines, it is continuously improved. However, over 10 years have passed since its development began, resulting in issues such as architectural obsolescence and an inability to meet users' diverse requirements. To address these challenges, we are developing a next-generation instrument control system.

2. IROHA2

IROHA2 is the software framework for controlling instruments at the MLF. Figure 1 shows a schematic diagram of the IROHA2 system and data flow. IROHA2 consists of four servers.

- **Device Control Server**
  communicates with the device to collect its status and send parameter values.
- **Instrument Management Server**
  manages the configuration of the devices used for the experiment and controls the measurements using the data acquisition (DAQ) system.
- **Sequence Management Server**
  controls automatic measurements.
- **Integrated Control Server**
  collects information from other servers and controls devices and automatic measurements centrally.

IROHA2 has a web UI that allows users to remotely execute experiments without the need to install dedicated software.

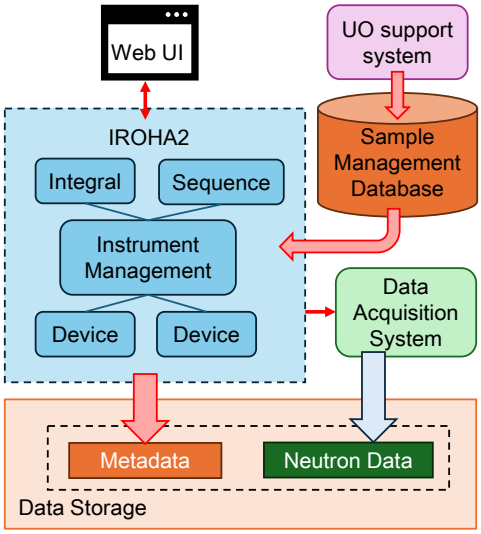

Figure 1. The schematic diagram of the IROHA2 system and data flow.

In recent years, the MLF has been promoting open access to experimental data. To achieve this, it is essential to attach metadata describing the measurements themselves to the neutron/muon data. In FY2024, we added a function to the instrument management server to collect information about experiment users and samples from the sample management database. The sample management database is integrated with the Users Office support system, enabling information on experimental users and samples to be managed. This information is provided to external services such as IROHA2. Instrument Management Server generates the metadata using the acquired information and appends it to the metadata. This enables the systematic generation of accurate metadata.

Several other functional improvements have also been implemented. A summary of the changes can be found on the IROHA2 portal site [3].

3. IROHA3 prototype

The development of IROHA2 commenced in the early 2010s, resulting in issues such as architectural obsolescence. To sustain development of control systems and meet the diverse requirements of users, it is necessary to renovate it. Therefore, we began developing a prototype of a next-generation instrument control system (IROHA3 prototype) in FY 2023.

The features of the IROHA3 prototype are as follows:

- **Data-centric system**
  Centralized management of device and measurement information enables efficient data access and integration with external services.
- **Cloud-enabled**
  It is possible to deploy a database that manages information of instrument and UI front-end on the cloud, enabling easy implementation of remote experiments and remote analysis.
- **Various DAQ system support**
  In contrast to IROHA2 whose system was designed to use DAQ middleware [4], the IROHA3 prototype was developed to operate independently of DAQ middleware, allowing it to handle other DAQ systems.
- **Various control protocol support**
  Introduction of an abstract interface class for device control enables support for various control protocols,

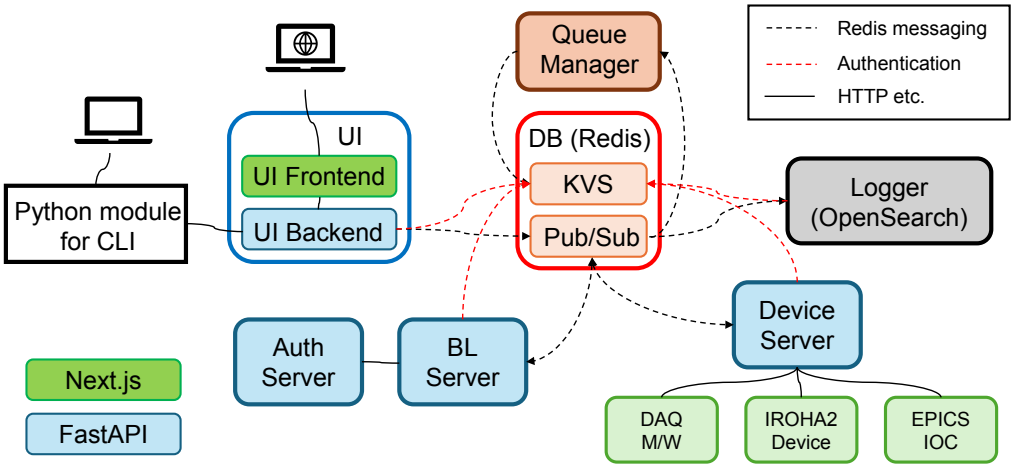

Figure 2. The schematic diagram of the IROHA3 prototype.

including EPICS [5].

- **Command-line interface**
  In addition to the web UI, a command-line interface (CLI) has been introduced. This enables users to create flexible measurement sequences.

The IROHA3 prototype consists of an in-memory database Redis, multiple servers, and user interfaces. Figure 2 shows the schematic diagram of the IROHA3 prototype.

Redis collects information on device status, parameters and DAQ system details in both on-premises and cloud environments. This information is then collected and distributed asynchronously to each server using Pub/Sub messaging. Queue Manager monitors Pub/Sub and synchronizes with KVS (Key-Value Store). KVS stores the latest values exchanged via Pub/Sub, as well as the authentication information required for users to log in to each server. On the other hand, Logger stores persistent data such as metadata and device status logs.

Device Server corresponds to the IROHA2 Device Control Server. It has an abstract interface class that supports various control protocols, and it implements programs for controlling the EPICS IOC, the IROHA2 device control modules and the DAQ middleware on an experimental basis. It periodically collects status information and publishes it to Redis. Furthermore, when the registered device parameters change, the Device Server subscribes to these changes and transmits the values to the devices.

BL Server corresponds to the IROHA2 Instrument Management Server. It manages configurations of devices used for measurement (device sets) and grants users operational and monitoring permissions for these device sets. Auth Server provides user management functions for creating users on the BL Server. This server also generates metadata when measurements are performed.

The prototype provides a web user interface (Web UI) that can be operated via a web browser. The backend uses FastAPI [6] and the frontend uses Next.js [7]. In addition, the CLI is available as a Python module. In FY2024, we upgraded the CLI to make it more user-friendly.

4. Future plan

We have developed the IROHA3 prototype, which is the successor to IROHA2. Over the next several years, we plan to evaluate its performance and identify issues, and then develop IROHA3 based on these findings.

References

[1] T. Nakatani *et al.*, JPS Conf. Proc. **8**, 03613 (2015).
[2] T. Nakatani *et al.*, Proceedings of NOBUGS 2016, 76-79 (2016).
[3] https://mlfinfo.jp/groups/comp/ja/iroha2.html
[4] K. Nakayoshi *et al.*, Nucl. Instr. and Meth. A **623**, 537 (2010).
[5] https://epics-controls.org
[6] https://fastapi.tiangolo.com
[7] https://nextjs.org

H. Hasemi[1], Y. Inamura[2], and K. Moriyama[3]
[1]Technology Development Section, Materials and Life Science Division, J-PARC Center; [2]Neutron Science Section, Materials and Life Science Division, J-PARC Center; [3]Neutron Science and Technology Center, CROSS

Muon Science

Current Status of MUSE

1. Overview

While the MLF achieved stable high-power operation at 1 MW at the beginning of this fiscal year, beamtime before summer maintenance and after February was cancelled due to problems at the neutron source. Though it is regrettable that the muon facility also lost the opportunity to produce results at 1 MW, each muon beamline has been upgraded for the future and stabilized to avoid unexpected trouble. This article provides an overview of some notable topics in the Muon Section.

2. H line extension

In the H-line, the highest-intensity muon beams with a wide-tunable range of momentum are available, and a precise measurement of the hyperfine structure of muonium (MuSEUM), a search for μ-e conversion (DeeMe), *etc.*, are at present conducted in only the H1 general-purpose experimental area. The extension plan for the new H2 area was launched, and a new branch was constructed. In the H2 area, the frontend part of the muon accelerator will be installed. It will be extended further to produce a novel low-emittance muon beam by accelerating muons up to 212 MeV using linear accelerators, most of which will be installed in an extension building next to the MLF. The low-emittance muon beam enables the J-PARC muon g-2/EDM experiment and a transmission muon microscope (TμM). The laser resonant ionization method developed in the U-line was adopted for muon cooling, which is key to efficient acceleration, and the preparation of an intense VUV laser system has been carried out. The beam commissioning is planned for the next fiscal year. As shown in Fig. 1, a new solenoid and a new quadrupole triplet with wide apertures of 610 mm and 400 mm, respectively, were installed after the bending magnet that switches between the two experimental areas. As the final focusing magnets to the H2 area, they can achieve a low-loss transmission and a low-leakage field on the muon stopping target.

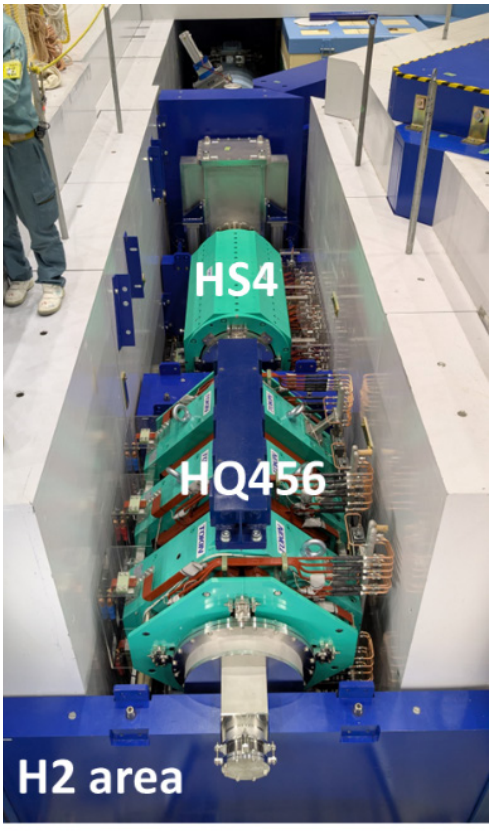

Figure 1. New magnets installed in the extension of the H line to the H2 area.

3. S line kicker system

The S line provides muon beams to all four experimental areas simultaneously; two areas are under operation, and the others are planned. A kicker magnet enables this operation by separating the double bunch structure of the muon beam. The kicker power supply consists of 24 MARX-type high-voltage generator units. In the original design, Si MOS-FETs were employed for fast switching (Fig. 2.). In recent years, the number of failure events in the MARX unit has increased, resulting in the stoppage of user experiments. The cause was identified as deterioration due to the aging of the Si MOS-FET (Fig. 3.). Because Si units were discontinued and SiC units became compatible, we started replacing the Si MOS-FETs with SiC units. In the last fiscal year, a

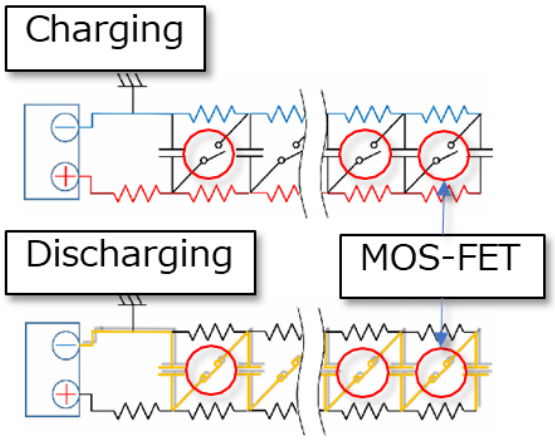

Figure 2. A schematic figure of the MARX circuit.

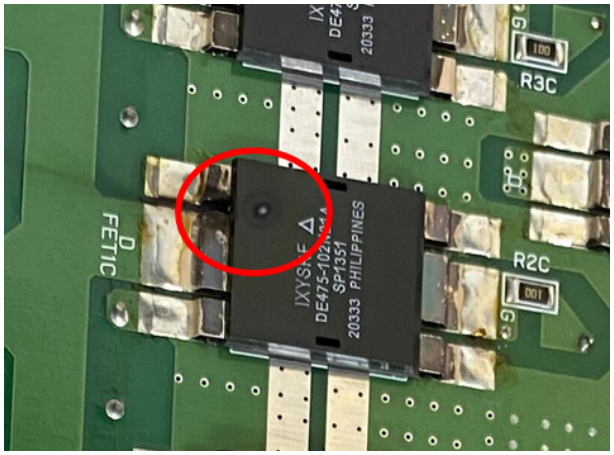

Figure 3. The outer mold is damaged in the failed MOS-FET, suggesting heat due to conduction between the drain and the source.

MARX unit was replaced with a SiC-based unit to demonstrate the operation mixed with the existing Si-based units. Based on the positive results, we replaced the other three units with SiC-based units and started fabricating substitutes for the remaining units in this fiscal year. In the next fiscal year, the whole system will be replaced. So far, no failures have occurred in the replaced units.

4. Progress in the U line

The U line provides the highest intensity surface muon beam among the four MUSE beamlines dedicated to generating the ultra-slow muon (USM) beam, which is essential for studying the material properties of thin films and interfaces. In the last fiscal year, improvements in USM beam transport efficiency and better agreement with simulations were achieved. In this fiscal year, we focused on understanding the surface muon beam to enhance the USM yield and stability further. The generation efficiency of USM is critically dependent on the spatial overlap between the surface

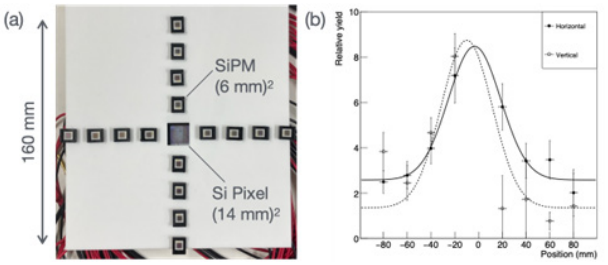

Figure 4. Surface muon beam profile monitor: (a) Photograph of the detector. A 50 μm thick scintillation film was placed directly on top of the SiPM. (b) Profile measurement result under the transport conditions normally used for USM generation.

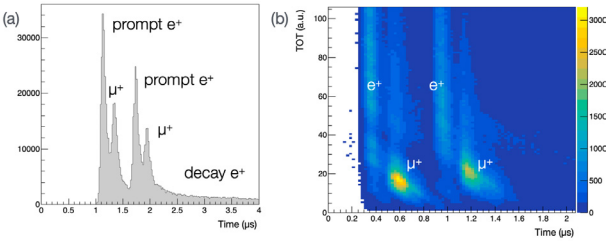

Figure 5. Surface muon measurement with a silicon pixel detector: (a) Time spectrum, (b) Correlation between TOT and time. TOT is a quantity corresponding to the pulse height of the signal when a particle hits a pixel. TOT distinguishes between muons and positrons.

in Fig. 4. A detector based on the Timepix3 chip, developed by CERN, was integrated into the central part of the monitor. Figure 5 shows the measured time spectrum and the time-over-threshold (TOT)-time correlation. It was demonstrated that the beam flux can be measured while avoiding pileup effects. Using this detector, we can observe the source beam directly to identify and resolve hardware issues in the transport system. Moving forward, we will increase the USM beam intensity and stability.

N. Kawamura[1,2]
[1]*Muon Science Section, Materials and Life Science Division, J-PARC Center,* [2]*Institute of Materials Structure Science, KEK*

Current Status of the muon production target

At J-PARC MLF, a 1-MW, high-intensity proton beam with an intensity of 0.33 milliamps is accelerated to 3 GeV and irradiated onto a graphite target to generate a high-intensity muon beam. The 2 cm thick, 33 cm diameter graphite target is used for this process. It rotates at 15 revolutions per minute to disperse radiation damage.

1. Replacement of rotation introducer

Maintaining the rotation system is crucial for ensuring the safety of the target. During the 2024 summer maintenance period, the rotation introducer, which transmits rotation torque to the rotation axis in a vacuum, was replaced. This was the first replacement since the vacuum rotation coupling was changed to an Oldham coupling two years ago [1]. Over the past two years, the rotation status has remained stable, with no significant increase in torque, which confirms the integrity of the Oldham-type coupling. The replacement work was carried out while managing radiation exposure, which was significantly below the legal limit.

2. Cask maintenance

Cask is transport container with a shielding function, used to transport and exchange high radiated targets and other assembly (Fig. 1). The cask has gripping device which can grab, hold, and release the objects, so it can remotely handling activated objects. Therefore, cask maintenance is important in order to be able to deal with emergencies such as sudden target changes. We have carried out an oil change in gearbox for the first time in seven years by the manufacturer's technical support (Fig. 2). And we measured the chain elongation, we checked elongation percentages is within 2%. And we carried out the operational tests ourselves (Fig. 3), We have confirmed that it works fine. As a result, the cask is ready for use, we have enabled to carry out the regular maintenance ourselves through this experience.

Figure 1. Moving casks with a crane.

Figure 2. Supply grease to bearing box.

Figure 3. Operational tests that handling jig for target.

References

[1] S. Matoba et al., KEK-MSL Report 2022, p3.

S. Matoba[1,2] and H.Sunagawa[1,2]

[1]*Muon Science Section, Materials and Life Science Division, J-PARC Center;* [2]*Institute of Materials Structure Science, KEK*

Development and commissioning of the D line

1. Introduction

The D-line at MLF MUSE features a long superconducting solenoid (Fig. 1) capable of providing positive and negative decay muons with momenta from a few MeV/c up to 120 MeV/c, in addition to surface muons. The MLF's primary proton beam energy is as high as 3 GeV, which results in a high negative muon yield. Furthermore, thanks to the recent increase in beam power, the world's highest intensity positive and negative muon beams are now available. Utilizing this high-intensity negative muon beam, various experimental applications have been developed, such as non-destructive elemental analysis using negative muon characteristic X-rays and negative muon spin rotation/relaxation(μSR). This report focuses on a technical issue encountered within the long solenoid magnet system and provides an update on its current status.

2. Small Gas Leak in the Refrigerator for the D-line Solenoid

This long superconducting solenoid magnet must be cooled below its superconducting transition temperature during operation. We utilize a refrigerator system (TCF50) to liquefy He gas and maintain this solenoid at a low temperature (Fig. 1).

During operation in FY2023, we observed that the opening of the adiabatic expansion valve (the so-called Joule-Thomson/JT valve, Fig. 2) had to be slightly closed compared to previous conditions to maintain the system's cooling efficiency. This observation suggested the possibility of a malfunction.

We initially suspected aging deterioration in the sealing sheet of the JT valve, and subsequently replaced this component in December 2023. However, test operation after the exchange revealed that the valve opening

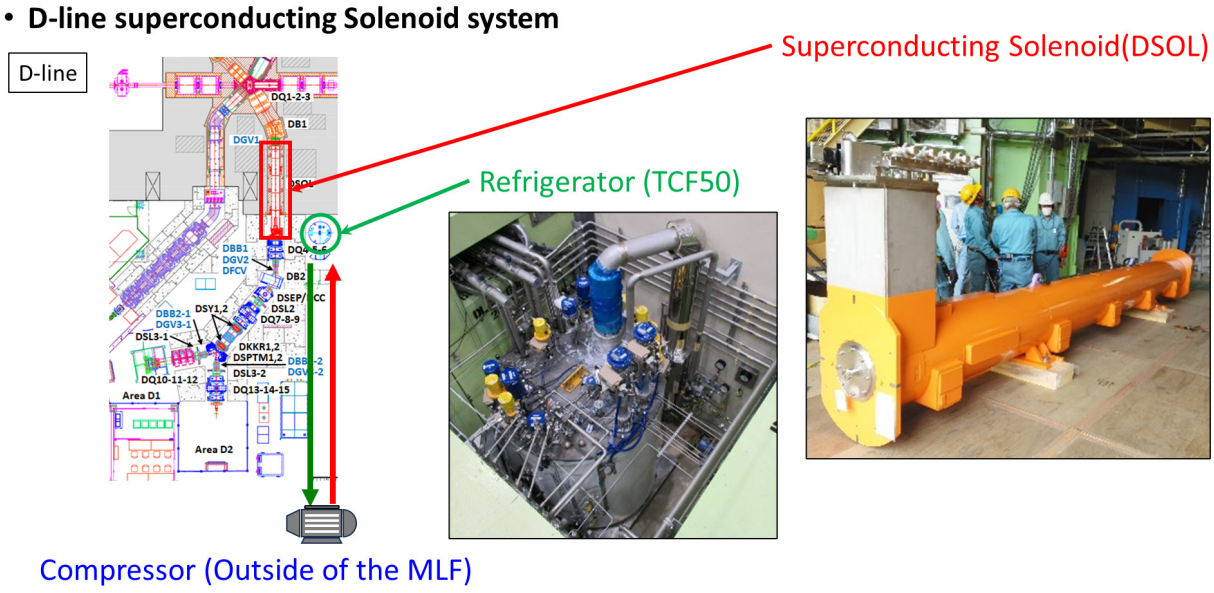

Figure 1. Schematic view of the superconducting solenoid system including its refrigerator and compressor.

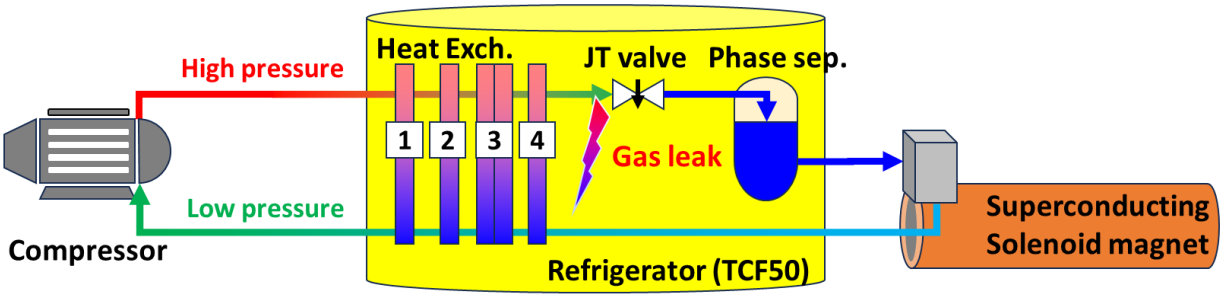

Figure 2. Schematic diagram of the Refrigerator and related system.

did not recover to its normal operation setting. For this reason, we then suspected that a small gas leak was occurring in another part of the refrigerator, specifically somewhere between the high-pressure line and the low-pressure line.

Consequently, during the 2024 summer shutdown, we opened the refrigerator's lid and removed the internal components to localize the leak. In this investigation, we used a stethoscope (Fig.3(a)) to check the origin of the leaking sound and finally identified that the sound originated from the **4th heat exchanging component** (Fig.3(b)) or further downstream (including the phase separator and related components on the superconducting magnet side).

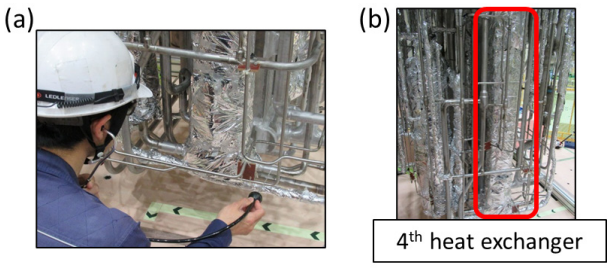

Figure 3. (a) Investigation of leaking sound using a stethoscope. (b) The location of the 4th heat exchanging.

Following these findings, we reviewed the refrigerator diagrams in detail once again and discovered piping inside the phase separator (vapor-liquid separator) that is unused in our operating configuration (Fig.4). Upon closer inspection, we confirmed that this piping was silver-brazed inside the phase separator.

Based on deductions made from the observed changes in the needle valve opening and the rate of at which liquid helium accumulation, we realized there is

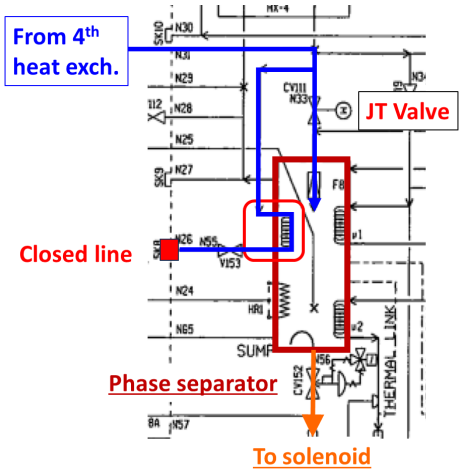

Figure 4. Schematic diagram around the phase separator.

a possibility that high-pressure line gas inside this unused piping is leaking into the phase separator side at the brazed joint. Since the work to remove piping inside the phase separator must be conducted during a long-term shutdown, we plan to disconnect this piping from the system during the Summer 2025 maintenance period.

3. Summary

A small helium gas leak was detected in the D-line solenoid refrigerator during FY2023 operation, observed by the necessity to adjust the JT valve. Initial repair attempts failed. Investigation during the 2024 summer shutdown localized the leak to the 4th heat exchanger or downstream. The probable cause is a leak at the brazed joint of unused piping inside the phase separator. This faulty piping will be disconnected during the Summer 2025 maintenance period to restore normal operation.

S. Takeshita[1,2] and P. Strasser[1,2]

[1]*Muon Science Section, Materials and Life Science Division, J-PARC Center;* [2]*Institute of Materials Structure Science, KEK*

Development of D1 Instrument and Sample Environment

Positive and negative muons are delivered to the D1 and/or D2 at the D-line. The μSR spectrometer is installed as a main and fixed instrument in the D1 area. Since the D1 has high-momentum muons, surface muons, and negatively charged muons, all types of μSR measurements except ultra-slow μSR can be carried out. In particular, unique sample environments, such as very low temperatures using the dilution refrigerator and high pressure, can only be achieved at the D1. Figure 1 shows the μSR spectrometer. D1 is used not only for μSR, but also in various scientific fields such as atomic or nuclear physics. Here, we report on the current development of the experimental apparatus for the experiment at D1.

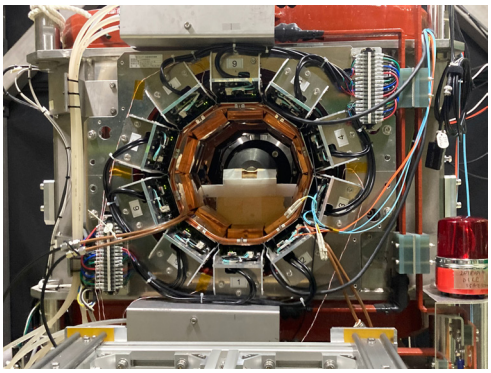

Figure 1. μSR spectrometer at the D1.

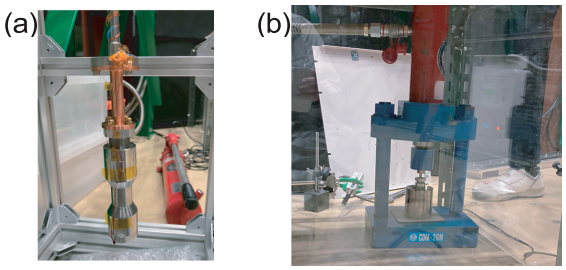

Figure 2. High-pressure μSR apparatus at the D1.

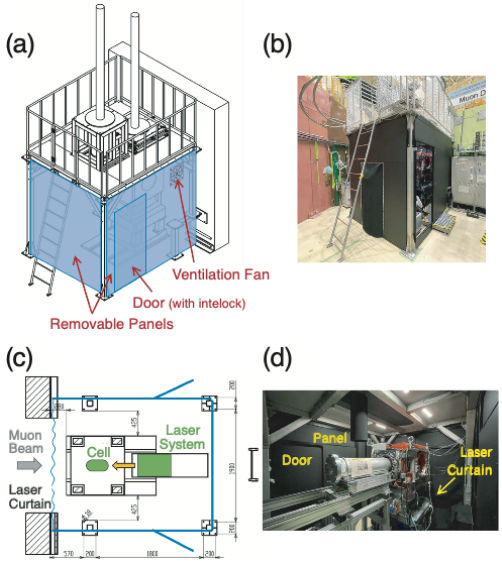

Figure 3. Removable laser enclosure for laser experiments.

1. High-pressure μSR apparatus at D1 area

Pressure is an important, controllable parameter in the study of materials. Applying pressure can tune interaction strengths and sometimes cause a phase transition. For μSR measurements, high pressure is also a crucial experimental condition and is often used to study material properties. A high-pressure μSR experiment has been developed at D1 (2024A0195, PI W. Higemoto), and μSR experiments under high pressure up to 1.5 GPa can currently be performed. As shown in Fig. 2(a), a piston cylinder type high-pressure cell was used for 2024A0195. Pressurization is carried out in the D1 area, as shown in Fig. 2(b). The details of the pressure cell are presented elsewhere [1].

2. A setup for experiments with laser at D1 area

A removable laser enclosure was constructed for the laser experiment (2024A0075, PI P. Strasser) in the D1 area. As shown in Figs. 3(a-d), the μSR spectrometer at D1 was covered by black, removable panels to prevent laser light leakage. The laser was installed and irradiated from the downstream side of the spectrometer. This setup can be prepared relatively easily because it allows the μSR spectrometer to be placed in position without being removed.

References

[1] S. Saito, W.Higemoto *et al.*, JPS Conf. Proc., *in press*.

W. Higemoto[1,2,3]

[1]*Advanced Science Research Center, JAEA;* [2]*Muon Science Section, Materials and Life Science Division, J-PARC Center;* [3] *Department of Physics, Institute of Science Tokyo*

Development of D2 (Muonic X-ray Element Analysis) Instrument and Sample Environment

The D2 experimental area provides various momentum of decay muons with a large space of about 4 m x 4.5 m, allowing users to bring in their own equipment or chambers needed to realize their experiments. This has led to publications of remarkable results in elemental analysis [1-2] and Ph.D. theses [3-4] and two prizes in FY2024. Dr. M. Katsuragawa (Kyoto Univ.) won the 6th Fumiko Yonezawa Memorial Award of the Physical Society of Japan for her research on application of muonic X-rays with CdTe-DSD detectors. Dr. S. Okada (Chubu Univ.) and his group won the Koshiba Awards of Foundation for High Energy Accelerator Science for their success of high-precision spectroscopy on X-rays from muonic atom using a cryogenic micro calorimeter based on a super conduction phase (TES) experiment revealing formation process of muonic atom and dynamics at femtosecond [5].

Unfortunately, we had to cancel some of user programs after May in 2024A and no beam in 2024B, respectively, due to the troubles of the neutron target at MLF, J-PARC. We have originally planned 6 proposals including the P-type proposals conducted at the D2 experimental area mostly using negative decay muons [6-7] in FY2024. Their themes were primarily elemental analysis, fundamental physics and nuclear capture. Only these experiments were performed in FY2024:

[2024A0202] Development of a new non-destructive elemental analysis method for trace components by muon-induced gamma-ray measurement (M. Inagaki)

[2024A0200] Evaluation of the SiC semiconductor sensor for the COMET muon beam monitor (Y. Fukao)

[2024A0199] Study of muon diffusion in cold metals aiming at the development of a new slow muon beam generation method (Y. Nagata)

A KEK long-term S2 project led by Dr. Umegaki (KEK) to achieve an imaging technique of muonic x-rays from lithium using Si DSD and SOI pixel imagers [8-9]. In the project, they also measured a beam profile using an imaging plate. They obtained an image convoluted with the beam profile (Fig. 1)[10].

For elemental analysis with muonic X-rays at D2, we have improved the semispherical chamber for a higher rate of measurements so that nine LEGe detectors can be installed in the chamber as Dr. Tampo's initial design [11] (Fig. 2). With combination of the chamber and the analysis software to analyze data instantly during measurements, we can easily get data in short time. The software was updated every year. Those were useful in experiments of "Integration of arts and sciences (Bunri-yugo)" program in 2024A, including parts of the shachi statue (Shachi-hoko) equipped on the roof of Nagoya castle and bronze cultural heritage samples.

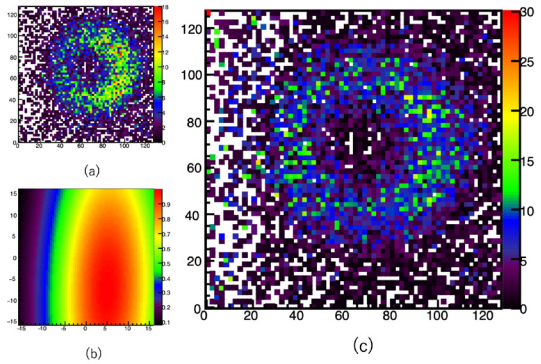

Figure 1. (a) A raw image obtained with Si DSD, (b) a profile of muon beam, and (c) an image deconvoluted with the beam profile.

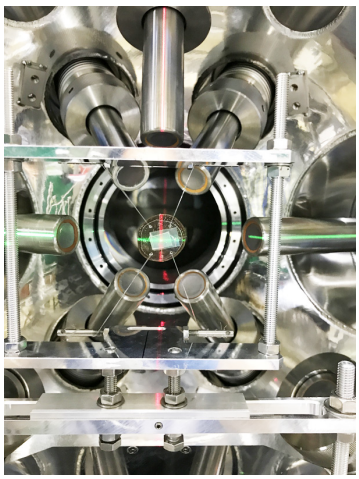

Figure 2. Measurement system with 9 Ge detectors.

Liq. N_2 is essential and needs to be supplied twice a day to Ge detectors. Dr. S. Takeshita has improved our automatic liq. N_2 filling system from 6 to 12 channels to cover 9 Ge detectors and additional detectors. This may

allow us to keep on an experiment without disturbing for liq. N_2 supply for several days.

We also applied a new automatic booster of high voltage power supply for Ge detectors to reduce staff effort, while HV power was manually supplied for each detector before.

Dr. S. Matoba and Dr. Tampo developed a technique of beam tuning with low momentum such as 4.5 MeV/c using a micro channel plate (MCP) [Fig. 3]. Since such low-momentum muons can only be used at J-PARC in the world, it has been highly demanded to get fine tune of the beam, especially for elemental analysis on the surface of samples with muonic X-rays. However, number of muons with momentum of 4.5 MeV/c is extremely low and we could not obtain enough signal intensity using a scintillator for automation tuning program "FORTUNE". In the program, parameters for current values of the 16 magnets on D-line should be changed and each point should take less than 10 minutes. Since the MCP produces a strong signal light even for muons with the momentum of 4.5 MeV/c, they have found that this technique can provide about 1.3 times stronger intensity, and it is sufficient for the tuning program. From this trial, it is expected that we succeed to accomplish the beam tuning for muons with lower momenta using the MCP.

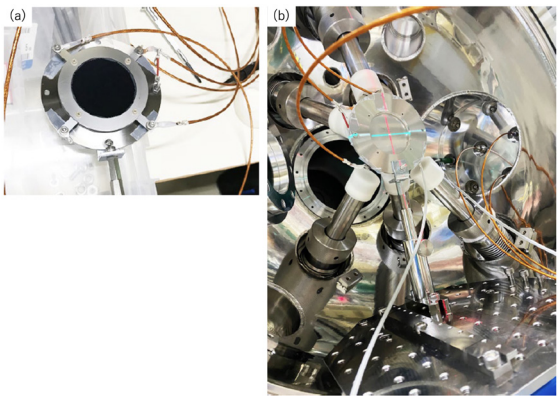

Figure 3. (a) The front of MCP and (b) MCP set at the center of the beamline in the hemispherical chamber.

In response to the growing interest in elemental analysis with muonic X-rays at J-PARC year by year, we have started to hold a sub-program advisory committee (PAC) for "Integration of arts and sciences (Bunri-yugo)" to make suggestions on the proposals for cultural heritage research to the Muon PAC. Before the PAC meeting, we opened proposals related to cultural heritage research from Japan. The proposals can be submitted in Japanese so that researchers with the background of history, heritage science, or museums can join to beam science. Then, the sub PAC meeting members evaluated 7 proposals with order of priority for 2024B. However, they were postponed to 2025FY due to the beam operation trouble in 2024B.

Acknowledgments

The development of the software that we showed here was conducted as a part of "integration of arts and sciences" research program promoted by the KEK IMSS MSL and a part of Dr. Miyake's S1 project. It was also supported by JSPS Grant-in-Aid for Scientific Research on Innovative Areas "Toward new frontiers: Encounter and synergy of state-of-the-art astronomical detectors and exotic quantum beams". Dr. Umegaki's S2-type project is supported by JST K Program Grant Number JPMJKP24J1.

The authors appreciate the cooperation of Mr. Shogo Doiuchi, Dr. Akiko Hashimoto, Mr. Sota Suzuki, Dr. Amba Datt Pant, Dr. Soshi Takeshita, Dr. Patrick Strasser and other members of the Negative Muon Group.

References

[1] K. Ninomiya *et al.*, Meteorit. Planet. Sci. **59**, 2044-2057 (2024).
[2] K. Ninomiya *et al.*, J. Radioanal. Nucl. Chem. **333**, 3445-3450 (2024).
[3] The Ph.D. thesis is related to R. Mizuno *et al.*, JPS meeting, Tokyo, 20pV2-2 (2024).
[4] The Ph.D. thesis is also related to M. Niikura *et al.*, Phys. Rev. C **109**, 014328 (2024).
[5] T. Okumura *et al.*, Phys.Rev. Lett. **127**, 053001 (2021).
[6] S. Takeshita *et al.*, Interact. **245**, 38(1-15) (2024).
[7] K. Shimomura *et al.*, Interact. **245**, 31(1-6) (2024).
[8] R. Nishimura *et al.*, JPS meeting, Tokyo, 16aWB105-5 (2024).
[9] Y. Mitani *et al.*, JPS meeting, Tokyo, 16aWB105-4 (2024).
[10] S. Takeda *et al.*, in preparation.
[11] M. Tampo *et al.*, Interact. **245**, 39(1-9) (2024).

I. Umegaki[1,2] and M. Tampo[1,2]
[1]*Muon Science Section, Materials and Life Science Division, J-PARC Center;* [2]*Institute of Materials Structure Science, KEK*

Muon Beamline Magnets and Power Supplies Update – Manufacturing of H-line Magnets and Power Supply –

1. Introduction

A triplet magnet (HQ4-5-6) and a solenoid magnet (HS4) were manufactured to transport muons to the new experimental area (H2 area) of the high-momentum muon beamline (H-line). We calculated the field of HQ4-5-6 and HS4 with a 3-dimensional field analysis program (OPERA-3d) to confirm that the desired specifications could be achieved. After the magnets were manufactured, magnetic field measurements were taken to compare them with the analysis model. After that, they were installed in the beamline and adjusted with their power supplies.

2. Design of HQ4-5-6 and HS4

Both HQ4-5-6 and HS4 have large-diameters (HQ4-5-6: φ 400 mm, HS4: φ 610 mm), but they should be fitted in a limited space in the beamline. In addition to these conflicting requirements, the magnets were designed using OPERA-3d to satisfy the magnetic field requirements to transport high-intensity surface muons to the H2 area.

For HQ4-5-6, the pole shapes and endguards were optimized to ensure a wide GL-homogeneity and minimize leakage magnetic fields, resulting in the design shown in Fig. 1.

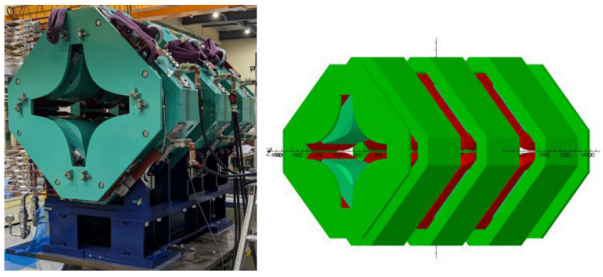

Figure 1. Photograph (left) and analysis model (right) of HQ4-5-6.

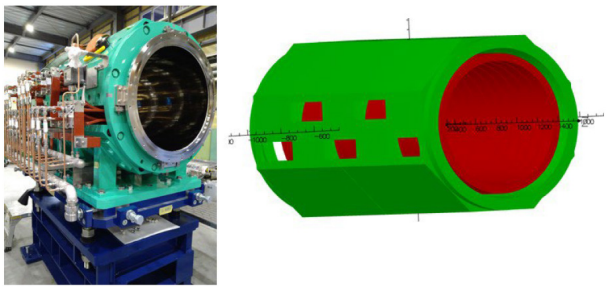

Figure 2. Photograph (left) and analysis model (right) of HS4.

For HS4, the number of yoke divisions and coil extraction ports were incorporated into the analysis model, and a model shown in Fig. 2 was created to confirm whether the required magnetic field could be achieved.

3. Parameter measurement

After manufacturing HQ4-5-6 and HS4, various parameter measurements and magnetic field measurements were performed. The parameters of HQ4-5-6 are shown in Table 1, and those of HS4 are shown in Table 2. Both were found to be generally consistent with the calculation results. Magnetic field measurements and comparisons with OPERA are shown in Fig. 3 and 4. The measurement and calculation agreed well for HQ4-5-6, but some differences were observed for HS4. We suppose that the cause might be misalignment during the magnetic field measurements (including probe settings).

Table 1. Parameters of HQ4-5-6.

	Calculation	Measurement
Coil Resistance (20°C) [mΩ]	106	93.9
Current [A]	500	400
Voltage [V]	53	48.5
Gradient of magnetic field [T/m]	1.32	1.276
Water Flow [L/min]	28.8	28
Temperature rise of cooling water Δt [°C]	15.0	8.9
Inductance [mH]	22.2	9.3 (120 Hz)/ 4.7 (1 kHz)

Table 2. Parameters of HS4.

	Calculation	Measurement
Coil Resistance (20°C) [mΩ]	265	254.5
Current [A]	500	500
Voltage [V]	132.5	133.65
Magnetic field [T]	0.18	0.1797
Water Flow [L/min]	46.1	59.5
Temperature rise of cooling water Δt [°C]	24	14.7
Inductance [mH]	26.8	29.4 (120 Hz)/ 4.7 (1 kHz)

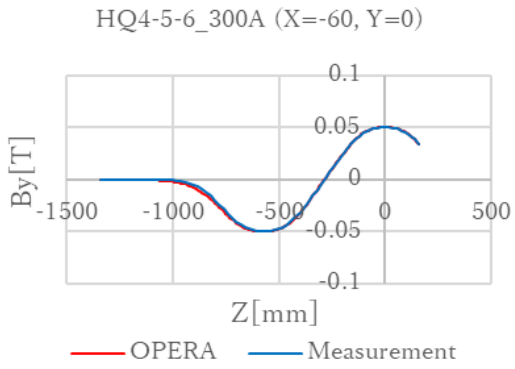

Figure 3. Comparison between measurement and calculation of the magnetic field along the Z-axis when HQ4-5-6 were excited simultaneously.

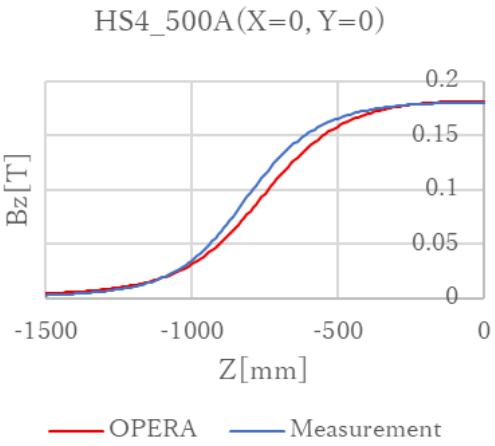

Figure 4. Comparison between measurement and calculation of the magnetic field along the Z-axis.

4. Power supply production and adjustment with magnets

Since there was no power supply for HS4, we evaluated the inductance based on calculations of the Nagaoka coefficient and stored energy from OPERA-3d and then manufactured a new power supply (160V 500A). On the other hand, the power supplies for HQ1-2-3 are also used for HQ4-5-6, because they have load switching functions. After installing each magnet, we connected its power supply, performed initial adjustments, and confirmed that the rated current could be applied safely.

5. Summary

HQ4-5-6, HS4, and HS4 power supply were manufactured to transport high-intensity surface muon beams to the H2 area. Each magnet was confirmed to generate the required magnetic field, and after adjustment with the power supplies, they have been operating without any problems.

T. Yuasa[1,2], T. Yamazaki[1,2], H. Fujimori[1,2], and N. Kawamura[1,2]
[1]Institute of Materials Structure Science, KEK; [2]Muon Science Section, Materials and Life Science Division, J-PARC Center

Transmission of D-line water leak detection point

1. Introduction

The muon beamlines, which transport muon beams to the experimental areas, are equipped with many electromagnets and corresponding power supplies. These devices require cooling water.

If cooling water leaks inside the devices, a short electrical circuit may occur, potentially resulting in device failure. To prevent this issue, each beamline is equipped with a water leak detection system that immediately detects such leaks.

These water leak status signals are transmitted to the MLF control room and notified to the operator. When the operator receives this signal, they contact the muon staff, and have them respond to the issues. Recently, there has been a request for information on the water leak location in the D-line, so we have increased the number of alarm signals from the water leak detection system to the MLF control room. This paper explains the transmission of these water leak detection signals.

2. The transmission of water leak signal

The water leak signals from the detection system are transmitted to the MLF control room via the following route:

- Detection of water leaks by the system
- Transmission of alarm signals to the PLC (Programmable Logic Controller) in the MLF experimental hall
- Transmission of alarm signals from the PLC to the MLF control room via MELSEC-Net [1]
- Indication of alarm signals in the MLF control room

The indicator for the water leak detection system in the D-line is installed in the D-line cabin. Figure 1 shows the indicator for the D-line water leak detection system.

Figure 1. The indicator for the D-line water leak detection system.

The water leak indicator accommodates five water leak detection sensors and sends individual signals indicating that each sensor has detected a water leak. It also sends a collective water leak signal that combines these individual signals.

Until now, the D-line water leak signal has been sent to the MLF control room only as a summary signal. To indicate the location of water leaks, it was necessary to transmit five additional contact signals to the PLC, which required the Installation of a new signal cable.

The MELSEC-Net is installed between the PLCs in the MLF experimental hall and the MLF control room.

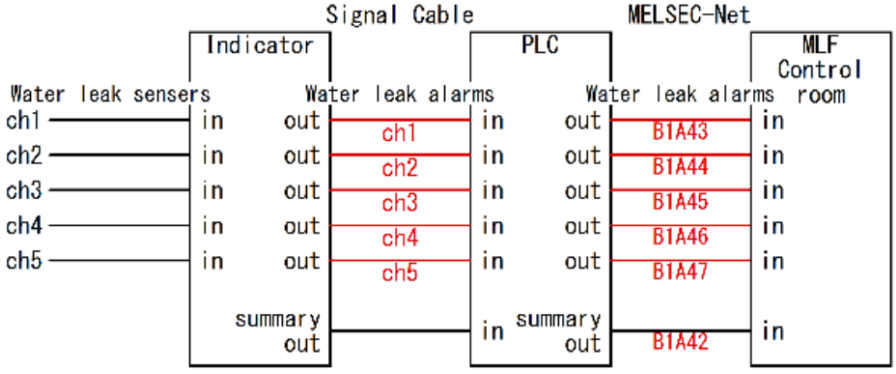

Figure 2. The transmission of water leak alarm signals. (Red notation: Newly added designs.)

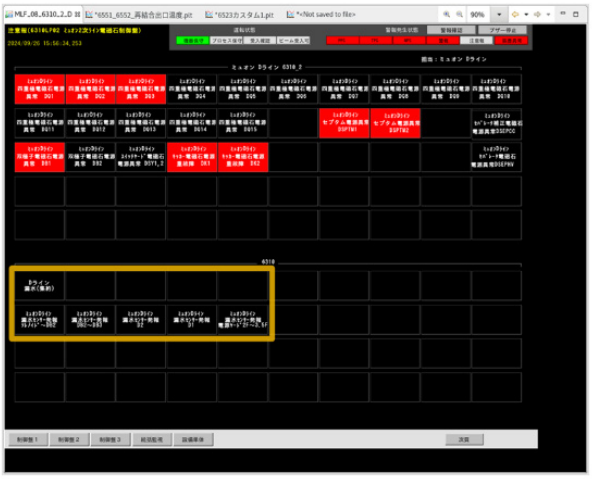

Figure 3. The monitor display with integrated water leak alarm signals for the D-line devices.
(Yellow frame: The water leak signals for the D-line devices.)

The five new bit-signal transmissions needed to be assigned to this network.

Figure 2 shows the transmission of water leak alarm signals.

These additional water leak alarm signals are displayed on the control PC screen in the MLF control room. Figure 3 shows the PC screen display updated with integrated water leak alarm signals. The PC screen updates were performed by staff of the Neutron Source Section.

3. Acknowledgements

We are grateful to Mr. K. Sakai and Ms. A. Suzuki of the Neutron Source Section for full co-operation about this works.

References

[1] K. SAKAI, M. OOI et al., Progress of General Control System for Materials and Life Science Experimental Facility at J-PARC, JAEA-Technology 2018-011, pp. 19-28.

Y. Kobayashi[1,2], I. Umegaki[1,2], S. Takeshita[1,2], A. Koda[1,2], and N. Kawamura[1,2]
[1]*Muon Science Section, Materials and Life Science Division, J-PARC Center;* [2]*Institute of Materials Structure Science, KEK*

FY2024 Progress Report on the USM-μSR

1. Introduction

The muon spin rotation/relaxation/resonance μSR technique using ultra-slow muons (USM) is a unique method for non-destructively probing depth-dependent magnetic properties of materials by controlling the muon implantation energy. By FY2023, energy calibration and beam spot evaluation of the U1A spectrometer were completed, culminating in a successful proof-of-principle experiment. In FY2024, the focus shifted to evolving this technology into a practical scientific research tool by enhancing measurement stability and efficiency, which led to the start of the first full-scale scientific experiment.

2. Present status and tasks

Following the recent success of a proof-of-principle USM-μSR experiment using a multilayer sample, the U1A experimental apparatus has transitioned from the commissioning phase to full-scale scientific applications. We are currently conducting the first scientific campaign with this setup, targeting thin films and performing comprehensive μSR measurements that include depth-profiling, sample cooling, and magnetic field application.

To establish USM-μSR as a widely available and stable experimental tool, it is essential to precisely evaluate the beam stability during long measurements and the spectrometer's background level to suppress systematic errors. In this regard, key challenges such as establishing conditions for a stable beam spot when changing implantation energy and implementing remote control of the monitor for seamless switching between beam tuning and data acquisition have been resolved through recent developments, significantly improving practical usability.

3. Progress in FY2024

The depth-profiling capability of USM-μSR is achieved by varying the energy of muons implanted into a sample. This is controlled by changing the electric potential of the high-voltage stage on which the entire spectrometer is placed. Previously, however, altering the stage voltage caused the beam spot to shift and its intensity to decrease at the sample position. This was due to the beam entering the stage at an angle.

In FY2024, through systematic, simulation-assisted beam tuning, we successfully identified conditions that keep the beam spot shape and intensity nearly constant at the sample position, even when the stage voltage is varied from 30 kV down to 0.5 kV. Figure 1 shows the results. This improvement has enabled reliable depth-resolved measurements at a practical level. Details of the beam specifications at the sample position have been reported in a publication [1].

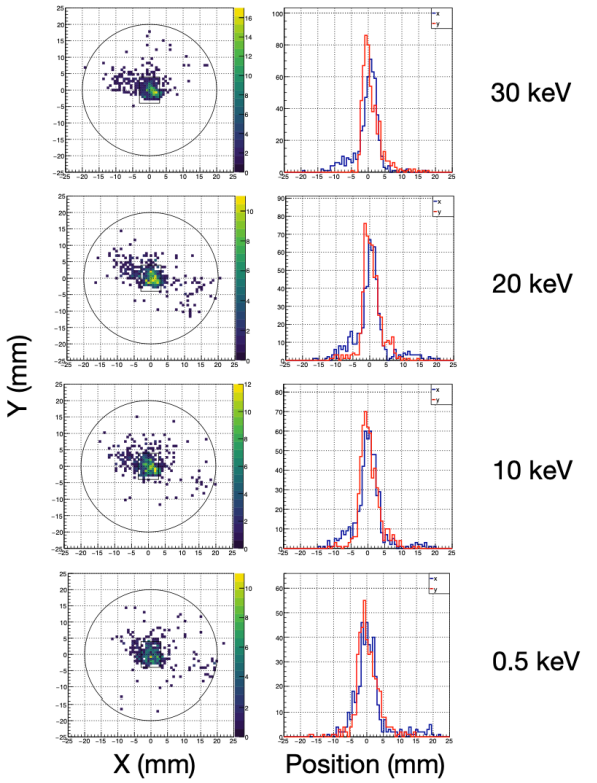

Figure 1. The beam profile at the sample position as the implantation energy was varied from 30 keV to 0.5 keV. During the energy scan, all beam transport parameters were held constant except for the voltage of the high-voltage platform.

During beam tuning, a beam profile monitor (MCP-DLD) at the sample position is used, which must be retracted for μSR measurements. Previously, this operation was performed manually, requiring the spectrometer's high voltage to be turned off each time, resulting in significant time loss. To solve this, the monitor's actuator was upgraded to a remote-controlled system, enabling a seamless switch between beam tuning and μSR measurement without interrupting the high voltage. This has significantly reduced the time required for experimental setup and execution.

Using data from a test sample, the data analysis framework for the spectrometer was developed. The spectrometer consists of 16 detector modules, and while their performance and operating conditions are aligned as much as possible, it is crucial to suppress

variations in the time response among the modules to leverage the high time resolution of USM-μSR. The time origin for each module was calibrated using the prompt positron peak. The results are shown in Fig. 2.

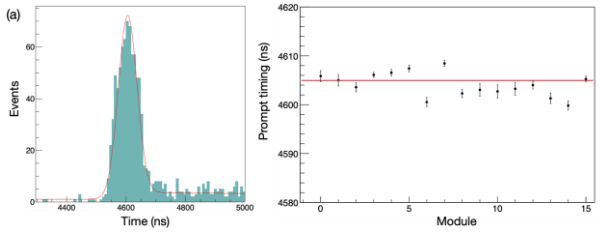

Figure 2. Time calibration using the timing of prompt positrons. (a) A typical prompt peak. The solid line shows the result of fitting with a Gaussian + background function. (b) Prompt timing for each module, determined from the fitting. The solid line indicates the weighted average. The time offset of each module was shifted so that its prompt timing matches the weighted average, thereby aligning the time origin for the measurement.

To calibrate the full asymmetry of the spectrometer, a USM-μSR measurement was performed using a bulk platinum (Pt) sample. The measurement was conducted at room temperature under a static magnetic field of 100 Gauss applied perpendicular to the sample. The implantation energy was set at 30 keV. Figure 3 shows a typical result.

In this analysis, the time spectra obtained from the 16 modules were phase-corrected and summed. The resulting spectrum was then fitted with an exponential + floor function for the muon decay, and the asymmetry was determined from the residuals of the fit. The exponent of the fitting function was fixed to the muon lifetime of 2197 ns, while the period was determined by fitting the asymmetry calculated for each module with a cosine function and then adopting their weighted average.

The amplitude obtained by fitting the summed asymmetry with a cosine function was 0.12, which is consistent with the predicted value considering the 50% polarization of the USM and the spectrometer's solid angle.

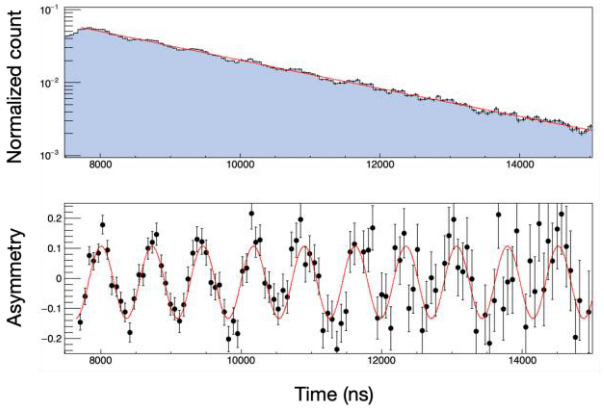

Figure 3. Measurement of the full asymmetry using a bulk Pt sample. (top) The time spectrum, corrected for phase differences between detector modules, and its fit with an exponential + floor function. (bottom) The asymmetry calculated from the fitting residuals and its fit with a cosine curve. The amplitude of the oscillation was 0.12.

Considering the event rate and solid angle of the spectrometer, it was estimated that approximately 230 USM/s are reaching the sample position. This was consistent with the counts from the MCP-DLD detector that can be installed at the sample position. The first materials science experiment has been on hold since the neutron target malfunction in June 2024, but we aim to complete the data acquisition as soon as operations resume.

4. Summary and outlook

In FY2024, we achieved the stabilization of depth-resolved measurements and a dramatic improvement in experimental efficiency, which together enabled the start of our first full-scale scientific experiment. Consequently, USM-μSR at U1A has reached a practical stage as a new research tool for thin film and interface science. In the near future, we will resume the interrupted measurements to produce the first scientific results, while continuing to enhance performance.

References

[1] S. Kanda *et al.*, to be published in the proceedings of J-PARC2024.

S. Kanda[1,2], Y. Hoshikawa[1,2], Y. Ikedo[1,2], W. Higemoto[1], and T. U. Ito[1]
[1]*Muon Science Section, Materials and Life Science Division, J-PARC Center;* [2]*Institute of Materials Structure Science, KEK*

FY2024 Progress Report on the Ultra-Slow Muon Beamline

1. Introduction

The Muon Science Establishment (MUSE) at the J-PARC Materials and Life Science Experimental Facility (MLF) aims to realize a practical ultra-slow muon (USM) beam, which is essential for studying the physical properties of thin films and interfaces. In FY2023, improvements in beam transport efficiency and better agreement with simulations were achieved through the correction of residual magnetic fields in the USM generation area and the upgrading of beam monitors. Building on these achievements, FY2024 efforts focused on resolving more fundamental issues and deepening the precise understanding of the beam to further enhance USM yield and stability.

2. Present status and tasks

Ultra-slow muons (USM) offer outstanding characteristics for materials science research, such as low energy, small emittance, and high time resolution. However, the primary challenge for practical applications that require high statistics is the need to improve the beam flux.

To address this, our strategy focuses on four key improvement tasks: (1) Optimizing the transport of the source surface muon beam, (2) Increasing the muonium conversion efficiency, (3) Enhancing the pulse energy of the ionization laser, and (4) Improving the USM extraction and transport efficiency. The progress detailed in this report was achieved primarily under tasks (1) and (4), marking significant steps toward realizing a high-intensity USM beam.

3. Progress in FY2024

The generation efficiency of USM is critically dependent on the spatial overlap between its source, the surface muon beam, and the ionization laser light. To measure the profile of the surface muon beam from the Super-Omega beamline, which had been difficult to assess precisely, a new detector combining a thin-film scintillator and a silicon photomultiplier (SiPM) was developed. Using this detector, the beam profile was successfully measured, providing fundamental data for the optimization of muon generation. Figure 1 shows a photo of the beam monitor and typical results from a profile measurement.

Furthermore, to accurately determine the total beam flux, we attempted the direct detection of the surface muon beam using a silicon pixel detector. A detector based on the Timepix3 chip, developed by CERN, was integrated into the central part of the monitor. Figure 2 shows the measured time spectrum and the time-over-threshold (TOT)-time correlation. It was demonstrated that by controlling the rate to a range where the detector operates stably, the beam flux can be measured while avoiding pile-up effects.

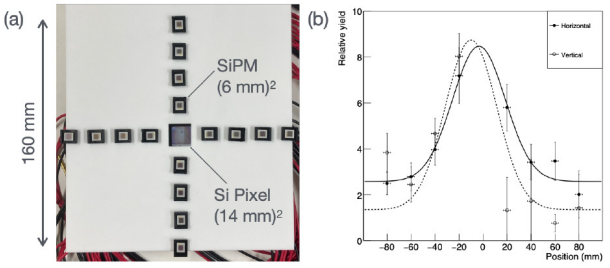

Figure 1. Surface muon beam profile monitor: (a) Photograph of the detector. A 50 μm thick scintillation film was placed directly on top of the SiPM. (b) Profile measurement result under the transport conditions normally used for USM generation.

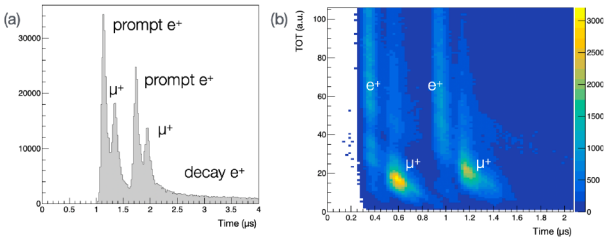

Figure 2. Surface muon measurement with a silicon pixel detector: (a) Time spectrum, (b) Correlation between TOT and time. TOT is a quantity corresponding to the pulse height of the signal when a particle hits a pixel. Muons and positrons can be distinguished by TOT because their pulse heights are significantly different.

The trajectory of USM is highly sensitive to the voltages of the electrostatic transport elements. While simulations previously used set values, direct measurements were conducted using a high-voltage probe. This investigation identified that the output of a specific electrostatic quadrupole (EQ) power supply was noisy and had an offset; this issue was resolved by changing the power supply system. Figure 3 shows a typical measurement result during voltage scanning. This

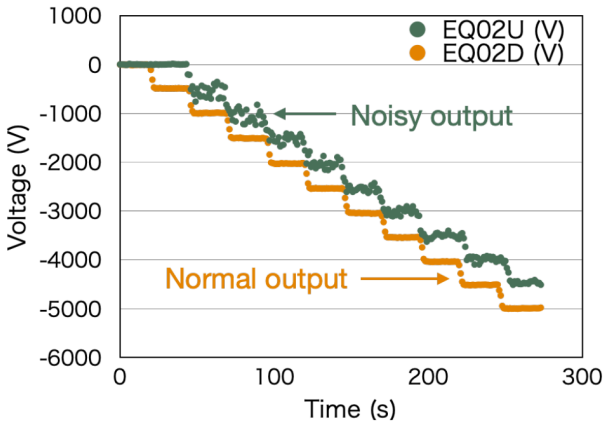

Figure 3. Results from measuring the voltage applied to an electrostatic quadrupole. During USM beam tuning, the voltage applied to the EQ is scanned. When the voltage trend during a scan, measured with a high-voltage probe, was compared between a normal channel and a malfunctioning channel, significant noise and offset were observed.

improvement was a significant step toward resolving the long-standing discrepancy between experimental results and simulations.

Furthermore, the time-of-flight (TOF) of the USM was precisely measured between two beam monitors (F3 and F3D, the beamline configuration is described elsewhere [1]) to compare the beam's average energy between experiment and simulation. The results showed excellent agreement within 3% accuracy, confirming a substantial improvement in the reliability of the beam transport simulations [2].

4. Summary and outlook

In FY2024, we achieved the direct observation of the source beam, the identification and resolution of hardware issues in the transport system, and improved accuracy in beam energy evaluation through TOF analysis. These advancements have deepened our understanding of beam transport and significantly enhanced the predictive accuracy of our simulations. Moving forward, we will leverage these results to further increase the USM beam intensity and stability, aiming for the realization of more advanced μSR experiments.

References

[1] S. Kanda *et al.*, to be published in the proceedings of J-PARC2024.
[2] Y. Nakazawa *et al.*, to be published in the J-PARC2024 proceedings.

S. Kanda[1,2], Y. Hoshikawa[1,2], Y. Ikedo[1,2], A. Miura[3], Y. Nakazawa[4], Y. Oishi[1,2], and K. Shimomura[1,2]
[1]*Muon Science Section, Materials and Life Science Division, J-PARC Center;* [2]*Institute of Materials Structure Science, KEK;* [3]*Osaka University;* [4]*Accelerator Laboratory, KEK*

Current Status of the S line and S1 area – Kicker power supply, Compressed air, Liquid helium, Experimental platform –

1. Kicker power supply

S line kicker power supply [1,2] consists of 24 MARX units (Fig.1), each of which is equipped with a Si-MOSFET (IXYSRF DE475-102N21A). Due to the deterioration caused by the aging of the Si-MOSFET, MARX board abnormalities have been occurring frequently, which can disturb user experiments. Therefore, we are proceeding with the replacement of the Si-MOSFETs with SiC-MOSFET (Genesic G3R20MT12K).

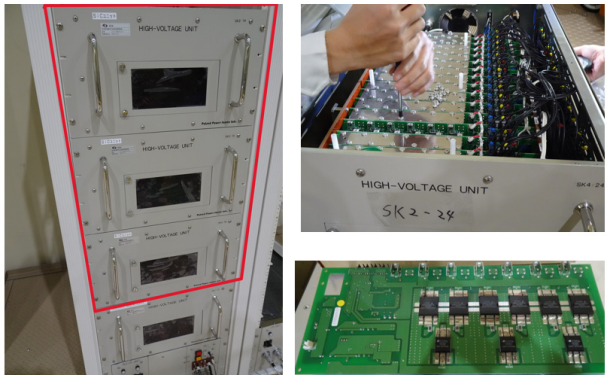

Figure 1. (Left, red-frame) MARX units equipped with SiC-MOSFET, (Upper right) MARX unit, (Lower right) MARX board.

In April 2023, MOSFETs were replaced in one MARX unit, and in the summer of 2024, MOSFETs were replaced in three MARX units. The three MARX units equipped with SiC-MOSFET were installed in the kicker power supply rack. Functional tests were conducted to confirm that there were no issues when operating the same load with a mix of SiC-MOSFET and Si-MOSFET units.

Figure 2 shows the number of MARX board abnormalities with a mixture of Si-FET and SiC-FET units. All abnormalities occurred in MARX board with Si-MOSFETs.

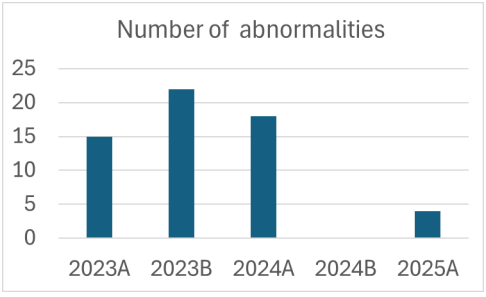

Figure 2. Number of MARX board abnormalities.

Currently, four of the 24 MARX units are equipped with SiC-MOSFET, while the remaining 20 are equipped with Si-MOSFETs. During the summer shutdown in 2025, all remaining MARX units will be replaced with SiC-MOSFET and will be put into operation in experiments starting in the 2025B beamtime.

2. Compressed air

As shown in Fig.3, a gate valve that separates the vacuum of the beamline is driven by compressed air. The compressed air flow is controlled by a solenoid valve. In the S line, compressed air is supplied using a small compressor. Due to aging over several years, the solenoid valves occasionally had problems, resulting in interruptions in the beam time. The solenoid valve had previously been installed inside the beamline shielding, requiring the ceiling shielding to be opened using a crane for repairs or replacements. In August 2024, the compressed air piping route was changed, and the

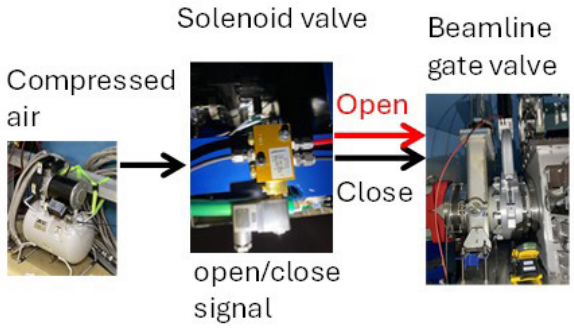

Figure 3. Beamline gate valve opened and closed by compressed air controlled by solenoid valve.

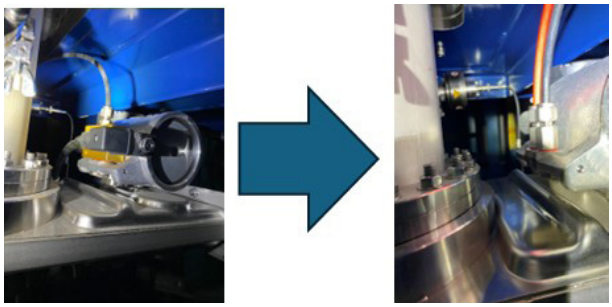

Figure 4. (Left) Gate valve with attached solenoid valve, (Right) Gate valve after relocating the solenoid valve.

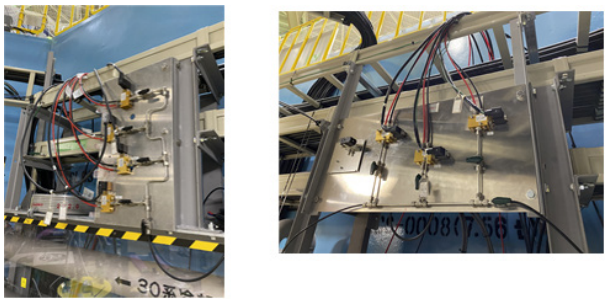

Figure 5. New solenoid valve panel. (Left) Downstream panel, (Right) Upstream panel.

solenoid valve was relocated to the outside of the shielding (Fig. 4, 5). As a result, the time required for repairs or replacements of the solenoid valve will be significantly reduced, minimizing beam time interruptions.

3. Liquid helium

S1 area, the first experimental area of the S line, conducts the most user experiments at the MLF muon facility, where many experiments are conducted in 2 or 3 days of beamtime. Figure 6 shows the ratio of sample environments of these experiments (ratios counted in days) used during the 2024A beamtime. More than half of the experiments are conducted with a minicryo or microstat, a small cryostat using liquid helium as a cryogen, while about 20% of the experiments are conducted with a helium-3 (^{3}He) cryostat.

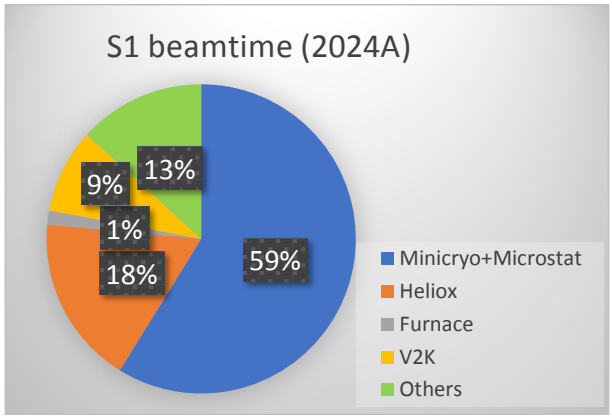

Figure 6. S1 beamtime ratio.

Liquid helium is commonly used, so it is important to resolve any issues immediately. During the commissioning experiments in Feb. 2025, an incident occurred in which the transfer tube was removed from the microstat without stopping the He pump for sample replacement at room temperature. As a result, air mixed into the helium recycle line from the return line of the transfer tube for approximately 43 minutes. To prevent this from occurring, the following actions were taken.

A mass flow meter and diaphragm pump (MVP 040-2, Pfeiffer Vacuum Ltd.) are installed on the return line of the helium transfer tube, and helium gas is transported to the recycle line. To clear operational status of the pump, an external switch for the pump and a "Pump On" indicator light (Fig. 7) were installed in Feb. 2025, and a helium purity alarm system (Fig. 8) was developed and installed. The alarm system accesses the existing data logger that records helium purity over the network. When purity decreases, it issues an audio warning through the computer's speaker and posts a notification to the online platform (Slack). Additionally, we updated the operating procedures manual, created a checklist, installed a valve to prevent backflow from the helium recycle line to the transfer tube, and improved the transfer tube cover.

Figure 7. (Left) External switch for the He pump, (Right) "Pump On" indicator light.

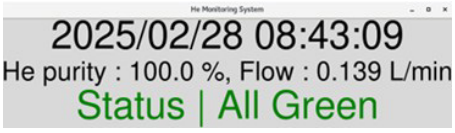

Figure 8. Display panel of helium purity alarm system. Two thresholds can be set to trigger warnings and alarms.

Figure 9. Installation of metal helium recovery line.

We also replaced the recycle line for the S1 area (Fig. 9). Previously, vinyl hoses were used as helium recycle line in the S1 area, but there were concerns that they might be damaged when cold helium flowed through them. To resolve this issue, we replaced the recycle line with metal straight pipes and flexible hoses.

4. Experimental platform

We have made some improvements to an aluminum platform [3] around the S1 spectrometer (Fig. 10). We changed the shape of several bridges and beams of the platform to improve workability next to the spectrometer and reduce the risk of bumping one's head. We also changed the shape of the fence to improve safety on top of the spectrometer.

Additionally, we also made improvements to the cryostat lifter [3]. Previously, it did not work well when moving Dry Lemon, which are heavier than the ^{3}He cryostat. We improved this by greasing the shaft axis, but unfortunately, we were unable to smoothly move the cryostat with the heaviest rotating target rod. We solved this problem by changing to a motor with one with higher torque.

Figure 10. Improved aluminum platform.

References

[1] A. Koda et al., KEK Progress Report 2022-7 KEK-MSL REPORT 2021, 23 (2023).
[2] A. Koda et al., KEK Progress Report 2023-8 KEK-MSL REPORT 2022, 21-22 (2024).
[3] J. G. Nakamura et al., KEK-MSL REPORT 2023.

J. G. Nakamura[1,2], T. Yuasa, S. Nishimura[1,2], H. Li[1], H. Osawa[1], S. Suzuki[1], and A. Koda[1,2]
[1]*Muon Science Section, Materials and Life Science Division, J-PARC Center;* [2]*Institute of Materials Structure Science, KEK*

Current Status of the H-line

The H-line is a high-intensity muon beamline for general use [1-3]. It is in the east experimental hall #1 of the MLF and has two experimental areas named H1 and H2. The first muon beam at the H1 area was generated in January 2022. Currently, using its high-intensity pulsed muon beam, precise measurements of the hyperfine structure of muonium (MuSEUM experiment [4]) and a search for μ-e conversion (DeeMe experiment [5]) are conducted. On the other hand, the construction of the H2 area began in FY2022. The H2 area will be used for ultra-slow muon (USM) generation and re-acceleration of USMs up to 4 MeV. It will be extended further to produce a novel low-emittance muon beam by accelerating muons up to 212 MeV using long linear accelerators. However, a new experimental building must be built on the east side of the MLF to install the long accelerators. Its detailed design is underway. The low-emittance muon beam enables the J-PARC muon g-2/EDM experiment [6] and a transmission muon microscope (TμM). So far, we have manufactured radiation shielding components and assembled them as the H2 area in FY2022. An ISO 6 (Class 1000) clean room for the laser system to ionize muoniums and generate USMs has been constructed beside the H2 area in FY2023. This report describes significant progress in the beamline to the H2 area and other upgrades of the H-line in FY2024.

A new solenoid (HS4) with a 610 mm aperture and a new quadrupole triplet (HQ456) with a 400 mm aperture to transport and focus muon beams to the H2 area were fabricated in FY2024. They were installed in the H-line in January 2025 (Fig. 1). A power supply for HS4 was also manufactured. After laying cables and cooling water plumbing for these magnets and their power supplies, we conducted in-situ tests of the magnets in March 2025, and everything worked well.

There are two upgrades in the upstream part of the H-line. One is the installation of a beamline slit (HSL1). It was developed by users of the H1 area from RIKEN and Chubu University. It has four 10-mm-thick stainless-steel blades as shown in Fig. 2 and can change the size of the horizontal and vertical apertures. Since it is installed downstream of the DC separator, it is useful to reduce positron backgrounds as well as to control the beam size and intensity. The other upgrade is a beam profile monitor (CsI-BPM) developed by Budker Institute of Nuclear Physics (BINP). A thin (3-5 μm) CsI foil is used as a target. Scintillation light from the target is observed using a lens and a CCD camera. Figure 3 is a photo of

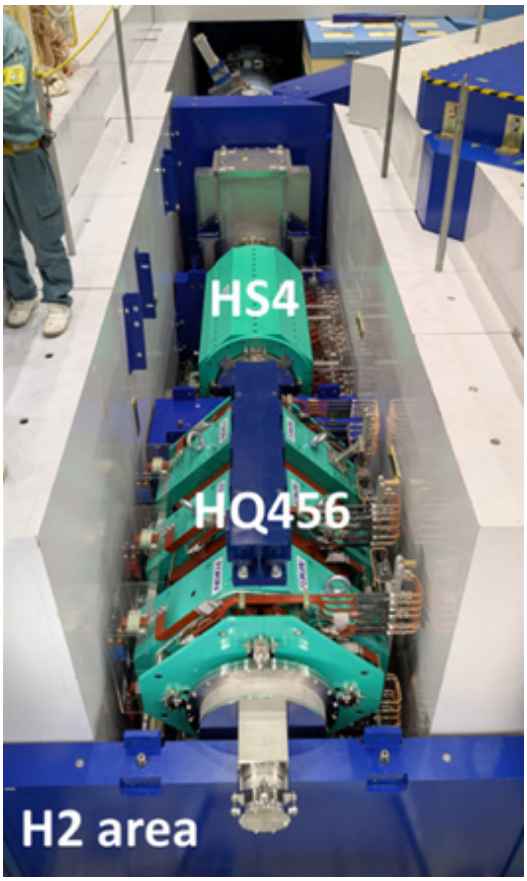

Figure 1. A new solenoid (HS4) and a new quadrupole triplet (HQ456) installed in the H-line.

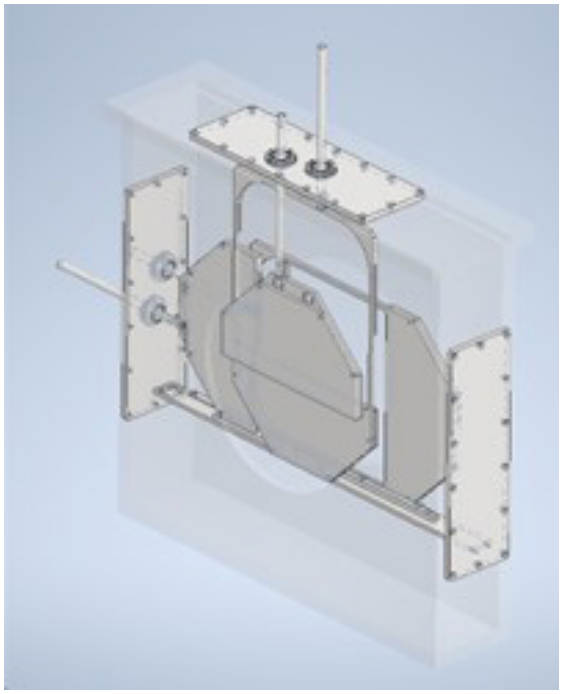

Figure 2. A 3D drawing of a beamline slit (HSL1) developed by RIKEN and Chubu University.

Figure 3. A thin (3-5 μm) CsI beam profile monitor developed by BINP.

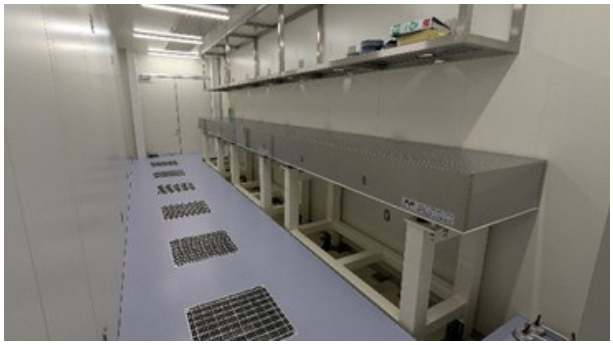

Figure 4. Three optical benches installed in the laser room.

the CsI-BPM. It is installed just before the second bending magnet (HB2), which is used to change the beam destination to the H1 or the H2 areas. Because the target is thin enough that it does not disturb muon beams, we can monitor the beam profile at any time. The beam test of the CsI-BPM is ongoing.

In addition, optical benches were installed in the laser room in January 2025, as shown in Fig. 4. The laser system will be installed in FY2025, and the first USM generation in the H2 area is scheduled in December 2025. In addition, optical fiber cables to transmit 12 MHz clock signals for the laser system and linear accelerators were laid from the J-PARC central control room (CCR) to a panel box near the H2 area. These signals are important to synchronize the lasers with the muon beams.

Another topic worth reporting on is the first maintenance of the cryocoolers in the H-line. We use two superconducting solenoids (HS2 and HS3) to transport muon beams. They are cooled down by GM cryocoolers, which should be maintained every two years. The maintenance of the cryocooler of HS3 is easy, and there ocoolers was successfully completed.

We reported on the current status and recent updates of the H-line. The major update is the completion of the H2 area. The H2 beam commissioning is scheduled for FY2025. The beamline slit (HSL1) and the CsI-BPM were developed by users of the H-line. The construction of the laser system for USM generation also progressed. The first maintenance of the cryocoolers in the H-line was completed without any problems.

References

[1] N. Kawamura, *et al.*, Prog. Theor. Exp. Phys. **2018**, 113G01 (2018).
[2] T. Yamazaki, *et al.*, EPJ Web of Conferences **282**, 01016 (2023).
[3] T. Yamazaki and N. Kawamura, KEK-MSL Report 2021, 26-27.
[4] K. Shimomura, AIP conf. proc. **1382**, 245 (2011).
[5] H. Natori, *et al.*, Nucl. Phys. B (Proc. Suppl.) **248-250**, 52-57 (2014).
[6] T. Mibe, *et al.*, Chin. Phys. C **34**, 745 (2010).

T. Yamazaki[1,2], Y. Oishi[1,2], and N. Kawamura[1,2]
[1]*Muon Science Section, Materials and Life Science Division, J-PARC Center;* [2]*Institute of Materials Structure Science, KEK*

MLF Safety

Research Safety

1. Radiation safety

Radiological license upgrade

In FY 2024, no application for radiological license upgrades was performed. However, a new application is planned to be permitted in FY 2026 as the following item.

(1) Installation of one of the general purpose μSR spectrometer (S3-line)
(2) Removal of beam plugs at neutron beam lines (BL07 and BL13)
(3) Upgrade of the off-gas treatment system
(4) Addition of safety keys to treat limited shielding blocks at neutron instrument in beam operation period
(5) Addition of pion particles as applicable particles in muon instruments

2. Chemical safety

The total number of chemical substances brought into the facility in FY2024 was 3,564, which represents a decrease compared to FY2023. This reduction was mainly due to the significant decrease in user operation days caused by unexpected facility troubles during the year. Although the total number decreased, the trend continues to reflect a high demand for experiments involving battery-related samples and hydrogen-storage alloys, which remained prevalent among the submitted sample types.

There were no notable increases in the handling of hazardous substances, and the overall usage of flammable gases, including methane and ethane, remained at a low level. The implementation of established safety procedures and the continuous collaboration between users and in-house staff contributed to maintaining a stable chemical safety environment throughout the fiscal year.

3. Crane safety

The total number of crane operations in FY2024 was 188, consisting of 181 operations by in-house staff and 7 by contractors. While the annual total was slightly lower than FY2023, this trend is consistent with the reduced experimental activity caused by the limited user operation period in FY2024.

For in-house activities, the increase in maintenance work associated with the facility recovery efforts helped sustain a stable level of crane usage, despite the reduction in user experiments. On the other hand, the crane usage by contractors remained limited, showing no significant change from the previous year. Overall, crane handling was carried out without major incidents, and the continuous improvement of operational procedures contributed to maintaining safe crane operation throughout the year.

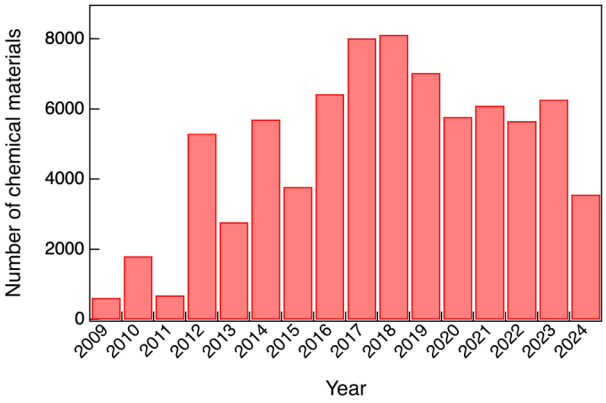

Figure 1. Trend of the amount of user-brought chemical materials for chemical safety check from the start of the MLF operation to FY2024.

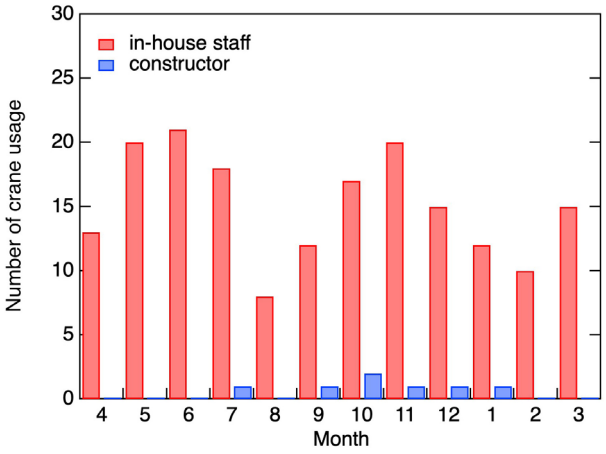

Figure 2. Trend of the total crane usages in one year.

M. Harada[1], S. Masuda[1], T. Ito[1], T. Tajima[1], R. Komine[2], N. Hashimoto[2], Y. Watanabe[2], H. Tanaka[2], W. Kambara[2], H. Inoue[2], K. Suzuya[3], N. Kawamura[4], Y. Sakaguchi[5], R. Takahashi[2], Y. Yamaguchi[5], and T. Oku[2]

[1]Neutron Source Section, Materials and Life Science Division, J-PARC Center; [2]Technology Development Section, Materials and Life Science Division, J-PARC Center; [3]Neutron Science Section, Materials and Life Science Division, J-PARC Center; [4]Muon Science Section, Materials and Life Science Division, J-PARC Center; [5]Neutron Science and Technology Center, CROSS

MLF Operations in 2024

Beam Operation Status at the MLF

1. Overall

In the Japanese Fiscal Year (JFY) 2024, beam operation at the MLF was planned to begin on April 7, 2024, and end on March 31, 2025. Figure 1 shows the records of the beam power and availability. In JFY 2024, beam operation began at 954 kW with a double-bunch beam, making record beam power at MLF. We achieved our goal of 1 MW beam power at 25 Hz, excluding the 3.8% duty loss due to beam sharing with the Main Ring (MR), with an MR cycle of 4.24 seconds. From April 7 to June 3, the beam power gradually decreased to 900 kW, mainly due to LINAC. After June 3, the beam power decreased to 825 kW because of a change in the MR duty cycle, with a period of 1.36 seconds to deliver the beam to the neutrino facility.

Although J-PARC had no fire accidents in JFY2024, which occurred twice in JFY2023, the duration of beam operation for user delivery was much shorter than the scheduled plan. This was caused by two major failures that happened at MLF. On June 24, a relatively high dew point was found in the gas for the helium vessel surrounding the neutron production target of the mercury vessel. After this event, beam operations at MLF were stopped until the summer outage. This failure was due to a pressure drop in the pressurized air system in MLF. This system is commonized to the target system and the users' application in the experimental hall. When the user consumes a large amount of pressurized air, the pressure cannot be maintained, allowing a tiny amount of air with relatively high humidity to enter the helium vessel from the outside. Although the amount of air introduced was small, this event happened many times at the end of June, which drastically increased the dew point.

The other major failure was related to the mercury loop. Due to electrical insulation degradation in the mercury loop pump motor caused by radiation in the hot cell, we replaced the pump assembly. However, the seal on the mercury flange was not fully reseated on the new pump assembly. Therefore, a very small amount of radioactive gas was released into the hot cell of the MLF during a test with the beam for the replaced target on December 11. Due to this failure, beam operation at high intensity was suspended until the seal was exchanged. To understand the gas release status for quick recovery, we maintained a low beam

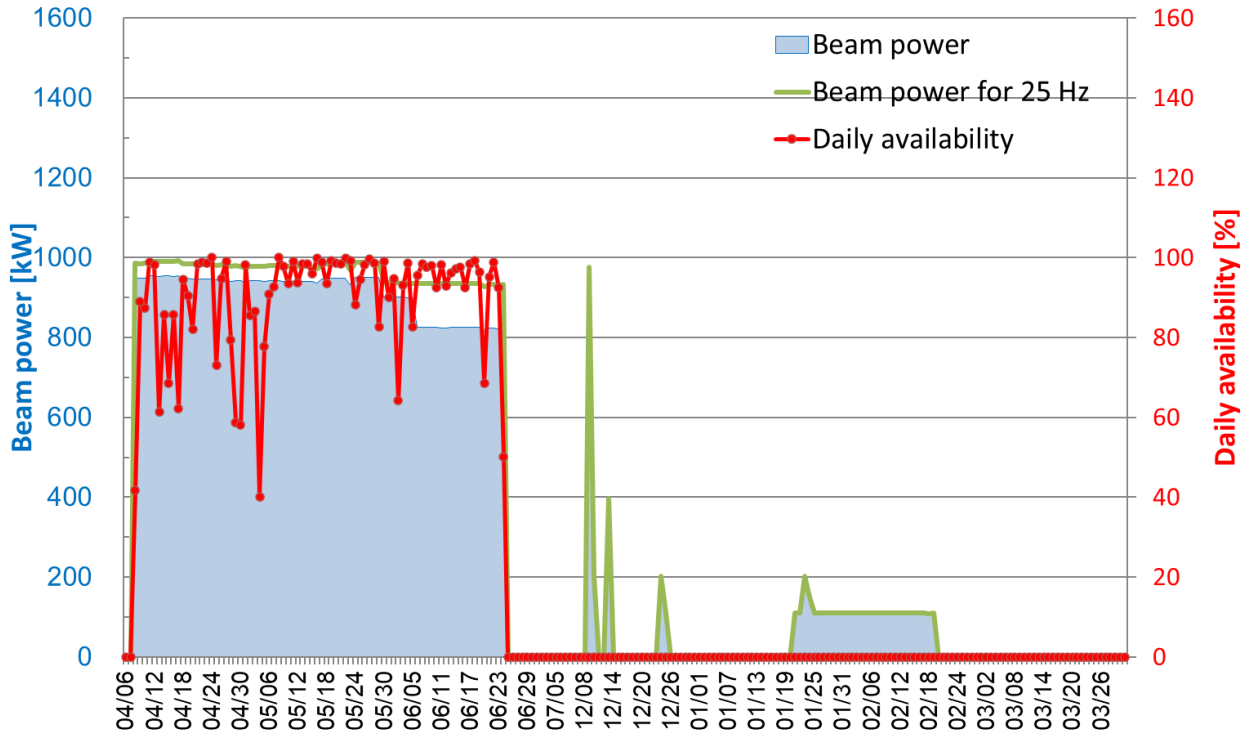

Figure 1. Beam power trend (blue line) at the MLF, beam power for the 25-Hz operation (green line), i.e., beam power per shot and including the loss of duty for MR delivery, and availability per day (red line).

Table 1. Run cycles, scheduled times, actual beam times, and availabilities.

Run cycle	Duration	Scheduled time (h)	Beam time (h)	Availability (%)
91 & 2024A	April 8 – June 30	1,659	1,487	89.6%
92 & 2024B	December 11 – March 31	1,905	0	0.0%
Overall	April 16 – March 31	3,564	1,487	41.7%

Table 2. Events that stopped the beam for a duration longer than 3 hours.

Date	Cause of the beam stop	Stop duration for each event
April 8 – May 24	RCS magnet power supply failure	96 hours for 20 days
June 2	Recovering from an instantaneous voltage dip in the commercial power supply	10 hours
June 20	LINAC Ion source failure	4 hours
June 24	Dew point anomaly in the helium vessel at the MLF	7 days
December 11	Failure of the mercury loop	89 days

power of 100 kW from December 24 to February 19, excluding the New Year's break. During this period, beam operations were not counted as user deliveries. It should be noted that we tried our best to recover from this failure without replacing the metal seal at the flange, which would have taken a very long time. However, it did not work well. Eventually, we decided to stop the beam entirely on February 20 to enable the high-intensity beam operation. At the end of JFY2024, the seal was successfully replaced, and we started beam delivery in JFY2025 with high intensity.

During the summer outage, the spent neutron production target #16 was replaced with a new target #15, which had been manufactured in advance. During the replacement, no significant issues were encountered with the target replacement. Since our precise inspection found no significant damage to target #16, we decided to continue after the outage with the 950-kW beam for the MR cycle of 4.24 seconds, if beam operation was possible.

Table 1 shows the scheduled time and availability in JFY 2024. Although the beam was stopped due to a high dew point in the helium vessel, caused by frequent drops in pressurized air for the vessel seal, a high availability of 89.8% was achieved through July 1 for 2024A. Eventually, the overall availability in JFY 2024 was 41.7%. Because of the mercury loop failure, the availability has been worse than ever.

Beam operation was halted several times due to minor failures. Table 2 summarizes the typical causes of a beam stop lasting longer than 3 hours and describes them below, except for those for MLF.

2. Causes of the beam stop

LINAC:

During JFY 2023, there were no water flow shortages at the magnet in LINAC, which had been the main reason for beam stops before JFY 2019. In JFY 2024, there were a few failures related to LINAC RF. On June 2, the AC commercial power supply dipped. Following this dip, the RF system malfunctioned at LINAC.

3-GeV Rapid Cycling Synchrotron (RCS):

The power supply to the main magnets at RCS was frequently tripped after April 8. When it happens, the recovery time is typically longer than 3 hours. The underlying reason for this failure was still unclear. However, the failure did not occur after May 25, following improvements to the power supply.

S. Meigo[1]
[1]*Neutron Source Section, Materials and Life Science Division, J-PARC Center*

Users at the MLF

The MLF beam operation for FY2024 started with a beam power 949 kW as a double-bunch, achieving the target of 1 MW beam power at 25 Hz, excluding the duty loss of beam sharing to the Main Ring (MR). On June 24th, due to the MLF target problem, the beam operation was suspended until the summer shutdown. After target change and test operation, to enable high-intensity beam operation, the beam was shut down on February 20th, and the seal replacement was completed by the end of JYF2024, with high-intensity beam supply restarted from YF2025. As a result, operation for FY 2024 was 68.5 days out of the planned 125 days, and for users who were unable to carry out experiments during 2024B, 53.5 days was postponed to 2025A.

The total number of MLF users in FY2024 was 1,642. Although the number of operation days was reduced due to the MLF target problem, the user number reflects a clear recovery from the COVID-19 restrictions on travel and a strong return of face-to-face meetings and symposiums. The trends in the number of users since the start of operations in FY 2008 is summarized in Table 1 and Figure 1.

Table 1. The number of domestic and foreign users by fiscal year.

	FY2008		FY2009		FY2010		FY2011		FY2012		FY2013		FY2014		FY2015	
	Domestic Users	Foreign Users	Domestic Users	Foreign Users	Domestic Users	Foreign Users	Domestic Users	Foreign Users	Domestic Users	Foreign Users	Domestic Users	Foreign Users	Domestic Users	Foreign Users	Domestic Users	Foreign Users
Neutron	107		317		476		259		708		449		824		559	
	95	12	303	14	432	44	238	21	628	80	399	50	711	113	476	83
Muon	18		40		50		23		56		61		91		69	
	18	0	38	2	42	8	21	2	46	10	50	11	78	13	59	10

	FY2016		FY2017		FY2018		FY2019		FY2020		FY2021		FY2022		FY2023		FY2024	
	Domestic Users	Foreign Users	Domestic Users	Foreign Users	Domestic Users	Foreign Users	Domestic Users	Foreign Users	Domestic Users	Foreign Users	Domestic Users	Foreign Users	Domestic Users	Foreign Users	Domestic Users	Foreign Users	Domestic Users	Foreign Users
Neutron	852		927		965		940		489		307		406		451		1395	
	744	108	742	185	789	176	827	113	448	41	257	50	296	110	333	118	957	438
Muon	99		179		161		138		92		117		238		281		247	
	83	16	149	30	146	15	127	11	88	4	112	5	203	35	242	39	221	26

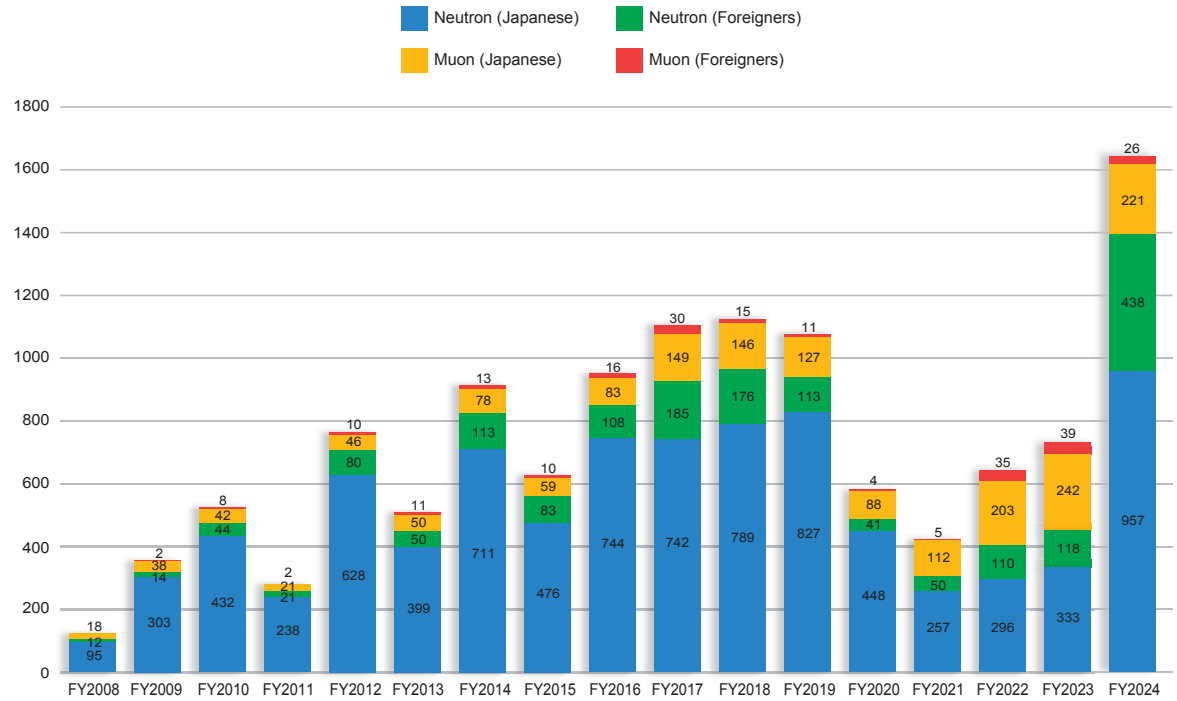

Figure 1. The number of domestic and foreign users by fiscal year.

MLF Proposals Summary – FY2024

Table 1. Number of Proposals by Beamline.

Beam-line	Instrument	2024A		2024B		Full Year			
		Submitted	Approved	Submitted	Approved	Submitted		Approved	
		GU	GU	GU	GU	PU/S	IU	PU/S	IU
BL01	4D-Space Access Neutron Spectrometer - ***4SEASONS***	33(1)	9(1)	29(1)	8(1)	0	2	0	2
BL02	Biomolecular Dynamics Spectrometer - ***DNA***	19(0)	8(0)	23(1)	5(1)	0	2	0	2
BL03	IBARAKI Biological Crystal Diffractometer - ***iBIX*** (100-b)‡	0	0	1	1	0	0	0	0
	(b)†	3	3	2	2	17※	0	17※	0
BL04	Accurate Neutron-Nucleus Reaction Measurement Instrument - ***ANNRI***	4	3	7	1	2	1	2	1
BL05	Neutron Optics and Physics - ***NOP***	5	5	7	4	1	1	1	1
BL06	Village of Neutron Resonance Spin Echo Spectrometers - ***VIN ROSE***	4	2	3	3	2	0	2	0
BL08	Super High Resolution Powder Diffractometer - ***SuperHRPD***	13	8	15	8	1	0	1	0
BL09	Special Environment Neutron Powder Diffractometer - ***SPICA***	2	2	6	4	1	0	1	0
BL10	NeutrOn Beam-line for Observation and Research Use - ***NOBORU***	10	7	13	9	2	1	2	1
BL11	High-Pressure Neutron Diffractometer - ***PLANET***	10(0)	8(0)	11(0)	5(0)	0	1	0	1
BL12	High Resolution Chopper Spectrometer - ***HRC***	11	7	9	3	1	0	1	0
BL14	Cold-Neutron Disk-Chopper Spectrometer - ***AMATERAS***	34	9	35	4	1	1	1	1
BL15	Small and Wide Angle Neutron Scattering Instrument - ***TAIKAN***	24(1)	11(1)	25(2)	11(2)	3	5	3	5
BL16	Soft Interface Analyzer - ***SOFIA***	11	9	19	8	1	1	1	1
BL17	Polarized Neutron Reflectometer - ***SHARAKU***	18(1)	11(1)	23(3)	10(3)	3	3	3	3
BL18	Extreme Environment Single Crystal Neutron Diffractometer - ***SENJU***	24(0)	6(0)	26(0)	6(0)	0	1	0	1
BL19	Engineering Materials Diffractometer - ***TAKUMI***	38	11	32	9	1	1	1	1
BL20	IBARAKI Materials Design Diffractometer - ***iMATERIA*** (100-b)‡	3	3	5	2	0	0	0	0
	(b)†	33	33	21	21	15	0	15	0
BL21	High Intensity Total Diffractometer - ***NOVA***	27	20	22	13	2	0	2	0
BL22	Energy Resolved Neutron Imaging System - ***RADEN***	14(0)	11(0)	17(2)	9(2)	2	2	2	2
BL23	Polarization Analysis Neutron Spectrometer - ***POLANO***	3	3	5	2	1	0	1	0
D1	Muon Spectrometer for Materials and Life Science Experiments - ***D1***	10(0)	8(0)	19(1)	6(0)	2	1	2	1
D2	Muon Spectrometer for Basic Science Experiments - ***D2***	5(1)	5(1)	5(0)	2(0)	2	1	2	1
S1	General purpose μSR spectrometer - ***ARTEMIS***	28(2)	21(2)	21(0)	13(0)	1	1	1	1
S2	Muonium Laser Physics Apparatus - ***S2***	0(0)	0(0)	0(0)	0(0)	0	1	0	1
U1A	Ultra Slow Muon Microscope - ***U1A***	0	0	0	0	0	1	0	1
U1B	Transmission Muon Microscope - ***U1B***	0	0	0	0	0	1	0	1
H1	High-intensity Muon Beam for General Use - ***H1***	0	0	2(1)	2(1)	0	1	0	1
Total		**384**	**221**	**401**	**169**	**49**	**29**	**49**	**29**

GU : General Use **PU** : Project Use or Ibaraki Pref. Project Use **S** : S-type Proposals **IU** : Instrument Group Use
† : Ibaraki Pref. Exclusive Use Beamtime (β = 80% in FY2024) **‡** : J-PARC Center General Use Beamtime (100-β = 20% in FY2024)
( ) : Proposal Numbers under the New User Promotion (BL01, BL02, BL11, BL15, BL17, BL18, BL22) or P-type proposals (D1,D2, S1) in GU
※ : Operations period is held twice per year (for each of the A and B periods), with only the yearly total shown above.
The actual total number of proposals in each beamline named in the table does not match the number shown in the "Total" cell, because some proposals are submitted or approved across multiple beamlines.

Table 2. Number of Long-Term Proposals by Fiscal Year.

Application FY	Submitted	Approved
2022	5	4
2023	0	0
2024	3	3

No Long-Term Proposals were called for FY2023.

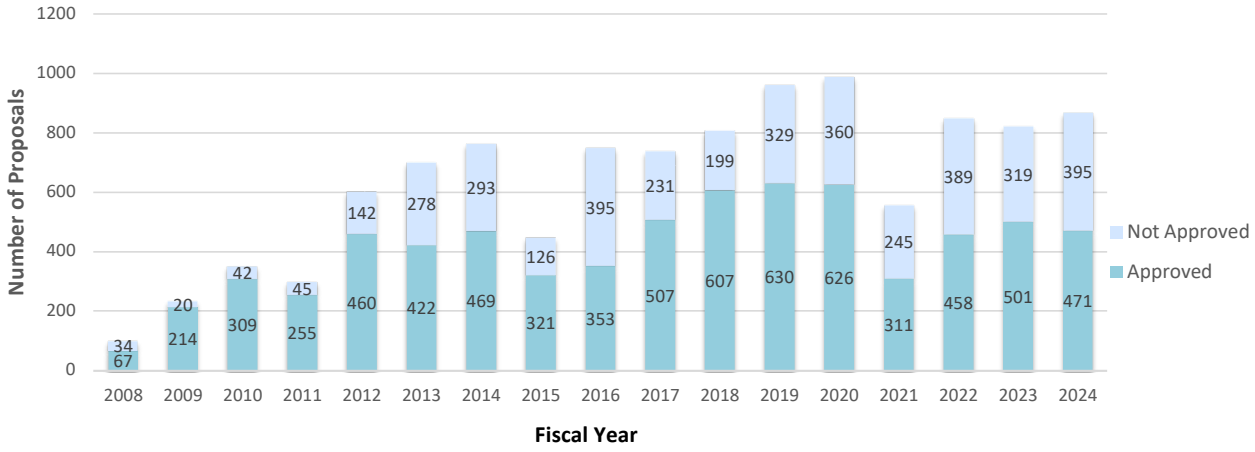

Figure 1. Number of MLF Proposals over Time.

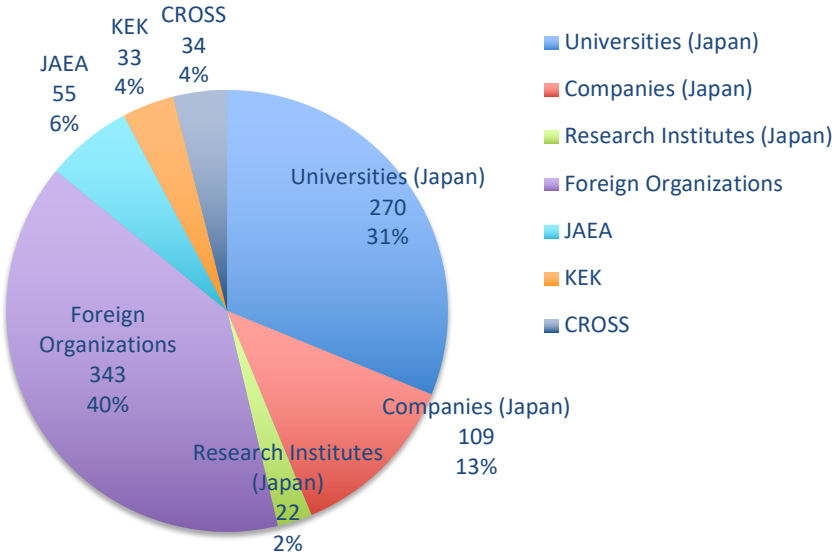

Figure 2. Origin of Submitted Proposals by Affiliation - FY2024.

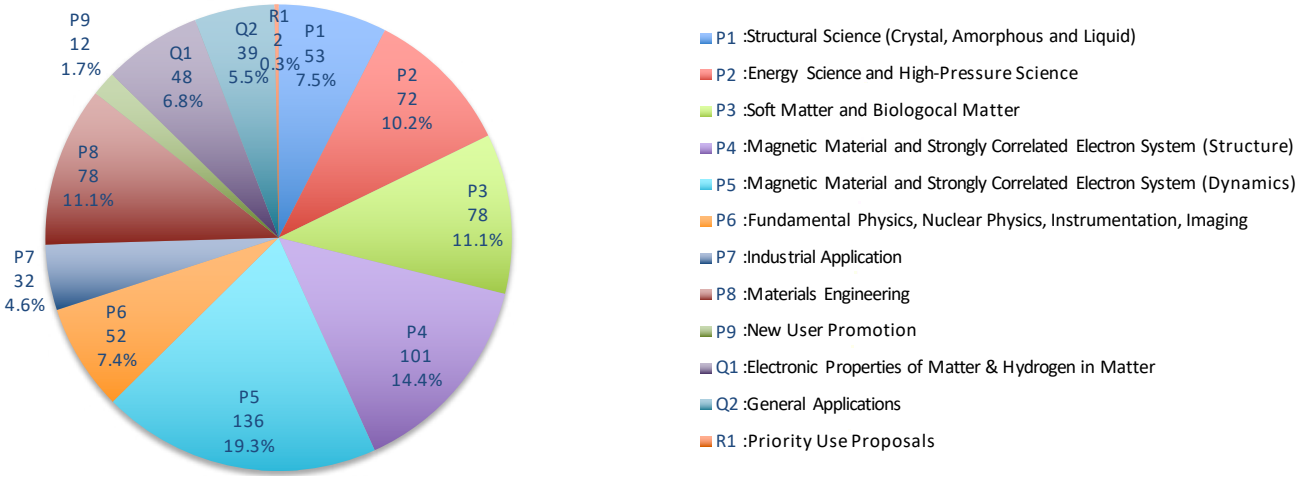

Figure 3. Submitted Proposals by Sub-committee/Expert Panel - FY2024.

MLF Division Staff 2024

*: additional duties

Toshiya Otomo (Head)
Yukinobu Kawakita (Deputy Head)
Koichiro Shimomura (Deputy Head)
Katsuhiro Haga (Deputy Head)
Masaaki Sugiyama (Invited Researcher)
Hiroshi Takada
Kazuya Aizawa
Kyoko Aizawa
Kenji Nakajima

Neutron Source Section

*: additional duties

<JAEA>

Masahide Harada (Leader)
Kenji Sakai (Sub-Leader)
Makoto Teshigawara
Tomokazu Aso
Hiroyuki Kogawa
Hidetaka Kinoshita
Takashi Wakui
Takashi Naoe
Koichi Saruta
Masakazu Seki
Shiho Masuda
Gen Ariyoshi
Hideki Muto
Shuna Fujita
Yoshihiko Kawakami
Shigeto Tanaka
Yoshinori Kikuchi
Toshiyuki Yasuhara
Masakazu Nakamura
Takahiro Tajima
Akiyoshi Futakawa
Taku Ito
Aya Suzuki
Shizuka Yoshinari
Rie Nemoto
Shin-ichiro Meigo *
Tetsuya Kai *
Kenichi Oikawa *
Shoichi Hasegawa *
Motoki Ooi *
Yuji Yamaguchi *
Shoya Suda *
Midori Yamamoto *

Neutron Science Section

*: additional duties

<JAEA>

Mitsutaka Nakamura (Leader)
Asami Sano (Sub-Leader)
Ryoichi Kajimoto
Takanori Hattori
Stefanus Harjo
Kenichi Oikawa
Takashi Ohhara
Takenao Shinohara
Hiroyuki Aoki
Tetsuya Kai
Seiko Kawamura
Shinichi Takata
Ryoji Kiyanagi
Yasuhiro Inamura
Takuro Kawasaki
Wu Gong
Kosuke Hiroi
Naoki Murai
Yusuke Tsuchikawa
Hiromu Tamatsukuri
Kentaro Suzuya
Masami Nirei
Pharit Piyawongwatthana
Tatsuya Ito
Shigeki Uzuki
Fangzhou Song
Shingo Takahashi
Tatsuya Kikuchi
Masashi Harada
Hiroshi Nozaki
Takeshi Harada
Hideaki Isozaki
Keiichi Inoue
Sakai Motonobu
Motohiro Aizawa
Keiko Nemoto
Yuko ohuchi
Naoko Shimizu
Koji Kaneko *
Hiroshi Nakagawa *
Atsushi Moriai *
Satoshi Morooka *
Atsushi Kimura *
Shoji Nakamura *
Shunsuke Endo *
Yosuke Toh *
Mariko Segawa *
Masahide Harada *
Masao Watanabe *
Dai Yamazaki *

<KEK>

Tetsuya Yokoo (Sub-Leader)
Shinichi Itoh
Hideki Seto
Toshiya Otomo *
Kazuhiro Mori
Hitoshi Endo
Takashi Ino
Takashi Honda
Daichi Ueta
Masako Yamada
Shuki Torii
Kaoru Taketani
Sara Yamauchi
Hiroyuki Aoki *
Asami Sano *
Takashi Saito
Kazuhiko Ikeuchi
Ginga Kitahara
Hiromi Miki
Seungyub Song
Yuki Hirota
Go Ichikawa
Setsuo Satoh
Norifumi Yamada
Hidetoshi Ohshita *
Tomohiro Seya *

Technology Development Section

*: additional duties

<JAEA>

Takayuki Oku (Leader)
Kazuyoshi Tatsumi (Sub-Leader)
Masao Watanabe
Yuhua Su
Ryota Komine
Hiroyuki Hasemi
Chie Shibazaki
Takashi Oda
Ryuju Kobayashi
Takuya Okudaira
Atsuko Ariga
The Dang Vu
Shusuke Takada
Motoyasu Adachi
Wataru Kambara
Yoko Watanabe
Hideaki Takahashi
Ryuta Takahashi
Norimichi Hashimoto
Hiromichi Tanaka
Hiroyuki Asai
Kenji Sakai *
Tetsuya Kai *
Hiroyuki Kogawa *
Kentaro Suzuya *
Mitsutaka Nakamura *
Shinichi Takata *
Tatsuya Nakamura *
Yasuhiro Inamura *
Tomokazu Aso *
Seiko Kawamura *

<KEK>

Tetsuya Yokoo *
Shuki Torii *
Takashi Ino*
Kaoru Taketani *
Naritoshi Kawamura *
Hiroshi Fujimori *

Neutron Instrumentation Section

*: additional duties

<JAEA>

Tatsuya Nakamura (Leader)
Kentaro Toh (Sub-Leader)
Dai Yamazaki
Ryuji Maruyama
Kaoru Sakasai
Masahiro Tobe
Yukio Hishinuma
Naoki Kashimura
Takaaki Hosoya
Yuta Asai
Yoshiko Saeki

<KEK>

Hidetoshi Ohshita
Tomohiro Seya

Muon Science Section

*: additional duties

<KEK>

Naritoshi Kawamura (Leader)	Hikaru Sunagawa	Shogo Doiuchi
Akihiro Koda (Sub-Leader)	Yu Oishi	Akiko Hashimoto
Koichiro Shimomura	Yukinori Nagatani	Yoshinori Ito
Patrick Strasser	Shoichiro Nishimura	Souta Suzuki
Soshi Takeshita	Motonobu Tampo	Hiroko Osawa
Takayuki Yamazaki	Masatoshi Hiraishi	Yuna Hoshikawa
Sohtaro Kanda	Ryosuke Kadono	Noriko Chinone
Izumi Umegaki	Amba-Datt Pant	Misono Fujii
Yutaka Ikedo	Yasuhiro Miyake	Yukiko Gunchi
Yasuo Kobayashi	Katsuhiko Ishida	Tomoko Ishikawa
Jumpei Nakamura	Hiroshi Fujimori	Aki Tomita
Shiro Matoba	Yasunori Bessho	Tsutomu Mibe *
Takahiro Yuasa	Hua Li	Shusei Kamioka *

<JAEA>

Wataru Higemoto *	Takashi Ito *	Masayoshi Fujihala *

CROSS Staff 2024

Neutron Science and Technology Center

Director Mitsuhiro Shibayama

Science Coordinators

Shamoto Shinichi
Jun Sugiyama
Matahiro Komuro
Midori Kamimura

Research & Development Division

*: additional duties

Masato Matsuura (Head)
Kazuki Ohishi (Deputy Head)
Hiromi Abe

<BL01 Group>
Kazuya Kamazawa (Leader)
Kazuki Iida (Sub-Leader)
Shohei Hayashida

<BL02 Group>
Takeshi Yamada (Leader)
Taiki Tominaga
Masato Matsuura *

<BL11 Group>
Shinichi Machida (Leader)
Jun Abe
Yuki Sakai

<BL15 Group>
Kazuki Ohishi (Leader)
Hiroki Iwase
Yukihiko Kawamura

<BL17 Group>
Kazuhiro Akutsu (Leader)
Takayasu Hanashima
Noboru Miyata *

<BL18 Group>
Akiko Nakao (Leader)
Koji Munakata
Yoshihisa Ishikawa

<BL22 Group>
Hirotoshi Hayashida (Leader)
Joseph Don Parker
Yoshihiro Matsumoto

<Technical Support Group>
Kazuki Ohishi * (Leader)
Nobuo Okazaki (Leader)
Toshiaki Morikawa (Sub-Leader)
Motoyuki Ishikado
Misaki Ueda
Keiichi Ohuchi
Yoshimasa Ohe
Hiroshi Kira
Shuoyuan Zhang
Koji Kiriyama *
Yoshifumi Sakaguchi *
Satoshi Kasai
Yuuki Nagai
Kentaro Moriyama
Ryo Murasaki *

Safety Division

*: additional duties

Mitsuhiro Shibayama * (Head)
Koji Kiriyama (Leader)
Yoshifumi Sakaguchi (Leader)
Tazuko Mizusawa *

Utilization Promotion Division

*: additional duties

Kenichi Funakoshi (Head)
Takashi Noma (Head)
Takayoshi Ito (Leader)
Toshiki Asai (Leader)
Miho Igarashi (Sub-Leader)
Taeko Ishikawa
Maya Endo
Midori Oi
Emi Goto
Hideyuki Niitsuma
Emi Hanashima
Tazuko Mizusawa
Hiromi Abe *
Nobuo Okazaki *
Kaoru Ouchi *

Administration Division

*: additional duties

Seiya Konishi (Head)
Junichi Sato * (Leader)
Rei Ito (Leader)
Yoshimi Akiba
Mami Uchida
Tomoko Sakuma
Mutsumi Shiraishi
Hiromi Watanabe
Shinobu Matsumoto *
Tomomi Takahashi *

Industrial Collaboration Promotion Division

*: additional duties

Mitsuhiro Shibayama * (Head)
Kazuki Mita (Deputy Head)
Noboru Miyata (Leader)
Kaoru Ouchi
Maiko Kawata
Jun Abe *
Hiroki Iwase *
Yoshihiro Matsumoto *
Takeshi Yamada *

Neutron Industrial Application Promotion Center

Director Jun-ichi Suzuki

<User Promotion Group> *: additional duties

Jun-ichi Suzuki * (Leader)
Mamoru Sato (Science Coordinator)
Tetsuroh Minemura (Science Coordinator)
Shiho Tanaka
Rika Oonuki
Michie Watahiki

<BL03 Group> *: additional duties

Katsuhiro Kusaka (Leader)
Terutoshi Sakakura
Haruki Sugiyama
Ritsuko Sakazume

<BL20 Group> *: additional duties, †: cross appointment

Kazutaka Ikeda (Leader)
Toru Ishigaki
Takafumi Hawai
Satoshi Koizumi †
Shigeo Sato †
Yohei Noda †

<BL Technical Group> *: additional duties

Jun-ichi Suzuki * (Leader)
Junichi Yasuda (Sub-Leader)
Shinju Shibata
Masatoshi Nakamura

Proposals Review System, Committees and Meetings

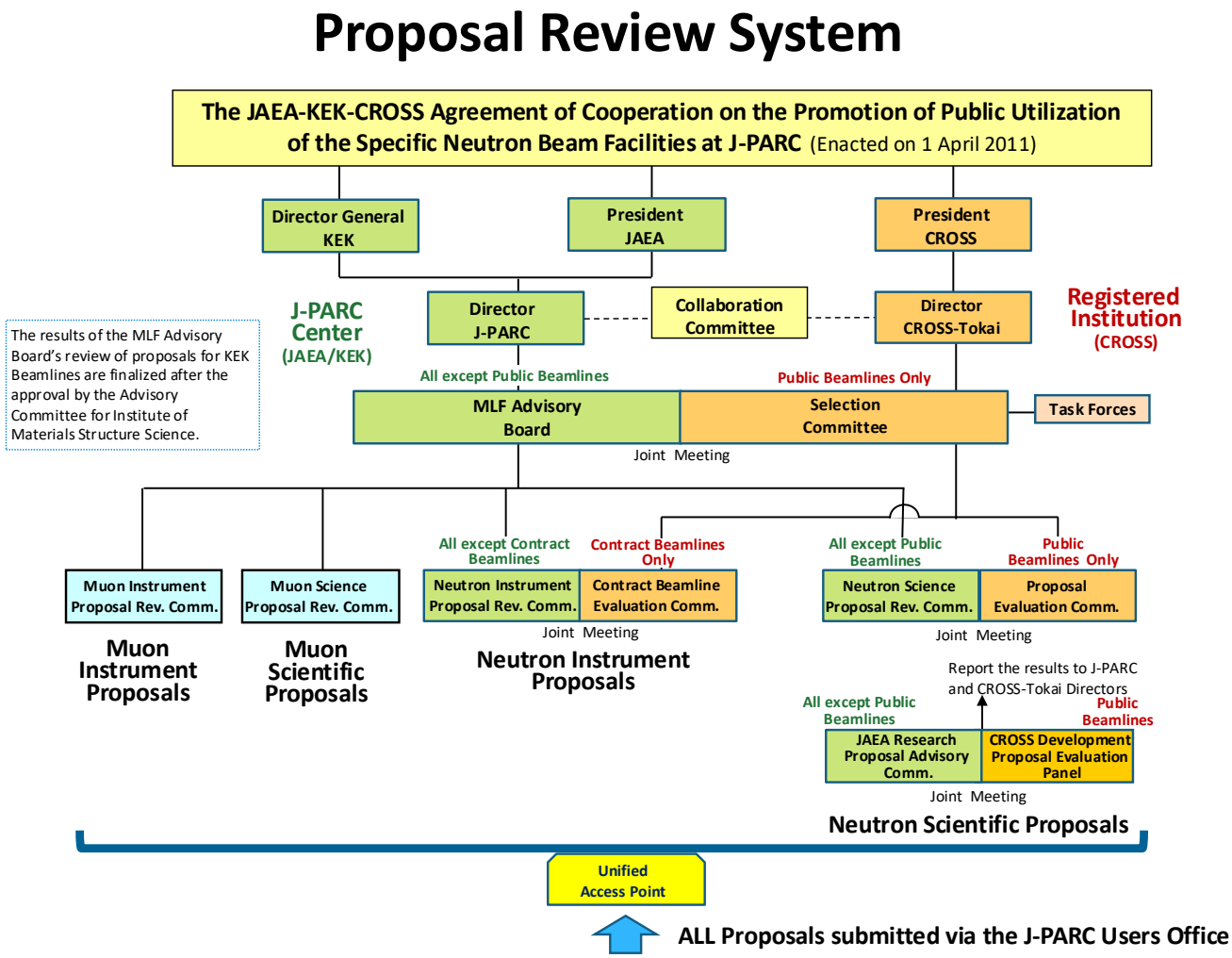

Figure 1. Proposals Review System Framework.

Materials and Life Science Facility Advisory Board

Tadashi Adachi	Sophia University
Taka-hisa Arima (Chair)	The University of Tokyo/RIKEN
Katsuhiro Haga	Japan Atomic Energy Agency
Masahiro Hino	Kyoto University
Kohzo Ito	The University of Tokyo/Research Center for Strategic Materials
Shinichi Itoh	High Energy Accelerator Research Organization
Hiroyuki Kagi	The University of Tokyo
Takashi Kamiyama	Hokkaido University
Yukinobu Kawakita	Japan Atomic Energy Agency
Naritoshi Kawamura	High Energy Accelerator Research Organization
Shigeru Kimura	Japan Synchrotron Radiation Research Institute
Hiroyuki Kishimoto	Sumitomo Rubber Industries, LTD.
Masato Matsuura	Comprehensive Research Organization for Science and Society
Kenji Nakajima	Japan Atomic Energy Agency
Mitsutaka Nakamura	Japan Atomic Energy Agency
Kenji Ohoyama	Ibaraki University
Yoshie Otake	RIKEN
Toshiya Otomo	High Energy Accelerator Research Organization
Koichiro Shimomura	High Energy Accelerator Research Organization
Yoko Sugawara	Kitasato University
Mikihito Takenaka	Kyoto University
Isao Watanabe	RIKEN
Osamu Yamamuro	The University of Tokyo

Term: through March 31, 2025

Neutron Science Proposal Review Committee

Mitsuhiro Hirai	Gunma University
Hiroshi Iikura	Japan Atomic Energy Agency
Hiroki Ishibashi	Osaka Metropolitan University
Shinichi Itoh	High Energy Accelerator Research Organization
Hiroyuki Kagi (Chair)	The University of Tokyo
Yukinobu Kawakita	Japan Atomic Energy Agency
Naritoshi Kawamura	High Energy Accelerator Research Organization
Koichi Mayumi	The University of Tokyo
Michihiro Nagao	University of Maryland and National Institute of Standards and Technology
Taro Nakajima	The University of Tokyo
Mitsutaka Nakamura	Japan Atomic Energy Agency
Yusuke Nambu	Tohoku University
Toshiya Otomo	High Energy Accelerator Research Organization
Noriyuki Tsuchida	University of Hyogo
Satoshi Tsutsui	Japan Synchrotron Radiation Research Institute
Tamaki Yoshioka	Kyushu University

Term: through September 30, 2025

Muon Science Proposal Review Committee

Tadashi Adachi	Sophia University
Kenta Amemiya	High Energy Accelerator Research Organization
Hidehito Asaoka	Japan Atomic Energy Agency
Katsuyuki Fukutani	The University of Tokyo
Wataru Higemoto	Japan Atomic Energy Agency
Adrian Hillier	Rutherford Appleton Laboratory
Hiromi Iinuma	Ibaraki University
Katsuya Inoue	Hiroshima University
Shinichi Itoh	High Energy Accelerator Research Organization
Ryosuke Kadono	High Energy Accelerator Research Organization
Naritoshi Kawamura	High Energy Accelerator Research Organization
Yasushi Kino	Tohoku University
Akihiro Koda	High Energy Accelerator Research Organization
Kenya Kubo (Chair)	International Christian University
Roderick Macrae	Marian University

Kenji Mishima	Nagoya University
Mitsutaka Nakamura	Japan Atomic Energy Agency
Takehito Nakano	Ibaraki University
Kazuhiko Ninomiya	Hiroshima University
Toshiya Otomo	High Energy Accelerator Research Organization
Hideki Seto	High Energy Accelerator Research Organization
Patrick Strasser	High Energy Accelerator Research Organization
Tatsushi Shima	Osaka University
Koichiro Shimomura	High Energy Accelerator Research Organization
Yoko Sugawara	Kitasato University
Isao Watanabe	RIKEN
Ichihiro Yamauchi	Saga University

Term: through March 31, 2025

Selection Committee

Tadashi Adachi	Sophia University
Taka-hisa Arima (Chair)	The University of Tokyo/RIKEN
Masahiro Hino	Kyoto University
Kohzo Ito	The University of Tokyo/Research Center for Strategic Materials
Hiroyuki Kagi	The University of Tokyo
Takashi Kamiyama	Hokkaido University
Shigeru Kimura	Japan Synchrotron Radiation Research Institute
Hiroyuki Kishimoto	Sumitomo Rubber Industries, LTD.
Kenji Ohoyama	Ibaraki University
Yoshie Otake	RIKEN
Yoko Sugawara	Kitasato University
Mikihito Takenaka	Kyoto University
Isao Watanabe	RIKEN
Osamu Yamamuro	The University of Tokyo

Term: through March 31, 2025

Proposal Evaluation Committee

Mitsuhiro Hirai	Gunma University
Hiroki Ishibashi	Osaka Metropolitan University
Hiroyuki Kagi (Chair)	The University of Tokyo
Yukinobu Kawakita	Japan Atomic Energy Agency
Koichi Mayumi	The University of Tokyo
Michihiro Nagao	University of Maryland and National Institute of Standards and Technology
Taro Nakajima	The University of Tokyo
Yusuke Nambu	Tohoku University
Toshiya Otomo	High Energy Accelerator Research Organization
Noriyuki Tsuchida	University of Hyogo
Satoshi Tsutsui	Japan Synchrotron Radiation Research Institute
Tamaki Yoshioka	Kyushu University

Term: through September 30, 2025

Neutron Advisory Committee (NAC)

NAC convened on 12 and 13 February 2025.

Taka-hisa Arima	The University of Tokyo/RIKEN
Bertrand Blau	Paul Scherrer Institute
Michael Dayton	Oak Ridge National Laboratory
Phillip King (Chair)	Rutherford Appleton Laboratory
Toyohiko Kinoshita	Japan Synchrotron Radiation Research Institute
Guenter Muhrer	European Spallation Source
Yoshie Otake	RIKEN
Sungil Park	Korea Atomic Energy Research Institute
Judith Peters	University Grenoble Alpes / Institut Laue-Langevin
Jon Taylor	Spallation Neutron Source

Muon Advisory Committee (MAC)

MAC convened on 20 and 21 February 2025.

Nori Aoi	Osaka University
Makoto Fujiwara	TRIUMF
Adrian Hillier	Science and Technology Facilities Council
Klaus Kirch (chair)	ETH Zurich / Paul Scherrer Institut
Kenji Kojima	TRIUMF
Kenya Kubo	International Christian University
Martin Månsson	KTH Royal Institute of Technology
Yoko Sugawara	Kitasato University
Koji Yoshimura	Okayama University

Workshops, Conferences, Seminars and Schools in 2024

Conferences held jointly by J-PARC MLF and CROSS

Neutron Industrial Application Report Meeting for FY2024
11-12 Jul. 2024, Akihabara Convention Hall, Tokyo, Hybrid

Photo of Neutron Industrial Application Report Meeting for FY2024
(photo courtesy of CROSS)

International Reviewing Committee for Two-year Operation of Target Vessel in J-PARC
30 Aug. 2024, Online

Photo of International Reviewing Committee for Two-year Operation of Target Vessel in J-PARC
(photo courtesy of J-PARC)

2024 Workshop on Neutron Imaging
22-23 Aug. 2024, Shimbashi Business Forum, Tokyo, Hybrid

13th Design and Engineering of Neutron Instruments Meeting (DENIM XIII)
24-27 Sep. 2024, JAEA Tokai Mirai Base, Tokai

Photo of DENIM XIII
(photo courtesy of CROSS)

The 19th Korea-Japan Meeting on Neutron Science
13 Oct. 2024, AYA'S LABORATORY Quantum Beam Research Center, Tokai

J-PARC Workshop 2024, Deuterium Science Entering an Advanced Phase
18 Oct. 2024, Ibaraki University, Mito

J-PARC Workshop 1 MWパワーで探れ、非晶質の中の小さな不思議—「自由」と「束縛」の協奏曲—
28 Oct. 2024, AYA'S LABORATORY Quantum Beam Research Center, Tokai

Photo of J-PARC Workshop
(photo courtesy of CROSS)

2024 Z-Code Beginner Level Training Course
8 Aug. -30 Sep. 2024, On-demand

2024 Z-Code Intermediate Level Training Course
4 Feb.-31 Mar. 2025, On-demand

2024 Quantum Beam Science Festa (The 16th MLF Symposium and the 42nd PF Symposium)
12-14 Mar. 2024, TSUKUBA International Congress Center, Tsukuba

Photo of Quantum Beam Science Festa
(photo courtesy of IMSS, KEK)

Conferences held by KEK

第9回文理融合シンポジウム　“量子ビームで歴史を探る ー加速器が紡ぐ文理融合の地平ー”
1-2 Nov. 2024, Akihabara Convention Hall, Tokyo

Photo of 文理融合シンポジウム
(photo courtesy of KEK)

Workshops held by KEK

Annual Muon Achievement Report Meeting 2023
21-25 Jul. 2024, Hotel Laforet Nasu, Nasu

Photo of Annual Muon Achievement Report Meeting 2023
(photo courtesy of KEK)

Kick-off Workshop for Transmission Muon Microscopy
29-30 Sep. 2024, KEK Tokai Building #1, Tokai

Photo of Kick-off Workshop for Transmission Muon Microscopy
(photo courtesy of KEK)

FUture on Muon Elemental analysis (FUME)
19-21 Oct. 2024, KEK Tokai Building #1, Tokai

Photo of FUME
(photo courtesy of KEK)

Studies on Dynamics in Condensed Matters by using the High Resolution Chopper Spectrometer (BL12)
20 Nov. 2024, Online

Materials structure science research using ultra-high-resolution neutron diffraction (BL08)
21 Nov. 2024, Online

Science diversity interweaving crystalline and amorphous materials (BL21)
22 Nov. 2024, Online

Cyprus Meets Japan
- New Science & Technology in Archaeology and Culture – International Workshop on Non-destructive Analysis in Cultural Heritage-
25-27 Nov. 2024, Cyprus Institute, Nicosia

Photo of Cyprus Meets Japan
(photo courtesy of KEK)

Study on Cross-correlated Physics by Polarized Neutron Spectrometer, POLANO (BL23)
28 Nov. 2024, Online

Neutron structural studies of energy and functional materials dedicating to SDGs (BL09)
2 Dec. 2024, Online

Study on dynamics of materials in mesoscopic spatiotemporal space by means of the neutron resonance spin echo spectrometers (VIN ROSE) (BL06)
16 Dec. 2024, KEK Tokai Building #1, Hybrid

Workshops and Seminars held by CROSS and other organizations

10th Joint Workshop for Complementary Use of Synchrotron Radiation and Neutrons
"粉末回折測定研修会"
19 Aug. 2024 Online, 17 Dec. 2024, JRR-3, IBARAKI Quantum Beam Research Center, Tokai

11th Joint Workshop for Complementary Use of Synchrotron Radiation and Neutrons
"小角散乱測定研修会"
28 Aug. 2024 Online

2024年度中性子実験技術基礎講習会（レベル1講習会）
25 Jun. 2024, Online

10th Symposium on the Collaborative Use of Large Research Institutions and the Super Computer
12 Sep. 2024, Akihabara UDX, Tokyo, Hybrid

CBI研究機構 量子構造生命科学研究所 中性子産業利用推進協議会 生物・生体材料研究会 合同シンポジウム

"神経疾患の分子メカニズム最先端"
19 Sep. 2024, Online

The 29th CROSSroads Workshop
"固体化学と固体物理の先端的量子ビーム利用研究"
1 Oct. 2024, AYA'S LABORATORY Quantum Beam Research Center, Hybrid

Photo of 29th CROSSroads Workshop
(photo courtesy of CROSS)

Workshop on Battery Materials
23 Dec. 2024, Kokukaikan Business Forum, Tokyo, Hybrid

2024 Workshop on Magnetic Materials
24 Jan. 2025, Tohoku University, Hybrid

中性子産業利用推進協議会 有機・高分子材料研究会／NanoTerasu・中性子連携利用フォーラム
20 Jan. 2025, Tohoku University, Sendai, Hybrid

小型中性子施設活用研究会・見学会
12-13 Feb. 2025, Rihga Royal Hotel Niihama, Niihama, SHI-ATEX Co.,Ltd. サイクロトロン5号機中性子源, Saijo

CBI研究機構 量子構造生命科学研究所 中性子産業利用推進協議会 生物・生体材料研究会 合同シンポジウム
"希少疾患への挑戦"
5 Mar. 2025, Online

2024 Workshop on Liquids and Amorphous Materials
15 Mar. 2025, TSUKUBA International Congress Center, Tsukuba, Hybrid

R6年度小角散乱＜実験デザイン解析＞研究会
19 Mar. 2025, Essam Kanda Hall, Tokyo, Hybrid

Workshops and Seminars held by Ibaraki Neutron Beamline and other organizations

第2回茨城県内企業向け量子線利用講座
22 Aug. 2024, Hitachinaka Techno Center, Hitachinaka

2024 1st Workshop on iBIX
29 Aug. 2024, Online

第1回金属材料研究会
1 Oct. 2024, Kokukaikan Business Forum, Tokyo

2024 2nd Workshop on iBIX
12 Nov. 2024, Online

第6回量子ビーム材料解析セミナー
（令和6年度iMATERIA研究会）
18 Mar. 2025, Tohoku University, Sendai, Hybrid

Schools in 2024

Hello Science from J-PARC
"True Molecular Shapes Derived from Neutrons and Single Crystals"
24 Apr. 2024, AYA'S LABORATORY Quantum Beam Research Center, Tokai, Hybrid

Photo of Hello Science from J-PARC
(photo courtesy of J-PARC)

Hello Science from J-PARC
"Studying rocks to understand the Earth ～The world expanding 6,371 kilometers underground～"
29 Nov. 2024, AYA'S LABORATORY Quantum Beam Research Center, Tokai, Hybrid

Photo of Hello Science from J-PARC
(photo courtesy of J-PARC)

Hello Science from J-PARC
"Observing stresses in metals"
28 Feb. 2025, AYA'S LABORATORY Quantum Beam Research Center, Tokai, Hybrid

Photo of Hello Science from J-PARC
(photo courtesy of J-PARC)

The 8th Neutron and Muon School
9-13 Dec. 2024, J-PARC Center, Tokai

Award List

2024 Quantum Beam Science Festa Student Award
Measurement of Neutron-Nuclear Scattering Length for Gaseous Samples using Multilayer Neutron Interferometer
T. Nambu (2025-03-13)

KEK Technology Award
Precise Measurement of Neutron Counts with Nitrogen Gas-Filled Neutron Beam Monitors at the MLF in J-PARC
H. Ohshita (2025-02-17)

The JSNS Young Researcher Prize
Deformation Mechanisms of Advanced Structural Materials Studied by Pulsed In-situ Neutron Diffraction
T. Yamashita (2024-12-05)

The JSNS President's Choice
Adhesion Interface Studied by Neutron Reflectometry
H. Aoki (2024-12-05)

The JSNS President's Choice
The Advantage of Small-angle Neutron Scattering Revealed through Analyzing the Overall Structure of a Fully Assembled Complex in Circadian Clock
Y. Yunoki, A. Matsumoto, K. Morishima, A. Martel, L. Porcar, N. Sato, R. Yogo, T. Tominaga, M. Yagi, R. Inoue, H. Kono, H. Yagi, K. Kato, M. Sugiyama (2024-12-05)

The JSNS President's Choice
Analysis of Water Behavior inside Polymer Electrolyte Fuel Cells toward Automotive Applications
W. Yoshimune (2024-12-04)

The 19th JPS in Division 10 Young Scientist Award
Research on layered chalcogenide materials by μSR experiments
J. Nakamura (2024-11-26)

The 8th Symposium for the Core Research Clusters for Materials Science and Spintronics and the 7th Symposium on International Joint Graduate Programs in Materials Science and Spintronics (CRCGP-MSSP2024), Best Poster Award
Spin Dynamics and Polarized Neutron Reflectometry of Compositionally-Graded Ru Doped Perovskite Manganese Oxide Thin Films
K. Kaminaga (2024-11-20)

The 65th High Pressure Conference of Japan, Poster Award
中性子回折・イメージングによる液体鉄中の水素量の測定
N. Takahashi (2024-11-14)

JAEA President Award 2024 R&D Achievement Prize
ミュオンを用いた電池材料のイオンダイナミクス解析の革新
T. U. Ito (2024-10-07)

The 75th Divisional Meeting of Division of Colloid and Surface Chemistry, Oral Presentation Award for Young Scientist
中性子反射率法を用いたドデカン酸カリウムとジグリセリン誘導体混合系の気/液界面における吸着挙動の評価
M. Abe (2024-10-02)

Student Presentation Award of JPS
Studies of targets in the target station 2(TS2) project of MLF
S. Kawakami (2024-09-19)

第42回関西界面科学セミナー 優秀ポスター賞
中性子反射率法によるドデカン酸カリウムとジグリセリン誘導体混合系の気/液界面における吸着特性の解明
M. Abe (2024-07-27)

Japanese Stomatological Society, Excellent Poster Award
Study on imparting and maintaining antibacterial properties to denture surfaces using new silica-based coating technology
R. Toda (2024-07-21)

Acta Materialia, Inc., Acta Student Award
High-density nanoprecipitates and phase reversion via maraging enable ultrastrong yet strain-hardenable medium-entropy alloy
H. Kwon (2024-06-30)

European Lubricating Grease Institute, 2024 ELGI Academic Award
Neutron imaging technique for understanding urea type grease fluidity inside bearings
K. Sakai (2024-05-30)

SPSJ Technology Award 2024
Adhesion to Polyolefins Using Novel Miscibility Technology
Y. Shiraki (2024-05-24)

International Magnesium Society, International Magnesium Science & Technology Award Excellent Paper of the Year
Strengthening of aMg and long-period stacking ordered phases in a Mg-Zn-Y alloy by hot-extrusion with low extrusion ratio
S. Harjo, W. Gong, K. Aizawa, T. Kawasaki, M. Yamasaki (2024)

JAEA: Japan Atomic Energy Agency
JPS: The Physical Society of Japan
JSNS: The Japanese Society for Neutron Science
SPSJ: The Society of Polymer Science, Japan

MLF Publication 2024

1 T. Katase, S. Nomoto, X. He, S. Kitani, T. Honda, H. Hiramatsu, H. Hosono, T. Kamiya
Simultaneous Realization of Single-Crystal-Like Electron Transport and Strong Phonon Scattering in Polycrystalline $SrTiO_{3-x}H_x$
ACS Appl. Electron. Mater., **6** 7424–7429 (2024).

2 S. Asano, J.-I. Hata, K. Watanabe, K. Shimizu, N. Matsui, N. L. Yamada, K. Suzuki, R. Kanno, M. Hirayama
Formation Processes of a Solid Electrolyte Interphase at a Silicon/Sulfide Electrolyte Interface in a Model All-Solid-State Li-Ion Battery
ACS Appl. Mater. Interfaces, **16** 7189–7199 (2024).

3 K. Uchida, T. Masuda, S. Hara, Y. Matsuo, Y. Liu, H. Aoki, Y. Asano, K. Miyata, T. Fukuma, T. Ono, T. Isoyama, M. Takai
Stability Enhancement by Hydrophobic Anchoring and a Cross-Linked Structure of a Phospholipid Copolymer Film for Medical Devices
ACS Appl. Mater. Interfaces, **16** 39104–39116 (2024).

4 K. Yamamoto, T. Imai, A. Kawai, E. Ito, T. Miyazaki, N. Miyata, N. L. Yamada, H. Seto, H. Aoki
Surface Depth Analysis of Chemical Changes in Random Copolymer Thin Films Composed of Hydrophilic and Hydrophobic Silicon-Based Monomers Induced by Plasma Treatment as Studied by Hard X-Ray Photoelectron Spectroscopy and Neutron Reflectivity Measurements
ACS Appl. Mater. Interfaces, **16** 66782–66791 (2024).

5 T. Ikami, H. Aoki, T. Terashima
Lamellar Microphase Separation and Phase Transition of Hydrogen-Bonding/Crystalline Statistical Copolymers: Amide Functionalization at the Interface
ACS Macro Lett., **13** 446–452 (2024).

6 J. Kim, B. R. Thompson, T. Tominaga, T. Osawa, T. Egami, S. Förster, M. Ohl, E. Senses, A. Faraone, N. J. Wagner
Suppression of Segmental Chain Dynamics on a Particle's Surface in Well-Dispersed Polymer Nanocomposites
ACS Macro Lett., **13** 720–725 (2024).

7 R. Sujita, H. Aoki, M. Takenaka, M. Ouchi, T. Terashima
Universal Access to Water-Compatible and Nanostructured Materials via the Self-Assembly of Cationic Alternating Copolymers
ACS Macro Lett., **13** 747–753 (2024).

8 K. Yamashita, K. Komatsu, T. Hattori, S. Machida, H. Kagi
Crystal Structure and Compressibility of Magnesium Chloride Heptahydrate Found under High Pressure
Acta Crystallogr. Sect. B Struct. Sci. Cryst. Eng. Mater., **80** 695–705 (2024).

9 W. Guo, X. Miao, J. Cui, S. Torii, F. Qian, Y. Bai, Z. Kou, J. Zha, Y. Shao, Y. Zhang, F. Xu, L. Caron
Significantly Enhanced Reversibility and Mechanical Stability in Grain-Oriented MnNiGe-Based Smart Materials
Acta Mater., **263** 119530 (2024).

10 B. Guo, H. Chen, Y. Chong, W. Mao, S. Harjo, W. Gong, Z. Zhang, J. J. Jonas, N. Tsuji
Direct Observations of Dynamic and Reverse Transformation of Ti-6Al-4V Alloy and Pure Titanium
Acta Mater., **268** 119780 (2024).

11 Y. Ma, M. Naeem, L. Zhu, H. He, X. Sun, Z. Yang, F. He, S. Harjo, T. Kawasaki, X.-L. Wang
Microscopic Insights of the Extraordinary Work-Hardening Due to Phase Transformation
Acta Mater., **270** 119822 (2024).

12 W. Mao, S. Gao, W. Gong, T. Kawasaki, T. Ito, S. Harjo, N. Tsuji
Martensitic Transformation-Governed Lüders Deformation Enables Large Ductility and Late-Stage Strain Hardening in Ultrafine-Grained Austenitic Stainless Steel at Low Temperatures
Acta Mater., **278** 120233 (2024).

13 K. V. Werner, M. Naeem, F. Niessen, L. Zhu, M. Villa, X.-L. Wang, M. A. J. Somers
Experimental and Computational Assessment of the Temperature Dependency of the Stacking Fault Energy in Face-Centered Cubic High-Entropy Alloys
Acta Mater., **278** 120271 (2024).

14 H. Zhong, Y. Song, F. Long, H. Lu, M. Ai, T. Li, Y. Yao, Y. Sakai, M. Ikeda, K. Takahashi, M. Azuma, F. Hu, X. Xing, J. Chen
Design of Excellent Mechanical Performances and Magnetic Refrigeration via in situ Forming Dual-Phase Alloys
Adv. Mater., **36** 2402046 (2024).

15 A. Åhl, E. Nocerino, U. T. Veettil, K. Uetani, S. Yu, J. Armstrong, F. Juranyi, L. Bergström
Moisture-Dependent Vibrational Dynamics and Phonon Transport in Nanocellulose Materials
Adv. Mater., **37** 2415725 (2024).

16 M. Ai, Y. Song, F. Long, Y. Zhang, K. An, D. Yu, Y. Chen, Y. Sakai, M. Ikeda, K. Takahashi, M. Azuma, N. Shi, C. Zhou, J. Chen
Significantly Promoting the Thermal Conductivity and Machinability of Negative Thermal Expansion Alloy via in situ Precipitation of Copper Networks
Adv. Sci., **11** 2404838 (2024).

17 R. Kadono, H. Hosono
Ambipolarity of Hydrogen in Matter Revealed by Muons
Adv. Phys., **72** 409–476 (2024).

18 K. Koruza, E. Krupinska, C. Sele, Á. Végvári, W. Knecht, S. Z. Fisher
Botryococcus Braunii Autolysate for the Production of Deuterium-Labeled Recombinant Protein
Algal Res., **79** 103459 (2024).

19 T. Ji, S. Su, S. Wu, Y. Hori, Y. Shigeta, Y. Huang, W. Zheng, W. Xu, X. Zhang, R. Kiyanagi, K. Munakata, T. Ohhara, T. Nakanishi, O. Sato
Development of an Fe^{II} Complex Exhibiting Intermolecular Proton Shifting Coupled Spin Transition
Angew. Chem. Int. Ed., **63** e202404843 (2024).

20 T. Hanashima, J. Suzuki, K. Kakurai, N. Miyata, K. Sakai, H. Deguchi, Y. Hara, S. Takeichi, T. Yoshitake
Temperature- and Magnetic Field-Induced Magnetic Structural Changes in the $Fe_3Si/FeSi_2$ Superlattice
Appl. Phys. Express, **17** 035002 (2024).

21 S. Shamoto, M. Akatsu, L.-J. Chang, Y. Nemoto, J. Ieda
Inelastic Neutron Scattering Study of Magnon Excitation by Ultrasound Injection in Yttrium Iron Garnet
Appl. Phys. Lett., **124** 112402 (2024).

22 Y. Kawamoto, T. Kikkawa, M. Kawamata, Y. Umemoto, A. G. Manning, K. C. Rule, K. Ikeuchi, K. Kamazawa, M. Fujita, E. Saitoh, K. Kakurai, Y. Nambu
Understanding Spin Currents from Magnon Dispersion and Polarization: Spin-Seebeck Effect and Neutron Scattering Study on

$Tb_3Fe_5O_{12}$
Appl. Phys. Lett., **124** 132406 (2024).

23 J. Li, X. Li, Y. Zhang, J. Zhu, E. Zhao, M. Kofu, K. Nakajima, M. Avdeev, P.-F. Liu, J. Sui, H. Zhao, F. Wang, J. Zhang
Crystal-Liquid Duality Driven Ultralow Two-Channel Thermal Conductivity in α-MgAgSb
Appl. Phys. Rev., **11** 011406 (2024).

24 M. Yoshida, H. Iwase, Y. Horikawa, T. Shikata
Evidence of a Rod-like Structure for Hydroxypropyl Cellulose Samples in Aqueous Solution
Biomacromolecules, **25** 4255–4266 (2024).

25 Y. Kameda, Y. Amo, T. Usuki, H. Watanabe, Y. Umebayashi, K. Ikeda, T. Honda, T. Otomo
Experimental Determination of Relationship between Intramolecular Bond Lengths and Their Stretching Vibrational Frequencies of N,N -Dimethylformamide and Acetonitrile Molecules in the Liquid State
Bull. Chem. Soc. Jpn., **97** uoad006 (2024).

26 Y. Kameda, Y. Oshita, Y. Amo, T. Usuki, H. Watanabe, Y. Umebayashi, K. Ikeda, T. Honda, T. Otomo
Experimental Determination of the Relationship between S=O Bond Length and Its Stretching Frequency of the DMSO Molecule
Bull. Chem. Soc. Jpn., **97** uoae120 (2024).

27 C. Wang, D. Sen, V. K. Aswal, L. Weiguang, P. Balaya
Enhanced Storage Performance of a Low-Cost Hard Carbon Derived from Biomass
Carbon Trends, **17** 100415 (2024).

28 T. Ichikawa, T. Yamada, N. Aoki, Y. Maehara, K. Suda, T. Kobayashi
Surface Proton Hopping Conduction Mechanism Dominant Polymer Electrolytes Created by Self-Assembly of Bicontinuous Cubic Liquid Crystals
Chem. Sci., **15** 7034–7040 (2024).

29 T. Katsumata, R. Suzuki, N. Satoh, R. Oda, S. Motoyama, S. Suzuki, M. Nakashima, Y. Inaguma, D. Mori, A. Aimi, Y. Yoneda, Y. J. Shan
Existence of Local Polar Domains in Perovskite Oxyfluoride, $BaFeO_2F$
Chem. Mater., **36** 3697–3704 (2024).

30 A. E. Baumann, T. Yamada, K. Ito, C. R. Snyder, J. R. Hoffman, C. M. Brown, C. M. Stafford, C. L. Soles
Measuring the Influence of CO_2 and Water Vapor on the Dynamics in Polyethylenimine To Understand the Direct Air Capture of CO_2 from the Environment
Chem. Mater., **36** 6130–6143 (2024).

31 Y. Kajita, T. Nagai, S. Yamagishi, K. Kimura, M. Hagihala, T. Kimura
Ferroaxial Transitions in Glaserite-Type $Na_2BaM(PO_4)_2$ (M = Mg, Mn, Co, and Ni)
Chem. Mater., **36** 7451–7458 (2024).

32 Y. Masubuchi, K. Koyama, A. Hosono, M. Higuchi, M. Takesada, K. Shitara, H. Moriwake, S. Kikkawa
Average Cubic $BaTaO_2N$ Crystal Structure Formed by 50 Nm Size Domains with Polar Nanoregions Consisting of Cis-TaO_4 N_2 Octahedral Chains
Chem. Mater., **36** 7504–7513 (2024).

33 R. Liu, M. Nakamura, K. Kamazawa, X. Lu
Low-Energy Spin Excitations in Detwinned FeSe
Chin. Phys. Lett., **41** 067401 (2024).

34 A. Yamaguchi, Y. Kojima, N. R. De Souza, H. Iwase, T. Kamijo
Quasielastic Neutron Scattering Study on Low-Hydrated Myoglobin inside Silica Nanopores
Colloids Surf. Physicochem. Eng. Asp., **698** 134559 (2024).

35 T. Miyazaki, N. Miyata, H. Arima-Osonoi, K. Shimokita, K. Yamamoto, M. Takenaka, Y. Nakanishi, M. Shibata, H. Aoki, N. L. Yamada, M. Yamada, H. Seto
Adsorption Isotherm and Kinetics of Diffusion of Water Accumulated between Polypropylene Thin Film and Si Substrate: Neutron Reflectivity Investigation
Colloids Surf. Physicochem. Eng. Asp., **701** 134928 (2024).

36 T. Ishii, Y. J. Shan, K. Fujii, T. Katsumata, H. Imoto, A. Baterdene, K. Tezuka, M. Yashima
Synthesis, Crystal Structure and Investigation of Ion-Exchange Possibility for Sodium Tellurate $NaTeO_3(OH)$
Dalton Trans., **53** 5373–5381 (2024).

37 Y. Mori, H. Kagi, K. Aoki, M. Takano, S. Kakizawa, A. Sano-Furukawa, K. Funakoshi
Hydrogenation of Silicon-Bearing Hexagonal Close-Packed Iron and Its Implications for Density Deficits in the Inner Core
Earth Planet. Sci. Lett., **634** 118673 (2024).

38 N. Kitamura, R. Nagai, C. Ishibashi, Y. Idemoto
Effect of Intermediate-Range Structure on Negative Electrode Properties of Wadsley–Roth Phase $Ti_2Nb_{10}O_{29}$
Electrochemistry, **92** 087002–087002 (2024).

39 Y. Idemoto, Y. Koitabashi, C. Ishibashi, N. Ishida, N. Kitamura
Operating-Temperature Dependence of the Average and Electronic Structures of $0.4Li_2MnO_3$–$0.6Li(Mn_{1/3}Ni_{1/3}Co_{1/3})O_2$
Electrochemistry, **92** 107003–107003 (2024).

40 L. Zheng, B. Zhou, B. Wu, Y. Tan, J. Huang, M. Tyagi, V. García Sakai, T. Yamada, H. O'Neill, Q. Zhang, L. Hong
Decoupling of the Onset of Anharmonicity between a Protein and Its Surface Water around 200 K
eLife, **13** RP95665 (2024).

41 F. Hu, T. Qin, N. Ao, Y. Su, L. Zhou, P. Xu, J. Don Parker, T. Shinohara, J. Chen, S. Wu
Gradient Residual Strain Determination of Surface Impacted Railway S38C Axles by Neutron Bragg-Edge Transmission Imaging
Eng. Fract. Mech., **306** 110267 (2024).

42 A. Kimura, S. Endo, S. Nakamura
Total and Double Differential Scattering Cross-Section Measurements of Isotropic Graphite
EPJ Web Conf., **294** 01002 (2024).

43 S. Nakayama, O. Iwamoto, A. Kimura
Evaluation of Thermal Neutron Scattering Law of Nuclear-Grade Isotropic Graphite
EPJ Web Conf., **294** 07001 (2024).

44 H. Iwase, J. Kobayashi, Y. Kasama, W. Fujii, H. Nanbu
Structural Analysis of Polyglycerol Fatty Acid Ester-Coenzyme Q10 Aggregates in Solution
Food Res. Int., **175** 113741 (2024).

45 N. Yamashita, T. Hirayama
A Method for Simultaneously Measuring Friction and Gap at Metal–Lubricant Interface by Combined Use of Atomic Force Microscopy and Line-and-Space Patterned Metal Films
Front. Mech. Eng., **10** 1470775 (2024).

46 M. Nakamoto, M. Sugano, T. Ogitsu, M. Sugimoto, R. Taniguchi, K. Hirose, T. Kawasaki, W. Gong, S. Harjo, S. Awaji, H. Oguro
Internal Strain Measurement by Neutron Diffraction Under Transverse Compressive Stress for Nb_3Sn Wires With and Without Cu-Nb Reinforcement
IEEE Trans. Appl. Supercond., **34** 1–6 (2024).

47 Y. Deng, Y. Watanabe, S. Manabe, W. Liao, M. Hashimoto, S.-I. Abe, M. Tampo, Y. Miyake

Impact of Irradiation Side on Muon-Induced Single-Event Upsets in 65-Nm Bulk SRAMs
IEEE Trans. Nucl. Sci., **71** 912–920 (2024).

48 T. D. Vu, H. Shishido, K. Aizawa, T. Oku, K. Oikawa, M. Harada, K. M. Kojima, S. Miyajima, K. Soyama, T. Koyama, M. Hidaka, S. Y. Suzuki, M. M. Tanaka, M. Machida, S. Kawamata, T. Ishida
Application of Energy-Resolving Neutron Imaging to Major-Component Analyses of Materials Using Four-Channel Superconducting Detector
IEEJ Trans. Electr. Electron. Eng., **19** 1888–1894 (2024).

49 X. He, H. Kagi, K. Komatsu, A. Sano-Furukawa, J. Abe, K. Fukuyama, T. Shinmei, S. Nakano
High-Pressure Behaviors of Hydrogen Bonds in Fluorine-Doped Brucite
Inorg. Chem., **63** 22349–22360 (2024).

50 K. Arai, K. Onagi, Y. Tang, T. Ishigaki, H. Sai, Y. Sasahara, G. Caruntu, H. Okabe, M. Harada, K. Nakashima, H. Kageyama
Promoted Hydride Substitution in $BaTiO_3$ Cubes
Inorg. Chem., **63** 23260–23266 (2024).

51 M. Fujihala, H. Okabe, A. Koda
μSR Studies on Copper Minerals
Interactions, **245** 13 (2024).

52 P. Jaikaew, S. Rimjaem, C. Thongbai, T. Adachi, I. Watanabe
Surface Muon Production at J-PARC Muon Facility
Interactions, **245** 24 (2024).

53 T. U. Ito, W. Higemoto, A. Koda, J. G. Nakamura, K. Shimomura
Muon Spin Relaxation in Mixed Perovskite $(LaAlO_3)_x(SrAl_{0.5}Ta_{0.5}O_3)_{1-x}$ with $X \simeq 0.3$
Interactions, **245** 25 (2024).

54 K. Shimomura, A. Koda, A. D. Pant, H. Sunagawa, H. Fujimori, I. Umegaki, J. Nakamura, M. Fujihala, M. Tampo, N. Kawamura, N. Teshima, P. Strasser, R. Kadono, R. Iwai, S. Matoba, S. Nishimura, S. Kamioka, S. Kanda, S. Takeshita, T. Yuasa, T. Ito, T. Yamazaki, T. Mibe, W. Higemoto, Y. Miyake, Y. Kobayashi, Y. Oishi, Y. Nagatani, Y. Ikedo
Pulsed Muon Facility of J-PARC MUSE,
Interactions, **245** 31 (2024).

55 R. Pudasaini, A. D. Pant, R. Adhikari
Muonium Behavior in Derivatives of Hemoglobin: A First-Principles Study
Interactions, **245** 34 (2024).

56 S. Takeshita, I. Umegaki, M. Tampo, P. Strasser, Y. Ikedo, A. Koda, W. Higemoto, T. Yuasa, N. Kawamura, Y. Miyake, K. Shimomura
Negative Muon Beam Status at the D-Line of MUSE, J-PARC
Interactions, **245** 38 (2024).

57 M. Tampo, Y. Miyake, T. Saito, T. Kutsuna, M. Tsumura, I. Umegaki, S. Takeshita, S. Doiuchi, Y. Ishikake, A. Hashimoto, K. Shimomura
Developments on Muonic X-Ray Measurement System for Historical-Cultural Heritage Samples in Japan Proton Accelerator Research Complex (J-PARC)
Interactions, **245** 39 (2024).

58 S. Tsutsui, T. U. Ito, J. Nakamura, M. Yoshida, Y. Kobayashi, Y. Yoda, J. G. Nakamura, A. Koda, R. Higashinaka, D. Aoki, T. D. Matsuda, Y. Aoki
^{149}Sm Synchrotron-Radiation-Based Mössbauer and μ^+SR Studies of $Sm_3Ru_4Ge_{13}$
Interactions, **245** 55 (2024).

59 P. Xie, M. Takahama, T. Taniguchi, H. Okabe, A. Koda, I. Watanabe, M. Fujita
Annealing and Doping Effects on Magnetism for T^*-Type (La, Eu, Sr)$_2CuO_{4-y}F_y$ Cuprates
Interactions, **245** 66 (2024).

60 Y. Goto, S. Fukumura, P. Strasser, T. Ino, R. Iwai, S. Kanda, S. Kawamura, M. Kitaguchi, S. Nishimura, T. Oku, T. Okudaira, H. M. Shimizu, K. Shimomura, H. Tada, H. A. Torii
New Muonic He Atom HFS Measurements at J-PARC MUSE
Interactions, **245** 75 (2024).

61 S. Kanda
Hexapole State Selector for Focusing and Polarizing Muonium
Interactions, **245** 78 (2024).

62 K. Ikeda, S. Sashida, T. Otomo, H. Ohshita, T. Honda, T. Hawai, H. Saito, S. Itoh, T. Yokoo, K. Sakaki, H. Kim, Y. Nakamura, A. Machida, D. Matsumura, W. A. Sławiński
Local Structural Changes in V–Ti–Cr Alloy Hydrides with Hydrogen Absorption/Desorption Cycling
Int. J. Hydrog. Energy, **51** 79–87 (2024).

63 K. Shimizu, K. Nishimura, K. Matsuda, N. Nunomura, T. Namiki, T. Tsuchiya, S. Akamaru, S. Lee, T. Tsuru, W. Higemoto, H. Toda
Novel Approach to Explore Hydrogen Trapping Sites in Aluminum: Integrating Muon Spin Relaxation with First-Principles Calculations
Int. J. Hydrog. Energy, **95** 292–299 (2024).

64 K. Hagihara, T. Mayama, M. Yamasaki, S. Harjo, T. Tokunaga, K. Yamamoto, M. Sugita, K. Aoyama, W. Gong, S. Nishimoto
Contributions of Multimodal Microstructure in the Deformation Behavior of Extruded Mg Alloys Containing LPSO Phase
Int. J. Plast., **173** 103865 (2024).

65 C. M. Wensrich, S. Holman, M. Courdurier, W. R. B. Lionheart, A. P. Polyakova, I. E. Svetov
Direct Inversion of the Longitudinal Ray Transform for 2D Residual Elastic Strain Fields
Inverse Probl., **40** 075011 (2024).

66 Y. Zhang, K. Marusawa, K. Kudo, S. Morooka, S. Harjo, G. Miyamoto, T. Furuhara
Multi-Aspect Characterization of Low-Temperature Tempering Behaviors in High-Carbon Martensite
ISIJ Int., **64** 245–256 (2024).

67 N. Tsuchida, S. Kuramoto, R. Ueji, W. Gong, S. Harjo, K. Hiroi, Y. Kawamura
Change in Mechanical Properties of High-Strength Martensitic Steel by the Combination of Pre-Strain and Deformation Temperature
ISIJ Int., **64** 354–360 (2024).

68 S. Uranaka, M. Takanashi, T. Maeda, T. Masumura, T. Tsuchiyama, Y. Kawamoto, H. Shirahata, Y. Kobayashi, R. Uemori
Effects of Retained Austenite upon Softening during Low-Temperature Tempering in Martensitic Carbon Steels
ISIJ Int., **64** 449–458 (2024).

69 R. Ueji, W. Gong, S. Harjo, T. Kawasaki, A. Shibata, Y. Kimura, T. Inoue, N. Tsuchida
Deformation-Induced Martensitic Transformation at Tensile and Compressive Deformations of Bainitic Steels with Different Carbon Contents
ISIJ Int., **64** 459–465 (2024).

70 K. Matsuda, T. Masumura, T. Tsuchiyama, Y. Onuki, M. Takanashi, T. Maeda, Y. Kawamoto, H. Shirahata, R. Uemori
Reverse Transformation Behavior in Multi-Phased Medium Mn Martensitic Steel Analyzed by in-situ Neutron Diffraction
ISIJ Int., **64** 486–490 (2024).

71 M. Watanabe, G. Miyamoto, Y. Zhang, S. Morooka, S. Harjo, Y. Kobayashi, T. Furuhara

Thermal Stability of Retained Austenite with Heterogeneous Composition and Size in Austempered Fe-2Mn-1.5Si-0.4C Alloy
ISIJ Int., **64** 1464–1476 (2024).

72 T. Yamashita, S. Morooka, W. Gong, T. Kawasaki, S. Harjo, T. Hojo, Y. Okitsu, H. Fujii
Role of Retained Austenite and Deformation-Induced Martensite in 0.15C-5Mn Steel Monitored by in-situ Neutron Diffraction Measurement during Tensile Deformation
ISIJ Int., **64** 2051–2060 (2024).

73 Y. Yamaguchi, M. Harada, N. Kawamura, I. Umegaki, M. Tampo, S. Takeshita, K. Haga
Preliminary experiment for measurement of radionuclide yield from nuclear capture reaction of negative muon
JAEA-Conf, 2023–001 (2024).

74 Y. Zhou, W. Song, F. Zhang, Y. Wu, Z. Lei, M. Jiao, X. Zhang, J. Dong, Y. Zhang, M. Yang, Z. Lu, S. Harjo, T. Kawasaki, W. Gong, Y. Zhao, D. Ma, Z. Lu
Probing Deformation Behavior of a Refractory High-Entropy Alloy Using in Situ Neutron Diffraction
J. Alloys Compd., **971** 172635 (2024).

75 C. González-Guillén, L. Romero-Resendiz, M. Naeem, A. L. Vidilli, L. B. Otani, E. Klyatskina, G. Gonzalez, V. Amigó
Microstructural and Mechanical Behavior of Second-Phase Hardened Porous Refractory Ti-Nb-Zr-Ta Alloys
J. Alloys Compd., **980** 173605 (2024).

76 K. Edalati, A. Q. Ahmed, S. Akrami, K. Ameyama, V. Aptukov, R. N. Asfandiyarov, M. Ashida, V. Astanin, A. Bachmaier, V. Beloshenko, E. V. Bobruk, K. Bryła, J. M. Cabrera, A. P. Carvalho, N. Q. Chinh, I.-C. Choi, R. Chulist, J. M. Cubero-Sesin, G. Davdian, M. Demirtas, S. Divinski, K. Durst, J. Dvorak, P. Edalati, S. Emura, N. A. Enikeev, G. Faraji, R. B. Figueiredo, R. Floriano, M. Fouladvind, D. Fruchart, M. Fuji, H. Fujiwara, M. Gajdics, D. Gheorghe, Ł. Gondek, J. E. González-Hernández, A. Gornakova, T. Grosdidier, J. Gubicza, D. Gunderov, L. He, O. F. Higuera, S. Hirosawa, A. Hohenwarter, Z. Horita, J. Horky, Y. Huang, J. Huot, Y. Ikoma, T. Ishihara, Y. Ivanisenko, J. Jang, A. M. Jorge, M. Kawabata-Ota, M. Kawasaki, T. Khelfa, J. Kobayashi, L. Kommel, A. Korneva, P. Kral, N. Kudriashova, S. Kuramoto, T. G. Langdon, D.-H. Lee, V. I. Levitas, C. Li, H.-W. Li, Y. Li, Z. Li, H.-J. Lin, K.-D. Liss, Y. Liu, D. M. M. Cardona, K. Matsuda, A. Mazilkin, Y. Mine, H. Miyamoto, S.-C. Moon, T. Müller, J. A. Muñoz, M. Yu. Murashkin, M. Naeem, M. Novelli, D. Olasz, R. Pippan, V. V. Popov, E. N. Popova, G. Purcek, P. De Rango, O. Renk, D. Retraint, Á. Révész, V. Roche, P. Rodriguez-Calvillo, L. Romero-Resendiz, X. Sauvage, T. Sawaguchi, H. Sena, H. Shahmir, X. Shi, V. Sklenicka, W. Skrotzki, N. Skryabina, F. Staab, B. Straumal, Z. Sun, M. Szczerba, Y. Takizawa, Y. Tang, R. Z. Valiev, A. Vozniak, A. Voznyak, B. Wang, J. T. Wang, G. Wilde, F. Zhang, M. Zhang, P. Zhang, J. Zhou, X. Zhu, Y. T. Zhu
Severe Plastic Deformation for Producing Superfunctional Ultrafine-Grained and Heterostructured Materials: An Interdisciplinary Review
J. Alloys Compd., **1002** 174667 (2024).

77 J. Abe, H. Arima-Osonoi, H. Iwase, S. Takata, K. Ohuchi, S. Kasai, T. Miyazaki, T. Morita, M. Shibayama
A High-Temperature High-Pressure Small-Angle Neutron Scattering Cell for Studying Hydrothermal Reactions in Supercritical Water
J. Appl. Crystallogr., **57** 306–313 (2024).

78 T. Kumada, R. Motokawa, H. Iwase
Low-Background Ultrahigh-Purity Aluminium Window for Small-Angle Neutron Scattering Using Monochromatic Cold Neutrons
J. Appl. Crystallogr., **57** 728–733 (2024).

79 K.-H. Lu, W.-R. Wu, C.-J. Su, P.-W. Yang, N. L. Yamada, H.-J. Zhuo, S.-A. Chen, W.-T. Chuang, Y.-K. Lan, A.-C. Su, U.-S. Jeng
Modulating Phase Segregation during Spin-Casting of Fullerene-Based Polymer Solar-Cell Thin Films upon Minor Addition of a High-Boiling Co-Solvent
J. Appl. Crystallogr., **57** 1871–1883 (2024).

80 S. Takeshita, K. Hori, M. Hiraishi, H. Okabe, A. Koda, D. Kawaguchi, K. Tanaka, R. Kadono
Slow Polymer Dynamics in Poly(3-Hexylthiophene) Probed by Muon Spin Relaxation
J. Appl. Phys., **136** 034701 (2024).

81 Z. Zhang, T. Hattori, R. Song, D. Yu, R. Mole, J. Chen, L. He, Z. Zhang, B. Li
Giant Barocaloric Effects in Sodium Hexafluorophosphate and Hexafluoroarsenate
J. Appl. Phys., **136** 035105 (2024).

82 Y. Matsumoto, K. Oikawa, K. Watanabe, H. Sato, J. D. Parker, T. Shinohara, Y. Kiyanagi
Nondestructive Analysis of Internal Crystallographic Structures of Japanese Swords Using Neutron Imaging
J. Archaeol. Sci. Rep., **58** 104729 (2024).

83 N. Yano, T. Kondo, K. Kusaka, T. Arakawa, T. Sakamoto, S. Fushinobu
Charge Neutralization and β-Elimination Cleavage Mechanism of Family 42 L-Rhamnose-α-1,4-D-Glucuronate Lyase Revealed Using Neutron Crystallography
J. Biol. Chem., **300** 105774 (2024).

84 F. Lin, S. Itoh, K. Fukuzawa, H. Zhang, N. Azuma
Correlation between Viscoelastic Response and Frictional Properties of Hydrated Zwitterionic Polymer Brush Film in Narrowing Shear Gap
J. Colloid Interface Sci., **655** 253–261 (2024).

85 A. Murmiliuk, H. Iwase, J.-J. Kang, S. Mohanakumar, M.-S. Appavou, K. Wood, L. Almásy, A. Len, K. Schwärzer, J. Allgaier, M. Dulle, T. Gensch, B. Förster, K. Ito, H. Nakagawa, S. Wiegand, S. Förster, A. Radulescu
Polyelectrolyte-Protein Synergism: pH-Responsive Polyelectrolyte/Insulin Complexes as Versatile Carriers for Targeted Protein and Drug Delivery
J. Colloid Interface Sci., **665** 801–813 (2024).

86 T. Kämäräinen, S. Nogami, H. Arima-Osonoi, H. Iwase, H. Uchiyama, Y. Tozuka, K. Kadota
Multiscale Structure Analysis of a pH-Responsive Gelatin/Hydroxypropyl Methylcellulose Phthalate Blend Using Small-Angle Scattering
J. Colloid Interface Sci., **669** 975–983 (2024).

87 K. Kawai, T. Sogabe, H. Nakagawa, T. Yamada, S. Koseki
Effect of Water Activity on the Mechanical Glass Transition and Dynamical Transition of Bacteria-Solute Systems
J. Food Eng., **375** 112066 (2024).

88 T. Ishida, T. D. Vu, H. Shishido, K. Aizawa, T. Oku, K. Oikawa, M. Harada, K. M. Kojima, S. Miyajima, T. Koyama, K. Soyama, M. Hidaka, S. Y. Suzuki, M. M. Tanaka, M. Machida, S. Kawamata
Neutron Transmission CB-KID Imager Using Samples Placed at Room Temperature
J. Low Temp. Phys., **214** 152–157 (2024).

89 K. Saito, K. Umeda, K. Fujii, K. Mori, M. Yashima
High Proton Conduction by Full Hydration in Highly Oxygen Deficient Perovskite
J. Mater. Chem. A, **12** 13310–13319 (2024).

90 L. Romero Reséndiz, T. Sánchez Cano, M. Naeem, A. Ur Rehman, E. Salamci, V. Torres Mendoza, E. Degalez Duran, L. Bazán Díaz, M. U. Salamci
Mechanical and Electrochemical Properties Comparison of Additively Manufactured Ti-6Al-4V Alloys by Electron Beam Melting

and Selective Laser Melting
J. Mater. Eng. Perform., **33** 9028–9038 (2024).

91 T.-D. Nguyen, C. Singh, Y. S. Kim, J. H. Han, D.-H. Lee, K. Lee, S. Harjo, S. Y. Lee
Mechanical Properties of Base Metal and Heat-Affected Zone in Friction-Stir-Welded AA6061-T6 at Ultra-Low Temperature of 20 K
J. Mater. Res. Technol., **31** 1547–1556 (2024).

92 K.-D. Liss, J.-K. Han, M. Blankenburg, U. Lienert, S. Harjo, T. Kawasaki, P. Xu, E. Yukutake, M. Kawasaki
Recrystallization of Bulk Nanostructured Magnesium Alloy AZ31 after Severe Plastic Deformation: An in situ Diffraction Study
J. Mater. Sci., **59** 5831–5853 (2024).

93 W. Mao, W. Gong, S. Harjo, S. Morooka, S. Gao, T. Kawasaki, N. Tsuji
In situ Neutron Diffraction Revealing the Achievement of Excellent Combination of Strength and Ductility in Metastable Austenitic Steel by Grain Refinement
J. Mater. Sci. Technol., **176** 69–82 (2024).

94 J. Ge, Y. Gu, Z. Yao, S. Liu, H. Ying, C. Lu, Z. Wu, Y. Ren, J. Suzuki, Z. Xie, Y. Ke, J. Zeng, H. Zhu, S. Tang, X.-L. Wang, S. Lan
Evolution of Medium-Range Order and Its Correlation with Magnetic Nanodomains in Fe-Dy-B-Nb Bulk Metallic Glasses
J. Mater. Sci. Technol., **176** 224–235 (2024).

95 S. Wang, J. Wang, S. Zhang, D. Wei, Y. Chen, X. Rong, W. Gong, S. Harjo, X. Liu, Z. Jiao, Z. Yang, G. Sha, C. Wang, G. Chen, H. Chen
Dual Nanoprecipitation and Nanoscale Chemical Heterogeneity in a Secondary Hardening Steel for Ultrahigh Strength and Large Uniform Elongation
J. Mater. Sci. Technol., **185** 245–258 (2024).

96 M. Takano, H. Kagi, Y. Mori, K. Aoki, S. Kakizawa, A. Sano-Furukawa, R. Iizuka-Oku, T. Tsuchiya
Low Reactivity of Stoichiometric FeS with Hydrogen at High-Pressure and High-Temperature Conditions
J. Mineral. Petrol. Sci., **119** 240122 (2024).

97 C. Micheau, Y. Ueda, R. Motokawa, K. Akutsu-Suyama, N. L. Yamada, M. Yamada, S. A. Moussaoui, E. Makombe, D. Meyer, L. Berthon, D. Bourgeois
Organization of Malonamides from the Interface to the Organic Bulk Phase
J. Mol. Liq., **401** 124372 (2024).

98 H. Abe, S. Maruyama, K. Hiroi, S. Takata
Probing Water-Driven Nanostructures in an Ionic Liquid Using Small- and Wide-Angle Neutron Scattering: 1-Dodecyl-3-Methylimidazolium Iodide
J. Mol. Liq., **404** 124952 (2024).

99 H. Liu, Z. Jing, Y. Zhou, T. Nagatoshi, K. Ito, K. Yoshida, T. Yamada, T. Yamaguchi
X-Ray Diffraction and Quasielastic Neutron Scattering Studies of the Structure and Dynamic Properties of Water Confined in Ordered Microporous Carbon Pores
J. Mol. Liq., **415** 126316 (2024).

100 X. He, H. Kagi, K. Komatsu, R. Iizuka-Oku, H. Okajima, T. Hattori, A. Sano-Furukawa, S. Machida, J. Abe, H. Gotou, S. Nakano
Hydroxyl Group/Fluorine Disorder in Deuterated Magnesium Hydroxyfluoride and Behaviors of Hydrogen Bonds under High Pressure
J. Mol. Struct., **1310** 138271 (2024).

101 M. Nirei, M. Kofu, K. Nakajima, T. Kikuchi, S. Ohira-Kawamura, N. Murai, M. Harada, Y. Inamura
Neutron Flux and Energy Resolution of Direct-Geometry Disk-Chopper Spectrometer AMATERAS at J-PARC
J. Neutron Res., **26** 75–82 (2024).

102 M. K. Ahmed Patwary, M. Segawa, M. Maeda, Y. Toh, S. Endo, S. Nakamura, G. Rovira, A. Kimura
Measurement of the Thermal Neutron Capture-Cross Section of ^{191}Ir at ANNRI MLF J-PARC
J. Nucl. Sci. Technol., **61** 1385–1396 (2024).

103 M. Segawa, Y. Toh, M. Maeda, T. Kai
Development of Neutron Self-Indication Thermometry at J-PARC
J. Nucl. Sci. Technol., **62** 268–277 (2024).

104 K. Nawa, R. Murasaki, S. Itoh, H. Saito, H. Nojiri, C. Dela Cruz, D. Okuyama, M. Yoshida, D. Ueta, H. Yoshizawa, T. J. Sato
Magnetism of Pseudospin-1/2 Pyrochlore Antiferromagnet $Na_3Co(CO_3)_2Cl$
J. Phys. Condens. Matter, **36** 495801 (2024).

105 T. Dang Vu, H. Shishido, K. Aizawa, T. Oku, K. Oikawa, M. Harada, K. M. Kojima, S. Miyajima, K. Soyama, T. Koyama, M. Hidaka, S. Y. Suzuki, M. M. Tanaka, M. Machida, S. Kawamata, T. Ishida
Neutron Transmission Imaging System with a Superconducting Kinetic Inductance Detector
J. Phys. Conf. Ser., **2776** 012009 (2024).

106 K. Ninomiya, M. K. Kubo, M. Inagaki, G. Yoshida, S. Takeshita, M. Tampo, K. Shimomura, N. Kawamura, P. Strasser, Y. Miyake, T. U. Ito, W. Higemoto, T. Saito
Development of a Non-Destructive Carbon Quantification Method in Iron by Negative Muon Lifetime Measurement
J. Radioanal. Nucl. Chem., **333** 3445–3450 (2024).

107 K. Matsuzaki, W. Zhang, K. Saito, K. Fujii, M. Yashima
Structural and Electrical Properties of $Bi_3GaSb_2O_{11}$ at High Temperatures
J. Solid State Chem., **329** 124380 (2024).

108 K. Hikima, K. Ogawa, R. F. Indrawan, H. Tsukasaki, S. Hiroi, K. Ohara, K. Ikeda, T. Watanabe, T. Matsunaga, K. Yamamoto, S. Mori, Y. Uchimoto, A. Matsuda
Structure and Particle Surface Analysis of Li_2S–P_2S_5–LiI-Type Solid Electrolytes Synthesized by Liquid-Phase Shaking
J. Solid State Electrochem., **28** 4377–4387 (2024).

109 W. Yi, T. Kawasaki, Y. Zhang, H. Akamatsu, R. Ota, S. Torii, K. Fujita
$La_2SrSc_2O_7$: A-Site Cation Disorder Induces Ferroelectricity in Ruddlesden–Popper Layered Perovskite Oxide
J. Am. Chem. Soc., **146** 4570–4581 (2024).

110 K. Matsuzaki, K. Saito, Y. Ikeda, Y. Nambu, M. Yashima
High Proton Conduction in the Octahedral Layers of Fully Hydrated Hexagonal Perovskite-Related Oxides
J. Am. Chem. Soc., **146** 18544–18555 (2024).

111 T. Nagai, M. Hagihala, R. Yokoi, H. Moriwake, T. Kimura
Ferroelectricity Induced by a Combination of Crystallographic Chirality and Axial Vector
J. Am. Chem. Soc., **146** 23348–23355 (2024).

112 S. Sato, M. Miyakawa, T. Taniguchi, Y. Onodera, K. Ohara, K. Ikeda, N. Kitamura, Y. Idemoto, S. Kohara
Synthesis of Hyperordered Permanently Densified Silica Glasses by Hot Compression above the Glass Transition Temperature
J. Ceram. Soc. Jpn., **132** 427–433 (2024).

113 S. Hosokawa, J. R. Stellhorn, N. Boudet, N. Blanc, E. Magome, L. Pusztai, S. Kohara, K. Ikeda, T. Otomo
Local- and Intermediate-Range Partial Structure Study of As–Se Glasses
J. Phys. Soc. Jpn., **93** 014601 (2024).

114 T. Miyatake, Y. Wako, R. Abe, S. Tsukamoto, M. Uehara
Neutron Diffraction Study of Layered Nickelates Pr_4Ni_{3-x} Co_xO_8 for High-Temperature Superconductor Candidate
J. Phys. Soc. Jpn., **93** 024709 (2024).

115 T. U. Ito, R. Kadono
Distinguishing Ion Dynamics from Muon Diffusion in Muon Spin Relaxation
J. Phys. Soc. Jpn., **93** 044602 (2024).

116 T. Nakajima, H. Saito, N. Kobayashi, T. Kawasaki, T. Nakamura, H. Kawano-Furukawa, S. Asai, T. Masuda
Polarized and Unpolarized Neutron Scattering for Magnetic Materials at the Triple-Axis Spectrometer PONTA in JRR-3
J. Phys. Soc. Jpn., **93** 091002 (2024).

117 T. Higuchi, H. Akatsuka, A. Brossard, D. Fujimoto, P. Giampa, S. Hansen-Romu, K. Hatanaka, M. Hino, G. Ichikawa, S. Imajo, B. Jamieson, S. Kawasaki, M. Kitaguchi, R. Mammei, R. Matsumiya, K. Mishima, R. Picker, W. Schreyer, H. M. Shimizu, S. Sidhu, S. Vanbergen
Polarized Cold-Neutron Reflectometry at JRR-3/MINE2 for the Development of Ultracold-Neutron Spin Analyzers for a Neutron EDM Experiment at TRIUMF
J. Phys. Soc. Jpn., **93** 091009 (2024).

118 K. Yamakawa, H. Nakada, K. Kimura, K. Oikawa, M. Harada, Y. Inamura, K. Ohoyama, K. Hayashi
Atomic Imaging of $BaTiO_3$ by Multiple-Wavelength Neutron Holography
J. Phys. Soc. Jpn., **93** 104601 (2024).

119 T. Taniguchi, K. Osato, H. Okabe, T. Kitazawa, M. Kawamata, S. Hashimoto, Y. Ikeda, Y. Nambu, D. P. Sari, I. Watanabe, J. G. Nakamura, A. Koda, J. Gouchi, Y. Uwatoko, S. Kittaka, T. Sakakibara, M. Mizumaki, N. Kawamura, T. Yamanaka, K. Hiraki, T. Sasaki, M. Fujita
Field-Induced Criticality in $YbCu_4Au$
J. Phys. Soc. Jpn., **93** 124706 (2024).

120 Z. Liu, R. Ide, T. Arima, S. Itoh, S. Asai, T. Masuda
Inelastic Neutron Scattering Study on Skyrmion Host Compound GaV_4Se_8
J. Phys. Soc. Jpn., **93** 124707 (2024).

121 T. Hirayama, N. Yamashita, W. Yamamoto, K. Shirode, A. Okada, N. Hatano, T. Tsuchiya, M. Yamada
Adsorption Characteristics and Mechanical Responses of Lubricants Containing Polymer Additives under Fluid Lubrication with a Narrow Gap
Langmuir, **40** 6229–6243 (2024).

122 K. Shimokita, K. Yamamoto, N. Miyata, M. Shibata, Y. Nakanishi, M. Arakawa, M. Takenaka, T. Kida, K. Tokumitsu, R. Tanaka, T. Shiono, M. Yamada, H. Seto, N. L. Yamada, H. Aoki, T. Miyazaki
Neutron Reflectivity Study on the Adsorption Layer of Polyethylene Grown on Si Substrate
Langmuir, **40** 15758–15766 (2024).

123 Y. Ueda, C. Micheau, K. Akutsu-Suyama, K. Tokunaga, M. Yamada, N. L. Yamada, D. Bourgeois, R. Motokawa
Fluorous and Organic Extraction Systems: A Comparison from the Perspectives of Coordination Structures, Interfaces, and Bulk Extraction Phases
Langmuir, **40** 24257–24271 (2024).

124 K. Yoshimura, A. Hiroki, A. Radulescu, Y. Noda, S. Koizumi, Y. Zhao, Y. Maekawa
Effects of Functional Graft Polymers on Phase Separation and Ion-Channel Structures in Anion Exchange Membranes Analyzed by SANS Partial Scattering Function
Macromolecules, **57** 1998–2007 (2024).

125 Y. Nakamura, T. Tominaga, T. Iwata, K. Inoue, Y. Fujii, N. Oshima, M. Naito
Spatial Dynamics of Water Molecules Confined in Deuterated Epoxies by Quasi-Elastic Neutron Scattering
Macromolecules, **57** 4254–4262 (2024).

126 M. Kawano, Y. Morimitsu, Y. Liu, N. Miyata, T. Miyazaki, H. Aoki, D. Kawaguchi, S. Yamamoto, K. Tanaka
In-Plane Movement of Isolated Poly(Methacrylate) Chains on a Hydrophilic Solid Surface
Macromolecules, **57** 6625–6633 (2024).

127 R. Kanno, M. Shibata, M. Takenaka, S. Takata, K. Hiroi, M. Ouchi, T. Terashima
Thermoresponsive Gelation and Phase Transition of PEG/Cation Random Terpolymer Micelles in Water in the Presence of Salts
Macromolecules, **57** 10071–10082 (2024).

128 W. Gong, R. Gholizadeh, T. Kawasaki, K. Aizawa, S. Harjo
Cryogenic Deformation Behavior of a Dual-Phase Mg–Li Alloy Investigated by in-situ Neutron Diffraction
Magnes. Technol. 2024, 89–90(2024).

129 W. Zhang, M. Yang, W. Mao, S. Takesue, M. Soshi
The Effect of Productive and Quality Deposition Strategies on Residual Stress for Directed Energy Deposition (DED) Process
Manuf. Lett., **41** 868–878 (2024).

130 P. Thirathipviwat, M. Hasegawa, Y. Onuki, S. Sato, O. V. Mishin
In situ Neutron Diffraction Study and Electron Microscopy Analysis of Microstructure and Texture Evolution during Annealing of Rolled CoCrFeNi Alloy Doped with 1 at.%C
Mater. Charact., **212** 113980 (2024).

131 Z. Pan, Z. Liang, X. Wang, Y.-W. Fang, X. Ye, Z. Liu, T. Nishikubo, Y. Sakai, X. Shen, Q. Liu, S. Kawaguchi, F. Zhan, L. Fan, Y.-Y. Wang, C.-Y. Ma, X. Jiang, Z. Lin, R. Yu, X. Xing, M. Azuma, Y. Long
Mixed Anion Control of Enhanced Negative Thermal Expansion in the Oxysulfide of $PbTiO_3$
Mater. Horiz., **11** 5394–5401 (2024).

132 K. Yamanaka, M. Mori, D. Yokosuka, K. Yoshida, Y. Onuki, S. Sato, A. Chiba
Effect of Matrix Dislocation Strengthening on Deformation-Induced Martensitic Transformation Behavior of Metastable High-Entropy Alloys
Mater. Res. Lett., **12** 1–9 (2024).

133 Y. S. Kim, H. Chae, D.-H. Lee, J. H. Han, S.-K. Hong, Y. S. Na, S. Harjo, T. Kawasaki, W. Woo, S. Y. Lee
In-situ Neutron Diffraction Study of Serration-Involved Ultra-Cryogenic Deformation Behavior at 15K
Mater. Sci. Eng. A, **899** 146453 (2024).

134 M. Naeem, R. J. Sánchez Cruz, M. A. Esquivel Neri, Y. Ma, V. Amigó Borrás, G. González, A. J. Knowles, W. Gong, S. Harjo, Y. T. Zhu, X.-L. Wang, L. Romero-Resendiz
Enhanced Cryogenic Mechanical Properties of Heterostructured CrCoNi Multicomponent Alloy: Insights from in-situ Neutron Diffraction
Mater. Sci. Eng. A, **916** 147374 (2024).

135 S. Futami, Y. Ikeda, H.-F. Zhao, Y. Umemoto, T. Honda, M. Fujita
Search for Significant Short-Range Ordering in Medium-Entropy Alloys Tr-Co-Ni (Tr = Cr, Mn, and Fe)
Mater. Trans., **65** 995–1000 (2024).

136 Y.-J. Zhang, T. Umeda, S. Morooka, S. Harjo, G. Miyamoto, T. Furuhara
Pearlite Growth Kinetics in Fe-C-Mn Eutectoid Steels: Quantitative Evaluation of Energy Dissipation at Pearlite Growth Front Via Experimental Approaches

Metall. Mater. Trans. A, **55** 3921–3936 (2024).

137 H. Chae, E.-W. Huang, J. Jain, D.-H. Lee, S. Harjo, T. Kawasaki, S. Y. Lee
Mechanical Stability of Retained Austenite and Texture Evolution in Additively Manufactured Stainless Steel
Met. Mater. Int., **30** 1321–1330 (2024).

138 X. Yang, G. Che, Y. Wang, P. Zhang, X. Tang, P. Lang, D. Gao, X. Wang, Y. Wang, T. Hattori, J. Abe, A. Guan, J. Xiang, Q. Li, X. Lin, X. Dong, H. Mao, H. Zheng, K. Li
High-Pressure Polymerization of Phenol toward Degree-4 Carbon Nanothread
Nano Lett., **25** 1028–1035 (2025).

139 A. A. Kaharudin, M. Ohnuma, S. Lee, T. Tsuchiya, Y. Asada, K. Ikeda, K. Ohishi, J. Suzuki, K. Matsuda, T. Homma
Unified Interpretations of Two Kinds of Needle-Shaped Precipitates Using Transmission Electron Microscopy and Small-Angle Neutron Scattering in Aged Al–Mg_2Si(-Cu) Alloys
Nanomaterials, **14** 176 (2024).

140 P.-F. Liu, X. Li, J. Li, J. Zhu, Z. Tong, M. Kofu, M. Nirei, J. Xu, W. Yin, F. Wang, T. Liang, L. Xie, Y. Zhang, D. J. Singh, J. Ma, H. Lin, J. Zhang, J. He, B.-T. Wang
Strong Low-Energy Rattling Modes Enabled Liquid-like Ultralow Thermal Conductivity in a Well-Ordered Solid
Natl. Sci. Rev., **11** nwae216 (2024).

141 S. Hasegawa, H. Kikuchi, S. Asai, Z. Wei, B. Winn, G. Sala, S. Itoh, T. Masuda
Field Control of Quasiparticle Decay in a Quantum Antiferromagnet
Nat. Commun., **15** 125 (2024).

142 E. Fogh, M. Nayak, O. Prokhnenko, M. Bartkowiak, K. Munakata, J.-R. Soh, A. A. Turrini, M. E. Zayed, E. Pomjakushina, H. Kageyama, H. Nojiri, K. Kakurai, B. Normand, F. Mila, H. M. Rønnow
Field-Induced Bound-State Condensation and Spin-Nematic Phase in $SrCu_2(BO_3)_2$ Revealed by Neutron Scattering up to 25.9T
Nat. Commun., **15** 442 (2024).

143 Z. Song, T. Wang, H. Yang, W. H. Kan, Y. Chen, Q. Yu, L. Wang, Y. Zhang, Y. Dai, H. Chen, W. Yin, T. Honda, M. Avdeev, H. Xu, J. Ma, Y. Huang, W. Luo
Promoting High-Voltage Stability through Local Lattice Distortion of Halide Solid Electrolytes
Nat. Commun., **15** 1481 (2024).

144 K. Komatsu, T. Hattori, S. Klotz, S. Machida, K. Yamashita, H. Ito, H. Kobayashi, T. Irifune, T. Shinmei, A. Sano-Furukawa, H. Kagi
Hydrogen Bond Symmetrisation in D_2O Ice Observed by Neutron Diffraction
Nat. Commun., **15** 5100 (2024).

145 Q. Yang, X. Yang, Y. Wang, Y. Fei, F. Li, H. Zheng, K. Li, Y. Han, T. Hattori, P. Zhu, S. Zhao, L. Fang, X. Hou, Z. Liu, B. Yang, B. Zou
Brightening Triplet Excitons Enable High-Performance White-Light Emission in Organic Small Molecules via Integrating n–Π/π–Π* Transitions*
Nat. Commun., **15** 7778 (2024).

146 X.-G. Zheng, I. Yamauchi, M. Hagihala, E. Nishibori, T. Kawae, I. Watanabe, T. Uchiyama, Y. Chen, C.-N. Xu
Unique Magnetic Transition Process Demonstrating the Effectiveness of Bond Percolation Theory in a Quantum Magnet
Nat. Commun., **15** 9989 (2024).

147 H. Yoshimochi, R. Takagi, J. Ju, N. D. Khanh, H. Saito, H. Sagayama, H. Nakao, S. Itoh, Y. Tokura, T. Arima, S. Hayami, T. Nakajima, S. Seki
Multistep Topological Transitions among Meron and Skyrmion Crystals in a Centrosymmetric Magnet
Nat. Phys., **20** 1001–1008 (2024).

148 Z. Zeng, C. Zhou, H. Zhou, L. Han, R. Chi, K. Li, M. Kofu, K. Nakajima, Y. Wei, W. Zhang, D. G. Mazzone, Z. Y. Meng, S. Li
Spectral Evidence for Dirac Spinons in a Kagome Lattice Antiferromagnet
Nat. Phys., **20** 1097–1102 (2024).

149 N. Kitamura, H. Matsubara, K. Kimura, I. Obayashi, Y. Onodera, K. Nakashima, H. Morita, M. Shiga, Y. Harada, C. Ishibashi, Y. Idemoto, K. Hayashi
Relationship between Network Topology and Negative Electrode Properties in Wadsley–Roth Phase $TiNb_2O_7$
NPG Asia Mater., **16** 62 (2024).

150 T. Hattori, K. Suzuki, T. Miyo, T. Ito, S. Machida
Development of 0.5 mm Gauge Size Radial Collimators for High-Pressure Neutron Diffraction Experiments at PLANET in J-PARC
Nucl. Instrum. Methods Phys. Res. Sect. Accel. Spectrometers Detect. Assoc. Equip., **1059** 168956 (2024).

151 T. Kanno, K. Ohoyama, H. Nakada, Y. Fukui, K. Yamakawa, S. Hoshi, M. Takano, Y. Kobayashi, Y. Tomimatsu, S. Takahashi, T. Oku, T. Okudaira, R. Kobayashi, S. Takada, M. Harada, K. Oikawa, Y. Inamura, T. Shishido, K. Sato, K. Hayashi
Development of Instruments for Imaging of Local Magnetic Structure by Magnetic Neutron Holography
Nucl. Instrum. Methods Phys. Res. Sect. Accel. Spectrometers Detect. Assoc. Equip., **1064** 169349 (2024).

152 R. Iwai, S. Fukumura, M. Fushihara, Y. Goto, S. Kanda, S. Nishimura, P. Strasser, K. Shimomura, H. Tada, K. S. Tanaka, H. A. Torii
Dual-Mode Rectangular Microwave Cavity for Precision Spectroscopy of Hyperfine Structure in Muonium
Nucl. Instrum. Methods Phys. Res. Sect. Accel. Spectrometers Detect. Assoc. Equip., **1064** 169434 (2024).

153 K. Horie, K. Kamada, M. Mihara, S. Shimizu, A. Yoshikawa
Measurement of Residual μ^+ Polarization in a LaF_3 Scintillating Material for a New μ^+ Polarimeter System
Nucl. Instrum. Methods Phys. Res. Sect. Accel. Spectrometers Detect. Assoc. Equip., **1066** 169606 (2024).

154 M. Teshigawara, Y. Lee, H. Tatsumoto, M. Hartl, T. Aso, E. B. Iverson, G. Ariyoshi, Y. Ikeda, T. Hasegawa
In-situ Measurement of Radiation Driven Back-Conversion from Para to Ortho Liquid Hydrogen State in Cold Moderators at J-PARC
Nucl. Instrum. Methods Phys. Res. Sect. B Beam Interact. Mater. At., **557** 165534 (2024).

155 W. Yoshimune, Y. Higuchi, F. Song, S. Hibi, Y. Matsumoto, H. Hayashida, H. Nozaki, T. Shinohara, S. Kato
Neutron Imaging for Automotive Polymer Electrolyte Fuel Cells during Rapid Cold Starts
Phys. Chem. Chem. Phys., **26** 29466–29474 (2024).

156 G. Che, Y. Fei, X. Tang, Z. Zhao, T. Hattori, J. Abe, X. Wang, J. Ju, X. Dong, Y. Wang, K. Li, H. Zheng
Pressure-Induced Polymerization of 1,4-Difluorobenzene towards Fluorinated Diamond Nanothreads
Phys. Chem. Chem. Phys., **27** 1112–1118 (2025).

157 Z. Huang, W. Wang, H. Ye, S. Bao, Y. Shangguan, J. Liao, S. Cao, R. Kajimoto, K. Ikeuchi, G. Deng, M. Smidman, Y. Song, S.-L. Yu, J.-X. Li, J. Wen
Microscopic Origin of the Spin-Reorientation Transition in the Kagome Topological Magnet $TbMn_6Sn_6$
Phys. Rev. B, **109** 014434 (2024).

158 P. Park, W. Cho, C. Kim, Y. An, M. Avdeev, K. Iida, R. Kajimoto, J.-G. Park
Composition Dependence of Bulk Properties in the Co-Intercalated Transition Metal Dichalcogenide $Co_{1/3}TaS_2$
Phys. Rev. B, **109** L060403 (2024).

159 Y. Gu, X. Li, Y. Chen, K. Iida, A. Nakao, K. Munakata, V. O. Garlea, Y. Li, G. Deng, I. A. Zaliznyak, J. M. Tranquada, Y. Li
In-Plane Multi-q Magnetic Ground State of $Na_3Co_2SbO_6$
Phys. Rev. B, **109** L060410 (2024).

160 S. Zheng, Y. Gu, Y. Gu, Z. Kao, Q. Wang, H. Wo, Y. Zhu, F. Liu, L. Wu, J. Sheng, J. Chang, S. Ohira-Kawamura, N. Murai, C. Niedermayer, D. G. Mazzone, G. Chen, J. Zhao
Interplay between Crystal Field and Magnetic Anisotropy in the Triangular-Lattice Antiferromagnet $NaTmTe_2$
Phys. Rev. B, **109** 075159 (2024).

161 M. Hase, R. Tamura, K. Hukushima, S. Asai, T. Masuda, S. Itoh, A. Dönni
Inelastic Neutron Scattering Studies on the Eight-Spin Zigzag-Chain Compound $KCu_4P_3O_{12}$: Confirmation of the Validity of a Data-Driven Technique Based on Machine Learning
Phys. Rev. B, **109** 094434 (2024).

162 A. Shimoda, K. Iwasa, K. Kuwahara, H. Sagayama, H. Nakao, M. Ishikado, A. Nakao, S. Ohira-Kawamura, N. Murai, T. Ohhara, Y. Nambu
Antiferromagnetic Ordering and Chiral Crystal Structure Transformation in $Nd_3Rh_4Sn_{13}$
Phys. Rev. B, **109** 134425 (2024).

163 P. Miao, X. Jin, W. Yao, Y. Chen, A. Koda, Z. Tan, W. Xie, W. Ji, T. Kamiyama, Y. Li
Persistent Spin Dynamics in Magnetically Ordered Honeycomb-Lattice Cobalt Oxides
Phys. Rev. B, **109** 134431 (2024).

164 S. Holm-Janas, M. Akaki, E. Fogh, T. Kihara, M. D. Le, P. C. Forino, S. E. Nikitin, T. Fennell, A. Painganoor, D. Vaknin, M. Watanabe, N. B. Christensen, H. Nojiri, R. Toft-Petersen
Magnetic Structure and Magnetoelectric Properties of the Spin-Flop Phase in $LiFePO_4$
Phys. Rev. B, **109** 174413 (2024).

165 D. Ueta, Y. Iwata, R. Kobayashi, K. Kuwahara, T. Masuda, S. Itoh
Neutron Scattering Study on Dimerized $4f^1$ Intermetallic Compound Ce_5Si_3
Phys. Rev. B, **109** 205127 (2024).

166 T. Yamaguchi, M. Furo, Y. Sakai, T. Nishikubo, H. Hojo, M. Azuma, K. Oka, D. Mori, Y. Inaguma, M. Mizumaki, K. Yamamoto, J. Kuneš, T. Mizokawa, A. Hariki
Mechanism of Intermetallic Charge Transfer and Bond Disproportionation in $BiNiO_3$ and $PbNiO_3$ Revealed by Hard X-Ray Photoemission Spectroscopy
Phys. Rev. B, **109** 205131 (2024).

167 K. Yadav, K. P, S. Singh, M. Hagihala, K. Mukherjee
Coexistence of Antiferromagnetism and Glassy Magnetic State and Signature of Quantum Interference Effects in the Frustrated Ternary Silicides HoScSi and ErScSi
Phys. Rev. B, **109** 224409 (2024).

168 J. Liao, Z. Huang, Y. Shangguan, B. Zhang, S. Cheng, H. Xu, R. Kajimoto, K. Kamazawa, S. Bao, J. Wen
Spin and Lattice Dynamics in the van Der Waals Antiferromagnet $MnPSe_3$
Phys. Rev. B, **109** 224411 (2024).

169 K. Lee, H. Das, Y. Sakai, T. Nishikubo, K. Shigematsu, D. Ono, T. Koike, N. Kawamura, M. Mizumaki, N. Ishimatsu, M. Azuma
High-Spin Co^{3+} as a Trigger of Weak Ferromagnetism in Co-Substituted $BiFeO_3$
Phys. Rev. B, **110** 024422 (2024).

170 T. Taniguchi, K. Kudo, S. Asano, M. Takahama, I. Watanabe, A. Koda, M. Fujita
Fermi Liquid State in T -Type $La_{1-x/2}Eu_{1-x/2}Sr_xCuO_4$ Revealed via Element Substitution Effects on Magnetism*
Phys. Rev. B, **110** 085116 (2024).

171 S. Araki, K. Iwamoto, K. Akiba, T. C. Kobayashi, K. Munakata, K. Kaneko, T. Osakabe
Ferrimagnetic Structure in the High-Pressure Phase of α–Mn
Phys. Rev. B, **110** 094420 (2024).

172 A. D. Pant, A. Koda, B. Geil, K. Ishida, R. Adhikari, K. Kuwahata, M. Tachikawa, K. Shimomura
Formation and Structure of MuOH in Ice Studied by Muon Spin Rotation
Phys. Rev. B, **110** 104104 (2024).

173 B. Hu, Y. Peng, X. Liu, Q. Li, Q. Gu, M. J. Krogstad, R. Osborn, T. Honda, J. Feng, Y. Li
Absence of Magnetoelastic Deformation in the Spin-Chain Compound $CuBr_2$
Phys. Rev. B, **110** 115142 (2024).

174 K. Kimura, S. Tsutsui, Y. Yamamoto, A. Nakano, K. Kawamura, R. Kajimoto, K. Kamazawa, A. Martin, K. G. Webber, K. Kakimoto, K. Hayashi
Ca-Induced Phonon Softening in $BaTiO_3$ Revealed by Inelastic X-Ray and Neutron Scattering
Phys. Rev. B, **110** 134314 (2024).

175 S. Yano, J. Yang, K. Iida, C.-W. Wang, A. G. Manning, D. Ueta, S. Itoh
Spin Reorientation and Interplanar Interactions of the Two-Dimensional Triangular-Lattice Heisenberg Antiferromagnets h–(Lu, Y) MnO_3 and h–(Lu, Sc) FeO_3
Phys. Rev. B, **110** 134444 (2024).

176 W. Lee, S. Yoon, Y.-S. Choi, S.-H. Do, A. N. Ponomaryov, S. A. Zvyagin, D. Gorbunov, J. Wosnitza, A. Koda, W.-T. Chen, K.-Y. Choi, S. Lee
Quasistatic Magnetism in the Breathing Pyrochlore Antiferromagnets $LiGa_{1-x}In_xCr_4O_8$ (x = 0.2, 0.5)
Phys. Rev. B, **110** 144435 (2024).

177 J. Kumar, R. Roy, D. Ranaut, J. G. Nakamura, S. Kanungo, K. Mukherjee
$YbTaO_4$: A Quasi-Two-Dimensional Frustrated Magnet Possessing Spin Orbit Entangled Kramers Doublet Ground State
Phys. Rev. B, **110** 174420 (2024).

178 M. Ma, P. Bourges, Y. Sidis, J. Sun, G. Wang, K. Iida, K. Kamazawa, J. T. Park, F. Bourdarot, Z. Ren, Y. Li
Ferromagnetic Interlayer Coupling in $FeSe_{1-x}S_x$ Superconductors Revealed by Inelastic Neutron Scattering
Phys. Rev. B, **110** 174503 (2024).

179 Y. Ishii, T. Sakakura, Y. Ishikawa, R. Kiyanagi, J. Lustikova, T. Aoyama, K. Ohgushi, Y. Wakabayashi, H. Kimura, Y. Noda
Nonferroelectric Phase with Loss of Cycloidal Magnetic Structure in $Tb_{0.515}Gd_{0.485}Mn_2O_5$
Phys. Rev. B, **110** 184404 (2024).

180 J. C. Jiao, K. W. Chen, A. D. Hillier, T. U. Ito, W. Higemoto, Z. Li, B. Lv, Z.-A. Xu, L. Shu
μ SR Study on the Noncentrosymmetric Superconductor $NbGe_2$
Phys. Rev. B, **110** 214516 (2024).

181 R. Nakabe, C. J. Auton, S. Endo, H. Fujioka, V. Gudkov, K. Hirota, I. Ide, T. Ino, M. Ishikado, W. Kambara, S. Kawamura, A. Kimura, M. Kitaguchi, R. Kobayashi, T. Okamura, T. Oku, T. Okudaira, M. Okuizumi, J. G. Otero Munoz, J. D. Parker, K. Sakai, T. Shima, H. M. Shimizu, T. Shinohara, W. M. Snow, S. Takada, R. Takahashi, S. Takahashi, Y. Tsuchikawa, T. Yoshioka
High Sensitivity of a Future Search for Effects of P-Odd/T-Odd

Interactions on the 0.75 eV p-Wave Resonance in n $^{\rightarrow}$+ ^{139}La $^{\rightarrow}$ Forward Transmission Determined Using a Pulsed Neutron Beam
Phys. Rev. C, **109** L041602 (2024).

182 T. Okudaira, R. Nakabe, C. J. Auton, S. Endo, H. Fujioka, V. Gudkov, I. Ide, T. Ino, M. Ishikado, W. Kambara, S. Kawamura, R. Kobayashi, M. Kitaguchi, T. Okamura, T. Oku, J. G. Otero Munoz, J. D. Parker, K. Sakai, T. Shima, H. M. Shimizu, T. Shinohara, W. M. Snow, S. Takada, Y. Tsuchikawa, R. Takahashi, S. Takahashi, H. Yoshikawa, T. Yoshioka
Spin Dependence in the p-Wave Resonance of ^{139} $^{\rightarrow}$La + n $^{\rightarrow}$
Phys. Rev. C, **109** 044606 (2024).

183 T. Fujiie, M. Hino, T. Hosobata, G. Ichikawa, M. Kitaguchi, K. Mishima, Y. Seki, H. M. Shimizu, Y. Yamagata
Development of Neutron Interferometer Using Multilayer Mirrors and Measurements of Neutron-Nuclear Scattering Length with Pulsed Neutron Source
Phys. Rev. Lett., **132** 023402 (2024).

184 M. Hiraishi, H. Okabe, A. Koda, R. Kadono, T. Muroi, D. Hirai, Z. Hiroi
Nonmagnetic Ground State in RuO_2 Revealed by Muon Spin Rotation
Phys. Rev. Lett., **132** 166702 (2024).

185 Y. Gu, Y. Gu, F. Liu, S. Ohira-Kawamura, N. Murai, J. Zhao
Signatures of Kitaev Interactions in the van Der Waals Ferromagnet VI_3
Phys. Rev. Lett., **132** 246702 (2024).

186 L. Zhu, H. He, M. Naeem, X. Sun, J. Qi, P. Liu, S. Harjo, K. Nakajima, B. Li, X.-L. Wang
Antiferromagnetism and Phase Stability of CrMnFeCoNi High-Entropy Alloy
Phys. Rev. Lett., **133** 126701 (2024).

187 M. Matsuura, J. Zhang, Y. Kamimura, M. Kofu, K. Edagawa
Singular Continuous and Nonreciprocal Phonons in Quasicrystal AlPdMn
Phys. Rev. Lett., **133** 136101 (2024).

188 Z. Liu, M. Ozeki, S. Asai, S. Itoh, T. Masuda
Chiral Split Magnon in Altermagnetic MnTe
Phys. Rev. Lett., **133** 156702 (2024).

189 M. Zhu, V. Romerio, N. Steiger, S. D. Nabi, N. Murai, S. Ohira-Kawamura, K. Yu. Povarov, Y. Skourski, R. Sibille, L. Keller, Z. Yan, S. Gvasaliya, A. Zheludev
Continuum Excitations in a Spin Supersolid on a Triangular Lattice
Phys. Rev. Lett., **133** 186704 (2024).

190 N. Subotić, M. Takahashi, T. Mochiku, Y. Matsushita, T. Kashiwagi, O. Takeuchi, H. Shigekawa, K. Kadowaki
Single Crystal Growth of FeRh from AuPb Flux
Phys. Rev. Mater., **8** 023401 (2024).

191 K. Taniguchi, P.-J. Huang, H. Sagayama, R. Kiyanagi, K. Ohishi, S. Kitou, Y. Nakamura, H. Miyasaka
Tuning of Spin-Orbit Coupling in Chiral Molecule-Incorporated Two-Dimensional Organic-Inorganic Hybrid Perovskite Copper Halides with Ferromagnetic Exchange Interactions
Phys. Rev. Mater., **8** 024409 (2024).

192 H. Okabe, M. Hiraishi, A. Koda, Y. Matsushita, T. Ohsawa, N. Ohashi, R. Kadono
Nanoscale Dynamics of Hydrogen in VO_2 Studied by μSR
Phys. Rev. Mater., **8** 024602 (2024).

193 H. Yamamoto, O. Ikeda, T. Honda, K. Kimura, T. Aoyama, K. Ohgushi, A. Suzuki, K. Ishii, D. Matsumura, T. Tsuji, S. Kobayashi, S. Kawaguchi, M. d'Astuto, T. Abukawa
Continuous Structural Phase Transition and Antiferromagnetic Order in Ilmenite-Type $NiVO_3$
Phys. Rev. Mater., **8** 094402 (2024).

194 M. Kofu, S. Ohira-Kawamura, N. Murai, R. Ishii, D. Hirai, H. Arima, K. Funakoshi
Magnetic Boson Peak in Classical Spin Glasses
Phys. Rev. Res., **6** 013006 (2024).

195 H. Yamauchi, D. P. Sari, Y. Yasui, T. Sakakura, H. Kimura, A. Nakao, T. Ohhara, T. Honda, K. Kodama, N. Igawa, K. Ikeda, K. Iida, D. Ueta, T. Yokoo, M. D. Frontzek, S. Chi, J. A. Fernandez-Baca, K. M. Kojima, D. Arseneau, G. Morris, B. Hitti, Y. Cai, A. Berlie, I. Watanabe, P.-T. Hsu, Y.-S. Chen, M. K. Lee, A. E. Hall, G. Balakrishnan, L.-J. Chang, S. Shamoto
Quantum Critical Behavior of the Hyperkagome Magnet Mn_3CoSi
Phys. Rev. Res., **6** 013144 (2024).

196 T. Nakajima, M. Watanabe, Y. Inamura, K. Matsui, T. Kanda, T. Nomoto, K. Ohishi, Y. Kawamura, H. Saito, H. Tamatsukuri, N. Terada, Y. Kohama
Stroboscopic Time-of-Flight Neutron Diffraction in Long Pulsed Magnetic Fields
Phys. Rev. Res., **6** 023109 (2024).

197 D. Sarenac, G. Gorbet, C. Kapahi, C. W. Clark, D. G. Cory, H. Ekinci, D. V. Garrad, M. E. Henderson, M. G. Huber, D. Hussey, P. A. Kienzle, J. D. Parker, R. Serrat, T. Shinohara, F. Song, D. A. Pushin
Cone Beam Neutron Interferometry: From Modeling to Applications
Phys. Rev. Res., **6** 023260 (2024).

198 J. Nagl, D. Flavián, S. Hayashida, K. Yu. Povarov, M. Yan, N. Murai, S. Ohira-Kawamura, G. Simutis, T. J. Hicken, H. Luetkens, C. Baines, A. Hauspurg, B. V. Schwarze, F. Husstedt, V. Pomjakushin, T. Fennell, Z. Yan, S. Gvasaliya, A. Zheludev
Excitation Spectrum and Spin Hamiltonian of the Frustrated Quantum Ising Magnet Pr_3BWO_9
Phys. Rev. Res., **6** 023267 (2024).

199 D. Sarenac, G. Gorbet, C. W. Clark, D. G. Cory, H. Ekinci, M. E. Henderson, M. G. Huber, D. S. Hussey, C. Kapahi, P. A. Kienzle, Y. Kim, A. M. Long, J. D. Parker, T. Shinohara, F. Song, D. A. Pushin
Phase and Contrast Moiré Signatures in Two-Dimensional Cone Beam Interferometry
Phys. Rev. Res., **6** L032054 (2024).

200 S. Shamoto, H. Yamauchi, K. Iida, K. Ikeuchi, K. Kaneko, Y.-S. Chen, S. Yano, P.-T. Hsu, M. K. Lee, A. E. Hall, G. Balakrishnan, L.-J. Chang
Magnetic Excitation in the Hyperkagome Antiferromagnet Mn_3RhSi
Phys. Rev. Res., **6** 033303 (2024).

201 Y. Ye, X. Chen, J. Huang, L. Zheng, Q. Tang, L. Long, T. Yamada, M. Tyagi, V. G. Sakai, H. O'Neill, Q. Zhang, N. R. De Souza, X. Xiao, W. Zhao, L. Hong, Z. Liu
Dynamic Entity Formed by Protein and Its Hydration Water
Phys. Rev. Res., **6** 033316 (2024).

202 S. Fukumura, P. Strasser, M. Fushihara, Y. Goto, T. Ino, R. Iwai, S. Kanda, S. Kawamura, M. Kitaguchi, S. Nishimura, T. Oku, T. Okudaira, H. M. Shimizu, K. Shimomura, H. Tada, H. A. Torii
Present Status of Spectroscopy of the Hyperfine Structure and Repolarization of Muonic Helium Atoms at J-PARC
Physics, **6** 877–890 (2024).

203 T. Yamanaka, Y. Nakamoto, M. Sakata, K. Shimizu, T. Hattori
Anisotropic Electrical Conductivity Changes in $FeTiO_3$ Structure Transition under High Pressure
Phys. Chem. Miner., **51** 4 (2024).

204 F. Kaneko, M.-M. Schiavone, H. Iwase, S. Takata, J. Allgaier, A. Radulescu

Microstructural Investigation of the Cooperative Gelation of Syndiotactic Polystyrene and High MW Polyethylene Glycol Di-Methyl Ether in Common Solution in THF
Polymer, **295** 126771 (2024).

205 Y. Shiraki, N. L. Yamada, K. Ito, H. Yokoyama
Adhesion to Untreated Polyethylene by Diffusion: Effect of Polyurethane Adhesive Molecular Weight on Polyethylene Penetration
Polymer, **302** 127073 (2024).

206 T. Komiya, N. L. Yamada, M. Kobayashi
Salt Concentration Dependency of the Hydrated Swollen Structure of Cholinephosphate-Type Polyzwitterion Brushes
Polym. J., (2024).

207 T. Morikawa, K. Ohishi, K. Hiroi, Y. Kawamura, S. Takata, J. Suzuki, T. Nakajima
Development of Polarization Analysis at TAIKAN under Magnetic Field at Low Temperature
Proc. 11th Int. Workshop Sample Environ. Scatt. Facil. ISSE Workshop Nasu 2022, J. Phys. Soc. Jpn., (2024).

208 J. G. Nakamura, A. Koda, H. Li, M. Hiraishi, H. Okabe, S. Nishimura, R. Kadono
Sample Environment for Low Temperature μSR Experiments at MLF, J-PARC
Proc. 11th Int. Workshop Sample Environ. Scatt. Facil. ISSE Workshop Nasu 2022, J. Phys. Soc. Jpn., (2024).

209 S. Takada, M. Fujita, Y. Goto, T. Honda, K. Ikeda, Y. Ikeda, T. Ino, K. Kaneko, R. Kobayashi, M. Okawara, T. Oku, T. Okudaira, T. Otomo, S. Takahashi
Study of Magnetic Environment for Neutron Spin Filters Using Polarized ^{3}He at J-PARC and JRR-3
Proc. 11th Int. Workshop Sample Environ. Scatt. Facil. ISSE Workshop Nasu 2022, J. Phys. Soc. Jpn., (2024).

210 D. Ueta, S. Itoh, T. Masuda, T. Yokoo, T. Nakajima, S. Asai, H. Saito, D. Kawana, R. Sugiura, T. Asami, S. Yamauchi, S. Torii, Y. Ihata, H. Tanino
Sample Environment of the HRC Spectrometer at J-PARC
Proc. 11th Int. Workshop Sample Environ. Scatt. Facil. ISSE Workshop Nasu 2022, J. Phys. Soc. Jpn., (2024).

211 S. Zhang, H. Hayashida, J. D. Parker, J. Suzuki
Advanced Biaxial Tensile State Evaluation Method Using Neutron Bragg-Edge Imaging
Proc. 11th Int. Workshop Sample Environ. Scatt. Facil. ISSE Workshop Nasu 2022, J. Phys. Soc. Jpn., (2024).

212 T. Tominaga
Network Devices Development at BL02 in J-PARC MLF
Proc. 11th Int. Workshop Sample Environ. Scatt. Facil. ISSE Workshop Nasu 2022, J. Phys. Soc. Jpn., (2024).

213 Y. Zhang, S. Morooka, W. Gong, S. Harjo, G. Miyamoto, T. Furuhara
In-situ Characterization of Tempering Behaviors and Alloying Effects on Tempering Kinetics in High-Carbon Martensitic Steels
Proc. Int. Symp. Steel Sci., **2024** 81–87 (2024).

214 R. Ueji, W. Gong, S. Harjo, T. Kawasaki, A. Shibata, Y. Kimura, T. Inoue, N. Tsuchida
Microstructure and Plastic Deformation Behavior of Si-Bearing Bainitic Steels with Different Carbon Contents
Proc. Int. Symp. Steel Sci., **2024** 119–128 (2024).

215 S. Harjo, W. Mao, W. Gong, T. Kawasaki
Deformation Behavior of Ultrafine-Grained TRIP Steel Observed by Neutron Diffraction
Proc. Int. Symp. Steel Sci., **2024** 205–208 (2024).

216 H. Dannoshita, H. Hasegawa, S. Higuchi, H. Matsuda, W. Gong, T. Kawasaki, S. Harjo, O. Umezawa
Role of Dislocation Characteristics on Deformation Behavior of Martensitic Steel Analyzed by Neutron Diffraction
Proc. Int. Symp. Steel Sci., **2024** 209–212 (2024).

217 T. Ito, Y. Ogawa, W. Gong, W. Mao, T. Kawasaki, K. Okada, A. Shibata, S. Harjo
In situ Neutron Diffraction Study to Elucidate Hydrogen Effect on the Deformation Mechanism in Type 310S Austenitic Stainless Steel
Proc. Int. Symp. Steel Sci., **2024** 237–240 (2024).

218 R. Iwai, M. Abe, S. Fukumura, M. Fushihara, Y. Goto, M. Hiraishi, S. Kanda, S. Nishimura, H. Okabe, K. Sasaki, P. Strasser, K. Shimomura, H. Tada, N. Teshima, H. A Torii
Precision muonium spectroscopy
Proc. Muon4Future 2023, 007, (2024).

219 S. Kamioka
J-PARC g-2/EDM experiment, Muon cooling at J-PARC
Proc. Muon4Future 2023, 008, (2024).

220 D. Cortis, D. Pilone, F. Grazzi, G. Broggiato, F. Campana, D. Orlandi, T. Shinohara, O. S. Planell
Functionally Graded Material via L-PBF: Characterisation of Multi-Material Junction between Steels (AISI 316L/16MnCr5), Copper (CuCrZr) and Aluminium Alloys (Al-Sc/AlSi10Mg)
Prog. Addit. Manuf., (2024).

221 K. Mishima, G. Ichikawa, Y. Fuwa, T. Hasegawa, M. Hino, R. Hosokawa, T. Ino, Y. Iwashita, M. Kitaguchi, S. Matsuzaki, T. Mogi, H. Okabe, T. Oku, T. Okudaira, Y. Seki, H. E. Shimizu, H. M. Shimizu, S. Takahashi, M. Tanida, S. Yamashita, M. Yokohashi, T. Yoshioka
Performance of the Fully Equipped Spin Flip Chopper for the Neutron Lifetime Experiment at J-PARC
Prog. Theor. Exp. Phys., **2024** 093G01 (2024).

222 P. Xu, S. Zhang, S. Harjo, S. C. Vogel, Y. Tomota
Principal Preferred Orientation Evaluation of Steel Materials Using Time-of-Flight Neutron Diffraction
Quantum Beam Sci., **8** 7 (2024).

223 O. Sans-Planell, T. Shinohara, F. Grazzi, F. Cantini, Y. Su, Y. Matsumoto, J. D. Parker, I. Manke
Redifining RADEN's High-Resolution Neutron Imaging Capabilities
Rev. Sci. Instrum., **95** 113702 (2024).

224 K. Ninomiya, M. K. Kubo, M. Inagaki, G. Yoshida, I.-H. Chiu, T. Kudo, S. Asari, S. Sentoku, S. Takeshita, K. Shimomura, N. Kawamura, P. Strasser, Y. Miyake, T. U. Ito, W. Higemoto, T. Saito
Development of a Non-Destructive Depth-Selective Quantification Method for Sub-Percent Carbon Contents in Steel Using Negative Muon Lifetime Analysis
Sci. Rep., **14** 1797 (2024).

225 H. Masai, M. Koshimizu, H. Kawamoto, H. Setoyama, Y. Onodera, K. Ikeda, S. Maruyama, N. Haruta, T. Sato, Y. Matsumoto, C. Takahashi, T. Mizoguchi
Combinatorial Characterization of Metastable Luminous Silver Cations
Sci. Rep., **14** 4638 (2024).

226 K. Watanabe, Y. Sugai, S. Hasegawa, S. Tanaka, K. Hitomi, M. Nogami, T. Shinohara, Y. Su, J. D. Parker, W. Kockelmann
Comparison between Carrier Transport Property and Crystal Quality of TlBr Semiconductors
Sci. Rep., **14** 25224 (2024).

227 K. Oikawa, Y. Matsumoto, K. Watanabe, H. Sato, J. D. Parker, T. Shinohara, Y. Kiyanagi
Energy-Resolved Neutron Imaging Study of a Japanese Sword Signed by Bishu Osafune Norimitsu

Sci. Rep., **14** 27990 (2024).

228 K. Shimizu, K. Nishimura, K. Matsuda, S. Akamaru, N. Nunomura, T. Namiki, T. Tsuchiya, S. Lee, W. Higemoto, T. Tsuru, H. Toda
Combining Muon Spin Relaxation and DFT Simulations of Hydrogen Trapping in Al_6Mn
Scr. Mater., **245** 116051 (2024).

229 H. Ying, X. Yang, H. He, A. Yan, K. An, Y. Ke, Z. Wu, S. Tang, Z. Zhang, H. Dong, S. Harjo, T. Ungár, H. Zhu, Q. Sun, X.-L. Wang, S. Lan
Anomalous Dislocation Response to Deformation Strain in CrFeCoNiPd High-Entropy Alloys with Nanoscale Chemical Fluctuations
Scr. Mater., **250** 116181 (2024).

230 K. Watanabe, Y. Sugai, S. Hasegawa, K. Hitomi, M. Nogami, T. Shinohara, Y. Su, J. D. Parker, W. Kockelmann
Comparison Between Neutron Bragg Dip and Electron Backscatter Diffraction Images of TlBr Semiconductors
Sens. Mater., **36** 149 (2024).

231 K. Matsumura, P. Rozier, E. Iwama, K. Ohara, Y. Orikasa, W. Naoi, P. Simon, K. Naoi
Comprehensive Investigation of the Crystal Structure of Cation-Disordered Li_3VO_4 as a High-Rate Anode Material: Unveiling the Dichotomy between Order and Disorder
Small, **20** 2405259 (2024).

232 H. Takagi, T. Yabutsuka, H. Hayashida, F. Song, T. Kai, T. Shinohara, K. Kurita, H. Iikura, N. Yamamoto, M. Nakajima, S. Takai
Tracer Diffusion Coefficient Measurements on NASICON-Type Lithium-Ion Conductor LAGP Using Neutron Radiography between 25°C and 500°C
Solid State Ion., **417** 116716 (2024).

233 S. Tomone, I. Takaaki, S. Harjo, K. Takuro, A. Kazuya
Strain Analysis by Neutron Diffraction on Nb_3Sn Strands in ITER Central Solenoid Conductors of Short and Long Twist Pitch
Supercond. Sci. Technol., **38** 015008 (2025).

234 K. Nagase, K. Yamaoka, R. Shimane, N. Kojima, N. L. Yamada, H. Seto, Y. Fujii
Temperature-Dependent Behavior of Poly(N-Isopropylacrylamide) Brushes via Neutron Reflectometry
Surf. Interfaces, **54** 105268 (2024).

235 E. Nocerino, O. K. Forslund, H. Sakurai, N. Matsubara, A. Zubayer, F. Mazza, S. Cottrell, A. Koda, I. Watanabe, A. Hoshikawa, T. Saito, J. Sugiyama, Y. Sassa, M. Månsson
Na-Ion Dynamics in the Solid Solution $Na_xCa_{1-x}Cr_2O_4$ Studied by Muon Spin Rotation and Neutron Diffraction
Sustain. Energy Fuels, **8** 1424–1437 (2024).

236 K. Matsuda, T. Masumura, T. Tsuchiyama, Y. Onuki, M. Takanashi, T. Maeda, Y. Kawamoto, H. Shirahata, R. Uemori
Reverse Transformation Behavior in Multi-Phased Medium Mn Martensitic Steel Analyzed by in-situ Neutron Diffraction
Tetsu-to-Hagane, **110** 83–88 (2024).

237 M. Koyama, T. Yamashita, S. Morooka, T. Sawaguchi, Z. Yang, T. Hojo, T. Kawasaki, S. Harjo
Microstructure and Plasticity Evolution During Lüders Deformation in an Fe-5Mn-0.1C Medium-Mn Steel
Tetsu-to-Hagane, **110** 197–204 (2024).

238 M. Koyama, T. Yamashita, S. Morooka, Z. Yang, R. S. Varanasi, T. Hojo, T. Kawasaki, S. Harjo
Hierarchical Deformation Heterogeneity during Lüders Band Propagation in an Fe-5Mn-0.1C Medium Mn Steel Clarified through in situ Scanning Electron Microscopy
Tetsu-to-Hagane, **110** 205–216 (2024).

239 T. Yamashita, S. Morooka, W. Gong, T. Kawasaki, S. Harjo, T. Hojo, Y. Okitsu, H. Fujii
Role of Retained Austenite and Deformation Induced Martensite in 0.15C-5Mn Steel Monitored by in-situ Neutron Diffraction Measurement during Tensile Deformation
Tetsu-to-Hagane, **110** 241–251 (2024).

240 S. Uranaka, M. Takanashi, T. Maeda, T. Masumura, T. Tsuchiyama, Y. Kawamoto, H. Shirahata, Y. Kobayashi, R. Uemori
Effects of Retained Austenite upon Softening during Low-Temperature Tempering in Martensitic Carbon Steels
Tetsu-to-Hagane, **110** 621–631 (2024).

241 G. Rovira, A. Kimura, S. Nakamura, S. Endo, O. Iwamoto, N. Iwamoto, Y. Toh, M. Segawa, M. Maeda, T. Katabuchi
Neutron Capture Cross Section Measurement of ^{129}I and ^{127}I Using the NaI(Tl) Spectrometer of the ANNRI Beamline at J-PARC
Eur. Phys. J. A, **60** 120 (2024).

242 T. Kikuchi, T. Tominaga, D. Murakami, N. R. De Souza, M. Tanaka, H. Seto
Detailed Dynamical Features of the Slow Hydration Water in the Vicinity of Poly(Ethylene Oxide) Chains
J. Chem. Phys., **160** 064902 (2024).

243 R. Inoue, Y. Nagata, T. Tominaga, S. Sato, Y. Kawakita, T. Yamawaki, K. Morishima, M. Suginome, M. Sugiyama
Dynamics of Side Chains in Poly(Quinoxaline-2,3-Diyl)s Studied via Quasielastic Neutron Scattering
J. Chem. Phys., **161** 054905 (2024).

244 F. Nemoto, F. Takabatake, N. L. Yamada, S. Takata, H. Seto
Difference in Structural Changes of Surfactant Aggregates near Solid Surface under Shear Flow versus Those in the Bulk
J. Chem. Phys., **161** 164902 (2024).

245 H. Li, Y.-H. Zheng, W. P. Gates, F. J. Villacorta, S. Ohira-Kawamura, Y. Kawakita, K. Ikeda, H. N. Bordallo
Role of Exchange Cations and Layer Charge on the Dynamics of Confined Water
J. Phys. Chem. A, **128** 261–270 (2024).

246 Y. Shinohara, T. Iwashita, M. Nakanishi, N. C. Osti, M. Kofu, M. Nirei, W. Dmowski, T. Egami
Proton Diffusion in Liquid 1,2,3-Triazole Studied by Incoherent Quasi-Elastic Neutron Scattering
J. Phys. Chem. B, **128** 1544–1549 (2024).

247 T. Takamuku, T. Haraguchi, R. Sasaki, Y. Hozoji, K. Sadakane, H. Iwase
Alcohol-Induced Denaturation of Hen Egg White Lysozyme Studied by Infrared, Circular Dichroism, and Small-Angle Neutron Scattering
J. Phys. Chem. B, **128** 4076–4086 (2024).

248 K. Chai, T. Yamaguchi, T. Zuo, J. Tseng, K. Ikeda, Y. Zhou
Structure, Microheterogeneity, and Transport Properties of Ethaline Decoded by X-Ray/Neutron Scattering and MD Simulation
J. Phys. Chem. B, **128** 7445–7456 (2024).

249 T. Takamuku, A. Ogawa, S. Tsutsui, K. Sadakane, H. Iwase, K. Mayumi, K. Ozutsumi
Effects of Heterogeneous Mixing of Imidazolium-Based Ionic Liquids with Alcohols on Complex Formation of Ni(II) Ion
J. Phys. Chem. B, **128** 8567–8577 (2024).

250 Y. Kameda, T. Mimuro, S. Kondo, T. Honda, T. Otomo
Structure of Ion Pair Receptor Combined with Li^+Cl^- in Concentrated Acetonitrile Solutions Studied by Neutron Diffraction with $^6Li/^7Li$ Isotopic Substitution Method
J. Phys. Chem. B, **128** 12533–12539 (2024).

251 T. Kumada, D. Iwahara, S. Nishitsuji, K. Akutsu-Suyama, D. Miura, R. Motokawa, T. Sugita, N. Torikai, N. Amino, T. Oku, M. Takenaka
Interpenetration of Rubber and Silane Coupling Agent on an Inorganic Substrate Revealed by Spin-Contrast-Variation Neutron Reflectivity
J. Phys. Chem. C, **128** 8797–8802 (2024).

252 C. Yu, Y. Kawakita, T. Kikuchi, M. Kofu, T. Honda, Z. Zhang, Z. Zhang, Y. Liu, S. F. Liu, B. Li
Atomic Structure and Dynamics of Organic–Inorganic Hybrid Perovskite Formamidinium Lead Iodide
J. Phys. Chem. Lett., **15** 329–338 (2024).

253 F. Lin, S. Itoh, T. Hirayama, C. Hirooka, Y. Song, K. Fukuzawa, H. Zhang, N. Azuma
Hydration–Lubrication Performance Improvement via Synergistic Effects of Free Polymers and Polymer Brushes
Tribol. Int., **191** 109189 (2024).

254 R. Dronskowski, T. Brückel, H. Kohlmann, M. Avdeev, A. Houben, M. Meven, M. Hofmann, T. Kamiyama, M. Zobel, W. Schweika, R. P. Hermann, A. Sano-Furukawa
Neutron Diffraction: A Primer
Z. Für Krist. - Cryst. Mater., **239** 139–166 (2024).

255 Y. Gomi, K. Takami, R. Mizuno, M. Niikura, Y. Deng, S. Kawase, Y. Watanabe, S.-I. Abe, W. Liao, M. Tampo, I. Umegaki, S. Takeshita, K. Shimomura, Y. Miyake, M. Hashimoto
Muon-Induced SEU Cross Sections of 12-nm FinFET and 28-nm Planar SRAMs
2023 23rd Eur. Conf. Radiat. Its Eff. Compon. Syst. RADECS, 1-4, (2024).

256 T. Nakamura, K. Toh, R. Kiyanagi, T. Ohhara, T. Hosoya, K. Sakasai
Detector Performances of Large Area Scintillator / Wavelength Shifting Fiber Neutron Detectors for SENJU Upgrade at J-PARC MLF
2024 IEEE Nucl. Sci. Symp. NSS Med. Imaging Conf. MIC Room Temp. Semicond. Detect. Conf. RTSD, (2024).

257 K. Toh, T. Nakamura, K. Sakasai, H. Yamagishi
Measurement of pulsed neutrons using real-time data display and storage module in neutron reflectometer at J-PARC MLF
2024 IEEE Nucl. Sci. Symp. NSS Med. Imaging Conf. MIC Room Temp. Semicond. Detect. Conf. RTSD, (2024).

Editorial Board - MLF Annual Report 2024

J-PARC

JAPAN PROTON ACCELERATOR RESEARCH COMPLEX

High Energy Accelerator Research Organization (KEK)
Japan Atomic Energy Agency (JAEA)

http://j-parc.jp/

Materials and Life Science Division
J-PARC Center

https://mlfinfo.jp/en

Comprehensive Research Organization for Science and Society
https://neutron.cross.or.jp/en

J-PARC 24-02